On the Theory of Cell Migration: Durotaxis and Chemotaxis

X. Diego
E. Oñate
M. Chiumenti

Monograph CIMNE Nº-144, June 2014

On the Theory of Cell Migration: Durotaxis and Chemotaxis

X. Diego
E. Oñate
M. Chiumenti

Monograph CIMNE Nº-144, June 2014

International Center for Numerical Methods in Engineering
Gran Capitán s/n, 08034 Barcelona, Spain

INTERNATIONAL CENTER FOR NUMERICAL METHODS IN ENGINEERING
Edificio C1, Campus Norte UPC
Gran Capitán s/n
08034 Barcelona, Spain
www.cimne.com

First edition: June 2014

ON THE THEORY OF CELL MIGRATION: DUROTAXIS AND CHEMOTAXIS
Monograph CIMNE M144

ISBN: 978-84-941686-8-0

Depósito legal: B-15425-2014

Als meus pares

Contents

Preface **9**
Abstract 9
Outline 11
Acknowledgments 15

1 Introduction to cell migration and durotaxis **17**
1.1 Biological relevance and motivation 17
1.2 Experimental motivation 19

2 Mathematical description of the biochemical regulation of cell migration **25**
2.1 Introduction to regulation of cell migration 25
2.2 RhoGTPases distribution and function in cell migration 26
2.3 Mathematical description of RhoGTPase regulation of cell migration 32
2.3.1 Derivation of the reaction-diffusion equations for a regulatory protein 32
2.3.2 General formulation of the RhoGTPase cycle 36
2.3.3 QSSA aproximation and the Edelstein-Keshet Model 41

3 Mathematical description of cell movement **45**
3.1 Deformation, Motion and Momentum balance 45
3.2 Active Viscoelastic Constitutive law for the cytoskeleton 51
3.3 Kinetic model of Focal Adhesions 60

4 Finite Element formulation of the cell migration model **73**
4.1 Updated Lagrangian description of cell migration 74
4.1.1 Problem statement 74
4.1.2 Derivation of the weak form of the governing equations . . 76
4.1.3 Discretization of geometry, test and trial functions 78
4.1.4 Nodal forces, concentrations rates and semi-discrete equations 82

4.2 Solution of the equations . . . 86
4.2.1 Staggered Scheme for the Mechanical-Regulatory Coupling 86
4.2.2 Time integration of the coupled problem . . . 89
4.3 Implementation . . . 95
4.3.1 1D FEM Formulation . . . 95
4.3.2 2D FEM formulation . . . 99

5 Exploring cell response to external stimuli 107
5.1 Spatially heterogeneous external signals . . . 107
5.1.1 Response to Linear Stimulus . . . 109
5.1.2 Response to Reversals of Linear Stimuli . . . 112
5.1.3 Response to a Localized Stimulus . . . 114
5.1.4 Variations of cell size and shape . . . 115
5.2 Analysis of the response to external stimuli . . . 119
5.2.1 Lack of response to secondary signals . . . 119
5.2.2 Emergence of Turing patterns . . . 124
5.3 Crosstalk model and the dynamics of the RhoGTPase system . . . 133
5.3.1 Interaction schemes: notation and definitions . . . 133
5.3.2 Feedback Loops, Turing Instability and adaptation . . . 137

6 Interaction Graph and Reaction Network Dynamics 141
6.1 General conditions for the Stability of RD systems . . . 141
6.1.1 Routh-Hurwitz conditions . . . 144
6.1.2 Expansion of the Characteristic Polynomial . . . 148
6.2 Reaction Graph . . . 152
6.3 Kinetic Matrix and stability . . . 162
6.3.1 $\mathbf{P}_0^+$-matrices and Turing patterns . . . 162
6.3.2 $\mathbf{P}_0^+$-matrices and Reaction Graph structure . . . 166

7 A new class of RhoGTPase polarization models 171
7.1 Theoretical framework: Reaction-Diffusion equations and waves . 171
7.2 A new class of RhoGTPase polarization models . . . 180
7.2.1 Polarization response to external stimuli . . . 185
7.2.2 Experimental evidence on RhoGTPase regulation and the New Class of models . . . 195
7.3 Migratory Response to external stimuli . . . 198
7.3.1 Simulation of Chemotaxis essays . . . 205
7.4 A short digression on Cell Polarization and the Physics of Cell Migration . . . 221
7.4.1 On cell polarization and gradient sensing models . . . 221

7.4.2 On the physics of migration and cell shapes 223

8 A new view on cell durotaxis **229**
8.1 Durotaxis: A simple physical mechanism? 231
8.2 Is cell mechanosesning controlled by strain or stress? Neither . . . 235
8.2.1 Area of Focal Adhesions in real time: theory and measurements 239
8.2.2 Force at Focal adhesions: theory and measurements 243
8.2.3 Stress at Focal Adhesions: theory and measurements 247
8.2.3.1 Constant power hypothesis: final considerations . 254
8.3 How cells integrate mechanical information to detect stiffness gradients? 256
8.3.1 Stiffness Gradient sensing: the mechanism 262
8.3.2 Mechano-induced cell polarization: theory and experiments 267
8.3.3 Durotaxis limits: theory and experiments 275
8.3.4 Migration speed vs rigidity or adhesiveness : theory and observations 280
8.3.5 Durotaxis: theory and observations 285
8.3.6 Why Cells *Durotax?* Why neurons *anti-durotax*? What about mechanics and *Cancer*? 290

9 Conclusions **295**
9.1 Conclusions 295

Bibliography **303**

Preface

Summary

Cell migration is a fundamental element in a variety of physiological and pathological processes. Alteration of its regulatory mechanisms leads to loss of cellular adhesion and increased motility, which are critical steps in the initial stages of metastasis, before a malignant cell colonizes a distant tissue or organ. Consequently, cell migration has become the focus of intensive experimental and theoretical studies; however the understanding of many of its mechanism remains elusive. Cell migration is the result of a periodic sequence of protrusion, adhesion remodeling and contraction stages that leads to directed movement of cells towards external stimuli. The spatio-temporal coordination of these processes depends on the differential activation of the signaling networks that regulate them at specific subcellular locations. Particularly, proteins from the family of small RhoGTPases play a central role in establishing cell polarization, setting the direction of migration, regulating the formation of adhesion sites and the generation of the forces that drive motion.

Theoretical models based on an independent description of these processes have a limited capacity to predict cellular behavior observed in vitro, since their functionality depends intrinsically on the cross-regulation between their signaling pathways. This thesis presents a model of cell migration that integrates a description of force generation and cell deformation, adhesion site dynamics and RhoGTPases activation. The cell is modeled as a viscoelastic body capable of developing active traction and protrusion forces. The magnitude of stresses is determined by the activation level of the RhoGTPases, whose distribution in the cell body is described by a set of reaction-diffusion equations. Adhesion sites are modeled as punctual clusters of transmembrane receptors that dynamically bind and unbind the extracellular matrix depending on the force transmitted to them and the distance with ligands on the substrate.

On the theoretical level, the major findings concern the relationship between the topology of a crosstalk scheme and the properties, as defined in [1], inher-

ited by the associated reaction network as a gradient sensing and regulatory system: *persistent* and *transient polarization* triggered by external gradients, *adaptation* to uniform stimulus, *reversible polarization*, *multi-stimuli response* and *amplification*. This leads to models that remain functional against the biological diversity associated to different cell types and matches the observed cell behaviour in Chemotaxis essays [2, 3, 4, 5]: the capacity of cells to amplify gradients, polarize without featuring Turing patterns of activation, and switch the polarization axis and the direction of migration after the source of the external stimulus is changed. The RhoGTPase model, derived on theoretical premises, challenges a long held view on the mechanisms of RhoGTPase crosstalk and suggests that the role of GDIs, GEFs and GAPs has to be revised. Recent experimental evidence supports this idea[6]. In addition, the model allows to recapitulate a continuous transition between the tear-like shape adopted by *neutrophiles* and the fan-like shape of *keratocytes* during migration [7] by varying the relative magnitudes of protrusion and contraction forces or, alternatively, the strength of RhoGTPase Crosstalk. The second mechanism represents a novel explanation of the different morphologies observed in migrating cells. Differences in RhoGTPase crosstalk strength could be mediated by differences between the activity or concentration of GEFs, GAPs and GDIs in different cell types; an idea that can be explored experimentally.

On cell mechanosensing, a new hypothesis based on a simple physical principle is proposed as the mechanism that might explain the universal preference of cells (bar neurons) to migrate along stiffness gradients. The theory provides a simple unifying explanation to a number of recent observations on force development and growth in real time at cell Focal adhesions [8, 9, 10, 11]. The apparently conflicting results have been attributed to the differences in experimental set-ups and cell types used, and have fueled a longstanding controversy on how cells prove the mechanical properties of the extra-cellular matrix. The predictions of the theory recapitulate these experimental observations, and its founding hypothesis can be tested experimentally. This hypothesis directly suggests the mechanism that could explain the preference of cells to migrate along stiffness gradients, and for the first time, a plausible biological function for its existence. This phenomenon is known as Durotaxis, and its abnormal regulation has been associated to the malignant behaviour of cancer cells.

Dissertation outline

The thesis is structured in three main parts. The first presents the formulation of the Regulatory and Biomechanical modules of the cell migration model, detailing the experimental evidence that supports the founding hypothesis. The second part introduces the numerical techniques used to solve the equations governing the model. The third part of the thesis is devoted to analyze the results of computational experiments replicating experimental essays. The predictions of the model are compared with experimental observations and the biological implications are discussed. A CD containing the movies of the results that are better understood in this form is provided in the physical form of this Thesis or can be submitted upon request to the author. The figures in the main text for which a movie can be found in the accompanying CD are marked with the symbol ⊗ preceding the caption. The contents of the chapters are summarized bellow:

- *Chapter 1*: provides a introduction to cell migration and its biological relevance. Describes how external signals promote cell migration, the main phases of the process and cellular structures involved. Particular attention is devoted to survey experimental essays focused on the study of cell's response to mechanical cues from the environment.

- *Chapter 2*: develops a set of reaction-Diffusion equations that describe the spatio-temporal distribution and activation of the proteins of a Regulatory network in a deforming body. The focus is narrowed to the study of the RhoGTPase proteins, which are central regulators of the migration process. The concept of crosstalk interaction between RhoGTPase proteins is introduced, emphasizing the relationship between experimentally-based hypothesis and the structure of the associated Interaction Scheme.

- *Chapter 3*: presents a mathematical description of cell deformation and motion on planar substrates in a continuum mechanics framework. This framework is used to develop the constitutive laws governing the kinematics and mechanics of the cell body and adhesion sites. Available data on the feedback channels that couple the dynamics of the RhoGTPases, cytsokeleton and adhesion sites is summarized in order to guide their introduction in the model. Based on this evidence, laws describing how the activation level of RhoGTPases determines the forces that drive movement and how adhesion-based signaling might guide the cell response to mechanical cues, are stated.

- *Chapter 4*: develops the Finite Element formulation used to solve the model's equations. From a computational standpoint, cell migration models present

numerous challenges associated to the resolution of the governing equations in a complex geometry that varies over time as the cell migrates and the interaction of multiple subsystems. As a result, theoretical models have been then left with the option of simplifying the process to an extent in which its usefulness to increase our understanding of migration might be compromised, or alternatively, to consider a level complexity that tends to shift the focus to the computational aspects of the problem. The Updated Lagrangian formulation developed here is particularly suited to address these issues. Thus, even though the focus of this work is not computational, the method is comprehensively detailed and formulated in a general way to provide a platform in which alternative models can be considered with relatively modest programming work.

- *Chapter 5*: analysis of the polarization response of a particular model of RhoGTPase regulation to different types of heterogeneous external signals. This model predicts behaviors that are not consistent with experimental evidence. Particularly, appearance of biologically meaningless patterns of RhoGTPase distribution and reduced sensitivity to secondary stimuli. The mathematical basis of this behavior is established and related to the founding hypothesis of the model.

- *Chapter 6*: introduces the analytical tools, drawn from Matrix and Graph Theory, required to establish the conditions that alternative Regulation models must fulfill to not feature the shortcomings discussed earlier.

- *Chapter 7*: a new class of RhoGTPase Regulation models is formulated systematically imposing the constraints derived from the previous results and experimental evidence. The computational experiments of Chapter 5 are repeated using a model of this class, showing the improved polarization response of the New Class of models. More precisely, the New Class of models reproduces *persistent* and *transient polarization* and feature the properties of *adaptation*, *reversible polarization*, *multi-stimuli response* and *amplification* as defined in [1]. The biological implications of the new assumptions and the predictions of the model are particularly relevant for the interpretation of experimental observations of RhoGTPase regulation and in the context of recent experimental essays on Chemotaxis [2, 3, 4, 5]. Mechanisms of determining the morphology of different cell types[7] during migration are investigated cell shape.

- *Chapter 8*: presents an hypothesis that might explain the currently unknown mechanisms underling the almost universal preference of cells to migrate

along gradients of substrate stiffness. The predictions derived from this hypothesis are shown to explain a number of recent observations on force development and growth at cell Focal adhesion[8, 9, 10, 11]. This hypothesis directly leads to suggest the mechanism that could explain the migration of cells along stiffness gradients. The mechanism is implemented in the migration model to compare its predictions with recent Durotaxis essays [12, 13] and suggests the biological function for cell durotaxis.

A cautionary note. Due to the scope of the topics covered, an important effort has been made to make the Chapters as self-contained as possible. The reader with a strong interest in biology is advised to focus on Chapters 7-8 (and the last section of Chapter 3 for the development of the FA model), which contain the more relevant predictions for the interpretation of unaccounted observations of the cell migration process. For the reader with an interest in theoretical modeling in biology and biophysics, Chapter 2-3 present the theoretical framework where the cell migration model is developed and Chapters 7-8 their most relevant predictions, and for those interested in the computational side, the details of the numerical scheme used to solve the cell migration equations are presented in Chapter 4. Finally, those interested in the foundations of the relationship between the spatio-temporal dynamics of regulatory networks, dynamical systems and cell gradient sensing advised to focus on chapters 5-6-7.

Acknowledgments

This has been a long journey. From Barcelona to Chicago and back again, from physics to cell migration, graphs and dynamical systems and back to physics. Not always smooth, and quite solitary.
The first person I'd like to thank is my advisor Eugenio Oñate; during these years he's found the way to strike a perfect balance between pushing me and giving me complete freedom to pursue my research interests. Speaks to his patience and ambition the fact that he, director of a Numerical Methods Institute (CIMNE) and chair of a department of Structures and Material Strength at UPC, managed to keep an interest in a Thesis on cell migration; a topic further removed from his field of expertize can hardly be imagined. I also would like to thank him for giving me the opportunity to go to Chicago, where, amongst other things, I chose the topic of my research. Ah, Chicago, what a wonderful city!

Next, the two persons that have been more important for me to survive this Thesis: Alvar and Carme. Alvar is my brother; since our mother passed away, right when I started my Ph.D, he and his sweetheart Maria have prepared a meal every single Wednesday of every single week for these long years. And organized

Christmas presents, and...everything. In short, after the wreckage they managed to keep us being a family while my father was not doing so well. His reverse psychology is also world-class. Countless times I've gone to him whining with a hackneyed grad-student quip of the type: *"This is going nowhere..."* To which every time he has answered along the following lines:*"Certainly not. Don't be a crybaby. You can quit and live off me, just don't want to hear about it anymore ".*
My father Javier is now doing better, and slowly becoming the best possible flatmate there could be. He's been incredibly supportive in the final writing stages. Hopefully, whenever I defend I'll manage to drag him go out to go fishing or celebrate somehow.

Then there is Carme. She has been my girl for almost the entire duration of my Ph.D. Sadly, we've had our discrepancies right at the end; mostly attributable to me spending too much hours in the lab and putting work before what really matters. I can't make up for that, but I hope that if anyone thinks that what you are about to read is of any value, she will feel that a bit of the success is hers. If not, I only can thank her for showing me the love of mountains, for the mornings of listening her play Beethoven in the piano while I was idling in bed (Amelie's soundtrack, not so much), the laughs, travels... She is wonderful. Her parents Antonio and Montse have been a family to me. In fact, I also have to thank them for letting me spend time secluded at their country-house in the fair town of Canyamars. There, throwing twigs at the fireplace, is where the pineapple hit my head and I came up with a way to make a general regulatory network Turing-stable but feature wave-like solutions.
And of course, my friends. Even in tough times, it is difficult not to have a good time when you hang out with guys that come up with the idea of going to Belfast to watch an amateur boxing tournament organized by the Dockworkers Union. They haven't forgotten about me and keep calling. A subset of them deserve a special mention: the Grupo Salvaje, my basketball team. The weekly game at the Madison has often times been my only escape from the travails of the Thesis. Manolo's, where the third time takes place, my sanatorium, sort of speak. Luis, the owner of the joint in Bac de Roda, is an artist at the grill who never charges as much as he should, and his tapas and gin-tonics are second to none. So, why not, thanks to him too.
A number of other persons have been important at some point during my Ph.D. Blas Echebarria is a physicist at the Technical School of Architecture at UPC, from him I first heard the words *Dynamical system*. He might not know it, but the interest he showed the few times that I visited him to explain what I was doing, out of nowhere, gave me the motivation to keep going. The same goes with Marino Arroyo, from the Applied Mathematics department. Two of the *Gid* people, the meshing engine developed at CIMNE, Abel Coll and Enrique Escolano, have al-

ways been very helpful when I had a question about how to use their program; Alexis Cid, the graphic designer at the institute, has always been willing to help me arrange posters; my labmates have been as far removed from my topic as close in companionship and support. Enrique Ortega and Roberto Flores, two aces of the aeronautics department, always gave me insightful tips in questions related to numerical analysis.

And then there is Vicente Medina and Xavi Martinez, both were friends of my brother from the Escola de Camins in UPC, who now have become associate professors and my friends. Vicente is something else, he is not only an inexhaustible source of wild stories, but also a walking *Enciclopedia* who can always answer you something interesting about any topic from landslides in latin-american rivers to nuclear fusion. And Xavier, who also knows tones of FEM stuff, has been a friend and has kept my feet on the floor.

This work, for better or worse, has involved little human contact and lots of reading; hence, I'd like to thank the authors out there who write good papers, well written, with novel ideas or puzzling results; those few papers that arouse one's curiosity for science and keep you motivated. The U. Schwarz's, the B. Geiger's, A. Hall's, M.Gardel's and many others. I've met some of them in the two PhysCell Congresses that I attended and it was probably the part that I enjoyed the most of this Thesis. Finally, I'd like to sincerely thank James Sharpe, the boss in my new scientific post: this Thesis was basically completed when the publication and serendipitous finding of this experiment [14] in January made me realize that all my theoretical speculations about cell mechano-sensing could actually match a good number of recent observations. His encouragement and understanding during the last month of rushed writing have been important, but more than that, he is the main reason that I am excited and happy to stay in this business.

To conclude, my thoughts go to three persons who I will not be able to hug when I present this Thesis. My beloved uncles Tito and Valeriano, and my mother Silvia. They could've benefited from us knowing a little more about why cells move when they shouldn't. If this Thesis contributes one bit to that end, it will have been worth it. So, this goes to them.

Xavier Diego

March 3, 2013 Barcelona

"... lest our necessary and highly successful preoccupation with cell fragments and fractions obscure the fact that the cell is not just an inert playground for a few almighty masterminding molecules, but is a system, a hierarchically ordered system, of mutually interdependent species of molecules, molecular groupings, and supramolecular entities; and that life, through cell life, depends on the order of their interactions".

Paul A. Weiss, developmental biologist

Chapter 1

Introduction to cell migration and durotaxis

1.1 Biological relevance and motivation

The study of the migration of biological cells has experienced a revolution in the last decade. The existence of this form of cell movement had been documented by researchers in the area of inflammation and wound healing during the XIXth century and of embryology in the early XXth century. However, the widespread assumption was that cell movement was somewhat subsidiary of the phenomenon of cell division and consequently cell migration attracted little attention. Thirty years ago, the number of observations and experimental data reached a critical stage that allowed the community of biologist to accept the ability to crawl on a solid surface as a fundamental feature of metazoan cells [15]. The pioneering work by Harris and coworkers [16, 17] with fibroblasts migrating on elastic sheets of silicone rubber constituted a turning point on cell migration research. Their observations of the deformations of the substrate surface caused by the fibroblasts movement provided a definitive evidence of the existence of a complex physiological machinery responsible of the generation of strong traction forces during cell crawling. Research groups around the world started to perform similar experiments aimed to understand the biological, biochemical and physical principles underlying cell movement.

The development of new imaging techniques and the outstanding improvement of the experimental methods aimed to explore intracellular events in vivo, lead to the establishment of a general descriptive theory of cell migration as a succession of phases of protrusion, adhesion and contraction. These efforts lead to a partial characterization of the main structures underlying these processes: the different types of cytoskeleton filament networks that support the extension

of new protrusion and contraction structures, molecular motors which in association with cytoskeleton filaments generate the forces that power migration, and Focal adhesion sites, the small clusters of transmembrane receptors in which the cell relies to adhere to the extracellular matrix and to gather biochemical and mechanical information. At the same time, a wealth of new techniques brought about by the advent of genomics and proteomics in the 90's lead to a revolution in molecular cell biology, which lead to the identification of most of the components of the signaling networks that govern cell migration [18]. A particularly important milestone was due to the work of Hall and coworkers, that resulted in the identification of the RhoGTPase proteins as the central orchestrators of cell migration[19]. Nowadays, cell migration is recognized as an essential process in the cell cycle and to have an important role in many diseases. Wound healing and embryological morphogenesis, for instance, depend on the precise distribution and movement of cells to repair the damaged areas and to form the structures that will become organs and tissues, respectively. Conversely, abnormal RhoGTPase function has been associated to the deregulation of cell migration processes that are involved in tumorigenesis and cancer [20] and it also plays a role in cardiovascular disease [21]. The American Cancer Society estimates that 577,190 people in the US will die from cancer in 2012 [22], the leading cause of mortality in persons younger than 85 and with metastasis being the ultimate cause of 90% of these deaths [23]. Elucidating the processes underlying cell migration could lead to the development of therapeutic strategies in cancer treatment. Potential applications in the emerging field of tissue engineering include directing cells to promote healing of spinal chord injuries or bone repair.

Consequently, cell migration has become a central research field in biology and biomedical engineering; nonetheless, the comprehension of many of its mechanism remains elusive. There are several reasons for this. Cell migration relies on the activation of molecular components at restricted subcellular locations at specific times and, also, on the precise coordination of the different migration stages. Traditional biological tools are extremely good at identifying functions and abundances of individual components, but the crossregulation of different cellular structures and the spatio-temporal element that is essential to cell migration can not be addressed by these approaches [18]. Hence, formulation of theoretical models is indispensable to understand how cell migration results from the dynamic interplay of physical and biochemical processes [24]. In addition, the overwhelming complexity of the cellular mechanisms and molecular components uncovered by the flood of data derived from new experimental techniques, defies the intuition and insights gained from qualitative models. Again, computational and theoretical approaches are necessary to integrate the available data into models where experimentally-based hypothesis can be tested and new predictions

made [25]. This problem was brilliantly and humorously illustrated in a recent commentary that considered how traditional biological approaches would fare if applied to the problem of fixing a broken radio[1] [26]. In summary, the importance of cell migration in physiological and pathological processed can not be overemphasized. Great advances made in the experimental techniques allow us to observe the dynamics of subcellular structures, molecular functions and interactions in real time. Theoretical and computational models are needed to integrate these data and might aid to fill the gaps in our understanding of this biological process. To this end, this work aims to shed light on some related open questions: First, cell response to external stimuli depends on the precise distribution of protein activation and dynamic rearrangement of intracellular structures. What are the biophysical mechanisms behind the spatial-temporal organization of cell migration? Second, the signaling networks regulating the different processes taking place during migration are extremely complex. Traditional methods of genetically targeting one molecule and assigning it a function according to the observed cell behavior might overlook dynamical effects emerging at the network-level and feedback loops between proteins in the network. What is the connection between the wiring of a regulatory network, its dynamical behavior, and its function? Finally, focal adhesion sites are known to act as local sensors of the mechanical properties of the extracellular matrix. How do they work? What are the mechanisms behind cell migration along gradients of stiffness?

1.2 Experimental motivation

Cell migration is nowadays recognized as a central element in the cell cycle, with an important role in critical phsysiological processes such as the development of the embryo, the immune response of an organism to infections or wound healing. Conversely, abnormal regulation of cell migration and adhesion are involved in the metastasis stage of cancer, coronary disease and other lethal pathologies. As a consequence, cell migration has become a field that attracts increasing research attention, yet many of its underlying processes remain poorly understood.

Cells remain stationary and adherent to a surface or start migrating depending on external factors. Migration is the cell response to these external cues, that can take the form concentrations of biochemical attractors, topographical features of the environment or variations in density of ligands coating the surface of the extracellular matrix. Directed migration in response to anisotropies of these properties have received the name of *chemotaxis*, *contact guidance* and *haptotaxis*, respectively.

[1]The comparison is not as farfetched as one could think. By an large, the function of signaling transduction pathway and a (russian) transistor are not that different

In recent years, a new type of guiding cue has been discovered to have a central role not only in migration, but also on specifying differentiation, gene expression, apopotosis and many other cell functions: the mechanical properties of the environment. A striking manifestation of this phenomenon was revealed in the experiments performed in 1997[27] and 2000 [28] by Yu Li Wang's group. The earlier essay was the first successful attempt to demonstrate that cells probe and respond to purely mechanical properties of the substrate. The hypothesis was tested by culturing *epithelial normal rat kidney* cells and *3T3 fibbroblasts* on elastic substrates of variable rigidity, coated with a homogeneous distribution of collagen to ensure that the observed response was caused exclusively by mechanical properties. The experiment showed a positive correlation between the rigidity of the substrate and cell spreading, Focal adhesion size and motility. In their second experiment, the addition of a gradient of stiffness showed that *fibroblasts* migrated preferentially towards the more rigid areas, a phenomenon that they called *durotaxis*. Ensuing studies have shown that *durotaxis* seems to be a universal guiding principle of cell migration, since this behavior is shared by virtually all cell types[29, 30] [2] .

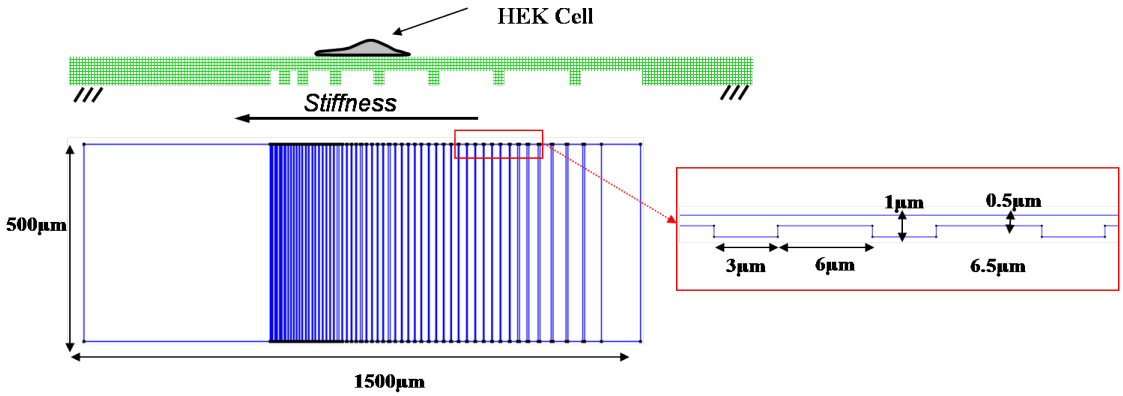

Figure 1.1: Ultra-thin PDMS membrane designed by A.Thangawng *et al.*to perform Durotaxis essays[33]

A related experiment, conducted by Abel Thangawng from Matt's Glucksberg group during my stay as Visiting Student at Northwestern University, provided

[2]The seminal papers by Pelham, Lo and Wang [27, 28] also proved that cells can sense externally applied prestrain on the substrate. The large number of experiments carried on since has established that durotaxis is a general property of animal cells (with the exception of *neurons* where the opposite trend is observed), regardless of cell type, substrate materials, and range of Young's modulus employed. Besides directional movement, the mechanical properties of the substrate have an important influence or determine the stability of Focal Adhesions, cytoskeleton remodeling, signaling pathways, migration speed, cell morphology, apoptosis[31] and metastatasis[32]

further confirmation of this principle and the initial motivation of this Thesis. The interest of the experiment consisted in the fact the stiffness gradient was created by manufacturing ultra-thin elastic membranes that featured a row of increasingly spaced ridges *under* the surface on which the cells were cultured. Therefore, in this case the experimental set-up guaranteed that the observed response was caused strictly by mechanical inputs. After non-confluent populations of *human embryonic kidney* cells were plated on the upper surface and left to migrate for several hours, the final distributions of cells clearly showed a regular trend to accumulate in particular areas of the device.

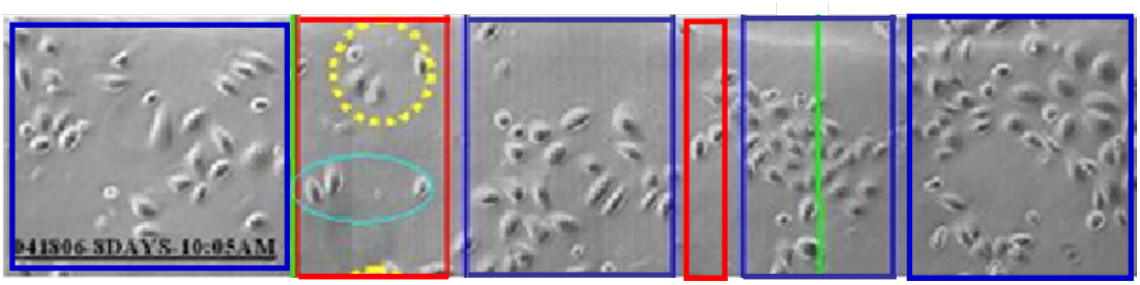

Figure 1.2: Accumulation zones of HEK cells on the PDMS membrane observed by A.Thangawng *et al.*[33] are framed in blue. Yellow and blue circles indicate dead cells and those whose velocity was tracked. Green vertical lines correspond to the areas where the membrane has a constant thickness of 1μm.

The striped pattern of cells accumulated on the membrane surface indicated that the cells had migrated away from certain areas and come to a halt on others. A simple calculation estimating the stiffness profile of the membrane, shown in figure 1.3, revealed the guiding principle: cells were moving towards the regions of higher rigidity, and the zones of cell accumulation matched the areas were the stiffness profile of the membrane was flat. These observations were only preliminary, but ensuing experimental studies are characterizing the cellular processes that bring about cell *durotaxis* with increasing detail: from the relationship between gradient strength, polarization and migration phenotype; rigidity and forces at focal adhesions; to the molecular and genetic factors involved[34, 35, 13, 36, 37, 14, 11, 38, 39]. However, the fundamental mechanisms that allow cells to detect stiffness gradients and trigger migration along them are not known. This Thesis proposes a theory of cell mechano-sensing and *durotaxis*. The predictions of the theory match a number of experimental observations made in the past two years that will be detailed in Chapter 8, and it suggests, to my knowledge for the first time, a plausible biological function for the existence cell *durotaxis*. To provide different cell types with an additional channel of informa-

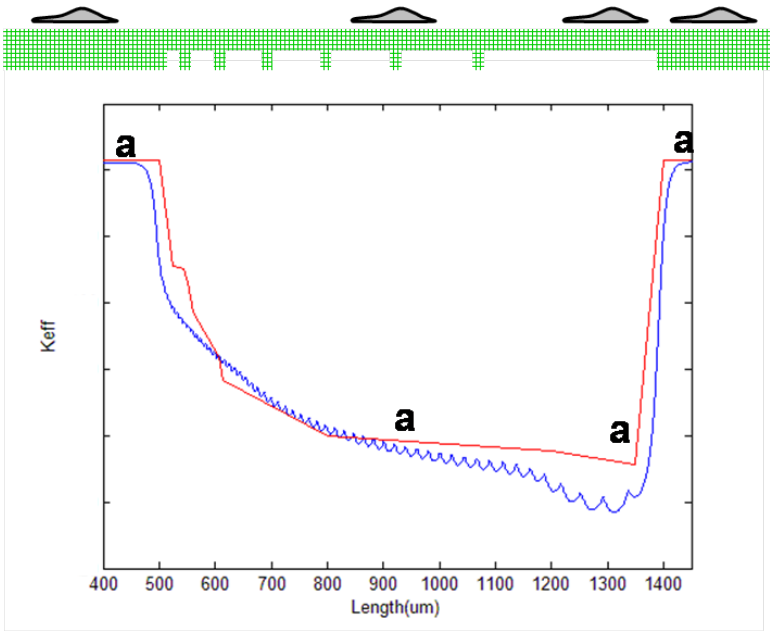

Figure 1.3: Effective Stiffness profile of the PDMS membrane calculated numerically with 1D beam Finite Elements of varying cross section (blue line) and Ansys (red line).

tion to infer its location in an organism and find its way to the tissues that are appropriate for their physiological functions. The capacity of cells to correctly detect its position in an organism is a crucial process in the development of the embryo[40]; conversely, malignant cancer cells have their sensitivity to mechanical properties altered[41, 42], allowing them to proliferate and colonize tissues alien to their function, in which cells under normal conditions would be programmed to die[32, 43, 44, 45]. Indeed, the theory predicts that there are two ranges of rigidities determined by the cell type in which two markedly different behaviors should be observed. First, a lower bound of rigidities bellow which a particular cell type can not establish mature focal adhesions, which is know to lead to *apotosis*. Second, an upper bound of rigidities where cells can no longer detect stiffness gradients and remain stationary and *adherent*, which should match the mechanical properties of the tissues in which this cell type is found in physiological conditions. For the stiffness within these bounds, the theory predicts that cell sensitivity to stiffness gradients is maximized, so that directed migration along the gradient allows cells to move into a position matching the mechanical properties of such tissues.
The experiment previously under discussion also illustrates the main cellular processes and structures that a realistic model of cell migration has to consider,

not only in the context of cell durotaxis but generally. Directed cell migration is powered by a dynamic mesh of cytoskeleton filaments that provide the protrusive and contraction forces that allow the cell move forward[46, 47]. This requires a tight control of the formation and turnover of adhesion sites, known as Focal adhesions[48]. This clusters of transmembrane proteins provide the mechanical link with the substrate, required to pull on the substrate in order to advance. Further, Focal adhesions are known to act as sensing and signaling centers, particularly in the context of migration guided by mechanical cues but also generally[49, 50, 51]. In turn, the dynamical rearrangement of the cytoskeleton and adhesion sites depends on a precise control and spatio-temporal coordination governed by complex regulatory networks. The central node of this network is constituted the family of small RhoGTPases[51, 52], which orchestrate the periodic remodeling of the cytoskeleton and the adhesion sites[53, 54, 55]. Particularly, RhoGTPases are crucial in establishing a polarized state characterized by an asymmetric distribution of protein activities and processes that is required for directed migration.
Therefore, cell migration triggered by external cues comprises the intervention of the corresponding sensing machinery and the dynamic interplay between forces, the cytoskeleton and adhesion sites. These processes are governed and coupled by a complex regulatory and signalling system, which in turn are cross-regulated by the family of small RhoGTPases[56, 57]. Therefore, a complete understanding of cell migration has consider the following set of coupled modules or processes:

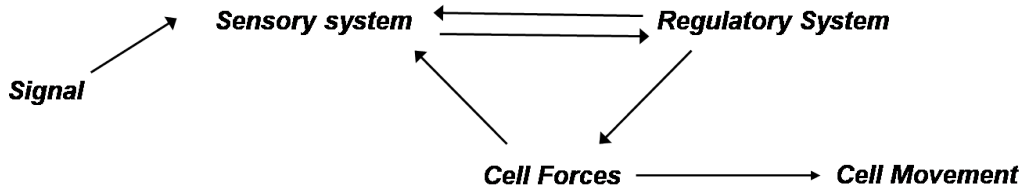

Figure 1.4: Fundamental modules involved in cell migration triggered by external signals. Bidirectional coupling between the sensing machinery and the regulatory system are mediated by the so called mechanisms of outside-in and inside-out signaling. Forces are coupled to these pathways by their influence in the dynamics of focal adhesions

.

Regarding the regulatory apparatus of the cell, the focus is set to study the family of RhoGTPases, whose theoretical description is developed in chapter 2. Certainly, this is an abstraction of a much more complex system, partially justified by the centrality of these proteins in cell migration, and partially, because the goal

is to advance our knowledge of the general principles governing the dynamic spatio-temporal organization of molecular effectors of cell migration.
The focus is further narrowed to two particular forms of cell migration triggered by external cues: *chemotaxis* and *durotaxis*. The sensing machinery involved in durotaxis, namely Focal adhesions, is explicitly modeled, together with a description of force development and cell movement in chapter3. Regarding chemotaxis, the first layer of receptors is lumped into a signal transduced to the RhoGTPases, and the focus is centered on the principles underlying the detection of chemotactic gradients, cell polarization, and movement. These processes are shared by other forms of cell movement, which leads to an idea that will be emphasized throughout this work, and that is the notion of *plasticity* of cell migration[58]. This notion refers to the idea that the different types of cell migration observed *in vivo* and in *in vitro*, characterized by variations in motility mode, morphology, adhesivity and other properties that define the migration of different cell types are manifestations of the different arrangements of a common underlying machinery. This notion is not just an interesting conceptual framework; it will be shown that is fruitful and leads to predictions that can be tested experimentally. Two of the central results of this Thesis stem from this idea. First, the fact that a common modeling framework allows to match the observed behavior of cells in *chemotaxis* and *durotaxis* essays, as discussed in chapters 7 and 8. The idea that common principles govern the cellular response to both types of gradients is in fact increasingly recognized due to the significant analogies observed in experiments[13]. A second example, is the capacity of the theory developed to recapitulate the characteristic shapes of different cell types observed during migration[7]. This result is shown at the end of chapter 7, where a continuous transition from the tear-lie shape of migrating *neutrophile* to the fan-like shape of migrating *keratocytes* is predicted by a varying a single parameter in the model. This result directly suggests a plausible mechanism that might explain the different moprhologies exhibited by cells during migration; for which there is no satisfactory explanation. It also illustrates the power of the idea to find common and unifying principles in biological systems.

If I could remember the names of all these particles, I'd be a botanist.

Enrico Fermi, physicist

Chapter 2

Mathematical description of the biochemical regulation of cell migration

2.1 Introduction to regulation of cell migration

Cell migration is triggered by external signals, such as gradients of mechanical properties in the extracellularmatrix, spatially heterogeneous concentrations of biochemical attractors or matrix ligands, and topological features of the substrate. Movement results from the cyclical succession of phases of protrusion at the cell front, continuous formation and remodeling of adhesion sites and contraction at the trailing edge that are coordinated to generate directed movement towards the stimulus[59].
To migrate, cells adopt a polarized state characterized by a prominent asymmetry between the morphology and signalling activity at the leading front and the trailing edge. Polarization reflects the spatial segregation at the subcellular level of the different biochemical and biomechanical processes taking place at different locations inside the cell. These processes, in turn, generate the different forces and morphological changes at the cell front and rear required to move the cell forward.
At the leading edge of the cell, actin filament polymerisation and depolymerisation produce the protrusive structures and pushing forces required to extend the cell front. Protrusion promotes the formation of integrin-based adhesive contacts that stabilize the new extensions and provide a firm attachment to the substrate. Focal adhesions, in turn, are not only the mechanical links and sensors of extracellular cues, but they are also centers of signalling activity that modulate actin polymerization and the organization of the cytoskeleton. At the cell

back, myosin-II motors associate with actin filaments to generate the contraction forces necessary to disassembly adhesion sites and pull the cell body forward [57]. Hence, effective migration requires exquisite spatial and temporal coordination of the signalling networks that regulate each of these processes.
Intensive research during the last two decades has resulted in the identification of most of the molecular components that form these networks. Comprehensive reviews of the biochemical machinery associated to focal adhesions dynamics [60] and cell migration [61] give an idea of the complexity of the governing signalling networks and the pathways coupling their dynamics during migration. However, it is becoming increasingly clear that identifying individual components, their effectors and targets, and assigning a static and linear effect inferred from experiments to their interactions is not enough to understand how signalling networks operate. This reductionist view is being replaced by one in which the individual components of a regulatory network can generate multiple outcomes due to the combinatorial overlap of their signals, where the topology, feedback structure and spatio-temporal properties are essential to understand their complex dynamics [62]. Particularly, for the networks governing the processes involved in cell migration, the spatial distribution and temporal dynamics of their signalling agents, and the coupling between different networks are a fundamental element of their regulatory function [63]. Amongst the different components of the regulatory apparatus of cell migration, the family of small RhoGTPases is widely recognized as the master determinants of the spatio-temporal organization of the process.
RhoGTPases proteins are the central hub that coordinates the biochemical machinery controlling the establishment of cell polarity, actin-based protrusion and adhesion dynamics. These proteins not only play a critical role in the regulation of cell migration, but also on other fundamental cellular processes such gene expression, differentiation and apoptosis [64]. Despite their biological importance and the extensive efforts aimed at their study, our understanding of mechanisms that govern their regulatory function remains incomplete[56, 65]. The biological relevance of improving our understanding of the RhoGTPase cycle can not be overemphasized, given their implication in cardiovascular disease [21] and cancer [66, 20].

2.2 RhoGTPases distribution and function in cell migration

The proteins of the family of small RhoGTPases are found in all eukaryotic cells, from the most primitive organisms such as yeast, to multicelular organisms like mammals. Three members of the family, Cdc42, Rac and RhoA are known act

as central regulators of the fundamental modules of cell migration, including the spatial polarization of signalling pathways, actin cytoskeleton reorganization and focal adhesion dynamics[55].
These processes are governed by the activation RhoGTPase proteins at specific subcellular locations, where their activity is required. During migration, RhoGTPases are distributed asymmetrically in the cell body according their function during migration, with high concentration of active Cdc42 and Rac at the front and high concentration of high RhoA at the back. Cdc42 is recognized as a mas-

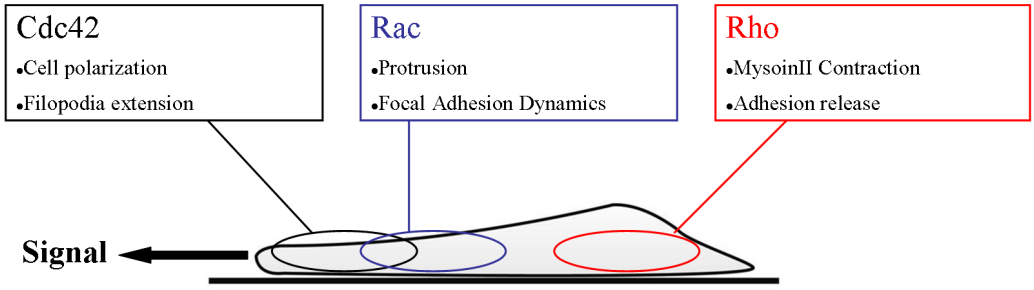

Figure 2.1: Representation of the spatial segregation of RhoGTPases and their function in a migrating cell

ter regulator of cell polarity and limits where the protrusive lamellipodia form. Its inhibition can disrupt the correct alignment of the polarization axis during migration, which suggest that Cdc42 is a direct target of the receptors that sense external cues. Rac and its downstream targets control the biochemical machinery that regulates actin polymerization and protrusion; during migration Rac is maintained active at the cell front. RhoA is responsible of myosin powered contraction of the cytoskeleton at the cell rear [67], and the forces triggered by its signalling activity are a main determinant of the fate of adhesion sites. Formation of small adhesion contacts at the cell front has been associated to Rac activation whereas their maturation at the back is linked to Rho signalling. However, adhesion sites also regulate the activation of the RhoGTPases, in what constitutes a complex bidirectional interaction that is poorly characterized [56]. Particularly, the mechanism by which cells coordinate the activation and inactivation of RhoGTPases and how these processes are spatially restricted to the required locations is an important open question [64].
There are two key levels of regulation in the RhoGTPase cycle, which includes the dynamic regulation of their activation state and their distribution inside the cell. First, the transition of RhoGTPases between different activition states, which is controlled by regulatory enzymes specific for each transition but not necessarily

for each protein. For instance, RhoGTPases could compete to bind the enzymes that activate them or inactivate them, a possibility that is hinted by experiments and also follows from the theoretical arguments presented in this work. Second, the local modulation of the rates of activation due to the interaction between RhoGTPase proteins, also know as crosstalk. It follows that crosstalk is a decisive factor underlying the spatial segregation of activity zones of the RhoGTPases found during migration. In addition, a third level of interaction involves the overlap of the signals of different RhoGTPases to a common target. The combination of their signals could have a different effect than that observed with the available experimental techniques, that usually involve manipulating the signalling activity of only one of the RhoGTPases[6]. The first two levels of the regulation process are discussed in more detail bellow [1]. The activation and inactivation

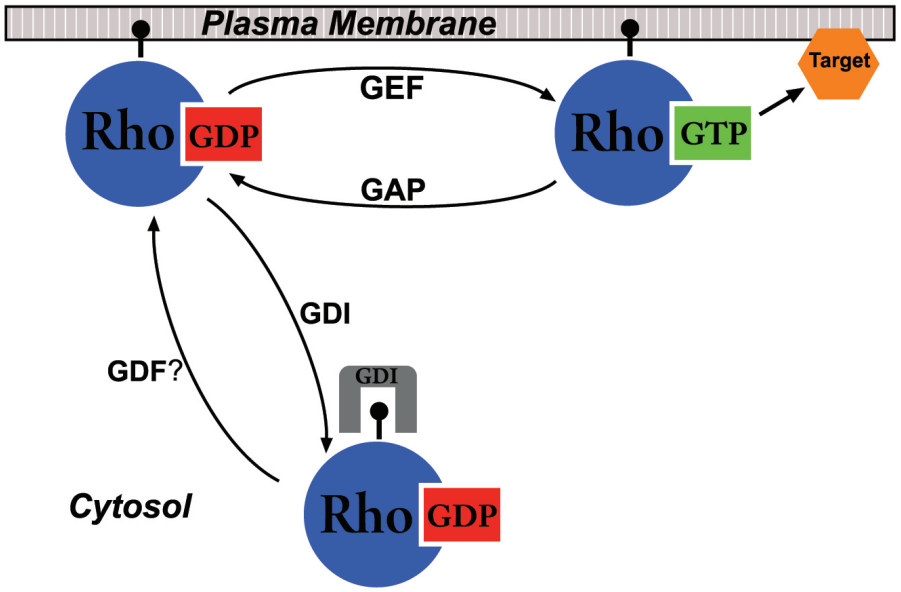

Figure 2.2: Accepted biological model of the RhoGTPase and corresponding reaction equations.

cycle of the RhoGTPases has been compared to a molecular switch: in the Plasma Membrane (PM), RhoGTPase proteins cycle between an inactive state bound to

[1] These two levels of RhoGTPase regulation are better characterized than the crosstalk through the combination of their downstream signals, possibly due to the difficulty of studying it experimentally

GDP and an active state bound to GTP. In addition, they can be removed from the Plasma Membrane and injected into the Cystosol (CS), which effectively acts as a reservoir in which the proteins are stored and from which they can be inserted back in the membrane in other locations of the cell.
Binding GTP activates the RhoGTPases and enables them to interact with downstream targets, setting off a cascade of signals that elicits the processes involved in migration. Since the rate of spontaneous exchange of GDP for GTP in RhoGTPases is very slow, the level of activity is controlled by a set of enzyme families that accelerate the exchange reactions.
Activation is triggered by the a family of enzymes called GEFs, whereas the reverse reaction is catalysed by GAPs. The flow between the membrane and the cytosol is controlled by another group enzymes. GDIs extract the RhoGTPase proteins from the plasma membrane to the Cytosol and keep them locked in the inactive state. Indirect evidence suggests the existence of another regulatory step, in which the RhoGTPase-GDI complexes would be disrupted and inserted back in the plasma membrane by GDFs [68].
The graphic representation of the transitions between states and the enzymes involved in these reaction is shown in figure 2.2. The associated kinetic reactions are shown in the equations (2.1) and (2.2). The reactions in the first set of equations describe the state transitions in the plasma membrane, the first reaction accounts for the inactivation catalyzed by GAPs, whereas the second accounts for the activation transition catalyized by GEFs.

Activation cycle

$$r^{PM}_{GTP} + GAP \xrightarrow{K^{GAP}} r^{PM}_{GDP} \tag{2.1a}$$

$$r^{PM}_{GTP} \xleftarrow{K^{GEF}} r^{PM}_{GDP} + GEF \tag{2.1b}$$

The next two reactions govern the protein flow between the membrane and the cytosol. The first reaction describes the extraction by GDI enzymes of inactive RhoGTPases from the membrane to the cytosol pool, and the second is the reverse reaction that insert the proteins back to the membrane where they can be activated again.

PM - CS transfer

$$r^{PM}_{GDP} + GDI \xrightarrow{K^{GDI}} r^{CS}_{GDP} \tag{2.2a}$$

$$r^{PM}_{GDP} \xleftarrow{K^{GDF}} r^{CS}_{GDP} + GDF \tag{2.2b}$$

A second level of regulation controls where RhoGTPase activation occurs inside the cell. During directed movement, areas of high Cdc42 and Rac activity appear at the cell front and remain low at the back, whereas the opposite distribution is found for RhoA. Polarization is necessary for movement, for each RhoGTPase has to be targeted to specific areas of the cell to perform a particular process [54]. Spatial segregation of areas of high activation of the different proteins is also observed in the processes of wound healing and cell division, showing that spatial organization at the subcelular scale is an essential element of RhoGTPases function [69]. The mechanism underlying the appearance of differentiated activity zones is crosstalk, the activating and inhibiting interactions between the members of the RhoGTPases family.

The generally accepted dogma is that crosstalk is mediated only by the signalling of active RhoGTPases, whose downstream targets modulate the GEF activity associated to the other RhoGTPase members, thereby controlling their activation level [70]. Consequently, a mathematical model based on this hypothesis assumes that the kinetic rates of activation k^{GEF} depend only on the local concentrations of active RhoGTPases. In this state, RhoGTPases are bound to GTP and inserted in the plasma membrane, where transport is slowed down by the lipid bilayer and the presence of embedded proteins. Therefore, the diffusion rates of the only carriers of crosstalk are small, which is an important ingredient of these regulation model, because the signals that they emit remain spatially bounded instead of rapidly spreading to the whole cell. In this way, the standard view on RhoGTPase regulation accounts for the heterogeneous distribution of active proteins found during migration, which stems from the local cross-modulation of the rates of activation by the GTP-bound proteins.

An example of a model based on such hypothesis was suggested by the observations of Giniger's lab [71] and formulated by Jilkine and coworkers [72]. The graphical representation of the interaction scheme is shown in figure 2.3. This interaction scheme assumes that crosstalk is carried out by the dependence of the kinetic rates on the active concentration activated RhoGTPases in the membrane.

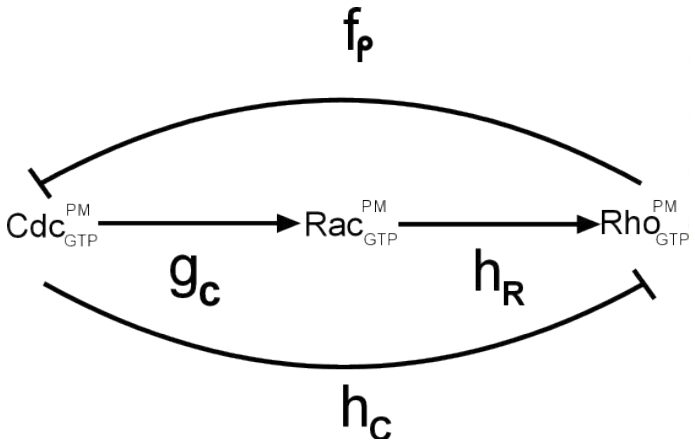

Figure 2.3: Giniger scheme mediated only by active RhoGTPases. Arrows and bars at the end of a line represent up-regulation and down-regulation.

Mathematically, this assumption results in kinetic rates that are functions that depend only of the concentration of active RhoGTPases.

$$k^{\mathrm{GEF}} = k^{\mathrm{GEF}}(\mathrm{r}^{\mathrm{PM}}_{\mathrm{GTP}}) \tag{2.3}$$

where $\mathrm{r}^{\mathrm{PM}}_{\mathrm{GTP}}$ represents the concentration of activated Cdc42, Rac, or Rho. In this view, the kinetic rates affecting the speed of inactivation or endocytosis[2] of a RhoGTPase protein are not influenced by the concentrations of the other proteins. Increasing experimental evidence showing that GAPs and GDIs are active players in Rho regulation, added to the theoretical arguments presented in the remaining of this thesis, lead to propose a new class of interaction schemes, in which the reaction rates associated to GAPs and GDIs are also actively regulated by RhoGTPase signaling.

$$k^{\mathrm{GEF}} = k^{\mathrm{GEF}}(\chi) \tag{2.4a}$$

$$k^{\mathrm{GAP}} = k^{\mathrm{GAP}}(\chi) \tag{2.4b}$$

$$k^{\mathrm{GDI}} = k^{\mathrm{GDI}}(\chi) \tag{2.4c}$$

where the variable χ can represent the concentrations of $\mathrm{r}^{\mathrm{PM}}_{\mathrm{GTP}}$, $\mathrm{r}^{\mathrm{PM}}_{\mathrm{GDP}}$ or $\mathrm{r}^{\mathrm{CS}}_{\mathrm{GDP}}$.

[2]Extraction of a proteins from the membrane to the cytosol

2.3 Mathematical description of RhoGTPase regulation of cell migration

The remaining of this chapter presents a mathematical description of the RhoGTPase cycle that provides a general framework to formulate alternative models of RhoGTPase regulation. Their predictions might allow to validate or refute the underlying hypothesis on crosstalk mechanisms and on the existence of interaction pathways between members of the network.

2.3.1 Derivation of the reaction-diffusion equations for a regulatory protein

The general form of the equation describing the dynamics of a signaling molecule inside the deforming body of a cell is derived in this section. This mathematical framework will then be used to formulate a general description of the RhoGTPase cycle in which particular hypothesis can be implemented to validate or rule out alternative models.
A starting assumption is that the number of molecules is large and can be described by a continuous concentration field. In this description, fluctuations and the stochastic nature of biochemical reactions are not considered, although they could be included adding a noise term. Let Δa be the number of molecules contained in a small material portion of the cell body that at time t occupies the volume $\Delta\Omega_t$. The concentration field is then defined as:

$$r(x,t) = \lim_{\Delta\Omega_t \to 0} \frac{\Delta a}{\Delta\Omega_t} \tag{2.5}$$

The total number of molecules contained at any time t in the an arbitrary material volume Ω_t is given by:

$$a = \int_{\Omega_t} r(x,t) d\Omega \tag{2.6}$$

The change in concentration in Ω_t is driven by diffusive flow of molecules outside the material volume and the reactions that might increase or decrease

its concentration. In addition, the possible volumetric changes of the material volume associated to cell deformation can lead to an effective change in concentration. Active transport by motors or vesicles are not considered.

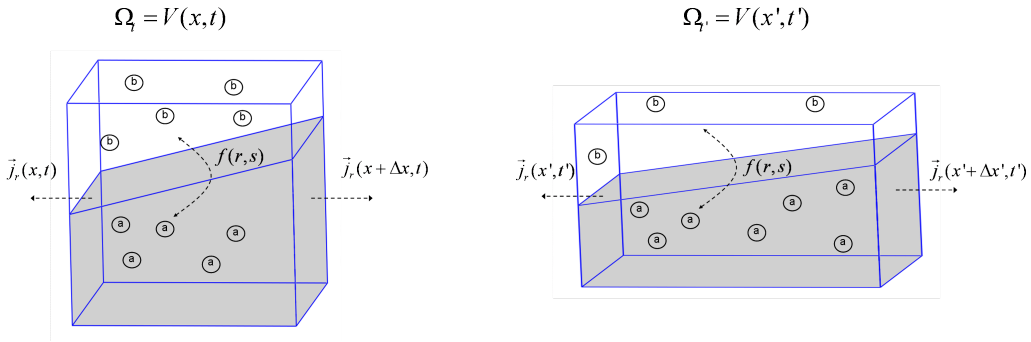

Figure 2.4: Reaction, diffusion and volumetric changes drive the change in concentration

The processes that bring about changes in concentration of the molecule a inside a cell material volume are depicted in figure 2.4.
It has been assumed, for the sake of clarity but without loss of generality, that molecule a undergoes a simple reversible reaction that transforms it into another molecule or state b. The concentration of b in Ω_t is denoted by $s(x,t)$. The biochemical reactions that constitute the regulatory machinery of cell migration are assumed to follow the Mass Action Law, so that the variables that determine the reaction rates are the concentration of the reactants. Hence, in the example reaction involving molecules a and b, the reaction term $f(r,s)$ is a scalar function of the cocentrations $r = r(x,t)$ and $s = s(x,t)$ equal to the increase or decrease in number of molecules a per unit of time and volume.
The diffusive flow is mathematically described by a vector $\vec{j}_r(x,t)$ that gives the number of molecules per unit of area and time crossing the surface of the material volume in each of the spatial directions. Then, the change in the content of a in the portion of the cell that occupies the volume Ω_t, determined by the processes described above, can be mathematically expressed as:

$$\frac{d}{dt}\int_{\Omega_t} r(x,t)\,d\Omega = \int_{\Omega_t} f(x,t)\,d\Omega - \int_{\Gamma_t} \vec{n}\cdot\vec{j}_r\,d\Gamma \tag{2.7}$$

where Γ_t is the surface boundary of the material volume. The operator $\frac{d}{dt}$ is the material derivative and should not be confused with the standard spatial derivative. The material derivative gives the rate of variation of a property in a material point moving with velocity $v(x,t)$, as opposed to a fixed spatial point, as it would be measured by an observer traveling with the particle.

$$\frac{d}{dt} = \frac{\partial}{\partial t} + v(x,t) \cdot \nabla \tag{2.8}$$

The reason to *follow* the concentrations at a set of *imaginary material points* of the cell is that in a Lagrangian description the system's boundary is automatically tracked as the cell moves[3]. In addition, in the complete model of cell migration, protein concentrations at a particular point of the cell will determine its material property changes and active cell forces. Thus, using a system of reference that follows these *imaginary particles* facilitates the treatment of constitutive laws stating the relationship between protein concentration, forces or any other variable of interest at these points. This is a description known as Updated Lagrangian: balance laws are stated in the deformed configuration of the cell, and measures of protein concentration, physical stress or any other variable are also defined in a fixed spatial reference system, although after formally transforming them to functions of the material coordinates, the solution of the governing equations provides their values at material points. This point will be explained in more detail in Chapter 3, where the constitutive for the cell cytoskeleton is introduced. Taking the material derivative inside the volume integral in the left hand side of eq.2.7 [73, see chapter 5], transforms the balance equation into:

$$\int_{\Omega_t} \left[\frac{dr(x,t)}{dt} + r(x,t)\, \vec{\nabla} \cdot \vec{v}(x,t) \right] d\Omega = \int_{\Omega_t} f(x,t)\, d\Omega - \int_{\Gamma_t} \vec{n} \cdot \vec{j_r}\, d\Gamma \tag{2.9}$$

The divergence theorem allows to transform the surface integral associated to diffusive flow as an integral over the cell volume:

[3] A lagrangian description also facilitates the treatment of history dependent constitutive laws an eliminates the need to deal with convection.

$$\int_{\Gamma_t} \vec{n} \cdot \vec{j_r}\, d\Gamma = \int_{\Omega_t} \vec{\nabla} \cdot \vec{j_r}\, d\Omega \tag{2.10}$$

The diffusive transport of proteins inside the cell cytosol and the plasma membrane is assumed to follows Fick's law.

$$\vec{j_r} = -D_r \vec{\nabla} r(x,t) \tag{2.11}$$

Note that diffusion of molecules in the membrane is slower than in the cytosol due to the obstacles presented by lipid rafts and transmembrane proteins. This results in smaller diffusion constants associated to the flow of biomolecules in the membrane than in the cytosol. Combining the last two equations and inserting them in eq. 2.9, the following expression is obtained:

$$\int_{\Omega_t} [\frac{dr(x,t)}{dt} + r(x,t)\, \vec{\nabla} \cdot \vec{v}(x,t) - f(x,t) - D_r \nabla^2 r(x,t)\,] d\Omega = 0 \tag{2.12}$$

Since this equality holds for any material volume inside the cell, the integrand must vanish and the local form of the balance equation follows:

$$\frac{dr(x,t)}{dt} + r(x,t)\, \vec{\nabla} \cdot \vec{v}(x,t) = f(x,t) + D_r \nabla^2 r(x,t) \tag{2.13}$$

Equation 2.13 is a nonlinear reaction-diffusion equation with a volumetric term associated to the deformation of the cell. Indeed, if $\nabla \cdot \vec{v}(x,t) > 0$ the material volume under consideration expands and the effective concentration of the biomolecules decreases, whereas $\nabla \cdot \vec{v}(x,t) < 0$ is associated to a compression of the volume and an increase in concentration. If the cell is assumed to be incompressible, the second term in 2.13 vanishes because by definition $\nabla \cdot \vec{v}(x,t) = 0$.
Finally, the reaction-diffusion equation governing the spatio-temporal evolution of the concentration of the biomolecule is given in non-dimensional form. Introducing a unit of concentration r_0, a characteristic length of the cell l_{cell}, and a

reference rate of reaction f_0, equation 2.13 becomes:

$$\frac{dr(x,t)}{dt} + r(x,t)\,\vec{\nabla}\cdot\vec{v}(x,t) = f(x,t) + \frac{1}{\Phi^2}\nabla^2 r(x,t) \tag{2.14}$$

The Thiele modulus Φ is a non-dimensional parameter defined as the ratio of characteristic times of reaction to diffusion:

$$\Phi^2 \equiv f_0 \cdot \frac{l_{cell}^2}{D_r} = \frac{T_D}{T_R} \tag{2.15}$$

Thus, the Thiele modulus provides information about which of the processes dominates the dynamics of a reaction-diffusion system. It follows that if $\Phi \gg 1$ the characteristic times of reaction are much shorter and dominate the dynamics of the system, whereas if $\Phi \ll 1$ the dynamics are dominated by diffusion.
In order to simplify the expression of the reaction-diffusion equations in the lagrangian description, the generalized material derivative of a field $\alpha(x,t)$ in particle traveling with velocity $v(x,t)$ is defined as:

$$\frac{\tilde{d}\,\alpha(x,t)}{\tilde{d}t} = \frac{d\alpha(x,t)}{dt} + \alpha(x,t)\nabla\cdot v(x,t) \tag{2.16}$$

In an incompressible material, this operator becomes the standard material derivative.

2.3.2 General formulation of the RhoGTPase cycle

The mathematical counterpart of the Rho GTPase cycle described previously in 2.2 is introduced in this section. The state of the cell's regulatory system is defined by the fraction and spatial distribution of each of the possible forms of Cdc42, Rac and Rho. The concentrations in a particular cell location change as a result of two processes: the transitions between the active an inactive states described in section 2.1, triggered by their associated enzymes, and the diffusion in the Plasma membrane and Cytosol. The reaction rates are assumed to follow the Mass Action Law, and therefore are proportional to the local concentration of RhoGTPases and enzymes. Protein diffusion inside the cell is assumed to follow Fick's law both in the cytosol and the membrane, although in the later is 10-100 times slower,

according to experimental estimations. These assumptions are consistent with the framework developed in the previous section. Therefore, for each of the 3 RhoGTPases, the evolution of the concentration of its three possible states can be described by a set of 3 nonlinear Reaction-Diffusion equations of this form:

$$\frac{\tilde{d}\mathrm{r}^{\mathrm{PM}}_{\mathrm{GTP}}}{\tilde{d}t} = k^{\mathrm{GEF}}\mathrm{r}^{\mathrm{PM}}_{\mathrm{GDP}} - \mathrm{k}^{\mathrm{GAP}}\mathrm{r}^{\mathrm{PM}}_{\mathrm{GTP}} + \frac{d}{\Phi^2}\nabla^2\mathrm{r}^{\mathrm{PM}}_{\mathrm{GTP}} \tag{2.17a}$$

$$\frac{\tilde{d}\mathrm{r}^{\mathrm{PM}}_{\mathrm{GDP}}}{\tilde{d}t} = k^{\mathrm{GAP}}\mathrm{r}^{\mathrm{PM}}_{\mathrm{GTP}} - (k^{\mathrm{GEF}} + k^{\mathrm{GDI}})\mathrm{r}^{\mathrm{PM}}_{\mathrm{GDP}} + k^{\mathrm{GDF}}\mathrm{r}^{\mathrm{CS}}_{\mathrm{GDP}} + \frac{d}{\Phi^2}\nabla^2\mathrm{r}^{\mathrm{PM}}_{\mathrm{GDP}} \tag{2.17b}$$

$$\frac{\tilde{d}\mathrm{r}^{\mathrm{CS}}_{\mathrm{GDP}}}{\tilde{d}t} = k^{\mathrm{GDI}}\mathrm{r}^{\mathrm{PM}}_{\mathrm{GDP}} - k^{\mathrm{GDF}}\mathrm{r}^{\mathrm{CS}}_{\mathrm{GDP}} + \frac{1}{\Phi^2}\nabla^2\mathrm{r}^{\mathrm{CS}}_{\mathrm{GDP}} \tag{2.17c}$$

The non-dimensional diffusion $d = D_{PM}/D_{CS} < 1$ is the ratio between the diffusion rates at the cell membrane and cytosol. The variables r^{y}_{x} denotes the concentration of Cdc42, Rac and Rho when r^{y}_{x} takes the values $\mathrm{r}^{x}_{y} = c^{x}_{y},\ r^{x}_{y},\ \rho^{x}_{y}$, with x = GTP , GDP specifying the state of activation and y = PM , CS the concentrations in the plasma membrane and the cytosol. Thus, the complete model of the RhoGTPases comprises a set of 9x9 PDEs, with each of the proteins described by a subsystem reaction-diffusion equations of the form of 2.17. The kinetic rates k^z of transition between states will be denoted by f^z , g^z and h^z in the subsystems associated to Cdc42, Rac and Rho, respectively, with z = GAP, GEF, GDI, GDF specifying the corresponding transition in the RhoGTPase cycle.

Modulation of the rates of reaction for a particular RhoGTPase by crosstalk is modeled through the variation of the kinetic rates with the concentration of the other proteins, as specified in equation 2.4. This part of the modelling framework is better illustrated with an example. Two previous models proposed by Jilkine et al.[72] and Otsuji et al[74], later analyzed to illustrate the need to revise our views on RhoGTPase regulation, the reactions were assumed to follow Hill kinetics, which leads to kinetic rate coefficients that are nonlinear functions of the proteins involved in crosstalk. The interaction scheme from figure 2.3 is the graphical representation of the crosstalk interaction assumed in Jilkine's model for the RhoGTPases. The interaction scheme postulates that downstream signaling of activated Cdc42 inhibits or downregulates Rho. How is this assumption included in the mathematical description of the system? In this framework, signaling from $c^{\mathrm{PM}}_{\mathrm{GTP}}$ could induce Rho inhibition either by decreasing the kinetic rate h^{GEF} controlling the activation rate of Rho mediated by GEF catalysis, or by increasing h^{GAP}, which represents the inactivation rate of Rho mediated by GAP hydrolysis.

Consequently, the kinetic rates could incorporate the experimentally observed interaction between the two proteins in one of the two following functional forms, consistent with the assumed Hill kinetics:

$$h^{\mathrm{GEF}} = h_0^{\mathrm{GEF}} \frac{1}{1 + (c_{\mathrm{GTP}}^{\mathrm{PM}})^n} \tag{2.18a}$$

$$h^{\mathrm{GAP}} = h_0^{\mathrm{GAP}} \frac{(c_{\mathrm{GTP}}^{\mathrm{PM}})^n}{1 + (c_{\mathrm{GTP}}^{\mathrm{PM}})^n} \tag{2.18b}$$

Hence, the assumed crosstalk scheme guides the selection of the kinetic rates for each protein in any model in this theoretical framework according to this principle. The underlying hypothesis and postulated interactions are then encapsulated in the Kinetic matrix, that includes the kinetic rates of all the reactions taking place in the system:

$$\mathbf{K}(\mathbf{r}) = \mathrm{diag}[\mathbf{F}_C, \mathbf{G}_R, \mathbf{H}_\rho] \tag{2.19}$$

The blocks associated to Cdc42, Rac and Rho in the Kinetic matrix are defined in 2.20. Despite the block diagonal structure of the Kinetic Matrix, the dynamics of the three proteins are coupled through crosstalk, which is reflected in the dependence of the Kinetic matrix on the vector of RhoGTPase concentrations.

$$\mathbf{F}_C = \begin{bmatrix} -f^{GAP} & f^{GEF} & 0 \\ f^{GAP} & -f^{GEF} - f^{GDI} & f^{GDF} \\ 0 & f^{GDI} & -f^{GDF} \end{bmatrix} \tag{2.20a}$$

$$\mathbf{G}_R = \begin{bmatrix} -g^{GAP} & g^{GEF} & 0 \\ g^{GAP} & -g^{GEF} - g^{GDI} & g^{GDF} \\ 0 & g^{GDI} & -g^{GDF} \end{bmatrix} \tag{2.20b}$$

$$\mathbf{H}_\rho = \begin{bmatrix} -h^{GAP} & h^{GEF} & 0 \\ h^{GAP} & -h^{GEF} - h^{GDI} & h^{GDF} \\ 0 & h^{GDI} & -h^{GDF} \end{bmatrix} \tag{2.20c}$$

The definitions of the vector of RhoPTPase concentrations $\mathbf{r}(x,t)$ and the diffusion matrix $\mathbf{D}$ consistent with the ordering and notation adopted for the Kinetic Matrix, are:

$$\mathbf{r} = \left[\begin{array}{cccccccccc} c^{\mathrm{PM}}_{\mathrm{GTP}} & c^{\mathrm{PM}}_{\mathrm{GDP}} & c^{\mathrm{CS}}_{\mathrm{GDP}} & r^{\mathrm{PM}}_{\mathrm{GTP}} & r^{\mathrm{PM}}_{\mathrm{GDP}} & r^{CS}_{\mathrm{GDP}} & \rho^{\mathrm{PM}}_{\mathrm{GTP}} & \rho^{\mathrm{PM}}_{\mathrm{GDP}} & \rho^{\mathrm{CS}}_{\mathrm{GDP}} \end{array} \right] \tag{2.21a}$$

$$\mathbf{D} = \mathrm{diag}[\ d \quad d \quad 1 \quad d \quad d \quad 1 \quad d \quad d \quad 1\ ] \tag{2.21b}$$

The system of reaction-diffusion equations that describe the evolution of the full regulatory system, constituted by the 3 sets of PDE's in 2.17 associated to the three RhoGTPases , is then given in matrix form by:

$$\frac{\tilde{d}\,\mathbf{r}}{\tilde{d}t} = \mathbf{K}(\mathbf{r}) \cdot \mathbf{r} + \frac{1}{\Phi^2}\mathbf{D}\bar{\nabla}^2\mathbf{r} \tag{2.22}$$

The dynamics of the Cdc42, Rac and Rho are coupled through reaction term, whose dependency on the complete concentration vector is shown explicitly in equation 2.22.
An important element of the description is the effect of external stimuli in the activation of the regulatory proteins that govern cell migration. The mechanism of sensing and transduction of external cues involves a complex chain of membrane receptors and mediators that signal to the RhoGTPases and other targets to initiate the migration response. In the models by Jilkine[72] and Otsuji[74], for instance, the cascade of signals induced by the external stimulus is lumped into a function $\mathbf{\Psi}$ that linearly shifts the kinetic rates of activation of the RhoGTPases to $\mathbf{K}(\mathbf{r}) + \mathbf{\Psi}(x,t)$. In the more general framework presented in this Thesis, the stimulus function $\mathbf{\Psi}(x,t)$ represents the spatio-temporal distribution of an external stimulus, such as the concentration of a chemo-attractant or the gradient of stiffness of the extracellular matrix, and the signal is transduced by a primary layer of receptors and modulates the kinetic rates in a generic form $\mathbf{K}(\mathbf{r}) \otimes \mathbf{\Psi}(x,t)$ to be derived later :

$$\frac{\tilde{d}\,\mathbf{r}}{\tilde{d}t} = [\mathbf{K}(\mathbf{r}) \otimes \mathbf{\Psi}(x,t)] \cdot \mathbf{r} + \frac{1}{\Phi^2}\mathbf{D}\bar{\nabla}^2\mathbf{r} \tag{2.23}$$

Hence, independently of the nature of the external signal, the stimulus matrix is assumed to effectively increase or reduce the kinetics rates of one or several RhoGTPases, displacing the equilibrium of the cell's regulatoy system.
Assuming that genetic transcription of new RhoGTPases does occur during the short time spans characteristic of migration and considering that there is no flow of proteins outside the cell, the total amount of each protein is conserved.

$$\mathrm{r}_{\mathrm{TOT}} = \int_{\Omega_{CELL}} (\mathrm{r}^{\mathrm{PM}}_{\mathrm{GTP}} + \mathrm{r}^{\mathrm{PM}}_{\mathrm{GDP}} + \mathrm{r}^{\mathrm{CS}}_{\mathrm{GDP}}) d\Omega \qquad \mathrm{r} = c,\ r,\ \rho \tag{2.24}$$

Consequently, the system of equations 2.23 is solved imposing homogeneous Neumann boundary conditions at the cell membrane.
Stationary cells, unperturbed by external signals, are unpolarized and feature a homogeneous distribution of RhoGTpases. Therefore, the initial state is characterized by a concentration of proteins $\mathbf{r_0}$ that is constant throughout the cell body. Hence, the initial state is an homogeneous steady state of the full reaction-diffusion system. These states are determined by the steady states of the ODE system associated the reaction term in eq. 2.22, called the Kinetic system:

$$\frac{d\mathbf{r}(t)}{dt} = \mathbf{K}[\mathbf{r}(t)] \cdot \mathbf{r}(t) \tag{2.25}$$

where the operator d/dt represents in this case the ordinary time derivative. The concentration values in the initial state $\mathbf{r_0}$ are then found solving the set of algebraic equations $\mathbf{K}(\mathbf{r_0}) \cdot \mathbf{r_0} = 0$. This set of algebraic equations is not independent, due to the conservation of total protein stated in 2.24. In order to obtain the initial state, the initial concentration of $\mathrm{r}^{\mathrm{CS}}_{\mathrm{GDP}}$ can be set to their experimentally measured values.
An important aspect of the model is that the nonlinearity of the kinetic rates might endow the system with several solutions for a given value of the inactive fraction of the proteins. Thus, the equilibrium concentrations of active RhoGTPAses might be different at different parts of the cell, even if the concentration of the fast-diffusing inactive RhoGTPases is uniform or almost uniform. This property, known as multistationarity [75], is a necessary condition for the system

to reproduce cell polarization. Hence, the reaction-diffusion system is required to be multistable, so that there exist at least two stable steady states corresponding to the high an low activation levels found in a polarized cell. The initial state is selected amongst the stable steady states found.

2.3.3 QSSA aproximation and the Edelstein-Keshet Model

The next chapter will analyze the response to external signals of the mathematical model of RhoGTPase regulation proposed by Jilkine, Edelstein-Keshet and coworkers in [72]. A similar and contemporary model proposed by Otsuji[74] and coworkers is not discussed further because is explicitly derived to obtain diffusion-driven instabilities as the underlying mechanism to support RhoGTPase polarization. This mechanism of biological pattern formation, first proposed in a groundbreaking paper by Allan Turing[76] has been proven to orchestrate digital patterning in the early stages of limb morphogenesis[77], but it is not suitable as a mechanism to control the dynamic spatio-temporal organization of protein distribution during migration. Several properties of models based on this pattern-forming mechanism are in clear contradiction with the dynamics observed in migrating cells; this topic will be discussed throughly in the remaining of this Thesis.

This section gives an overview of Jilkine's model and its main hypothesis. This interesting study was one of the first theoretical attempts to describe the complete system of Cdc42, Rac and Rho in the context of cell migration. It is also a paradigm of the dominant view on how RhoGTPases interact and organize in a spatially polarized fashion. New experimental evidence suggest that this view might need to be refined, and the results presented in the chapter 5 point also in this direction.

The model postulates the interaction scheme depicted in 2.3, which is based on experimental observations, as the mechanism of RhoGTPase crosstalk. A central hypothesis is that crosstalk is mediated only by GTP-bound RhoGTPAses, whose signals control the activity of GEF enzymes. This hypothesis has two important consequences: the only kinetic rates that are modulated by crostalk are k^{GEF} , and they are functions only of the activated RhoGTPase concentrations. Thus, the general framework for the kinetic rates given in eq. 2.4 is reduced to:

$$k^{\mathrm{GEF}} = k^{\mathrm{GEF}}(\chi) \qquad \chi = \mathrm{r}^{\mathrm{PM}}_{\mathrm{GTP}} \tag{2.26}$$

The model makes the additional assumption that the flow of inactive RhoGTPases between the plasma membrane and the cytosol is very fast compared with the characteristic times of reactions in the plasma membrane. This hypothesis, known as the quasi-steady state approximation (QSS), is equivalent to assume that r^{CS}_{GDP} and r^{PM}_{GDP} are in quasi-equilibrium.

$$k^{GDI} r^{PM}_{GDP} - k^{GDF} r^{CS}_{GDP} \approx 0 \tag{2.27}$$

Defining the total concentration of inactive protein $r_{GDP} = r^{CS}_{GDP} + r^{PM}_{GTP}$ as the sum of the concentration of inactive protein inserted in the membrane and in the cystosol, r^{PM}_{GDP} and r^{CS}_{GDP} can be expressed in terms of the new variable.

$$r^{PM}_{GDP} = \frac{k^{GDF}}{k^{GDF} + k^{GDI}} r_{GDP} \tag{2.28a}$$

$$r^{CS}_{GDP} = \frac{k^{GDI}}{k^{GDF} + k^{GDI}} r_{GDP} \tag{2.28b}$$

The quasi-steady state approximation leads to a simplification of the system of PDEs describing the dynamics of each protein. Substitution of 2.27 in eqs. 2.17 and addition of the second and third equations allows to replace them by a single equation describing the evolution of the total amount of inactive protein. Thus, the reaction-diffusion equations describing the spatio-temporal distribution of the active and inactive fractions of a RhoGTPase in the QSS approximation become:

$$\frac{\tilde{d} r_{GTP}}{\tilde{d} t} = +(\Psi + k^{GEF})(k^I) r_{GDP} - k^{GAP} r_{GTP} + \frac{d}{\Phi^2} \nabla^2 r_{GTP} \tag{2.29a}$$

$$\frac{\tilde{d} r_{GDP}}{\tilde{d} t} = -(\Psi + k^{GEF})(k^I) r_{GDP} + k^{GAP} r_{GTP} + \frac{D}{\Phi^2} \nabla^2 r_{GDP} \tag{2.29b}$$

where averaged kinetic rates of Insertion k^I and Extraction k^E are defined in terms of the GDI and GDF kinetic coefficients as:

$$k^I \equiv \frac{\mathrm{k}^{\mathrm{GDF}}}{\mathrm{k}^{\mathrm{GDF}} + \mathrm{k}^{\mathrm{GDI}}} \tag{2.30a}$$

$$k^E = \frac{\mathrm{k}^{\mathrm{GDI}}}{\mathrm{k}^{\mathrm{GDF}} + \mathrm{k}^{\mathrm{GDI}}} \tag{2.30b}$$

and the averaged diffusion constant of the inactive fraction is given by:

$$D = k^I \cdot d \ + k^E \cdot 1 \tag{2.31}$$

In the QSS approximation the kinetic matrices defined in 2.20 to express the equations in matrix form take the following structure:

$$\mathbf{K}_{\mathrm{r}} = \begin{bmatrix} -k^{\mathrm{B}} & k^{\mathrm{A}} \\ k^{\mathrm{B}} & -k^A \end{bmatrix} \qquad \mathrm{r} = c\,,\, r\,,\, \rho \tag{2.32}$$

where the combined activation rate is defined as $k^{\mathrm{A}} = k^{\mathrm{GEF}} \cdot k^{\mathrm{I}}$, and k^{GAP} has been renamed k^B to simplify the notation. The Quasy-steady state approximation rests on the assumption that the flow of RhoGTPases between the membrane and the cytosol is very fast. Thus, it is important to remark that if, as the experimental evidence suggests [78] , the flow of proteins between the membrane and the cystosol is actively regulated, the assumption might not hold. Furthermore, even if the transfer of proteins between the membrane and the cytosol is very fast compared to the rest of the kinetic processes, there still might be a mechanism of active control of the ratio of inactive proteins inserted in the membrane to those destined to the cytosol reservoir. The equilibrium point of the two fractions then would be balanced by the modulation of the kinetic rates k^{GDI} and k^{GDF}, controled by signals from the regulatory system of the cell. This scenario can be naturally accommodated in the QSSA framework by considering the explicit dependence of the combined activation rate k^A on the kinetic rates k^{GDI} and k^{GDF} and the current

availability availability of inactive protein in the membrane. This notion will be central in the derivation of an alternative class of RhoGTPase regulatory models that .

In Chapter 5, the polarization response to several types of external stimuli of the Jilkine-Keshet model regulatory model is analyzed. This model and also the model proposed by Otsuji[74] are based on the assumption that Crosstalk is mediated only by GTP-bound RhoGTPases, and that it affects only GEF activity. Certain predictions of this class of models are inconsistent with experimental observations. The shortcomings of such models also indicate that a more sophisticated mechanism regulates RhoGTPase activity during cell migration, and that some of the dominating biological hypothesis need to be refined.

The second central element in which these models are founded is the topology of the Crosstalk scheme, which are constrained as a result of the first hypothesis. These models require the existence of direct feedback loops between the proteins, such as the mutual inhibition loop between Cdc42 and Rho of the scheme proposed by Giniger[71] (depicted fig.2.3) and adopted in the model authored by Jilkine and Edelstein-Keshet[72]. In this study, it is stated that this is a necessary condition for the system to capture the spatial segregation of the RhoGTPases during cell polarization. The switch between the initial homogeneous state and a polarized state is supported by the high level of active Cdc42 that suppresses Rho at one end of the cell, while at the other end the level of Rho is high and suppresses Cdc42. Two main arguments are given to support or disregard alternative models of Crosstalk interaction proposed in the literature. The first is based on the evidence of RhoGTPases inhibitory and activating interactions gathered from experiments; the second is given on theoretical grounds described above, stating that the existence of a mutual inhibition loop is a necessary condition for the system to have multiple equilibrium states and the capacity to reproduce spatial segregation. Regarding the first, it is increasingly clear that the current interpretation of the experiments from which the wiring of the RhoGTPase network is inferred has to be revised, evidenced by recent experimental evidence[6, 79] that will be summarized in section 7.2.2. As to the second, a new Class of Models that bypass these topological requirements is developed in Chapter7. This new Class will be shown to endow the associated RhoGTPase reaction network with properties as a gradient sensing and regulatory system that are not shared by the studies discussed previously, but are, however, observed in experiments.

It seems that if one is working from the point of view of getting beauty in one's equations, and if one has really a sound insight, one is on a sure line of progress.

Paul A.M. Dirac, physicist

Chapter 3

Mathematical description of cell movement

This chapter presents a mathematical model that describes cell deformation and motion during migration. The founding assumption behind this model is that the whole cell can be represented as a continuous material, and accordingly cell kinematics and motion will be described within the framework of continuum mechanics. First, the conservation of momentum in a cell body that deforms and moves over time is stated for a general constitutive law. Motion is the result of the balance between internal forces and external forces. Next, a particular constitutive law is introduced. The cell is modeled as a viscoelastic body capable of developing active traction and protrusion forces. The magnitude of the forces is determined by the activation level of the RhoGTPases, whose distribution in the cell body is described by the set of reaction-diffusion equations introduced in chapter 2. Adhesion sites are modeled as punctual clusters of receptors that dynamically bind and unbind the ECM depending on the force transmitted to them and the ligand-receptor distance.

3.1 Deformation, Motion and Momentum balance

Let Ω_0 be the volume occupied by the cell at time t_0, with Γ_0 denoting the boundary of such volume. The position of every point P in the cell at t_0 is given by a vector $\mathbf{X} = [X_1, ..., X_d]$, where d is the number of spatial dimensions that the model considers and X_i are the components of the position vector in some rectangular coordinate system. The position of the point at t_0 can be used to identify it in subsequent times, and for this reason the vector $\mathbf{X}$ provides a convenient label for every point in the cell, usually known as the material or Lagrangian

coordinates. The position of the cell points at any posterior time t, as the cell moves, is given another vector $\mathbf{x}(t) = [x_1, ..., x_d]$ expressed in the coordinate system introduced previously. The dependence on t of the current position of P has been written explicitly to stress the difference with the material coordinates, that are not dependent on time.

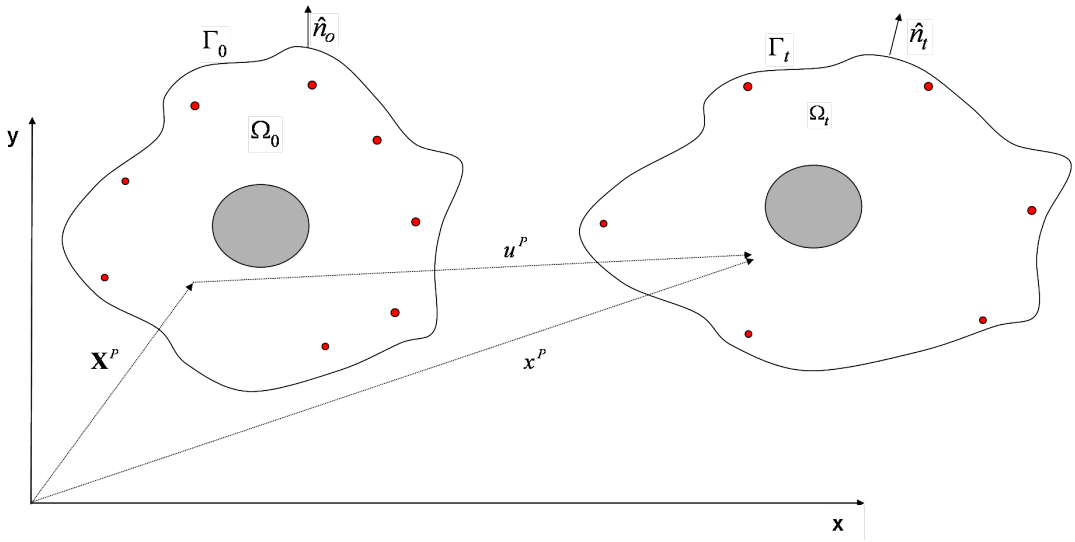

Figure 3.1: Cell modeled as a continuum material. Different structures, such as focal adhesions (red dots) and the nucleus, can be included in this description

The motion of the cell is then fully described by a mapping φ providing the position of the cell material points X at any time:

$$\mathbf{x} = \varphi(\mathbf{X},\mathrm{t}) \qquad \forall \mathbf{X} \in \Omega_0 \tag{3.1}$$

which satisfies the condition $\varphi(\mathbf{X}, 0) = \mathbf{X}$. The deformation of the cell during its motion can be obtained from this mapping. Let P and Q be two neighboring cell material points separated in the initial configuration by the vector $d\mathbf{X}^{PQ}$. In the current configuration, the relative position of these two points changes as the cell deforms, and their relative positions will then be given by another vector $d\mathbf{x}^{PQ}$. This idea leads to the definition of the deformation gradient, a second-order tensor that characterizes the local deformation in the cell continuum:

$$\mathbf{F} = \frac{\partial \mathbf{x}(\mathbf{X}, t)}{\partial \mathbf{X}} \tag{3.2}$$

Deformations are caused by the existence of active forces exerted by the cell and by passive forces that resist the deformation of the cell body. A fundamental hypothesis of continuum mechanics is that the forces at any point inside the continuum can be described defining a second order tensor σ, called the Cauchy stress or physical stress [80, Chap. 1]. Consider an arbitrary plane with unit normal $\hat{n}$ cutting through a point P inside the material. The Cauchy stress principle states that the force per unit area of this plane acting on point P is given by:

$$\hat{n} \cdot \sigma = \mathbf{t} \tag{3.3}$$

where $\mathbf{t}$ is the force per unit area on the plane defined by $\hat{n}$, that is, the traction force or stress. Different assumptions on how the action of forces determines the deformation of the cell, described mathematically by a constitutive relationship $\sigma(\mathbf{F})$ between the stress and some function of the deformation gradient, is the fundamental hypothesis that will define alternative cell models. A viscoelastic constitutive law will be introduced later, but the developments of this section are general.
The value of any other physical property, such as the density, velocity or the concentration of the RhoGTPases, can also be described by the corresponding continuous field $\rho(\mathbf{X},t)$, $\mathbf{v}(\mathbf{X},t)$ and $\mathbf{r}(\mathbf{X},t)$, defined in the whole cell domain for any time $t > t_0$. Particularly, the displacement field $\mathbf{u}(\mathbf{X},t)$ is difference between the position of a particle at the current time and its initial position:

$$\mathbf{u}(\mathbf{X},t) = \mathbf{x}(\mathbf{X},t) - \mathbf{X} \tag{3.4}$$

The velocity is the rate of change in time of the position of the particle, given by the time derivative of the displacement

$$\mathbf{v}(\mathbf{X},t) = \frac{\partial \mathbf{u}(\mathbf{X},t)}{\partial t} \tag{3.5}$$

and the acceleration is the rate of change of the velocity of the cell point:

$$\mathbf{a}(\mathbf{X},\mathrm{t}) = \frac{\partial^2 \mathbf{u}(\mathbf{X},\mathrm{t})}{\partial t^2} \tag{3.6}$$

All these fields have been defined with the material coordinates as their independent variables; for a fixed **X** they provide the time evolution of the corresponding variable at this particular material point. This description is known as Lagrangian, it follows the material points of the body and is commonly reserved for solid-like materials, where a reference to an undeformed configuration is generally needed to define deformation, and stresses at material point might be history-dependent. Alternatively, one could be interested in the value of these fields for a fixed spatial position. In this case, the appropriate description is the Eulerian, in which the fields of interest are defined as functions of the spatial coordinates x as independent variables. A (formal) inversion of the mapping 3.1 allows to switch between these two descriptions.
Conservation of linear momentum, particularly, is naturally stated in the current configuration of the cell using an Eulerian description. Consider a small material volume of the cell body with density $\rho(x,t)$ and moving with velocity $\mathbf{v}(x,t)$ relative to the substrate. This slice of the cell occupies at time t' the space bounded by a surface Γ'_t that encloses a volume Ω'_t. The forces acting on this cube can be divided in external and internal forces, as depicted schematically in figure 3.2:

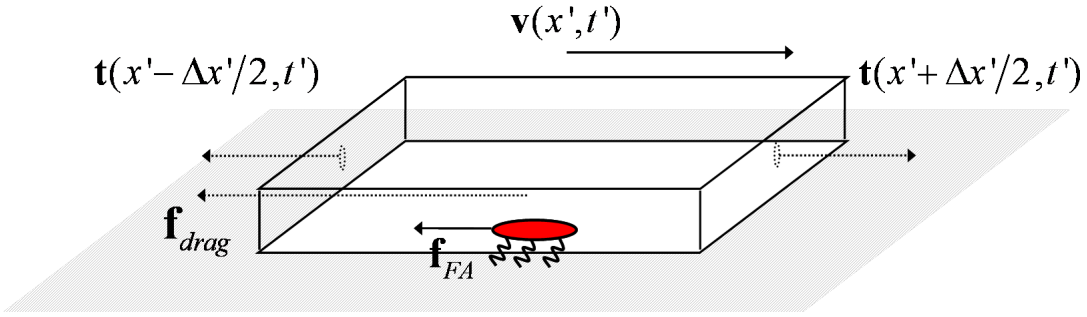

Figure 3.2: Balance of forces acting on an arbitrary cell volume

The internal forces, contained in the traction vector **t**, are the result of the passive response of the cytoskeleton to be deformed and the active stresses generated

by the actin-myosin contractile machinery. The external forces $\mathbf{f}_{drag}$ and $\mathbf{f}_{FA}$ result from two types of adhesion between the cell and the extracellular matrix. First, a non-specific adhesion between the basal part of membrane and the surface on which the cell is moving. This force is modeled as a continuous viscous drag, proportional to the relative velocity between the two surfaces and an effective friction constant β.

$$f_{drag} = -\delta(z)\beta \cdot \mathbf{v} \tag{3.7}$$

The effective constant β is a phenomenological parameter that accounts for the cell substrate-friction, with units of drag per unit of area, that can be estimated from experimental observation.
The second type of external forces acts only if the slice of the cell under consideration contains a Focal adhesion. In this case, an elastic restoring force concentrated at the discrete point where the Adhesion site has been formed arises from the stretch of the bonds between the Focal adhesion receptors and ligands fixed on the substrate. For now, the resultant force is postulated to behave like a Hookean spring, but a detailed description of the mechanics of FA-substrate bonds is developed in the next section that justifies this assumption. The spring constant $k_{FA}(N)$ of the Focal Adhesion is a function of N, the number of receptors bounded to a ligand. Hence, $\mathbf{f}_{FA}$ is proportional to the relative displacement between the current position of the adhesion and the position in which it was originally formed.

$$f_{FA} = -\delta(x_{FA})k_{FA}(N) \cdot (\mathbf{u} - \mathbf{u}_0^{FA}) \tag{3.8}$$

The Dirac delta functions account for the fact that the friction term only acts on the basal surface of the cell, whereas the elastic force associated to Focal adhesions is only present at the discrete points where a an adhesion site provides a mechanical link with the substrate[1].
The balance between the postulated external forces and the internal stresses integrated over the volume Ω_t' determines the resultant of the forces acting on the

[1]Dimensionally, the external forces must have units of force per unit volume. The units of the Dirac Delta function are the inverse of those of the argument, so that $\delta(z)$ and $\delta(x_{FA})$ are respectively L^{-1} and L^{-3}, making the definitions of the external forces consistent.

material cell volume under consideration. Therefore, according to Newton's second law for a continuum, the rate of change of linear momentum of this arbitrary cell volume is given by:

$$\frac{d}{dt}\int_{\Omega_t'} \rho \cdot \mathbf{v} d\Omega = \int_{\Gamma_t'} \mathbf{t}\, d\Gamma - \int_{\Omega_t'} \delta(z)\beta \cdot \mathbf{v} d\Omega - \int_{\Omega_t'} \delta(x_{FA}) k_{FA}(N) \cdot (\mathbf{u} - \mathbf{u}_0^{FA})\, d\Omega \qquad (3.9)$$

where the operator d/dt is the material time derivative introduced in the previous chapter. The last two terms on the right of eq.3.9 are the external forces acting on the material volume. The surface integral associated to the internal stresses can be transformed to a volume integral using Cauchy's law and the divergence theorem:

$$\int_{\Gamma_t'} \mathbf{t}\, d\Gamma = \int_{\Gamma_t'} \hat{n} \cdot \sigma\, d\Gamma = \int_{\Omega_t'} \nabla \cdot \sigma d\Omega \qquad (3.10)$$

The inertial term is transformed inserting the time derivative in the volume integral, using Reynold's theorem and invoking mass conservation [81]:

$$\frac{d}{dt}\int_{\Omega_t'} \rho \cdot \mathbf{v} d\Omega = \int_{\Omega_t'} (\frac{d}{dt}(\rho \cdot \mathbf{v}) + \nabla \cdot \mathbf{v}(\rho \cdot \mathbf{v})) d\Omega = \int_{\Omega_t'} \rho \frac{d\mathbf{v}}{dt} d\Omega \qquad (3.11)$$

The inertial term is usually neglected on the basis that inertial forces are very small compared to the others acting on the cell. This approximation is well justified by the fact that if cells have a density similar to that of water, the inertial forces at the micrometer scale characteristic of biological cells are indeed several orders of magnitude smaller than viscous or adhesion forces. Nonetheless, this term is kept in order to make the developments of this section as general as possible. Substitution of eqs. 3.10 and 3.11 into eq. 3.9 leads to

$$\int_{\Omega_t'} \rho \frac{d\mathbf{v}}{dt} - [\nabla \cdot \sigma - \delta(z)\beta \cdot \mathbf{v} - \delta(x_{FA}) k_{FA}(N) \cdot (\mathbf{u} - \mathbf{u}_0^{FA})] d\Omega = 0 \qquad (3.12)$$

The integrand must vanish because this equation holds for any material volume Ω_t' inside the cell, and the local form of the momentum equation follows:

$$\nabla \cdot \sigma = \rho\, \ddot{\mathbf{u}} + \delta(z)\beta \cdot \dot{\mathbf{u}} + \delta(x_{FA})k_{FA}(N) \cdot (\mathbf{u} - \mathbf{u}_0^{FA}) \tag{3.13}$$

where velocities and acceleration can be expressed in terms of (material) displacement derivatives. The momentum equation is the key equation to describe cell motion. It has been derived under general assumptions to accommodate a wide range of constitutive laws for the cell cytoskeleton and adhesion contacts. The next sections of this chapter present a viscoelastic constitutive law for the cell cytoskeleton and a kinetic equation based on Bell's theory for specific biological adhesion for the adhesion sites[82].

3.2 Active Viscoelastic Constitutive law for the cytoskeleton

This section develops a constitutive law that relates the active and passive stresses generated in the cell to the deformation of the cell body during it motion. The cytoskeleton organizes the molecular contents of the cell spatially, connects the cell physically and biochemically to the environment and also generates the forces required for cell migration[83]. The mechanical properties of the cell are primarily determined by the cytoskeleton, a dynamical and adaptive network of actin, intermediate and microtubule filaments embedded in the cytosol fluid and enclosed by a highly elastic membrane [84]. Amongst the three types of filaments, actin filaments have the most prominent role in force generation for movement.
A large number of regulatory factors controls the dynamical organization of the cytoskeleton: nucleation proteins promote filament formation, capping proteins stop their growth, and severing and depolymerization agents trigger their disassembly. On a higher level of organization, crosslinking and branching proteins bind filaments together and arrange them into different network architectures, and molecular motors associate with them to transport cargo along the filaments and to rearrange the network structures[85]. Particularly, bundled networks of aligned actin filaments and branched networks of actin filaments form the basis of filopodia and lamellipodia protrusions at the cell periphery, which are essen-

tial for the extension of the leading edge of migrating cells[83]. Actin filaments have different biochemical polarity at their tips, called plus and minus ends. This property is essential for the two basic processes associated to the development of the protrusion and contraction forces that drive cell migration. Protrusion force is produced by asymmetric growth of actin filaments caused by the addition of free actin monomers to the plus ends of the filaments and disassembly at the minus end, a mechanism known as treadmilling. The filaments at the cell periphery are oriented preferentially with their plus end toward the plasma membrane, so that when thermal fluctuations create a gap between the filament tip and the membrane, addition of an actin subunit pushes the cell edge forward[86]. Contraction force is also made possible by the polar nature of the filaments. Mysoin-II is a two-headed molecular motor that binds to actin and advances towards the plus end of filaments consuming chemical energy stored in ATP molecules. Effective contraction is generated when a motor binds two filaments in antiparallel configuration, because the advancement of the motor causes the relative sliding of one filament against the other. These two processes are depicted schematically in figure 3.3:

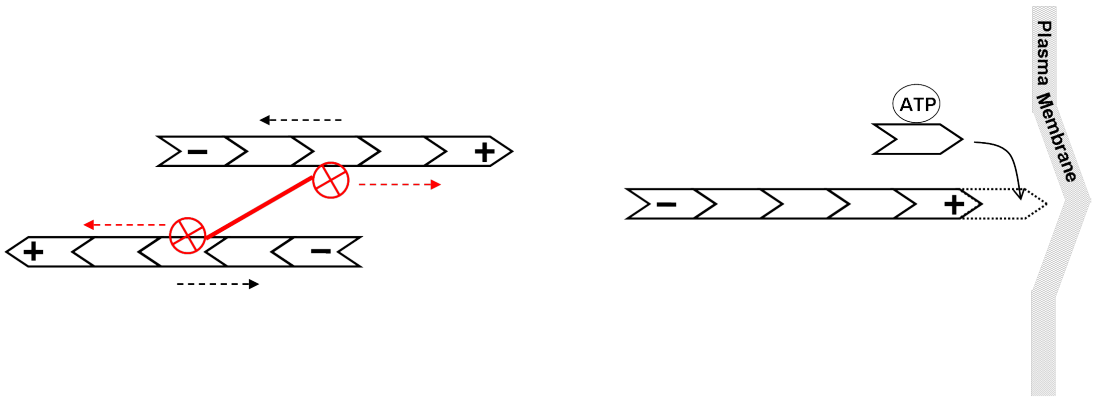

(a) Sliding of antiparallel actin filaments due to Myosin-II non-processive walk toward plus ends

(b) Filament growth by addition of ATP-bound actin subunits at the plus end

Figure 3.3: Basic molecular processes behind force generation in cell migration

A detailed description of the cytoskeleton, going down to the biochemical regulation and filament organization dynamics, is not he focus of this work. Excellent reviews are available on the different modeling efforts of the cytoskeleton, from biophysical models focused on descriptions of actin-networks dynamics[87, Chapter 16], to development of constitutive laws for single cell mechanics [88] and their application to models of cell motility [89]. Rather, the goal of this work is

to develop a constitutive law that, while capturing the qualitative features of cell mechanics and deformation, provides a mathematical framework and test bench where the models of RhoGTPase regulation and discrete Focal adhesions can be integrated in a comprehensive description of cell migration.
From a mechanical point of view the cell can be regarded as crosslinked polymer network. Classical polymer physics provides a description of this type of materials from the fundamental components at the sub-micron scale[90], whereas at a larger scale they are characterized by combining elastic and viscous behavior[91]. The predominance of one type of rheological behavior over the other depends on the lifetime of the polymer crosslinks, the time-scale of interest and the magnitude of the deformation. Biological cells present the additional complexity that the cytoskeleton is an active material that generates forces and responds to external loads rearranging its internal organization[92].
At the experimental level, cell and tissue rheology has become an extensive field of its own, and the measurements broadly support the approximation of the cell as a viscoelastic material. However, the rheological properties of biological cells an tissues are extremely complex, different experimental techniques yield different responses depending on the part and scale of the cell that is being tested[93]. Therefore, it is not possible to fit all the complexity of cellular rheology in a single model or constitutive law [87, Chapter 16], but rather to develop a model that adequately describes the cellular process of interest. The process of cell migration requires a model that captures the elastic and viscous resistance to deform at the whole-cell scale and at time scales of the order of minutes-hours. A Linear viscoelastic model arising from the generalization of mechanical combinations of springs and dashpots fulfills this requirement and keeps unnecessary levels of complexity from the description. The seminal work of Dimilla and Lauffenburger [94] used this approach to develop a model of a 1D cell strip as a combination six mechanical Kelvin-Voigt subunits, with two additional springs at the front and rear to represent discrete links with the substrate.

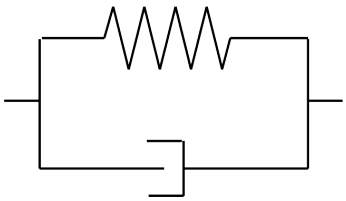

Figure 3.4: A Kelvin-model is formed by a spring and a dashpot in parallel. It is the most simple model that predicts viscous creep

Despite its simplicity, prescribing an asymmetry of the adhesions at the front and the rear, the model was able to explain the observed bell-shaped relationship

between adhesiveness and the velocity of the cell. Gracheva and Othmer [95], as well as Mogilner and coworkers[96] extended this work developing a one dimensional continuum counterpart of the Dimilla model to describe cell crawling. In both cases, discrete adhesions were not considered, and an asymmetry in either the force distribution or the movement of the cell edges was prescribed in order to obtain polarization and directed movement. Following their ideas, a constitutive law is developed extending the simple rheological Kelvin-Voigt model to two dimensions and disregarding the ad hoc introduction of asymmetries in the cell to obtain the desired movement.
A preliminary step in the formulation of the constitutive law involves the choice of the measures of stress and deformation. The choice is limited by the constrains imposed by the principle of material objectivity, which essentially states that a valid constitutive law must not predict the generation of stresses or strains when rigid-body motion is superimposed on the material. A Lagrangian measure of strain is commonly reserved for solid materials, in which the deformations can be naturally defined relative to an undeformed configuration. A description based on Lagrangian measures of stress and strain has the advantage that objectivity is automatically satisfied. However, the definition of an undeformed configuration for the cell cytoskeleton is rather problematic, and the constant rearrangement and flow of the filament networks makes the reference to the deformation of a material line or volume artificial. Therefore, an Eulerian description is adopted, and the appropriate measure of stress is the Cauchy stress σ, introduced in the previous section along with its physical interpretation. The Almansi strain tensor is the object adopted to measure the deformation of cell:

$$\mathbf{e}_{ij} = \frac{1}{2}\left[\frac{\partial u_i}{\partial x_j} + \frac{\partial u_j}{\partial x_i} - \frac{\partial u_k}{\partial x_i}\frac{\partial u_k}{\partial x_j}\right] \tag{3.14}$$

The Almansi strain fulfills the principle of material objectivity. The physical interpretation of the Almansi strain tensor sheds light into the implications of assuming this measure of deformation. Consider a small segment of the cell of original length dL and currently stretched to a length dl and oriented along the direction $\hat{n}$. The stretch of this segment relative to the *current* length is given by the coordinates of the Almansi strain as $\hat{n} \cdot 2\mathbf{e} \cdot \hat{n} = (dl^2 - dL^2)/dl^2$. Thus, a constitutive relationship between σ and $\mathbf{e}$ implies that the stresses in the cytoskeleton arise from the deformation compared to the actual or current configuration of the cell, as opposed to the deformation compared to an original unstressed configuration. The elastic stiffness matrix $\mathbf{E}$ determines the relationship between the

deformation and the elastic component of the stress. The form of the stiffness matrix will be given under the hypothesis of plane stress. This approximation is valid because the thickness of cells in two-dimensional cultures is 1-2 orders of magnitude smaller than its horizontal dimensions, so that the in-plane stresses dominate the migration process and the vertical stresses can be safely neglected. A realistic constitutive law should consider the microstructure of the cytoskeleton, determined by the time-dependent density $a(\theta, \bar{x})$ of actin filaments and their orientation. In this description, the cytoskeleton could be modeled as a fiber-reinforced composite material and described in the framework of serial/parallel mixing theory[97]. The stiffness matrix of this type of materials is the resultant of the contribution of the fibers aligned in different directions. Analogously, consider the cytoskeleton filaments oriented along a direction x' forming an angle θ with the global coordinate system. It is assumed that two Young moduli $E_{x'}$ and $E_{y'}$ and the corresponding Poisson coefficients, could characterize the mechanical response of the filaments along its longitudinal and orthogonal directions. The contribution associated to the filaments with this orientation, expressed in the set of rotated axis (x', y'), takes the form of an orthotropic stiffness matrix under the hypothesis of plane stress [98, Chapter 5]:

$$\mathbf{E}'_\theta = \frac{1}{1 - \upsilon_{x'y'}\upsilon_{y'x'}} \begin{bmatrix} E_{x'} & \upsilon_{x'y'}E_{x'} & 0 \\ \upsilon_{y'x'}E_{y'} & E_{y'} & 0 \\ 0 & 0 & (1 - \upsilon_{x'y'}\upsilon_{y'x'})G_{x'y'} \end{bmatrix} \tag{3.15}$$

This matrix can expressed in the global axis according to the transformation $\mathbf{E}_\theta = \mathbf{T}(\theta)^T \cdot \mathbf{E}'_\theta \cdot \mathbf{T}(\theta)$, where $\mathbf{T}(\theta)$ is the matrix that transforms the stress and strain fields from $(x, y) \rightarrow (x', y')$[98, see pag. 160]. The complete stiffness matrix, defining locally the rheological response of the cytoskeleton, would be the resultant of the sum of all the contributions weighted by the density of filaments $a(x, \theta)$ along each direction:

$$\mathbf{E} = \int_0^{\pi/2} d\theta \, a(x, \theta)[\mathbf{T}(\theta)^T \cdot \mathbf{E}'_\theta \cdot \mathbf{T}(\theta)] \tag{3.16}$$

This general formulation has been developed to accommodate future theories describing the dynamic reorganization of the cytoskleton, but it will not be pursued further, since a detailed description of the cytoskeleton microstructure is not the focus of this model. Instead, as a first approximation, the orientation of actin

filaments is considered random, which leads to the stiffness matrix of a simple isotropic material:

$$\mathbf{E} = \frac{E}{1-\upsilon^2}\begin{bmatrix} 1 & \upsilon & 0 \\ \upsilon & 1 & 0 \\ 0 & 0 & 1/2(1-\upsilon) \end{bmatrix} \tag{3.17}$$

where E and υ are the material coefficients that characterize the averaged isotropic response of the cytoskeleton. A higher stiffness of the cell nucleus or of particular areas of the cell can still be included in the model through a spatial dependence of the Youngs's moudulus in 3.17.
The viscous part of the resistance to deform of the cytoskeleton is assumed to be similar to that of a Newtonian isotropic fluid. In this case, the appropriate measure of strain rate is the rate of deformation tensor, which is also an objective tensor:

$$\mathbf{d}_{ij} = \frac{1}{2}\left[\frac{\partial \mathbf{v}_i}{\partial x_j} + \frac{\partial \mathbf{v}_j}{\partial x_i}\right] \tag{3.18}$$

and the viscous component of the stress is proportional to the isotropic viscosity tensor $\mu = 2\mu\,\mathbb{I}$. The simplest viscoelastic law that reproduces the transient viscous creep and non-elastic recovery characteristic of biopolymer networks is the Kelvin-Voigt model. The 2D continuous formulation of this law is then given in terms of the strain and stress measures introduced above as:

$$\sigma = \mathbf{E} : \mathbf{e} + \mu : \mathbf{d} \tag{3.19}$$

Before the constitutive law is extended with the additional terms that account for the active generation of stress, its most important limitation is discussed. This rheological law has the drawback that once the system is driven to a deformed state defined by a fixed strain **e**, the stress does not decrease over time, a behaviour known as stress relaxation. Stress relaxation in the cytoskeleton is associated to the rearrangement of the filaments network and crosslinks, and it allows the cell to adapt to changing circumstances by adopting different shapes permanently. The

addition of a spring in series to the Kelvin-Voigt element of figure 3.4, transforms it into the Linear Standard Solid, which features exponential stress relaxation. However, on the short time-scales that are relevant for cell migration, the passive component of the stress is dominated by the solid-like resistance of the cell to be deformed, since the dynamic reassembly of the cytoskeleton associated to stress relaxation takes places on longer characteristic times. Following with the program of not adding additional complexity than needed to reproduce the kinematics of the migration process qualitatively, this modification is left for future work[2].
The constitutive based on the Kelvinn-Voigt model is now extended to include the generation of active stresses. Contractile stresses are caused by the anti-parallel sliding of actin filaments caused by the directional walk of the mysoin-II molecular motors. The depiction of this process in figure 3.3 serves to introduce a simple analogy with a Hookean spring of varying equilibrium length that motivates the development of the term associated with contractile stress. Consider a spring of equilibrium length l_0 sustaining a tensile force F, which under the Hookean assumption is proportional to the stretch relative to the equilibrium length. The relative sliding of the filaments can be represented by the decrease of the equilibrium length to $l_0 - l^{cont}$, where l^{cont} is a function of the biochemical activity of the cell to be specified later:

$$F = k[l - (l_0 - l^{cont})] = k[l - l_0] + \tau \tag{3.20}$$

Therefore, for a fixed tensile force sustained by the spring, an increase in the contractile term τ leads to a decrease of it actual length.

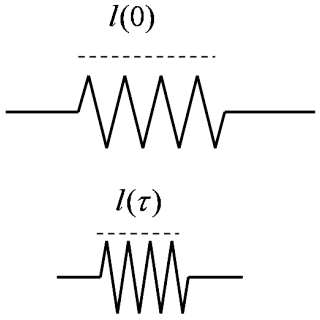

$$l(\tau) = l_0 + \frac{(F - \tau)}{k}$$

Figure 3.5: Hookean spring analogy of the actin-myosin contraction

Again, the 2D counterpart of this process requires an assumption regarding how the microstructure of the cytoskeleton is translated in different contractions

[2]A formulation based on the LSS model requires adding an additional stress rate term to the left hand side in eq.3.19 of the KV model. Unfortunately, a direct extension using $\dot{\sigma}$ is not valid because the material time derivative of the Cauchy stress is not objective, and it must be replaced by an objective measure of the stress rate, such as the Truesdell or Jaumann stress rate[99].

along the different spatial directions. The general contractile term that follows from this analogy is given by:

$$\begin{bmatrix} \tau_x \\ \tau_y \\ \tau_{xy} \end{bmatrix} = \mathbf{E} \cdot \begin{bmatrix} e_x^{cont} \\ e_y^{cont} \\ e_{xy}^{cont} \end{bmatrix} \tag{3.21}$$

The assumption of random orientation of the filaments results in an isotropic contraction term that produces an locally uniform deformation. In this case, the shear component of the contractile term vanishes and $e_x^{cont} = e_y^{cont}$. Adding the contractile term to eq.3.19 leads to the final expression of the constitutive law for the cytoskeleton: 3.22.

$$\sigma = \mathbf{E} : \mathbf{e} + \mu : \mathbf{d} + \tau(\mathbf{r}, N_{\mathrm{FA}}) \tag{3.22}$$

The dependence of the contractile term $\tau(\mathbf{r}, N_{FA})$ on the local concentration of the RhoGTPase proteins $\mathbf{r}(x,t)$ is made explicit to emphasize the coupling of the mechanical model with the RhoGTPase model introduced in the previous chapter. The model also considers direct signaling from Focal adhesions, whose theoretical description is developed in the next section, to the biochemical apparatus that governs cell contractility. Cell contraction is mediated by complex network signaling pathways connecting RhoA to Myosin-II activation. The most thoroughly characterized biochemical channel involves signaling from integrin receptors in Focal Adhesion that leads to RhoA activation and binding of ROCK kinases, triggering in turn MLC (mysoin light chain) kinases phosphorylation and finally the positive regulation of Myosin-II activity[55]. Numerous additional pathways play a role in the regulation of this process, some involving the other RhoGTPase proteins indirectly through crosstalk. A detailed description of the signaling pathways is not possible because many of the actors and interactions are not known, but in addition, such a description would not aid significantly in the goal of understanding the mechanisms of spatio-temporal regulation of the migration process at the whole-cell level. Instead, the complexity of the biochemical apparatus is reduced by assuming a direct relationship between the activation level of the initiators of the signaling cascade, that is, RhoGTPases proteins and Focal Adhesion receptors, with the magnitude of the contractile stress. Thus, the magnitude and distribution of the contractile stresses are not prescribed ad hoc

as in [94, 95, 96]; in this model the forces powering cell migration are determined by the activation level of the factors at top of the signaling cascade that regulate migration. Different explicit forms of the this relationship, given formally in the following equation, will be tested in the second part of chapter 8:

$$\tau^{cont} = \tau^{cont}[C(x,t), R(x,t), \rho(x,t), N_{FA}] \tag{3.23}$$

Thus, different hypothesis on how the local, time-dependent concentration of the RhoGTPase proteins and Focal adhesion state determines the contractile term defined in eq.3.21 will lead to different motility modes, which can be compared to experimental observations.
The last process that has to be included in the constitutive description of cell migration are the protrusive forces. Cell protrusion is driven by the forces generated as a result of actin filament polymerization at the cell edge , as depicted in figure 3.3. The protrusion forces are applied at the plasma membrane of the cell and consequently, the process is naturally introduced in the description through the imposition of boundary conditions. The forces powering protrusion are assumed to be normal to the cell membrane, so that the associated boundary conditions take the form of a prescribed stress at the boundary Γ_t of the cell:

$$\hat{n}_t \cdot \sigma = \mathbf{t}^{prot}(\mathbf{r}) \qquad \vec{x} \subset \Gamma_t \tag{3.24}$$

The biochemical apparatus that regulates this process, as in the case of contraction, involves a large number of proteins and signaling pathways. Most notably, the combined signaling of Cdc42 and Rac mediate the activation of the WASP/WAVE family and subsequent activation of the Arp2/3 complex, which stimulates the formation and extension of branched actin filament networks at the front of the cell. Again, no attempt is made of including the myriad of biochemical players that are involved in the regulation of cell protrusion. Instead, the magnitude of the protrusion force is assumed to be determined by the level of activation of the RhoGTPases proteins. Explicit laws relating their activation level and the protrusion force magnitude will be stated in chapter 7, according to the available experimental evidence.

3.3 Kinetic model of Focal Adhesions

Focal Adhesion (FAs) is the generic term applied to several types of micron-sized clusters of proteins of different structural and molecular composition that link the cell cytoskeleton with the extracellular matrix. The dynamic formation and disassembly of these discrete adhesions plays a crucial role during cell migration because they provide the mechanical support required to exert forces on the substrate and pull the cell body forward. Focal Adhesions also serve two other important functions in cell migration. First, being the primary nexus with the environment, they gather mechanical and biochemical properties of the extracellular matrix, thereby acting as the cell sensors of external signals[50]. Second, Focal adhesions transform this information into biochemical signals that determine the rearrangement of the cytoskeleton and initiate the activation of other regulatory modules, including the RhoGTPases, which enables the cell to give an adequate response to external cues[100]. Focal adhesion dynamics and fate, in turn, are determined by the forces applied by the actin filaments anchored on them, and by signaling from the RhoGTPases. Thus, cell migration relies on the finely coordinated interplay between adhesion formation and turnover, RhoGTPases signaling and cytoskeleton rearrangements and force generation. Complex feedback loops encompassing biochemical and mechanical interactions couple the dynamics of these three systems and constitute the core of the regulatory engine of cell migration[56, 57]. The mathematical description of the last element of this triplet, Focal Adhesions, is developed in this section.

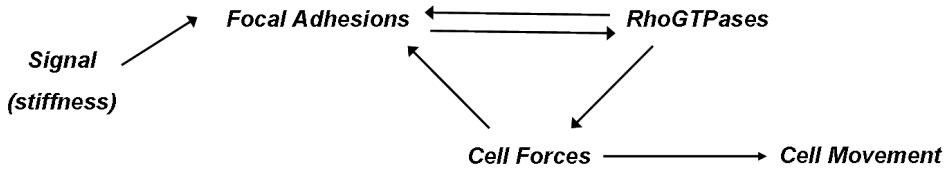

Figure 3.6: Cell migration results from the coupled dynamics of FA's, rhoGTPase signalling and Cytoskleton generated forces

More than 156 molecular components of Focal adhesions and 690 interactions between them have been identified[60]. This remarkable study, combining computational data-mining techniques with experimental observations, classified FA's components into 20 functional groups according to their activity. The most populous groups are formed by the constituents of the physical structure of adhesion sites: adhesion receptors, adaptor proteins and actin regulators. The rest of the groups are mostly enzymes that regulate either adhesion assembly and turnover

or signaling from FAs to the inner cell. The most important structural element in Focal Adhesions are Integrin receptors, which physically tether the adhesion to matrix ligands and also send and receive signals that mediate the interaction between the extrcellular matrix, adhesions and the cytoskeleton [101, 102]. Integrins are transmembrane proteins that form bonds with actin filaments on their intracellular domain and with ligands coating the extracellular matrix, such as collagen or fibronectic, on their exterior domains. Upon engagement, Integrin receptors mediate a bidirectional stream of outside-inside and inside-outside signals that lay at the core of the sensing and migratory response of the cell to external cues [103]. The outside-inside channel comprises direct signalling to the RhoGTPases, triggers the activation of signaling pathways that lead to further Integrin clustering, reinforcing the adhesion and recruiting actin-adaptor proteins to regulate the level of force, depending on the biochemical or mechanical composition of the extracellular matrix. The inside-outside channel encapsulates the mechanisms that modulate the adhesiveness of individual adhesions, which allows cells to reinforce the contacts that sustain traction at the front and to release them at the back in order to move forward.
Consequently, Integrin mechanical loading is a key determinant of the lifetime of their bonds to extracellular ligands, thereby modulating the stability of Focal Adhesions and the signaling activity that shapes the cell response to mechanical properties of the environment. In this work, the focus is set on to explore the principles that govern Cell Durotaxis, and the main hypothesis is that this phenomenon can be explained by the local mechanosensing properties of Focal Adhesions. Multiple hypothesis [104, 105, 106] exist on the biophysical basis that allows Focal adhesions to act as mechanosensors, and despite the fact that its precise nature is not fully understood, experimental evidence points to a combination of physical and biochemical mechanisms working in parallel to define the cell's mechanosensory response [105, 107]. Thus, a model aiming to elucidate Cell Durataxis requires a theoretical description of Focal Adhesions that considers the purely mechanical as well as the biochemical regulatory aspects of their function. On account of the molecular complexity of Focal adhesions described above, all modeling efforts conducted to date condense the molecular details into a simplified physico-biochemical portrait that captures the particular adhesion process of interest. Theoretical models of Focal adhesion mechanosensvity can be classified in two broad categories. First, models built in a statistical physics [108, 109] or thermodynamic framework [110, 111], in which the definition of an energy functional containing an elastic term and chemical potential allows to study the equilibrium size and stability of an adhesion under mechanical forces. The models in the second category [82, 112, 113], which will be referred as Kinetic models, use a mechanistic description of ligand-receptor bonds as pairs of

connected springs, whose rates of binding and unbinding are described in the framework of Kramer's theory for thermally activated escapes over an energy barrier [114]. The first approach has been used to study FAs in adherent (non-motile) cells, in which the description of static adhesions as a system in thermal equilibrium might be reasonable. In this thesis, however, the goal is to study cell migration, in which FAs are dynamic structures and requires a detailed description of the mechanical link with the rest of the cell; for these reasons, the last approach is adopted.
The first theory of this type, studying the effects of mechanical forces on the lifetime of biological bonds is found in the pioneering work of G.I. Bell, who adapted the previous theories by Zhurkov[115] on material strength. A more modern treatment is found in the work of Seifert [112] and Schwarz's group [116], which will be used as the basis to develop the FA model. A schematic portrait of the mechanical system representing the Kinetic model of a Focal Adhesion is shown in figure3.7.

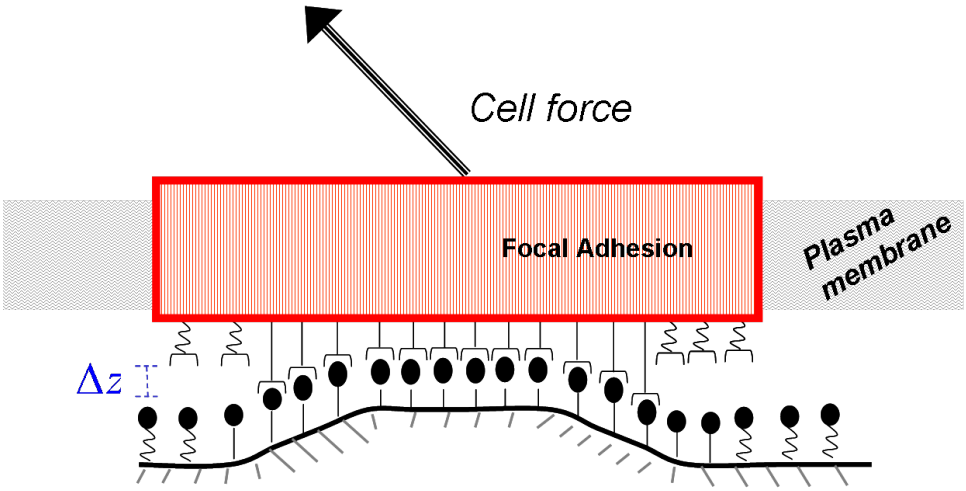

Figure 3.7: Kinetic FA model as a cluster of parallel springs binding and unbinding substrate ligands

The adhesion is formed by a cluster of N_T integrin receptors that can bind ligands fixed on the substrate. The number of integrins forming a bond with a ligand is denoted by n, whereas the number of unbound integrins is given $N_T - n$. Thermal excitation limits the lifetime of a molecular bond, but also drives the formation of new pair of ligand-receptor bonds. The associated stochastic rates of rupture and formation are also modulated by forces applied to them and by the ligand-receptor distance. Let f_n and r_n denote the rates of bond formation and

rupture in an adhesion having n closed bonds, and p_n the probability of having n bonds. Then, the change in the probability of having n closed bonds is determined by the formation and rupture events according to the following one-step master equation [117]:

$$\frac{dp_n}{dt} = r_{n+1} \cdot p_{n+1} + f_{n-1} \cdot p_{n-1} - (f_n \cdot p_n + r_n \cdot p_n) \tag{3.25}$$

A stochastic description of the adhesion process is necessary when the number of bonds is small, particularly during the initial process of nucleation of a new adhesion, in which the fluctuations of the number of bonds can be as large as the number of bonds itself. An exact treatment of the master equation is beyond the scope of this work due to the theoretical and computational challenges associated to the formulation of a model of cell migration combining stochastic and deterministic elements. Thus, the nucleation phase of adhesion formation will be replaced by an experimentally-based phenomenological law and a deterministic approximation of the master equation 3.25 is developed to describe the ensuing evolution of a Focal Adhesion. The key variable in the deterministic description is the mean number of closed bonds $N(t)$, which can expressed in terms of $p_n(t)$ as:

$$\langle n \rangle = \sum_{n=0}^{N_T} n \cdot p_n \equiv N \tag{3.26}$$

The mean field approximation of the master equation is obtained by taking the time derivative of the number of closed bonds:

$$\frac{dN}{dt} = \sum_{n=0}^{N_T} n \cdot \frac{dp_n}{dt} = -\langle r_n \rangle + \langle f_n \rangle \tag{3.27}$$

The next step is to obtain the mean rates of bond binding and unbinding for the adhesion and their dependency on applied loads. The frequencies of rupture and formation for an individual bond will be derived in the framework of Kramers Kinetic theory and are denoted by W_r and W_f. Then, the mean rupture rate in

the whole adhesion is approximated as $\langle r_n \rangle \approx W_r \cdot N$, the frequency of rupture for a single bond multiplied by the number of existing bonds. Likewise, the mean binding rate is approximated as $\langle f_n \rangle \approx W_f \cdot (N_T - N)$, the binding frequency multiplied by the number of available integrins. Substitution of these expressions into eq.3.27 leads to the deterministic equation describing the evolution of number of molecular bonds in a Focal Adhesion:

$$\frac{dN}{dt} = -N \cdot W_r + (N_T - N) \cdot W_f \tag{3.28}$$

The Kinetic theory of Kramers[118] with the extension of Bell [82] for mechanically loaded bonds is now used to derive an expression for the intrinsic rates W_r and W_f. In this theory, the ligand-receptor system is characterized by a potential or energy landscape $E_b(\chi)$ with two minimums corresponding to the bounded and unbounded state and a energy barrier that separates them [119]. The transition over the barrier is assisted by thermal fluctuations and corresponds to the binding and unbinding events. It is assumed that the transition takes place along a preferred path on the energy landscape, denoted by the reaction coordinate χ.

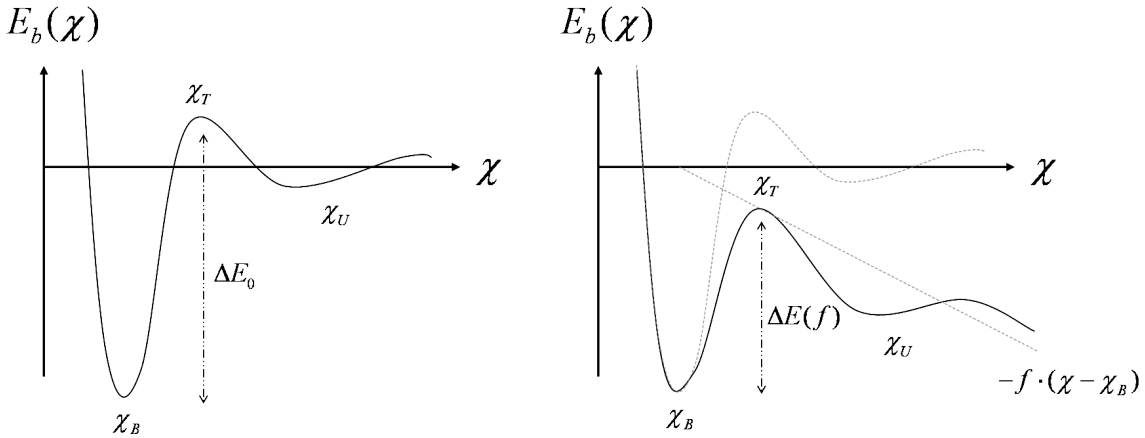

Figure 3.8: Energy Landscape of the ligand-receptor system along reaction coordinate χ. The energy barrier ΔE is tilted by the application of a mechanical load

The bond state, transition state and unbound state correpsond to χ_B, χ_T and χ_U. The expression for the rate of transition $\chi_B \leftrightarrow \chi_U$ over the barrier is given

by[119]:

$$W_{\chi_B \leftrightarrow \chi_U} = \frac{\delta}{l_a\, l_b}\, e^{-\frac{\Delta E(f)}{K_B T}} \tag{3.29}$$

The factor $\frac{\delta}{l_a\, l_b}$ is associated to the frequency of escape attempts and reflects the diffusive nature of the process. δ is a molecular damping constant and the lengths l_a and l_b are determined by the profile of the energy landscape. Particularly, l_a is a measure of the departure from the minimum corresponding to the initial state for a $K_B \cdot T$ increase in energy and l_b is set by width of the energy barrier form the initial state to the target state [120]. $\Delta E(f)$ is the energy difference between the bound state and the transition state. The probability of overcoming the barrier has an exponential decrease with the height of the barrier, weighted by the Boltzmann factor $K_B \cdot T$. The transition rate of eq.3.29 is applied to derive the expressions of the rupture rate of a closed bond subjected to a mechanical load. The application of a force f to a pair of bonded ligand-receptors tilts the energy landscape, lowering the energy barrier. Following Bell, the force introduces a mechanical potential to the energy landscape that decreases the height of the energy barrier to $\Delta E(f) = \Delta E_0 - f \cdot (\chi_T - \chi_B)$, as depicted in fig. 3.8. Grouping the attempt frequency and the constant part of the energy barrier into $w_0 = (\delta / l_c\, l_s) \exp(-\Delta E_0 / K_B T)$ and defining an internal force scale $f_0 = K_B T / (\chi_T - \chi_B)$, the rupture rate as a function of the external force f is:

$$W_r(f) = w_0\, e^{\frac{f}{f_0}} \tag{3.30}$$

Analogously, the generic transition rate of eq.3.29 is used to derive an expression for the rate of formation of new ligand-receptor bond. Any force applied to the Focal Adhesion is borne by the currently bound receptors but not by the free receptors, and consequently, the binding rate is not modulated by this force. The initial state of system is the minimum χ_U, which in figure3.7 corresponds to the pairs of unoccupied ligands and integrin receptors recoiled towards the adhesion plaque. The formation of a new bond is driven by thermal excitations that jolt the receptor to a position sufficiently close to the ligand, which allows the binding event to occur. The ligand-receptor distance is then the key variable that modulates the rate of bond formation. The thermally driven departure of the receptor from the recoiled state adds an extra energy term to the ligand-receptor

potential, associated to the stretch of the receptor molecule required to reach the point in which it can bind the ligand. In the absence of applied force to the FAs, a characteristic minimum ligand-receptor distance z_0 is determined by intrinsic repulsive forces between the cell membrane and the extracellular matrix. After the cell pulls on a Focal adhesion with a force F, the plaque of the adhesion is displaced a certain distance $\bar{u} = u - u_0^{FA}$ from the position in which it was originally formed. Assuming that the force is not completely parallel to the substrate, the adhesion plaque will be displaced vertically a small distance $z(u) \approx \bar{u} \cdot sin\theta > 0$.

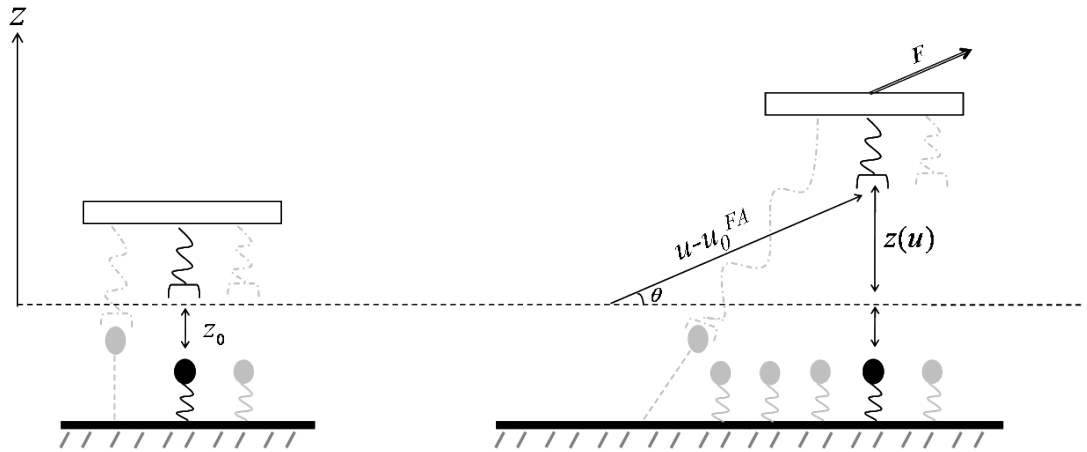

Figure 3.9: Distance dependence of bond formation rate

Let $\Delta E = \Delta E_0'(z_0)$ be the energy barrier between the unbound state and the bound state for the unloaded ligand-receptor system. For the Focal Adhesion subjected to a load, the mechanical energy associated to the receptor stretch required to cover the increased ligand-receptor distance results in a total energy barrier $\Delta E(u) \approx \Delta E_0' + 1/2 \cdot k_R(\bar{u} \cdot \sin\theta)^2$, where k_R represents the spring constant of an integrin receptor. Introducing $\Delta E(u)$ in the transition rate given in eq. 3.29 leads the distance dependent rate of bond formation:

$$W_f(u) = w_0' \, e^{-(\frac{\bar{u}}{u_0})^2} \tag{3.31}$$

where the constant terms have been lumped into $w_0' = (\delta/l_a \, l_b) \exp(-\Delta E_0' \big/ K_B T)$ and the displacement scale is $u_0 = (2 \cdot K_B T / k_R \sin^2\theta)^{1/2}$.
The last element that has to be considered to complete the description of Focal

Adhesions is the regulatory interaction with the RhoGTPases and the coupling with cytoskeleton-generated forces. Experimental evidence indicates that the cell actively regulates the dynamics and fate of Focal Adhesions by modulating the avidity of individual contacts. This is the channel of regulation referred previously as inside-out, and RhoGTPases are one of its central players. Avidity is the effective adhesive strength of a Focal Adhesion, the amount of force that it can sustain[121]. It is the result of two factors: the affinity of individual ligand-receptor pairs, which determines the strength of individual bonds, and the number of bonds in the adhesion, also known as valency. Therefore, there are two mechanisms by which the overall adhesiveness of an adhesion could be modified. First, signals from the cell regulatory apparatus could trigger conformational changes in the molecular structure of integrin receptors, modifying the energy landscape of the ligand-receptor potential and possibly the mechanical properties of integrins. Thus, a conformational change would lead to a modification of the rates of bond formation and rupture and an alteration of the ligand-receptor affinity. Affinity regulation is naturally introduced in the FA model by considering the dependence on regulatory signals of the parameters that are determined by the energy landscape profile and the integrin spring constant. The biochemical details of the signaling pathways involved are not fully known, but since the experimental evidence suggests that RhoGTPases are the initiators of the process, it is assumed that they depend on the activation levels of these proteins. According to this hypothesis, an integrin conformational change implies a modification in k_R that results in functional dependency on the activation level of RhoGTPases of the parameter u_0 that sets the distance scale for the binding events. Likewise, the shift in the distance $\chi_B - \chi_U$ between the bound and unbound states that accompanies an alteration of the energy landscape results in dependency of the force parameter f_0 that sets the scale of the rupture events. Specific forms of the functional dependency of these molecular parameters on RhoGTPase concentration will be tested in Chapter8 , in which the complete cell migration model is used to simulate durotaxis essays.

$$u_o = u_o(\mathbf{r} - \mathbf{r}_0) \tag{3.32a}$$

$$f_0 = f_0(\mathbf{r} - \mathbf{r}_0) \tag{3.32b}$$

The second mechanism of inside-out regulation could involve modification of the valency of a Focal Adhesion, that is, the number of bonds in the FA. Experimental observation shows that shortly after a small adhesion nucleates, its growth

depends on the level of force applied to it. For example, treatments that inhibit myosin II-driven contractility prevent the maturation of small initial contacts into large FAs and leads to rapid disassembly of the existing ones [8, 122]. Related to this phenomenon are the observations that cells cultured in flexible substrates, in which adhesions bear a smaller traction, feature FAs of smaller average size [27], whereas the connections between adhesions and the cytoskeleton are reinforced in rigid substrates, allowing the cells to develop stronger forces to be exerted on the substrate[123]. These negative effects on FA growth can be bypassed by application of an external force on the adhesion site [49], suggesting early FAs act like a mechanosensor whose growth is directly determined by the level of force applied on them. Fast regulation of adhesion size depending of the state of mechanical loading seems to point out to an inside-out mechanism involving the modulation of the adhesion valency, promoting integrin recruitment or disassembly from the adhesion plaque to control the number of available receptors per adhesion. This regulation mechanism is introduced by postulating a dependence of the total number of available integrins per adhesion N_T on the force applied to the adhesion. The experimental evidence summarized above imposes that N_T must be a growing function of the mechanical loading applied to the adhesion that goes to zero in the absence of force and bounded by the availability of integrin receptors. According to these constrains, N_T will be defined in terms of the mechanical energy $e_P(f)$ stored by each ligand-receptor pair due to pulling forces as:

$$N_T(e_P) \;=\; N_{FA} \;\cdot \left(\frac{e_P(f)}{e_P(f) + e_0} \right) \tag{3.33}$$

where N_{FA} is the maximum number of integrins per Focal adhesion and e_0 is a parameter that sets the energy scale of receptor activation by the inside-out mechanism of valency regulation. In this way, the model implements the feedback interaction between the cytoskeleton and the RhoGTPases with adhesion sites channeled by the inside-out signalling channels. Introducing the force and distance dependent expressions of reaction rates and the postulated dependency of adhesion parameters on inside-out regulation, the definitive equation to describe Focal Adhesions becomes:

$$\frac{dN(t)}{dt} = -w_0\, e^{\frac{f(t)}{f_0(\mathbf{r})}} \cdot N(t) + w_0'\, e^{-\left(\frac{\bar{u}(t)}{u_0(\mathbf{r})}\right)^2} [N_T(e_P(t)) - N(t)] \tag{3.34}$$

The forces and ligand-receptor distances in equation 3.34 are determined by the coupled dynamics of Focal adhesions and the model of the cell introduced in the first section of this chapter. Displacements and forces on FAs are determined by the traction forces and movement of the cell, governed by the balance of momentum stated in eq. 3.13 from which the motion of the cell results. In turn, the external forces defined in eq.3.8 for every point containing a Focal adhesion, associated to the reaction force that resists the stretch of FA-substrate links, has to be considered in the balance of momentum that determines cell movement. Therefore, the kinematic and mechanical description of the coupled system composed by substrate-FA-cytoskeleton has to be addressed.
The substrate is considered an incompressible linear elastic half-space with Young' s modulus E_s. Each closed ligand-receptor pair is anchored to a point on the substrate that provides a linear elastic restoring force to the loads exerted by the cell. The reaction force of the anchorage point is proportional to a spring constant $k_S(E_S)$ that depends on the Young's modulus of the substrate. Derivation of k_S as a function of the substrate stiffness is addressed using Boussinesq-Cerruti theory of elastic potential [124, Chapter 3]. This theory provides a solution to the classic problem of determining the displacement field produced by the application of point loads or distributed loads on the surface of an elastic half space. Thus, the process of an ligand-receptor pair pulling on the substrate can be approximated as the problem of calculating the displacement u_s produced on the surface of an infinite half space by a tangential load f distributed on a circular area of radius r_P equal to the radius of an integrin or collagen molecule. The spring constant of the anchorage point is then approximated as $k_S(E_S) = f/u_s$

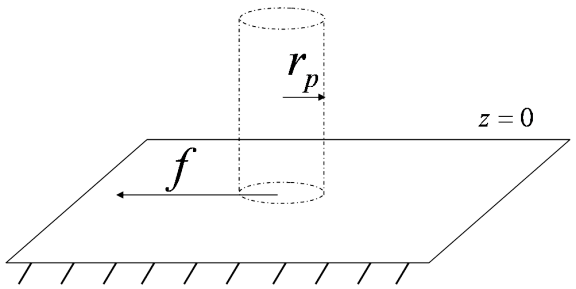

Figure 3.10: Integrin-ligand tangential load on the substrate

The traction on the circular contact is assumed to follow a distribution given by $q = (f/2\pi r_P^2)(1 - (r/r_P)^2)^{-1/2}$, which produces constant displacement of the

surface within the contact area [3]. The analytical value of this displacement along the direction of the force for $r < r_P$ is $u_s = (\pi \cdot r_P/2 \cdot E_s)(1-\upsilon)(2-\upsilon)(f/2\pi r_P^2)$. Substitution of the Poisson ratio for an incompressible material then leads to the effective spring constant of the anchorage points:

$$k_S(E_S) = \left(\frac{4}{3}\right)^2 \cdot E_S \cdot r_P \tag{3.35}$$

After this brief detour, it is now possible to proceed with the description of the FA-substrate system. Let F be the total force applied by the cytoskeleton filaments anchored on a Focal Adhesion with N closed bonds. The force transmitted to each ligand-receptor pair is $f = F/N$. The spring constants of receptors and ligands are k_R and k_L, respectively. The compound spring constant of a ligand-receptor pair in series is then given by $k_P^{-1} = k_R^{-1} + k_L^{-1}$. The stretch of a ligand-receptor pair relative to its resting length is denoted by u_P, whereas the stretch of the anchorage point in the substrate is u_S The total displacement imposed by the pulling forces of the cell is then equal to the sum the stretch of the ligand-receptor pairs and the deformation of their points of attachment to the substrate; that is $u - u_0^{FA} = u_P + u_S$, where u_0^{FA} is the position in which the contact was formed. Mechanical equilibrium of the system then leads to:

$$u - u_0^{FA} = u_P + u_S = F \cdot \left[\frac{1}{N \cdot k_P} + \frac{1}{N \cdot k_S(E_S)}\right] \tag{3.36}$$

Hence, the total reaction force that arises from the stretch of a FA, which enters in the cell momentum equation as the external force defined in 3.8, can be expressed as $F = -k_{FA}(N) \cdot (u - u_0^{FA})$, where $k_{FA}(N)$ is the effective spring constant of the Focal Adhesion defined as:

$$k_{FA}(N) = N \cdot \frac{k_P \cdot k_S(E_S)}{k_P + k_S(E_S)} \tag{3.37}$$

[3] Alternative traction distributions do not result in significant changes in $k_s(E_s)$. For instance, considering the displacement on the boundary of the contact circle produced by a concentrated point load on the center leads to $k_s(E_s) = (2/3) \cdot \pi \cdot E_S \cdot r_P$, which only differs in a small numerical prefactor from the adopted value

Thus, cell motion depends on the state of Focal Adhesions through the reaction force 3.8 associated to existence of a cell-substrate contacts, and in turn, the dynamics of Focal adhesion depend on displacements and forces imposed on them by the motion of the cell. The force per ligand-receptor pair $f = F/N$ in a FA that determines the bond rupture rate in eq.3.34 is then:

$$f = \frac{k_P \cdot k_S(E_S)}{k_P + k_S(E_S)} \cdot (u - u_0^{FA}) \tag{3.38}$$

The mechanical energy stored by each ligand-receptor pair and associated to its stretch, referred previously as e_P, can be calculated from this expression.

$$e_P = f^2/(2 \cdot k_P) \tag{3.39}$$

Note that if the spring constant of ligand and receptor are considered equal leads to $k_P = k_R/2$, which allows to relate the last expression with e_R (the energy stored by cell receptors instead of ligand-receptor pairs) parameters defining the energy landscape of the ligand-receptor potential rate of rebinding events.
In Chapter 8, the cell migration model will be applied to explore the mechanisms that explain cell preferred movement along stiffness gradients. The mechanical energy stored in adhesion receptors will be the variable assumed to determine the magnitude of the signal transmitted through the outside-inside channel from FAs to the RhoGTPase system to guide the cell response. This signal of mechanical origin will replace the abstract stimulus function Ψ received by the RhoGTPases in the chapter devoted to the study of Cell Durotaxis.

And yet it moves.

Galileo

Chapter 4

Finite Element formulation of the cell migration model

A Finite Element formulation the Cell Migration model is developed in this chapter. The choice of the numerical method is determined by the numerous challenges presented by the migration process from a computational perspective. In biological cells, the notion of a reference or undeformed configuration is rather artificial. Hence, the cell constitutive equations, momentum balance and protein transport equations were formulated in the deformed cell configuration. The governing equations must be solved in a complicated geometry that varies over time as the cell body deforms and advances during its motion. For these reasons, an Updated Lagrangian (UL) description of the cell migration process is the natural framework. The nodes of the Lagrangian Finite Element mesh follow the material points of the cell, automatically tracking its boundaries and facilitating the imposition of boundary conditions. The UL scheme is also convenient because history-dependent properties characteristic of biological materials are handled easily.

Another source of complexity stems from the coupling between the mechanical and regulatory modules of the cell migration model. Migration is viewed as the result of two physically distinct processes: the mechanical deformation and displacement of the cell, and the dynamics of the protein network that controls the protrusion and contraction forces driving this motion. The numerical procedure adopted to solve the equations assumes that the coupling between these two modules is weak, and an explicit time integration algorithm is used to integrate the equations. The stability of the numerical scheme and alternative methods are discussed. The formulation is valid for any number of spatial dimensions, although special emphasis is put in 1D and 2D models of cell migration. It is also a general formulation in the sense that it can incorporate geometric and material

nonlinearities associated to the cell movement and complex constitutive behavior.

4.1 Updated Lagrangian description of cell migration

4.1.1 Problem statement

The goal of this section is to develop the weak form of the governing equations of the cell migration model in an Updated Lagrangian framework. The spatial coordinates of a point are denoted by $\mathbf{x} = [x_1, .., x_d]$, where d stands for the number of spatial dimensions considered. Every point in the cell is assigned a fixed label, called material coordinates and denoted by $\mathbf{X} = [X_1, ..., X_d]$. The material coordinates are defined by the spatial coordinates of the cell point in the initial configuration at t_0. In the remaining of the chapter, bold and regular font letters are used for vectors and their components respectively .

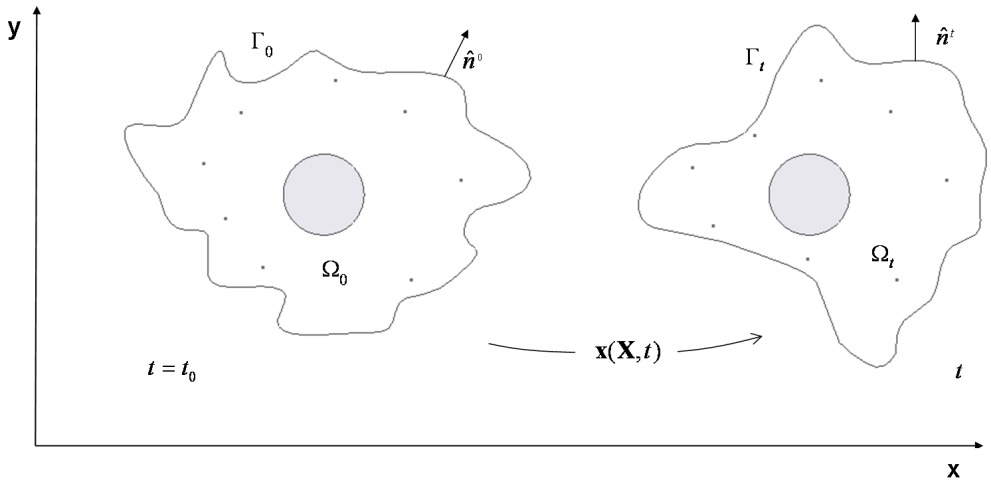

Figure 4.1: Initial and current configuration of a 2D migrating cell.

The motion of the cell is then given by a continuous map between material coordinates and their spatial position as a function of time:

$$\mathbf{x}(\mathbf{X}, t) = \mathbf{X} + \mathbf{u}(\mathbf{X}, t) \tag{4.1}$$

where the displacement $\mathbf{u}(\mathbf{X}, t)$ is the difference between the current and the initial position of a material point of the cell. In a Lagrangian description of a dy-

namical process, the properties and variables of interest are considered functions of the material coordinates. Hence. since the framework for the Finite Element formulation of the migration model is Lagrangian, the displacement, protein concentrations and other fields required to describe the cell motion are considered functions of **X**.
The equations governing the mechanical deformation of the cell were derived in Chapter 3 from the balance of momentum in the spatial domain Ω_t occupied the cell body at a time t. In every spatial dimension considered in the model, conservation of linear momentum leads to a partial differential equation (PDE) that must be fulfilled in deformed configuration:

$$\frac{\partial \sigma_{ji}}{\partial x_j} - [\rho \ddot{u}_i + \delta(z)\beta \cdot \dot{u}_i + \delta(\mathbf{x}_{FA})\, k_{FA} \cdot \, u_i] = 0 \qquad \mathbf{x} \in \Omega_t \tag{4.2a}$$

$$n_j^t \cdot \sigma_{ji} = t_i^{Prot} \qquad \mathbf{x} \in \Gamma_t \tag{4.2b}$$

The stress σ_{ji} can be expressed as a function of the displacements using its relationship with a measure of strain, as stated in the cell constitutive law. The motion is then determined by the displacements obtained from solving equation 4.2a in Ω_t. The solution of this equation requires prescribing the stresses or the displacements on the cell edge Γ_t. The stress values in the boundary condition 4.2b are set by the protrusion force of the migration model, which specifies the traction force along the current normal $\hat{n}^t$ to the cell boundary Γ_t. The magnitude of the protrusion and contraction forces propelling migration, in turn, are determined by the network of regulatory proteins introduced in Chapter 2. The spatial distribution of each of the proteins inside the cell is given by a component of the concentration vector $\mathbf{r}(\mathbf{X}, t)$. The changes in concentration are driven by the reactions between proteins and transport by diffusion. These processes can be described by a reaction-diffusion equation, derived from the mathematical expression of the conservation of protein mass in Ω_t, so that the evolution of every component of $r_\alpha(\mathbf{X}, t)$ is given by an equation of this form:

$$\dot{r}_\alpha + r_\alpha \nabla \cdot \dot{\mathbf{u}} - [f_\alpha(\mathbf{r}, \Psi) + \frac{\mathrm{d}_\alpha}{\Phi^2} \frac{\partial^2 r_\alpha}{\partial x_j^2}] \, = 0 \qquad \mathbf{x} \in \Omega_t \tag{4.3a}$$

$$n_j^t \cdot (\frac{d_\alpha}{\Phi^2} \frac{\partial r_\alpha}{\partial x_j}) = 0 \qquad \mathbf{x} \in \Gamma_t \tag{4.3b}$$

where the subindex α goes over all the proteins in the network. The reaction term $f_\alpha(\mathbf{r}, \Psi)$ is shaped by the reactions between proteins and the external signals represented by Ψ. The boundary condition 4.3b states that there is no outward flow of proteins at the cell edge.
The system of PDEs that constitute the cell migration model can not be solved analytically. Hence, a numerical solution of the systems is sought developing a discrete form of the equations based on the Finite Element Method (FEM). The first step in the derivation of the FEM formulation requires the expression of the corresponding weak form, an integral form of the equations also known as the principle of virtual power.

4.1.2 Derivation of the weak form of the governing equations

The weak form is obtained taking the product of the differential equations governing the mechanical and regulatory modules with an arbitrary function, known as test function, and integrating over the current domain. The space of test functions is formed by two sets of arbitrary functions, the virtual displacements $\delta\mathbf{u}$ for the mechanical module and the virtual concentrations $\delta\mathbf{r}$ for the regulatory module. Test functions are required to be consistent with the constraints of their corresponding subproblem. Since the boundary conditions 4.2b and 4.3b do not prescribe values of the displacements nor the concentrations, test functions are only required to be continuous, but they do not need to vanish on Γ_t. The differential equations 4.2a and 4.3a are zero in every point of Ω_t, therefore this also holds true for their integral form.
According to this procedure, the product of the momentum equation with an arbitrary virtual displacement and integration over the current domain leads to:

$$\int_{\Omega_t} \delta u_i \left(\frac{\partial \sigma_{ji}}{\partial x_j} - [\rho \ddot{u}_i + \delta(z)\beta \cdot \dot{u}_i + \delta(\mathbf{x}_{FA})\, k_{FA} \cdot u_i] \right) d\Omega = 0 \tag{4.4}$$

Applying the divergence theorem to the first term in eq. 4.4 and considering that the traction at the boundary is given by condition 4.2b, the stress term transforms as:

$$\begin{aligned}\int_{\Omega_t} \delta u_i \frac{\partial \sigma_{ji}}{\partial x_j} d\Omega &= \int_{\Gamma_t} \delta u_i \, n_j^t \sigma_{ji} \, d\Gamma - \int_{\Omega_t} \frac{\partial(\delta u_i)}{\partial x_j} \sigma_{ji} \, d\Omega = \\ &= \int_{\Gamma_t} \delta u_i \, t_i^{Prot} \, d\Gamma - \int_{\Omega_t} \frac{\partial(\delta u_i)}{\partial x_j} \sigma_{ji} \, d\Omega\end{aligned} \tag{4.5}$$

The weak form of the momentum equation is found substituting the transformed expression 4.5 in the integral equation 4.4.

$$\int_{\Omega_t} \delta u_i \left[\rho \ddot{u}_i + \delta(z)\beta \cdot \dot{u}_i + \delta(\mathbf{x}_{FA}) k_{FA} \cdot u_i\right] d\Omega - \int_{\Gamma_t} \delta u_i \, t_i^{Prot} d\Gamma + \int_{\Omega_t} \frac{\partial(\delta u_i)}{\partial x_j} \sigma_{ji} d\Omega = 0 \tag{4.6}$$

Proceeding analogously for the regulatory module, the product of an arbitrary virtual concentration of protein α with the corresponding reaction-diffusion equation in system 4.3a and integration over Ω_t leads to:

$$\int_{\Omega_t} \delta r_\alpha \left(\dot{r}_\alpha \quad + r_\alpha \nabla \cdot \dot{\mathbf{u}} - [f_\alpha(\mathbf{r}, \Psi) + \frac{\mathrm{d}_\alpha}{\Phi^2} \frac{\partial^2 r_\alpha}{\partial x_j^2}] \right) d\Omega = 0 \tag{4.7}$$

Again, the divergence theorem is applied to expand the diffusion term in 4.7 to obtain

$$\begin{aligned}\int_{\Omega_t} \delta r_\alpha \frac{\mathrm{d}_\alpha}{\Phi^2} \frac{\partial^2 r_\alpha}{\partial x_j^2} \, d\Omega &= \int_{\Gamma_t} \delta r_\alpha \, (n_j \cdot \frac{d_\alpha}{\Phi^2} \frac{\partial r_\alpha}{\partial x_j}) d\Gamma - \int_{\Omega_t} \frac{\partial(\delta \mathrm{r}_\alpha)}{\partial x_j} \frac{d_\alpha}{\Phi^2} \frac{\partial r_\alpha}{\partial x_j} \, d\Omega = \\ &= - \int_{\Omega_t} \frac{\partial(\delta \mathrm{r}_\alpha)}{\partial x_j} \frac{d_\alpha}{\Phi^2} \frac{\partial r_\alpha}{\partial x_j} \, d\Omega\end{aligned} \tag{4.8}$$

The no flux boundary given in 4.3b states that the contour term along Γ_t in 4.8 vanishes. Substitution of 4.8 in 4.7 then leads to the weak form of the reaction-diffusion equation:

$$\int_{\Omega_t} \delta r_\alpha \left[\dot{r}_\alpha + r_\alpha \nabla \cdot \dot{\mathbf{u}}\right] d\Omega + \int_{\Omega_t} \frac{\partial(\delta r_\alpha)}{\partial x_j} \frac{d_\alpha}{\Phi^2} \frac{\partial r_\alpha}{\partial x_j} d\Omega - \int_{\Omega_t} \delta r_\alpha f_\alpha(\mathbf{r})\, d\Omega = 0 \tag{4.9}$$

The weak forms 4.6 and 4.9 are equivalent to the systems 4.2 and 4.3 composed of the governing equations and the boundary conditions, they contain the same information. The next step in the development of the FEM formulation is the introduction of discrete approximations of the geometry and the unknown variables of the problem.

4.1.3 Discretization of geometry, test and trial functions

The discrete equations for the Updated Lagrangian formulation are obtained introducing in the weak forms an approximation for the cell geometry, the test functions and trial solutions. The initial cell domain Ω_0 is subdivided into a mesh of n_e elements spanning the total domain.

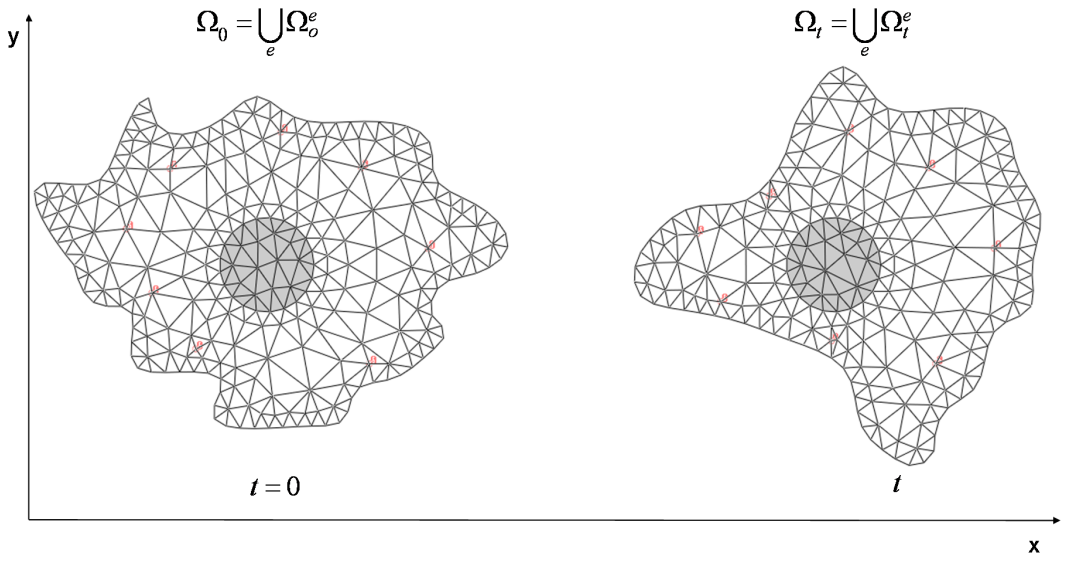

Figure 4.2: 2D cell meshed with 6-node triangular elements. Red nodes match the position of adhesions sites.

Every element has m nodes, and the total number of nodes in the mesh is denoted by n. Each Adhesion site has a node attached to it in order to facilitate the treatment of punctual forces. The boundary between the nucleus and the cell

body is also matched by element edges, so that different material properties can be assigned to them.
A set of interpolation functions is introduced to approximate the problem variables in the elements in terms of their nodal values. The interpolation functions are standard shape functions [125] defined by the type of element used in the discretization.

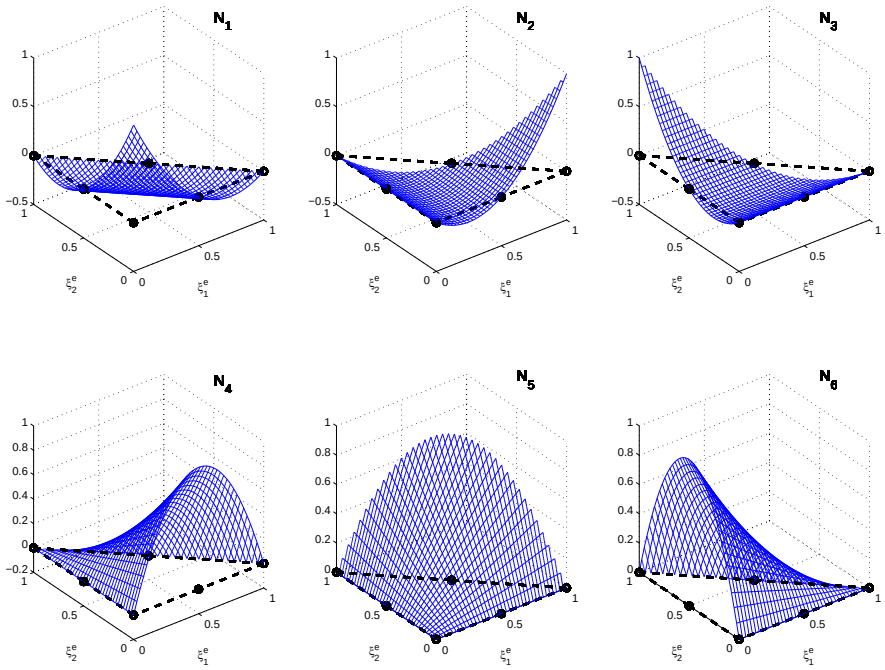

Figure 4.3: Quadratic shape function for the 6-node triangle element

The shape functions, as shown in figure 4.3, fulfill the interpolation condition by which the shape function associated to node I vanishes at the position of any other node J.

$$N_I(\xi_J^e) = \delta_{IJ} \qquad \sum_I^m N_I(\xi^e) = 1 \tag{4.10}$$

The second condition in 4.10 is required to ensure rigid body motion can be interpolated without causing strain. The shape function variables $\xi^e = [\xi_1, ..., \xi_d]$ are a set of local element coordinates, known as parent coordinates, introduced to

facilitate FEM calculations. Parent coordinates are a parameterization of the element domain, so that locally there is a one-to-one correspondence $\mathbf{X}(\xi^{\mathbf{e}})$ between the material coordinates of a particle and its parent coordinates. An upper case subindex will be used to label nodes to avoid confusion with the spatial components of a vector, which are indicated with a lower case subindex.

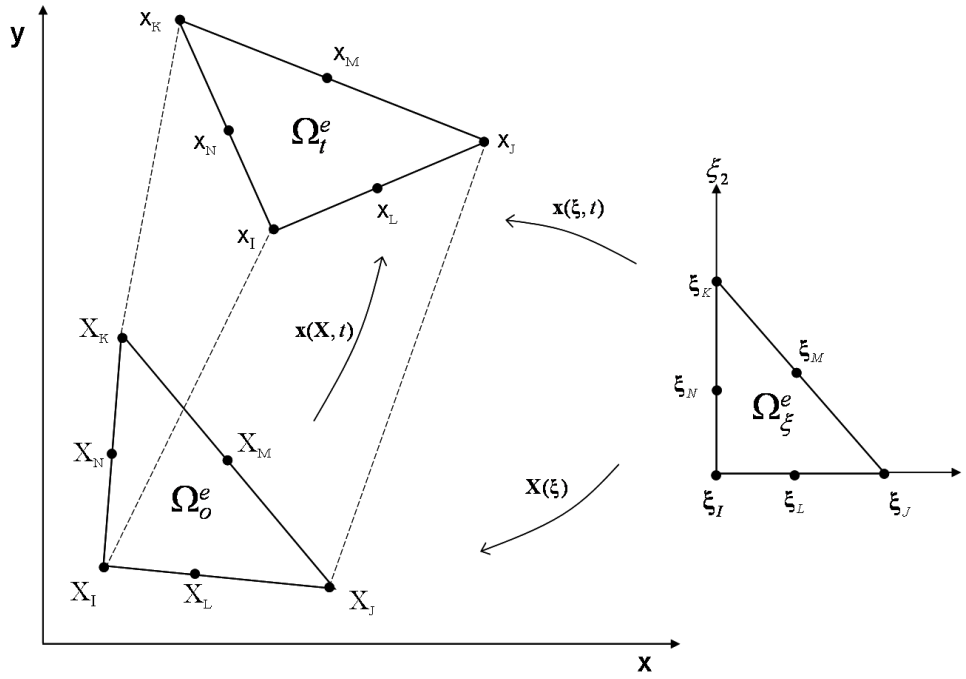

Figure 4.4: Initial, current and parent coordinates of a triangular element and mapping between them.

Parent coordinates are effectively a substitute of the material coordinates and can also be used as a label for a material point. The mapping between the material coordinates of any particle inside the cell domain and its parent coordinates can then be interpolated in terms of the nodal values using the shape functions:

$$\mathbf{X}(\xi^{\mathbf{e}}) = \sum_{I}^{n} N_I(\xi^{\mathbf{e}}) \cdot \mathbf{X}_{\mathrm{I}} \tag{4.11}$$

The superscript e in the local element coordinates will be omitted from now on to simplify the notation. The nodes of the Lagrangian mesh follow the material point to which they were originally attached during the motion, so that the mapping

between the parent coordinates and the material coordinates is time-independent. Hence, the motion mapping 4.1 between the current and initial configurations of the cell can also be interpolated using the current positions of the nodes:

$$\mathbf{x}(\mathbf{X}, t) = \sum_{I}^{n} N_I(\xi(\mathbf{X})) \cdot \mathbf{x}_I(t) \tag{4.12}$$

The interpolation used to approximate the geometry is also used to define the trial solutions of the mechanical and regulation modules. The displacement field is approximated subtracting the interpolation of the current and material coordinates of a particle given in eqs. 4.12 and 4.11. Velocities and accelerations are be approximated in terms of the nodal values taking the time derivative of eq: 4.12:

$$\mathbf{u}(\xi, t) = \sum_{I}^{n} N_I(\xi)[\mathbf{x}_I(t) - \mathbf{X}_I] = \sum_{I}^{n} N_I(\xi)\mathbf{u}_I(t) \tag{4.13a}$$

$$\dot{\mathbf{u}}(\xi, t) = \sum_{I}^{n} N_I(\xi)\partial\mathbf{x}_I(t)/\partial t = \sum_{I}^{n} N_I(\xi)\dot{\mathbf{u}}_I(t) \tag{4.13b}$$

$$\ddot{\mathbf{u}}(\xi, t) = \sum_{I}^{n} N_I(\xi)\partial^2\mathbf{x}_I(t)\Big/\partial t^2 = \sum_{I}^{n} N_I(\xi)\ddot{\mathbf{u}}_I(t) \tag{4.13c}$$

where the explicit reference to the material coordinates has been dropped, using their one-to-one correspondence with parent coordinates.
The unknown variables associated to the regulation module are also be interpolated using their nodal values. Concentrations and concentration change rates are then given by:

$$\mathbf{r}(\xi, t) = \sum_{I}^{n} N_I(\xi)\mathbf{r}_I(t) \tag{4.14a}$$

$$\dot{\mathbf{r}}(\xi, t) = \sum_{I}^{n} N_I(\xi)\partial\mathbf{r}_I(t)/\partial t = \sum_{I}^{n} N_I(\xi)\dot{\mathbf{r}}_I(t) \tag{4.14b}$$

In all of the interpolations above, the shape functions are constant in time and the time-dependence of the trial solutions is contained in the nodal coefficients. The test functions, according to the Galerkin method, are also expressed in terms of the shape functions and the virtual nodal displacements and concentrations.

$$\delta\mathbf{u}(\xi) = \sum_{I}^{n} N_I(\xi)\delta\mathbf{u}_I \tag{4.15a}$$

$$\delta\mathbf{r}(\xi) = \sum_{I}^{n} N_I(\xi)\delta\mathbf{r}_I \tag{4.15b}$$

The virtual nodal values in 4.15 are arbitrary and time-independent.

4.1.4 Nodal forces, concentrations rates and semi-discrete equations

The discrete counterparts of the weak forms are obtained substituting the FEM approximations of the test and trial functions in the integral equations 4.6 and 4.9. The resulting equations are expressed more clearly introducing the definition of the different terms according to their physical origin. For the mechanical module, the internal nodal forces stemming from the active and passive cell response are defined as:

$$f_{iI}^{Prot} = \int_{\Gamma_t} N_I t_i^{Prot}\, d\Gamma \tag{4.16a}$$

$$f_{iI}^{Ctk} = \int_{\Omega_t} \frac{\partial N_I}{\partial x_j}\sigma_{ji}\, d\Omega \tag{4.16b}$$

The term f_{iI}^{Prot} gives the nodal forces generated at the cell boundary by the protrusion force that pushes the cell forward. f_{iI}^{Ctk} contains the internal forces originated by the rheological response of the cell cytoskeleton. The stress σ_{ji} in

f_{iI}^{Ctk}, given by the constitute law introduced in Chapter 3, can be split in two parts: a passive contribution to the internal forces associated to the viscoelastic resistance of the cytoskeleton to deformation, and an active term associated to the contraction forces generated by the cell.
The next definitions are derived from the inertial term in 4.6 and those terms corresponding to the external forces experienced by the cell during its motion.
f_{iI}^{Inert} is the inertial term associated to the change in linear momentum given by the balance between external and internal forces. Considering that the density of the cell is similar to that of water, the inertial term at the cellular scale is several orders of magnitude smaller than the others and is usually neglected[1].

$$f_{iI}^{FA} = -\int_{\Omega_t} (\delta(x_{FA})\, k_{FA} \cdot N_I N_J \, d\Omega) \cdot u_{iJ} \tag{4.17a}$$

$$f_{iI}^{Drag} = -\int_{\Omega_t} (\delta(z)\beta \cdot N_I N_J \, d\Omega) \cdot \dot{u}_{iJ} \tag{4.17b}$$

$$f_{iI}^{Inert} = \int_{\Omega_t} (\rho \cdot N_I N_J \, d\Omega) \cdot \ddot{u}_{iJ} \tag{4.17c}$$

The external forces are originated by the interaction between the cell and the substrate during its motion. f_{iI}^{Drag} are the nodal forces caused by the sliding of the basal surface of the cell on a substrate and is proportional to the migration velocity. It is similar to a continuous friction force, in this case generated by the interaction between the receptors on the cell basal surface and the ligands coating the substrate on which the cell is moving. f_{iI}^{FA} are punctual forces at the locations x_{FA} where the cell has established an adhesion site. These are reaction forces from the substrate, equal and opposite to the forces exerted by the cell to pull the adhesion sites and transmitted to the substrate through the spring-like bonds

[1]The Einstein convention for the sum of repeated indices has been adopted also for the nodal labels. For instance, the integrand in the definition of the inertial force has been transformed in this way:

$$\rho \cdot N_I \sum_J N_J \cdot \ddot{u}_{iJ} \xrightarrow{\text{EINSTEIN}} \rho \cdot N_I N_J \cdot \ddot{u}_{iJ}$$

The same convention applies to the rest of the nodal forces.

between adhesion and substrate.

Next, the expressions obtained in the derivation of the discrete equations of regulatory module from the weak form are defined in terms of nodal concentration rate changes:

$$w_{\alpha I}^{Der} = \int_{\Omega_t} (N_I N_J d\Omega) \cdot \dot{r}_{\alpha J} \tag{4.18a}$$

$$w_{\alpha I}^{Dil} = \int_{\Omega_t} (N_I N_J [\nabla \cdot \dot{\mathbf{u}}]\, d\Omega) \cdot r_{\alpha J} \tag{4.18b}$$

The variation of the content of protein α in a material volume of the cell is given by two separate factors. The term $w_{\alpha I}^{Der}$ is the discrete counterpart to the change in protein content caused by the variations of concentration in the material volume associated to node I. Thus, it is given by the material time derivative of the concentration at that particular node. The dilution term $w_{\alpha I}^{Dil}$ has a geometrical origin: it accounts for the variation in concentration caused by the compression or expansion of the material volume with constant protein content. The customary assumption that the cell behaves as an incompressible material is expressed mathematically as $\nabla \cdot \dot{\mathbf{u}} = 0$, which makes the contribution of this term vanish.
The physical processes that bring about the changes in concentration are included in the following nodal rates of concentration change:

$$w_{\alpha I}^{Diff} = \int_{\Omega_t} (\frac{\partial N_I}{\partial x_j} \frac{d_\alpha}{\Phi^2} \frac{\partial N_J}{\partial x_j}\, d\Omega) \cdot r_{\alpha J} \tag{4.19a}$$

$$w_{\alpha I}^{React} = \int_{\Omega_t} N_I f_\alpha(\mathbf{r})\; d\Omega \tag{4.19b}$$

where $w_{\alpha I}^{Dif}$ and $w_{\alpha I}^{React}$ account for the changes in concentration caused by diffusion and reaction, respectively.
The last step required to arrive at the semi-discrete equations is introduce the approximations of the test functions, trial functions and their time derivatives in

the integral weak forms. In this way, using the definitions of the nodal forces and substituting the approximations of the displacements, velocities and accelerations introduced in the former section, the weak form 4.6 of the equation governing the mechanical module can be written as:

$$\delta u_{iI}[f_{iI}^{Inert} - f_{iI}^{Fric} - f_{iI}^{FA} - f_{iI}^{Prot} + f_{iI}^{Ctk}] = 0 \qquad \forall \delta u_{iI} \tag{4.20}$$

Similarly, substitution of the approximations of the trial concentrations and their time derivatives and the introduction of the definitions of the nodal rates of concentration change allows to express the weak form 4.9 as:

$$\delta r_{\alpha I} \cdot [w_{\alpha I}^{Der} + w_{\alpha I}^{Dil} + w_{\alpha I}^{Diff} - w_{\alpha I}^{\mathrm{Re}act}] = 0 \qquad \forall \delta r_{\alpha I} \tag{4.21}$$

Since the equation above apply to arbitrary values of the virtual displacements $\delta \mathbf{u}_I$ and arbitrary values of the virtual concentrations $\delta \mathbf{r}_I$, it follows that the non-trivial solution to eqs. 4.20 and 4.21 is:

$$[f_{iI}^{Inert} - f_{iI}^{Fric} - f_{iI}^{FA} - f_{iI}^{Prot} + f_{iI}^{Ctk}] = 0 \qquad \forall (I,i) \tag{4.22a}$$

$$[w_{\alpha I}^{Der} + w_{\alpha I}^{Dil} + w_{\alpha I}^{Diff} - w_{\alpha I}^{React}] = 0 \qquad \forall (I,\alpha) \tag{4.22b}$$

The equations 4.22 are called semi-discrete because the time domain has not yet been discretized. They constitute a system of nonlinear ordinary differential equations (ODE's), with the nodal coefficients of the trial solutions $\mathbf{u}_I$, $\mathbf{r}_{\alpha I}$ and their time derivatives as unknowns. The size of the system is equal to the number of nodal degrees of freedom. Being n the number of mesh nodes, d number of the spatial dimensions considered and N_P the number of proteins, the number of equations is $n \cdot d$ in the mechanical subsystem 4.22a and $n \cdot N_P$ in the regulatory subsystem 4.22b.
Factoring out the column vectors of nodal unknowns from the nodal forces and nodal concentration rates, the discrete equations 4.22 can be expressed in matrix form:

$$\begin{bmatrix} \mathbf{M}_{uu} & 0 \\ 0 & 0 \end{bmatrix} \begin{bmatrix} \ddot{\mathbf{u}} \\ \ddot{\mathbf{r}} \end{bmatrix} + \begin{bmatrix} \mathbf{C}_{uu} & 0 \\ 0 & \mathbf{C}_{rr} \end{bmatrix} \begin{bmatrix} \dot{\mathbf{u}} \\ \dot{\mathbf{r}} \end{bmatrix} + \begin{bmatrix} \mathbf{K}_{uu} & 0 \\ 0 & \mathbf{K}_{rr} \end{bmatrix} \begin{bmatrix} \mathbf{u} \\ \mathbf{r} \end{bmatrix} = \begin{bmatrix} \mathbf{F}_u \\ \mathbf{R}_r \end{bmatrix} \tag{4.23}$$

where $\mathbf{M}$, $\mathbf{C}_{xy}$, $\mathbf{K}_{xy}$ and $\mathbf{F}_x$ can be assembled from the definitions of the nodal forces and nodal concentration rates into regular Finite Element matrices of mass, damping and stiffness. An example of the explicit form of these matrices will be given for 1D and 2D isoparametric elements in the next section.
The system of equations 4.23 are the general Finite Element formulation of a cell migration model in arbitrary dimensions, and apply to large deformations and material non-linearities. Furthermore, in this FEM framework, alternative assumptions regarding the behavior of the cytoskeleton and adhesion sites dynamics can be readily considered introducing different constitutive laws in f^{Ctk} and f^{FA}. Likewise, replacement of the reaction term in w^{React} allows the introduction of a more detailed description of the regulation mechanism of migration or alternative crosstalk schemes between the proteins. A method to solve the semi-discrete equations is developed in the following section.

4.2 Solution of the equations

The goal of this section is to develop a solution method for the semi-discrete equations of the migration model. The coupling between the mechanical and regulatory modules is assumed to be weak, which allows the division of the nonlinear coupled system 4.22 into two smaller sub-problems. The systems of ODEs governing the evolution of the nodal variables of the two subproblems are then transformed, using a time-discretization scheme, into two sets of nonlinear algebraic equations for the values of the nodal displacements and protein concentrations. Sequential resolution of these algebraic systems provides the transient solution in the form of the values of the nodal unknowns at each time step.

4.2.1 Staggered Scheme for the Mechanical-Regulatory Coupling

The numerical solution of system 4.22 requires a time-marching scheme for the advancement in time of the nodal variables: displacements and concentrations. The time domain $[t_0, t_f]$ in which a solution of the problem is sought is divided into n_T time steps $\Delta t^k = t^k - t^{k-1}$, from $k = 1$ to $k = n_T$. From an initial value of the two sets of nodal variables $(\mathbf{u}^0, \mathbf{r}^0)$, the transient solution is then constructed

approximating their values ($\mathbf{u}^k, \mathbf{r}^k$) at subsequent time steps.
The solution procedure has to take into account that the systems of equations that govern the mechanical and regulatory modules are not independent. In the mechanical module, the forces that propel cell motion are dependent on the concentrations of the proteins. Particularly, the protrusion force $\bar{t}^{Prot}(\mathbf{r})$ specified in the boundary condition 4.2b and the active contraction term of the total stress σ_{ji} are functions of the protein activity. Similarly, the spring constant $k_{FA}(\mathbf{r})$ of each adhesion site depends on the local protein concentration, because the strength and lifetime of adhesion sites are controlled by the regulatory network. Hence, protein concentrations enter the equation 4.22a governing the mechanical module through the following nodal forces:

$$f_{iI}^{Prot} = f_{iI}^{Prot}(\mathbf{r}) \tag{4.24a}$$

$$f_{iI}^{Ctk} = f_{iI}^{Ctk}(\mathbf{u}, \mathbf{r}) \tag{4.24b}$$

$$f_{iI}^{FA} = f_{iI}^{FA}(\mathbf{u}, \mathbf{r}) \tag{4.24c}$$

Conversely, the regulatory module is coupled to the mechanical module through the transduction of mechanical signals from adhesion sites. The mechanical information, gathered when the contacts are stretched, is converted into biochemical signals that change the equilibrium of the protein reactions. The dependence on the displacements of the external stimulus term $\Psi(\mathbf{u})$ in the reaction term captures this interaction.
The dilution term is also dependent on the mechanical deformation of the cell. Even if the cell is considered incompressible, changes in the cell geometry also affect indirectly the dynamics of the regulatory module, as the domain in which the proteins are distributed changes. Hence, the following nodal concentration rates are coupled to the current state of cell deformations:

$$w_{\alpha I}^{Dil} = w_{\alpha I}^{Dil}(\mathbf{r}, \dot{\mathbf{u}}) \tag{4.25a}$$

$$w_{\alpha I}^{React} = w_{\alpha I}^{React}(\mathbf{r}, \mathbf{u}) \tag{4.25b}$$

From the previous discussion of the coupling between the migration processes, it follows that the matrices of the mechanical and regulatory subsytems in eqs 4.23

are dependent on the unknown variables of the other and the full system is nonlinear.
An staggered time-stepping scheme will be used to integrate the coupled system 4.23. In a staggered scheme, the two interacting subsystems are integrated sequentially, so that when the variables of one of the problems are advanced in time, the variables of the other subproblem are frozen[126]. Thus, let $(\mathbf{r}^{k-1}, \mathbf{u}^{k-1})$ be the values of the nodal variables at time t^{k-1}. Then, the displacements at $\mathbf{u}^{k-1}$ are used to predict a tentative solution of the concentrations $\mathbf{r}^{k}_{(p)}$, which are subsequently used to advance the displacements to a tentative value $\mathbf{u}^{k}_{(p)}$. The subsystems are assumed to be weakly coupled, in the sense that small variations in the mechanical variables result in small variations of regulatory variables and viceversa. Thus, this assumption allows using the staggered time-stepping algorithm without enforcing equilibrium at each time step.

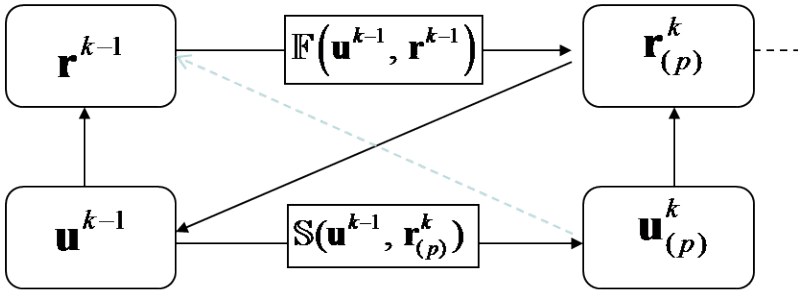

Figure 4.5: Staggered advance of the nodal variables in a weakly coupled problem.

$\mathbb{F}$ and $\mathbb{S}$ represent the discrete operators associated to the method used for the advancement of the nodal variables in each time step. The staggered strategy is independent of the time-integration method; a different method can be used for each of the subsystems. This is particularly advantageous when the time scales or the stability restrictions of the subproblems are very different. In this case, an implicit method can be used to advance with large time-steps the stiff terms, such as the diffusion term in the regulatory module, whereas the slow-changing mechanical subsystem is integrated using an explicit method with an equally large time-step. In the next section, the details of a fully explicit Runge-Kutta method of integration for both subsystems are given.
If the weak coupling assumption does not hold, the accuracy of the strategy is

degraded. In this case, the scheme can be modified to enforce equilibrium between the modules using an iterative procedure in each time step. The displacements $\mathbf{u}^k_{(p)}$ obtained in the staggered advancement are substituted to recalculate a trial solution for the concentrations $\mathbf{r}^k_{(p)}$, and the procedure is repeated until their values converge, with the corresponding modification to the scheme is depicted in figure 4.5 with a dashed line. Alternatively, a reduction in the size of the time-steps can lead to the the same accuracy; the choice of the method must be made in terms of the computational efficiency of performing more iterations in a smaller number of steps against dividing the simulation time in more steps of cheaper computational cost. The preceding remarks showcase the trade-off paid for using an staggered scheme instead of solving the full system simultaneously as it is done in monolithic schemes: the accuracy of a staggered method may be compromised if large time-steps are used. On the other hand, a partitioned scheme, comprised of different integration methods for each subproblem, leads to symmetric systems for which standard optimized solvers exists and allows the selection of the most computationally efficient method for each of them.

4.2.2 Time integration of the coupled problem

In this section the staggered scheme introduced previously is combined with a Runge-Kutta method for the advancement of the nodal variables in each time-step. The resultant method of integration of the coupled system will be referred as SRK4. In SRK4, the integration of both subsystems is carried out using a 4th-order Runge-Kutta (RK4) method with adaptative time-step [127]. RK4 is an explicit integration method, in which the derivatives of the nodal unknowns at t^k are approximated using the variables values at previous time points in Δt^k according to the followng expression:

$$\dot{\mathbf{u}}^k_{(p)} = \frac{\mathbf{u}^k_{(p+1)} - \mathbf{u}^{k-1}}{\Delta t^k_{(p)}} \tag{4.26a}$$

$$\dot{\mathbf{r}}^k_{(p)} = \frac{\mathbf{r}^k_{(p+1)} - \mathbf{r}^{k-1}}{\Delta t^k_{(p)}} \tag{4.26b}$$

The derivatives are evaluated four times in each RK4 step: at the beginning of the step, twice at trial midpoints, and once at the end the step. The subindex in

$\Delta t^k_{(p)}$ indicates that in the stages $p = 1, 2$, the variables are advanced only a fraction of the step.

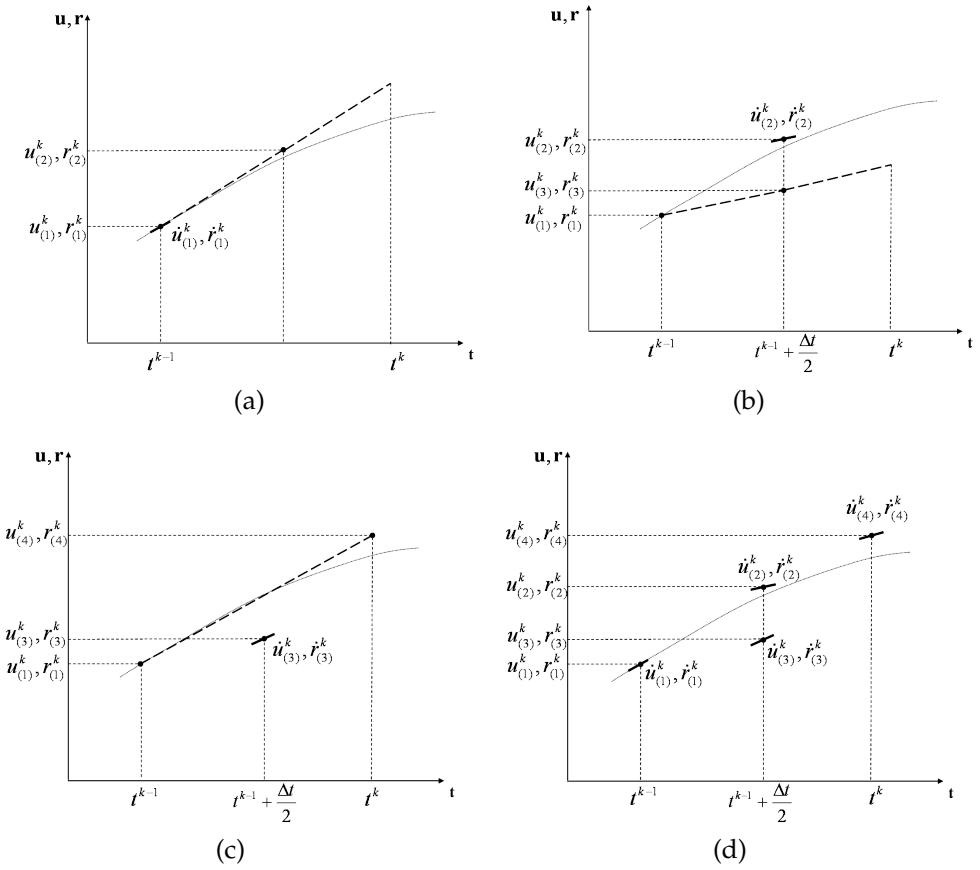

Figure 4.6: 4th-order Runge-Kutta integration scheme.

The derivatives on the left-hand side of expression 4.26 are known: they are evaluated substituting in the discrete system of equations the values $(\mathbf{u}^k_{(p)}, \mathbf{r}^k_{(p)})$ calculated previously. The evaluation of the derivatives is done according to the staggered scheme. First, $(\mathbf{u}^k_{(p)}, \mathbf{r}^k_{(p)})$ are substituted in the subsystem of the discrete equations 4.23 associated to the regulatory module to obtain the following expression for the derivative of the nodal concentrations:

$$\dot{\mathbf{r}}^k_{(p)} = \mathbf{C}^{-1}_{rr} \cdot [\mathbf{R}_r - \mathbf{K}_{rr} \cdot \mathbf{r}^k_{(p)}] = \mathbb{F}(u^k_{(p)},\ r^k_{(p)}) \tag{4.27}$$

where all the matrices and the reaction term on the right hand side of eq.4.27 have been updated using the values $(\mathbf{u}^k_{(p)}, \mathbf{r}^k_{(p)})$. For the stage $p = 1$, the evaluation is done taking the values $\mathbf{u}^k_{(1)} = \mathbf{u}^{k-1}$ and $\mathbf{r}^k_{(1)} = \mathbf{r}^{k-1}$ obtained at the end of the preceding time step. The nodal concentrations are then advanced to a new tentative value $\mathbf{r}^k_{(p+1)}$ obtained from the right hand side of expression 4.26b:

$$\mathbf{r}^k_{(p+1)} = \mathbf{r}^{k-1} + \Delta t^k_p \, \dot{\mathbf{r}}^k_{(p)} \tag{4.28}$$

Analogously, $\mathbf{u}^k_{(p)}$ and the new value of the concentration $\mathbf{r}^k_{(p+1)}$ are substituted in the mechanical subsystem of the discrete equations to evaluate the displacements derivatives:

$$\dot{\mathbf{u}}^k_{(p)} = \mathbf{C}^{-1}_{uu} \cdot [\mathbf{F}_u - \mathbf{K}_{uu} \cdot \mathbf{u}^k_{(p)}] = \mathbb{S}(u^k_{(p)}, \; r^k_{(p+1)}) \tag{4.29}$$

where, according to staggered scheme, the stiffness, damping and force matrices have been updated and assembled using the new trial value of the concentrations.
Note that the original subsystem has been reduced to a set of first order ODEs neglecting the inertial term in the 4.29 under the assumption of small inertial forces compared to the remaining terms. This assumption bears no loss of generality in the method: if the inertial term is considered, the original 2th order ODE system can be transformed into 2 sets of first order ODE equations, to which SRK4 scheme can be applied in the exact the same way as presented here.
Advancement of the of nodal displacements using $\dot{\mathbf{u}}^k_{(p)}$ completes the p-th substep:

$$\mathbf{u}^k_{(p+1)} = \mathbf{u}^{k-1} + \Delta t^k_{(p)} \, \dot{\mathbf{u}}^k_{(p)} \tag{4.30}$$

In turn, the trial values $(\mathbf{u}^k_{(p+1)}, \mathbf{r}^k_{(p+1)})$ will be used to take the next substep $p + 1$. The staggered advancement is repeated 4 times, as schematically shown in fig. 4.6. Finally, the trial values of the the unknowns are discarded and the solution of the nodal variables at t^k is computed according to the standard RK4 expression:

$$\mathbf{u}^k = \mathbf{u}^{k-1} + \frac{\Delta t^k}{6}(\dot{\mathbf{u}}^k_{(1)} + 2\dot{\mathbf{u}}^k_{(2)} + 2\dot{\mathbf{u}}^k_{(3)} + \dot{\mathbf{u}}^k_{(4)}) \tag{4.31a}$$

$$\mathbf{r}^k = \mathbf{r}^{k-1} + \frac{\Delta t^k}{6}(\dot{\mathbf{r}}^k_{(1)} + 2\dot{\mathbf{r}}^k_{(2)} + 2\dot{\mathbf{r}}^k_{(3)} + \dot{\mathbf{r}}^k_{(4)}) \tag{4.31b}$$

which constitutes a 4th order method in accuracy, for the error in every step is of order $O(\Delta t^4)$. The flowchart for the advancement of the nodal unknowns is summarized in the following box:

Box 4.1 : SRK4 step

1. Set initial values for step k

$$\mathbf{u}^k_{(1)} = \mathbf{u}^{k-1},\ \mathbf{r}^k_{(1)} = \mathbf{r}^{k-1}$$

2. For $p = 1 : 4$

i) Update trial concentration derivatives

$$\dot{\mathbf{r}}^k_{(p)} = \mathbb{F}\left(\mathbf{u}^k_{(p)},\ \mathbf{r}^k_{(p)}, t^k_{(p)}\right)$$

ii) Advance trial concentrations

$$\mathbf{r}^k_{(p+1)} = \mathbf{r}^{k-1} + \dot{\mathbf{r}}^k_{(p+1)} \cdot \Delta t^k_{(p)}$$

iii) Update trial displacement derivatives

$$\dot{\mathbf{u}}^k_{(p)} = \mathbb{S}\left(\mathbf{u}^k_{(p)},\ \mathbf{r}^k_{(p+1)}, t^k_{(p)}\right)$$

iv) Advance trial displacements

$$\mathbf{u}^k_{(p+1)} = \mathbf{u}^{k-1} + \dot{\mathbf{u}}^k_{(p)} \cdot \Delta t^k_{(p)}$$

3. Calculate $\mathbf{u}^k,\ \mathbf{r}^k$ by equation 4.31

After step k is completed, the size of the next step is adapted to enforce that it falls in the range of numerical stability. Although the stability analysis of an staggered method is far from trivial, staggered schemes can be designed to inherit the stability properties of the underlying integrations methods; for a detailed analysis of stability issues see [128]. Generally, the upper bound of stability for the scheme is given by the minimum critical step of the partitions integrated with

a conditionally stable method. For the SRK4 method, the critical step is estimated using the Courant-Friedrichs-Lewy (CFL) [81] condition in the regulatory partition, which relates the size of the critical step to the size of the mesh elements:

$$\Delta t^k_{\text{CFL}} = \frac{1}{\frac{\mathbf{D}_{\max}}{\min_e[\Delta h_e^2]} + \max[\lambda(\mathbf{R_r})]} \approx \frac{\min_e[\Delta h_e^2]}{\mathbf{D}_{\max}} \tag{4.32}$$

where $\mathbf{D}_{\max}$ is the maximum diffusion coefficient of the proteins and Δh_e is a characteristic measure of the node to node distance of the elements in the mesh. The term $\lambda(\mathbf{R}_{\text{r}})$ stands for the eigenvalues of the Jacobian of the reaction term, but since protein diffusion is much faster than the characteristic times of reaction in cell processes, it can be safely neglected in the estimation of the critical step. In 1-dimensional meshes, the characteristic length h_e is taken simply as the distance between nodes. For triangular mesh in a 2-dimensional cell model, h is taken as the minimum height. At every time-step taken , the length h_e is determined by minimum amongst all the elements and the CFL condition is used to determine the step size as:

$$\Delta t^k = \frac{1}{\alpha}\Delta t^k_{\text{CFL}} \tag{4.33}$$

where α is a safety factor.
The major drawback of the SRK4 method is a result of the dependence of the critical step on the minimum Δh_e amongst all the elements. During motion the cell contracts the trailing area of the cell body while the front expands. Thus, it is possible that a severe restriction in the marching step of the entire mesh is imposed by a few elements becoming flattened during cell contraction, as depicted in figure 4.7 . The reduction in the element height produces a second order reduction in the stable step.
The characteristic values of the variables in Δt_{CFL} are used to estimate the magnitude of the problem: the typical duration of 10 minutes in a migration observation is taken as the simulation time, a characteristic element size of $h_e^2 \sim 0.5\mu m^2$ to obtain an acceptable resolution in cells of length $\text{L}_{\text{cell}} \sim 10{-}20\mu m$ and $\mathbf{D}_{\max} = 10\mu m^2/s$ from the diffusion coefficient of GDP-bound RhoGTPases and a safety coefficient $\alpha = 6$. This results in a critical time step of $0.5 \cdot 10^{-2}$ seconds and requires approximately $140 \cdot 10^3$ time steps. In a desktop PC computer with an Intel Core TM(2)

Duo processor, L2 Cache of 4M and 2.66 GHz clock speed, running a 1D simulation with quadratic elements with these parameters without considering cell contraction took around 6 minutes. This is a reasonable simulation time for modeling purposes, which generally requires running large number of similar simulations to evaluate the effect that different assumptions or parameter changes have in the results. However, once a cell contraction of the order of (20%) in certain areas is enabled the efficiency of the method is degraded substantially, as the equivalent simulation took approximately 15 minutes.

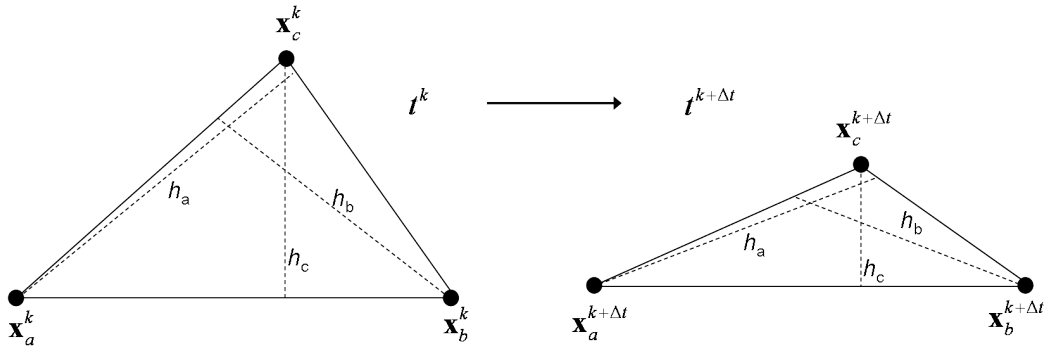

Figure 4.7: Geometry of CFL condition for triangular element.

The preceding remark underscores the main handicap of SRK4 as method of solution of the cell migration equations, as a result of treating the diffusion term explicitly. However, as an explicit method presents an important advantage for modelling purposes, because modifications in the model equations can be readily implemented without the need of linearizing the new terms or making major modifications in the code, as it is the case in a implicit method. Still, the time-step restriction could be bypassed[2] treating implicitly the diffusion term only and integrating the rest of the terms in the same way, as it is done in implicit-explicit (IMEX) methods for reaction-diffusion equation [129]. However, even with an unconditionally stable method, large steps can not be taken: the reaction diffusion equations of the regulatory model feature wave-like solution that are essential to explain the spatio-temporal distribution of the proteins. Capturing the propagation of such waves and the formation of complex patterns requires tracking the high frequency portion of the response [81][Ch.6], for which small-

[2]Other alternatives are available to solve the step restriction: remeshing to obtain elements less distorted in the problematic areas, and using the subcycling technique, in which the domain is subdivided and each subdomain is integrated independently using their stable step.

step explicit methods are more robust [130], [131]. These reasons, despite its relative slowness, justify the choice of SRK4 as a solution method.

4.3 Implementation

This section describes the computational implementation of the FEM formulation of the migration model. Two-dimensional cell domains are meshed using the mesh-generator of the pre and post-processing software GID developed at CIMNE[132]. The mainframe of the Finite element code was programmed in Matlab 7.0, and the more computationally costly subroutines were programmed in Fortran 90 and linked to the mainframe code as external MEX libraries. The general expressions of the nodal forces of the mechanical module and nodal concentrations rates of the regulatory module, introduced in section 4.1.4, is developed in terms of FEM matrices for 1D and 2D problems. The explicit form of the matrices for the Kelvin-Voigt model in small displacements is given for the elements that were regularly used in the simulations: quadratic isoparametric bars for 1D problems and linear triangles for 2D problems.

4.3.1 1D FEM Formulation

The definitions of the nodal forces and the nodal concentration rates given in equations 4.16a-4.19b are used to develop the FEM matrices for 1-dimensional problems. The interpolation of the displacements, concentrations or any other variable field v in a isoparametric bar element with m nodes is expressed as the product of a column vector$\mathbf{v}^e$ containing the variable values at the m nodes and a shape function matrix $\mathbf{N}(\xi)$ defined as :

$$v = \mathbf{N}(\xi) \cdot \mathbf{v}^e = \begin{bmatrix} N_1 & \dots & N_m \end{bmatrix} \begin{bmatrix} v_1^e \\ \dots \\ v_m^e \end{bmatrix} \tag{4.34}$$

where ξ is the parent coordinate and the element domain is $\xi = [-1, 1]$. The spatial derivative of the field $v_{,x}$ is given in matrix form by $v_{,\,x} = \mathbf{B} \cdot \mathbf{v}^e$, where $\mathbf{B} = \begin{bmatrix} N_{1,x} & \dots & N_{m,x} \end{bmatrix}$ is known as the element strain matrix:

$$\mathbf{B} = \frac{1}{x^e_{,\xi}} \mathbf{B}^0 = \frac{1}{x^e_{,\xi}} \begin{bmatrix} N_{1,\xi} & \dots & N_{m,\xi} \end{bmatrix} \tag{4.35}$$

The factor $x^e_{,\xi}$ is the derivative of the spatial coordinate x with respect to the parent coordinate ξ; it stems from applying the chain rule to obtain the spatial

derivatives of fields that are interpolated using the shape functions, which are functions of ξ. In 1 dimensional problems, this term is also the Jacobian of the transformation between the parent coordinate and the spatial coordinate $x_{,\xi} = |J^e|$. This leads to an important simplification of the final expression of the nodal forces and concentrations, but it does not carry over to 2D or 3D problems. It can be computed using the following expression:

$$x^e_{,\xi} = |J^e(\xi)| = \mathrm{N}_{\mathrm{I},\xi} \cdot x^e_{\mathrm{I}} \tag{4.36}$$

For the 3-node quadratic element, the shape functions matrix, the strain matrix and the jacobian are given by:

$$\mathbf{N}(\xi) = [\ \tfrac{1}{2}(\xi^2 - \xi) \quad (1 - \xi^2) \quad \tfrac{1}{2}(\xi^2 + \xi)\ ] \tag{4.37a}$$

$$\mathbf{B}_0(\xi) = \frac{1}{2}[\ (2\xi - 1) \quad -4\xi \quad (2\xi + 1)\ ] \tag{4.37b}$$

and the jacobian can be expressed in terms of the element length and the nodes coordinates as $x^e_{,\xi} = \frac{l^e}{2} + \xi(x_1 + x_3 - 2x_2)$.

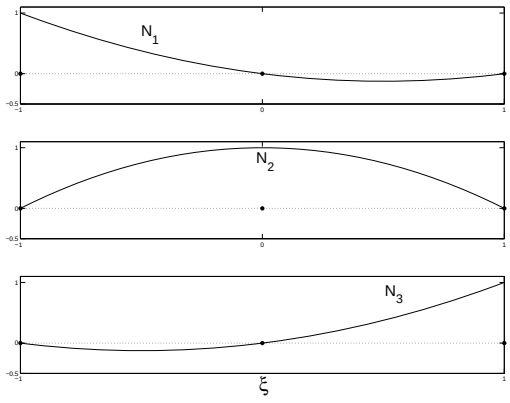

Figure 4.8: Shape functions for the 3- node 1d element.

The notation required to derive the matrix form of the 1D formulation has been introduced. The nodal forces and nodal concentrations introduced in section

4.1.4, were defined in terms of integrals over the total current domain of the mesh. The integration is split into a sum of integrals over individual element domains. The contribution of each element defines the element nodal forces $\mathbf{F}_e^x$ and concentrations $\mathbf{W}_e^x$, from which their global counterparts are assembled scattering their components according to the mesh connectivity [81]. The matrix form of the 1D nodal concentrations is obtained according to this procedure and given in box 4.2:

Box 4.2 : 1D Regulatory Module

$$w_{\alpha I}^{\text{Der}} = \mathbf{W}_{IJ}^{\text{Der}} \cdot \dot{\mathbf{r}}_{\alpha J} \qquad \mathbf{W}_{(e)}^{\text{Der}} = \int_{\Omega_0^e} \mathbf{N}^T \mathbf{N}\, x_{,\xi}\, d\Omega_o$$

$$w_{\alpha I}^{\text{Dil}} = \mathbf{W}_{IJ}^{\text{Dil}} \cdot \mathbf{r}_{\alpha J} \qquad \mathbf{W}_{(e)}^{\text{Dil}} = \int_{\Omega_0^e} \mathbf{N}^T \mathbf{N}\, (\mathbf{B}_0 \dot{\mathbf{u}})\, d\Omega_o$$

$$w_{\alpha I}^{\text{Diff}} = \mathbf{W}_{IJ}^{\text{Diff}} \cdot \mathbf{r}_{\alpha J} \qquad \mathbf{W}_{\alpha\,(e)}^{\text{Diff}} = \int_{\Omega_0^e} \frac{d_\alpha}{\Phi^2} \mathbf{B}_0^T \mathbf{B}_0 \frac{1}{x_{,\xi}}\, d\Omega_o$$

$$w_{\alpha I}^{\text{React}} = \mathbf{W}_{\alpha I}^{\text{React}} \qquad \mathbf{W}_{\alpha\,(e)}^{\text{React}} = \int_{\Omega_0^e} \mathbf{N}^T \mathbf{N} \cdot \mathbf{f}_\alpha\; x_{,\xi}\, d\Omega_0$$

The computation of the integrals over the element domains is performed in the parent domain of the element using a coordinate transformation and Gaussian numerical integration.

$$\int_{\Omega_t^e} f(x,t)\, d\Omega = \int_{\Omega_0^e} f(\xi,t)\, |J^e(\xi)|\, d\Omega_0 = \sum_G w(\xi_G) f(\zeta_G,t)\, |J^e(\xi_G)| \tag{4.38}$$

where ξ_G and $w(\xi_G)$ are the Gauss points and weights determined by the order of the numerical quadrature selected [133]. For the 3-node bar element, a 4-point quadrature was used.
The element matrices contributing to the global 1D nodal forces in the mechanical module are derived analogously and given in Box 4.3:

Box 4.3 : 1D Mechanical Module

$$f_I^{Ctk} = \int_{\Omega_0} \frac{\partial N_I}{\partial x} \sigma \, d\Omega \qquad \mathbf{F}_{(e)}^{\mathrm{Ctk}} = \int_{\Omega_0^e} \mathbf{B}_0^T \sigma \, d\Omega_0$$

$$f_I^{FA} = \mathbf{F}_{IJ}^{FA} \cdot u_J \qquad \mathbf{F}_{IJ}^{FA} = k_{FA} \cdot \delta_{IJ}^{FA}$$

$$f_I^{Fric} = \mathbf{F}_{IJ}^{Fric} \dot{u}_J \qquad \mathbf{F}_{(e)}^{\mathrm{Fric}} = \int_{\Omega_t} (\delta(z)\beta \cdot \mathbf{N}^T \mathbf{N} \, x_{,\xi} \, d\Omega_0$$

$$f_I^{Inert} = \mathbf{F}_{IJ}^{Inert} \ddot{u}_J \qquad \mathbf{F}_{(e)}^{\mathrm{Inert}} = \int_{\Omega_0^e} \rho \cdot \mathbf{N}^T \mathbf{N} \cdot x_{,\xi} d\Omega_0$$

$$f_I^{Prot} = \int_{\Gamma_0^e} N_I t^{\mathrm{Pr}\,ot} \, d\Gamma \qquad \mathbf{F}_{(e)}^{\mathrm{Prot}} = \mathrm{sign}(\hat{\mathbf{n}}) \cdot t^{\mathrm{Pr}\,ot}$$

where δ_{IJ}^{FA} is equal to 1 if there is an adhesion site at the node and 0 otherwise. The protrusion force in 1D is a scalar defined only at the leading and trailing nodes and whose sign is given by sign($\hat{\mathbf{n}}$), the outward normal at these nodes.
If deformations are small, the strain tensor and the rate of deformation become $\epsilon = \mathbf{B} \cdot \mathbf{u^e}$ and $d = \mathbf{B} \cdot \dot{\mathbf{u}}^{\mathbf{e}}$. Under this assumption, the term $\mathbf{F}^{Ctk}$ of the Kelvin-Voigt model for the Cytoskeleton comprises a sum of an elastic, viscous and contractive terms:

$$\mathbf{F}_{(e)\,I}^{Ctk} = \mathbf{F}_{(e)\,IJ}^{El} \cdot \mathbf{u}_J + \mathbf{F}_{(e)\,IJ}^{Visc} \cdot \dot{\mathbf{u}}_J + \mathbf{F}_{(e)\,I}^{Cont} \tag{4.39}$$

where the different constituents of the cytoskeleton forces are given by:

$$\mathbf{F}_{(e)\,IJ}^{El} = \int_{\Omega_0^e} \frac{1}{x_{,\xi}} \mathbf{B}_{0\,I}^T \mathbf{E} \, \mathbf{B}_{0\,J} \, d\Omega_0 \tag{4.40a}$$

$$\mathbf{F}_{(e)\,IJ}^{Visc} = \int_{\Omega_0^e} \frac{1}{x_{,\xi}} \mathbf{B}_{0\,I}^T 2\mu \, \mathbf{B}_{0\,J} \, d\Omega_0 \tag{4.40b}$$

$$\mathbf{F}_{(e)\,I}^{Cont} = \int_{\Omega_0^e} \mathbf{B}_{0\,I}^T \tau \, d\Omega_0 \tag{4.40c}$$

In a more general description of the Cytoskeleton or if large deformations are considered, the Cauchy stress in $\mathbf{F}^{Ctk}$ will be a function $\sigma(\mathbf{e}, \mathbf{d})$ of the finite measure of strain $\mathbf{e}$ and rate of deformation $\mathbf{d}$ determined by the constitutive law. In 1D, the rate of deformation can be calculated with the same expression given for the infinitesimal case, whereas the Almansi strain $\mathbf{e} = 1/2(1 - (\partial x/\partial X)^{-2})$ requires computing the deformation gradient $\mathbf{F} = \partial x/\partial X$, whose interpolation in a 1D the element is given by:

$$\mathbf{F} = \frac{1}{(\partial X/\partial \xi)} \frac{\partial x}{\partial \xi} = \frac{1}{(\mathbf{B}_{0K} \mathbf{X}^e_K)} \mathbf{B}_{0I} x^e_I \tag{4.41}$$

4.3.2 2D FEM formulation

The development of 2D FEM formulation closely parallels the presentation given to its 1-dimensional counterpart. The matrix forms of the equations will be given for a generic 2d isoparametric element with m nodes and then made specific for 3-node linear triangles (**LT3**), for which a closed analytical form exists.
As before, scalar fields such as the concentration of a protein is interpolated inside an element domain defining the matrix of shape functions, which takes the form given in equation 4.34 for the 1-dimensional case.
Inverting the Jacobian of the mapping between the space coordinates (x, y) and the element parent coordinates (ξ_1, ξ_2), the expression of the spatial gradient of a function f in terms of the derivatives with respect to the element coordinates is given by:

$$J^e = \begin{bmatrix} \frac{\partial x}{\partial \xi_1} & \frac{\partial y}{\partial \xi_1} \\ \frac{\partial x}{\partial \xi_2} & \frac{\partial y}{\partial \xi_2} \end{bmatrix} \quad \begin{bmatrix} \frac{\partial f}{\partial x} \\ \frac{\partial f}{\partial y} \end{bmatrix} = \frac{1}{|J^e|} \begin{bmatrix} \frac{\partial y}{\partial \xi_2} & -\frac{\partial y}{\partial \xi_1} \\ -\frac{\partial x}{\partial \xi_2} & \frac{\partial x}{\partial \xi_1} \end{bmatrix} \begin{bmatrix} \frac{\partial f}{\partial \xi_1} \\ \frac{\partial f}{\partial \xi_2} \end{bmatrix} \tag{4.42}$$

where the derivatives $\partial x_i \big/ = \partial \xi_j$ can be computed using the mesh-based interpolation as $\partial x_i \big/ \partial \xi_j = x_I N_{I,\xi_j}$. According to this expression, the spatial derivatives of the shape functions $N_{I,x}$ and $N_{I,y}$ can be computed as:

$$N_{I,x}(\xi) = \frac{b_I^e}{|J^e|} \tag{4.43a}$$

$$N_{I,y}(\xi) = \frac{c_I^e}{|J^e|} \tag{4.43b}$$

with the coefficients b_I^e and c_I^e defined as:

$$b_I^e = \frac{\partial y}{\partial \xi_2}\frac{\partial N_I}{\partial \xi_1} - \frac{\partial y}{\partial \xi_1}\frac{\partial N_I}{\partial \xi_2} \tag{4.44a}$$

$$c_I^e = \frac{\partial x}{\partial \xi_1}\frac{\partial N_I}{\partial \xi_2} - \frac{\partial x}{\partial \xi_2}\frac{\partial N_I}{\partial \xi_1} \tag{4.44b}$$

Using these expressions, the 2D dilatation rate $\nabla \cdot \dot{\mathbf{u}}$ that appears in the dilution term of the regulatory module can be computed as:

$$\nabla \cdot \dot{\mathbf{u}} = (\frac{\partial v_x}{\partial x} + \frac{\partial v_y}{\partial y}) = \dot{u}_{x\,I} N_{I,x} + \dot{u}_{y\,I} N_{I,y} = \frac{1}{|J^e|}(b_K^e \cdot \dot{u}_{x\,K} + c_K^e \cdot \dot{u}_{y\,K}) \tag{4.45}$$

As stated earlier, in the particular case of 3-node linear triangles, the mapping between the parent coordinates and spatial coordinates can be inverted explicitly. This allows to express the shape functions in terms of the current spatial coordinates and to provide a closed analytical expression for the quantities defined previously. The shape functions for this element are given by the triangular coordinates, also known as area coordinates:

$$N_I(x, y) = \frac{1}{2A_e}[a_I^e + b_I^e \cdot x + c_I^e \cdot y] \tag{4.46a}$$

(4.46b)

where $a_I^e = x_J y_K - x_K y_J$, $b_I^e = y_J - y_K$ and $c_I^e = x_K - x_J$. The Jacobian of the transformation, in turn, is given by the current area of the element as $|J^e| = 2A_e$. Hence, the spatial derivatives of the shape functions of the **LT** element are simply given by:

$$N_{I,x} = \frac{b_I^e}{2A_e} \qquad N_{I,y} = \frac{c_I^e}{2A_e} \tag{4.47}$$

The integrals of the **LT3** shape functions products over the deformed triangular domain can also be calculated analytically. In order to give a compact expression of the FEM matrices of the regulatory module, it is convenient to introduce the following defintion:

$$\int_{\Omega_o} \mathbf{N}^T \mathbf{N} \cdot |J| \, d\Omega_o = \frac{h_e A_e}{12} \begin{bmatrix} 2 & 1 & 1 \\ 1 & 2 & 1 \\ 1 & 1 & 2 \end{bmatrix} \equiv h_e A_e \mathbf{m} \tag{4.48}$$

where $\mathbf{m}$ is known as the element mass matrix and h^e is the element thickness. Introduction of these expressions in the definitions of the nodal concentrations leads to the matrix form of the 2d regulatory module, which are gathered in following box:

Box 4.4 : 2D Regulatory Module

$$w_{\alpha I}^{Der} = \mathbf{W}_{IJ}^{Det} \cdot \dot{\mathbf{r}}_{\alpha J} \qquad \mathbf{W}_{(e)IJ}^{Der} = \int_{\Omega_0^e} N_I N_J \, |J^e| \, d\Omega_o = h_e A_e \mathbf{m}_{IJ}$$

$$w_{\alpha I}^{Dil} = \mathbf{W}_{IJ}^{Dil} \cdot \mathbf{r}_{\alpha J} \qquad \mathbf{W}_{(e)IJ}^{Dil} = \int_{\Omega_0^e} N_I N_J (\nabla \cdot \dot{\mathbf{u}}) \, |J^e| \, d\Omega_o = \frac{h_e}{2} (b_k^e \cdot \dot{u}_{xK} + c_K^e \cdot \dot{u}_{yK}) \mathbf{m}_{IJ}$$

$$w_{\alpha I}^{Diff} = \mathbf{W}_{\alpha IJ}^{Diff} \cdot \mathbf{r}_{\alpha J} \qquad \mathbf{W}_{(e)\alpha IJ}^{Diff} = \int_{\Omega_0^e} \frac{1}{|J^e|} \frac{d_\alpha}{\Phi^2} (b_I^e \cdot b_J^e + c_I^e \cdot c_J^e) d\Omega_0 = \frac{h_e}{4A_e} \frac{d_\alpha}{\Phi^2} (b_I^e \cdot b_J^e + c_I^e \cdot c_J^e)$$

$$w_{\alpha I}^{React} = \mathbf{W}_{\alpha IJ}^{\mathrm{React}} f_\alpha(\mathbf{r}) \qquad \mathbf{W}_{(e)\alpha I}^{\mathrm{React}} = \int_{\Omega_0^e} N_I N_J \, f_{\alpha J}(\mathbf{r}) \, |J^e| \, d\Omega_0 = h_e A_e \, \mathbf{m}_{IJ} \cdot \mathbf{f}_{\alpha J}$$

where the expression for a general 2D element is given after the first equal sign and the second expression corresponds to the **LT3** element.
Next, the definitions required to derive the matrix form of the Mechanical module are introduced. The fundamental difference lays in that the independent variables are a 2-dimensional vector field of displacements and the necessity of dealing with second order tensors such as the strain or stress. To this end, the 2d-matrix of shape functions is defined as ${}^{\Delta}\mathbf{N} = [\mathbf{N}_1 \ldots \mathbf{N}_m]$, with its $2x2$ components being:

$$ {}^{\Delta}\mathbf{N}_I = \begin{bmatrix} N_I & 0 \\ 0 & N_I \end{bmatrix} \tag{4.49} $$

Ordering the values of the two components of any 2D field at the element's m nodes in a column vector $\mathbf{v} = [v_{x1} \ v_{y1} \ \ldots v_{xm} \ v_{ym}]^T$, allows to express the interpolation of v in the element as $\begin{bmatrix} v_x & v_y \end{bmatrix}^T = {}^{\Delta}\mathbf{N} \cdot \mathbf{v}$. This ordering of vectors components is also adopted for the nodal forces; as an example, the Internal nodal forces are written as:

$$ \mathbf{f}_I^{Ctk} = \begin{bmatrix} f_{xI}^{Ctk} & f_{yI}^{Ctk} \end{bmatrix}^T \tag{4.50} $$

Second order tensors, under the assumption of plane stress, are transformed to column vectors using Voigt's notation. Thus, the Cauchy stress, Almansi strain, and rate of deformation tensors are given by:

$$ \sigma = [\ \sigma_{xx} \quad \sigma_{yy} \quad \sigma_{xy} \ ]^T \tag{4.51a} $$
$$ \mathbf{e} = [\ e_{xx} \quad e_{yy} \quad e_{xy} \ ]^T \tag{4.51b} $$
$$ \mathbf{d} = [\ d_{xx} \quad d_{yy} \quad d_{xy} \ ]^T \tag{4.51c} $$
$$ \tag{4.51d} $$

In a general formulation of a viscoelastic cytoskeleton with large deformations, the stress tensor that determines the Internal forces is given by the relationship

with the strain and rate of strain measures stated in the constitutive law. The Almansi strain and the rate of deformations are defined in terms of the deformation gradient **F** and the velocity gradient **L** as [73, ch. 4]:

$$\mathbf{e} = \frac{1}{2}(\mathrm{I} - \mathbf{F}^{-T} \cdot \mathbf{F}^{-1}) \tag{4.52a}$$

$$\mathbf{d} = \frac{1}{2}(\mathbf{L} + \mathbf{L}^{T}) \tag{4.52b}$$

and can be computed using the following expression for the interpolations of **F** and **L** at the element level [99, ch.9]:

$$\mathbf{F}_{ij} = \frac{\partial x_i}{\partial \mathbf{X}_j} = x_{iI} N_{I,\mathbf{x}_j} \tag{4.53a}$$

$$\mathbf{L}_{ij} = \frac{\partial v_i}{\partial x_j} = v_{iI} N_{I,x_j} \tag{4.53b}$$

The calculation of **F** requires evaluating the derivatives of the shape functions with respect to the material coordinates, which can be obtained from the expression of N_{I,x_i} given in eqs. 4.43a in the orginal configuration $x(o) = \mathbf{X}$. In the approximation of small deformations, the Almansi strain is reduced to the infinitesimal tensor $\mathbf{e} \approx \varepsilon$ and the rate of deformations becomes $\mathbf{d} \approx \dot{\varepsilon}$. The infinitesimal tensors can be expressed compactly in the FEM framework as

$$\begin{bmatrix} \varepsilon_{xx} & \varepsilon_{yy} & \varepsilon_{xy} \end{bmatrix}^T = {}^{\Delta}\mathbf{B} \cdot \mathbf{u} \tag{4.54a}$$

$$\begin{bmatrix} \dot{\varepsilon}_{xx} & \dot{\varepsilon}_{yy} & \dot{\varepsilon}_{xy} \end{bmatrix}^T = {}^{\Delta}\mathbf{B} \cdot \dot{\mathbf{u}} \tag{4.54b}$$

where ${}^{\Delta}\mathbf{B} = [\mathbf{B}_1 \ldots \mathbf{B}_m]$ is the 2D element strain matrix, whose $3x2$ matrix components are given by:

$$ {}^{\Delta}\mathbf{B}_I = \begin{bmatrix} N_{I,x} & 0 \\ 0 & N_{I,y} \\ N_{I,y} & N_{I,x} \end{bmatrix} = \frac{1}{|J^e|} \begin{bmatrix} b_I^e & 0 \\ 0 & c_I^e \\ c_I^e & b_I^e \end{bmatrix} = \frac{1}{|J^e|} {}^{\Delta}\mathbf{B}_I^0 \tag{4.55} $$

Substitution of the previous expressions in the definition of the nodal forces of the mechanical module then leads to the 2D matrix form in terms of element matrices, which are detailed in box 4.6:

Box 4.5 : Mechanical Module 2D FEM form

$$ \mathbf{f}_I^{Ctk} = \int_{\Omega_t} {}^{\Delta}\mathbf{B}_I^T \sigma \, d\Omega \qquad \mathbf{F}_{(e)I}^{\text{Ctk}} = \int_{\Omega_0^e} {}^{\Delta}\mathbf{B}_{0I}^T \sigma \, d\Omega_0 = \frac{h^e}{2}[b_I^e \sigma_{xx\,I} + c_I^e \sigma_{xy\,I} \,,\, c_I^e \sigma_{xy\,I} + b_I^e \sigma_{xy\,I}]^T $$

$$ \mathbf{f}_I^{Prot} = \int_{\Gamma_t} {}^{\Delta}\mathbf{N}_I \mathbf{t}^{\text{Prot}} \, d\Gamma \qquad \mathbf{F}_{(e)I}^{Prot} = \int_{\Gamma_0^e} {}^{\Delta}\mathbf{N}_I^T {}^{\Delta}\mathbf{N}_J \, \mathbf{t}_J^{\text{Prot}} \; \ell^e d\Gamma_0 = \frac{\ell_{IJ}^e h^e}{6}[2t_{xI}^{\text{Prot}} + t_{xJ}^{\text{Prot}},\, 2t_{yI}^{\text{Prot}} + t_{yJ}^{\text{Prot}}]^T $$

$$ \mathbf{f}_I^{FA} = \mathbf{F}_{IJ}^{FA} \mathbf{u}_J \qquad \mathbf{F}_{(e)IJ}^{FA} = k_{FA} \delta_{IJ}^{FA} $$

$$ \mathbf{f}_I^{\text{Fric}} = \mathbf{F}_{IJ}^{Fric} \dot{\mathbf{u}}_J \qquad \mathbf{F}_{(e)IJ}^{\text{Fric}} = \int_{\Omega_0^e} \delta(z)\beta \cdot {}^{\Delta}\mathbf{N}_I^T {}^{\Delta}\mathbf{N}_J \, |J^e| \, d\Omega_0 = \beta A^e \mathbf{M} $$

$$ \mathbf{f}_I^{\text{Inert}} = \mathbf{F}_{IJ}^{Inert} \ddot{\mathbf{u}}_J \qquad \mathbf{F}_{(e)IJ}^{\text{Inert}} = \int_{\Omega_0^e} \rho \cdot {}^{\Delta}\mathbf{N}_I^T {}^{\Delta}\mathbf{N}_J \; |J^e| d\Omega_0 = \rho_0 h_0^e A_0^e \mathbf{M} $$

The protrusion force is only prescribed in outer edges of the elements at the boundary of the cell, so that expression of $\mathbf{F}_I^{\text{Prot}}$ corresponds to the force at node I resulting form the prescription of protrusion forces along the edge ℓ^e joining I and another node J.

The first expression of the element matrices in Box 4.6 applies to any general element and the integrals must be performed numerically, whereas the second is valid only for 3-node triangles, for which the 2D integrals can be performed analytically. Particularly, the 2d mass matrix $\mathbf{M}$ has been defined as:

$$\int_{\Omega_0^e} \mathbf{N}_I^T \mathbf{N}_J \ |J^e| d\Omega_0 = \frac{h_0^e A_0^e}{12} \begin{bmatrix} 2 & 0 & 1 & 0 & 1 & 0 \\ 0 & 2 & 0 & 1 & 0 & 1 \\ 1 & 0 & 2 & 0 & 1 & 0 \\ 0 & 1 & 0 & 2 & 0 & 1 \\ 1 & 0 & 1 & 0 & 2 & 0 \\ 0 & 1 & 0 & 1 & 0 & 2 \end{bmatrix} = \frac{h_0^e A_0^e}{12} \mathbf{M} \tag{4.56}$$

As in the 1d case, the specific form of the internal force for the Kelvin-Voigt model of the Cytoskeleton is constituted of an elastic, viscous and contractive terms. Under the assumption of small deformations, the 2d element contributions to $\mathbf{F}_{(e)I}^{Ctk} = \mathbf{F}_{IJ}^{El} \cdot \mathbf{u}_J + \mathbf{F}_{IJ}^{Visc} \cdot \dot{\mathbf{u}}_J + \mathbf{F}_I^{Cont}$ are given by:

$$\mathbf{F}_{(e)IJ}^{El} = \int_{\Omega_0^e} \frac{1}{|J^e|} \mathbf{B}_{0\,I}^T \mathbf{E}\, \mathbf{B}_{0\,J}\, d\Omega_0 = \frac{h^e}{4A^e} \mathbf{B}_{0\,I}^T \mathbf{E}\, \mathbf{B}_{0\,J} \tag{4.57a}$$

$$\mathbf{F}_{(e)IJ}^{Visc} = \int_{\Omega_0^e} \frac{1}{|J^e|} \mathbf{B}_{0\,I}^T 2\mu\, \mathbf{B}_{0\,J}\, d\Omega_0 = \frac{h^e}{2A^e} \mathbf{B}_{0\,I}^T \mu\, \mathbf{B}_{0\,J} \tag{4.57b}$$

$$\mathbf{F}_{(e)I}^{Con} = \int_{\Omega_0^e} \mathbf{B}_{0\,I}^T \tau\, d\Omega_0 = \frac{h^e}{6} \sum_K [b_I^e \tau_{x\,K}^{Con} + c_I^e \tau_{xy\,K}^{Con},\, c_I^e \tau_{y\,K}^{Con} + b_I^e \tau_{xy\,K}^{Con}]^T \tag{4.57c}$$

where again the second equality is only valid for **LT3**.
Finally, the FEM form of the governing equations for 1D and 2D problems is obtained substituting in the discrete equations 4.23 the expressions developed in the last two sections for the nodal forces and concentrations. Thus, using the definitions contained in Box 4.2-4.3 for 1D problems and those in Box 4.4-4.5 for 2D, the FEM formulation governing equations cell migration is expressed as:

Box 4.6 : Cell Migration FEM Governing Equations

$$\mathbf{F}_{IJ}^{\text{Inert}} \cdot \ddot{\mathbf{u}}_J + \mathbf{F}_{IJ}^{\text{Fric}} \cdot \dot{\mathbf{u}}_J + \mathbf{F}_{IJ}^{FA} \cdot \mathbf{u}_J = \mathbf{F}_I^{\text{Prot}} - \mathbf{F}_I^{Ctk}$$

$$\mathbf{W}_{IJ}^{\text{Der}} \cdot \dot{\mathbf{r}}_J + [\mathbf{W}_{IJ}^{\text{Diff}} + \mathbf{W}_{IJ}^{\text{Dil}}]\mathbf{r}_J = \mathbf{W}_I^{\text{React}}$$

If you haven't found something strange during the day, it hasn't been much of a day.

John Archibald Wheeler, astrophysicist

Chapter 5

Exploring cell response to external stimuli

The response of a particular regulation model introduced in chapter 2 to different types of external cues is analyzed to test its power to reproduce the spatio-temporal organization of the RhoGTPases observed in experiments. This model of RhoGTPase regulation, authored by Jilkine, Edelstein-Keshet and coworkers [72], is based on the hypothesis that spatial segregation of the proteins is sustained by the existence of a direct mutual inhibition loop between Cdc42 and Rho, and that the interaction is mediated only by GTP-bound RhoGTPase signaling. Another important ingredient of the model is the quasi-steady state approximation, assuming that the flow of proteins between the membrane and the cytosol is fast and that it is not actively regulated. The results of the analysis show that the model features solutions that might be inconsistent with observations, more precisely, appearance of Turing instabilities and reduced sensitivity to secondary stimuli. The mathematical basis of this behavior is established and related to the founding assumptions of the model. The conclusions drawn from the analysis are general, applying to every model of this class, and will aid in the formulation of alternative models of regulation.

5.1 Spatially heterogeneous external signals

The dynamical response of the RhoGTPase system will be studied after the cell is exposed to different classes of spatially heterogeneous external stimulus. Cell movement and mechanical deformation are not considered in the simulations of this chapter, the goal is to focus in the dynamics of the regulatory response. In this case, the external signal is only an abstraction of the real stimuli that lead cells

to migrate.

Figure 5.1: Different distributions of external signals considered

The abstract signal could represent a mechanical gradient in the extracellular matrix, an heterogeneous distribution of chemo-attractors or a variation in the concentration of ligands coating the surface on which the cell are placed. Regardless, the signal is detected by the sensing machinery of the cell, which in turn up-regulates locally the activation of Cdc42. The stimulus are represented by a continuous function $\psi(x,t)$ that models their spatial and temporal distribution. The analysis focuses in the variation of the response of the RhoGTPase model to different types of external stimuli. The generic classes of stimulus depicted in figure 5.1 were suggested in [134]. In addition, the computational experiments analyze how variations in cell geometry and size, inclusion of the nucleus, and the difference in assuming that the receptors of the external signals are present only in the cell boundary instead of the whole cell affect the response. All the computational experiments are simulated with the same initial conditions: the cell is originally at rest, the distribution of the RhoGTPases is homogeneous and the rates of activation and inactivation are balanced.

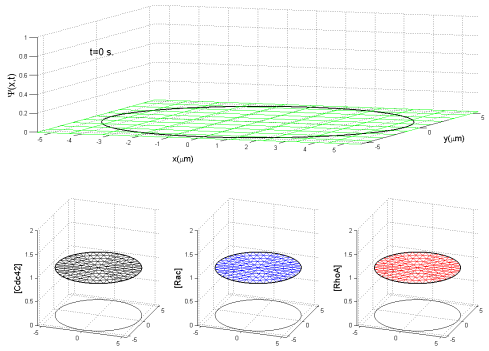

Figure 5.2: Initial distribution of the RhoGTPases in the cell

Unless stated otherwise, the adopted cell geometry for the simulations is a circle of 10μm of radius. In the figures showing the results of the simulation, the concentrations of the RhoGTPases are normalized to the initial concentrations, so that the values above (bellow) 1 mean that the fraction of active proteins is bigger

(smaller) than in the original equilibrium state. Cdc42, Rac and Rho are plotted with black, blue and red curves, respectively. The stimulus field is depicted with a meshed green surface and normalized to its maximum value. In order to facilitate the visual interpretation of the simulations, in some cases the concentration of each RhoGTPase will be displayed in different subwindows, but it should be understood that the actual distribution in the cell is the overlapping of the three plots.

5.1.1 Response to Linear Stimulus

The first signal is a tilted plane representing the linear gradient of an external stimulus that rises continuously between $[t_0, t_1]$, is held constant for an interval of time $[t_1, t_2]$ and then decays to zero in $[t_2, t_3]$. This case belongs to the class labeled as Linear Stimulus that are depicted in the left of figure 5.1. The stimulus function $\psi(x, t)$ goes form 0 to 1/100 of the value of the kinetic rate of Cdc42 in a spatial range equal to half of the cell's length.

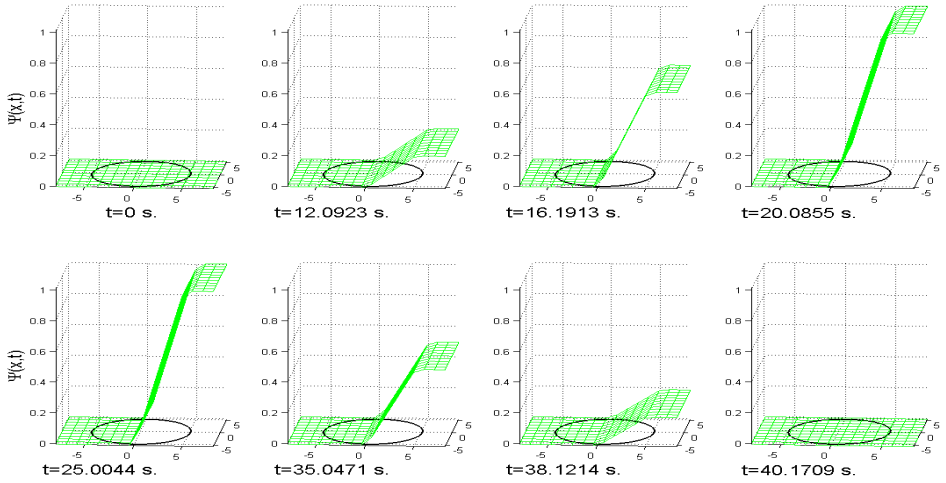

Figure 5.3: Linear gradient of external stimulus

The simulation of the effect of this stimulus on the spatial organization of the RhoGTPases is depicted in figure 5.4. These results show that the Jilkine-Keshet model endows the cell with the capacity to sense this type of signals and that it reproduces the asymmetric distribution of the proteins found in a polarized cell. After the onset of the external perturbation at $t_1 = 10$sec., the concentration of active Cdc42 starts rising where the stimulus is higher. According to the Interaction

scheme of this model, $Cdc42_{GTP}$ signaling locally activates Rac_{GTP} and triggers a rise in its concentration, whereas the inhibitory crosstalk leads to a local decrease of active Rho concentration in this region of the cell. The increase of $Cdc42_{GTP}$

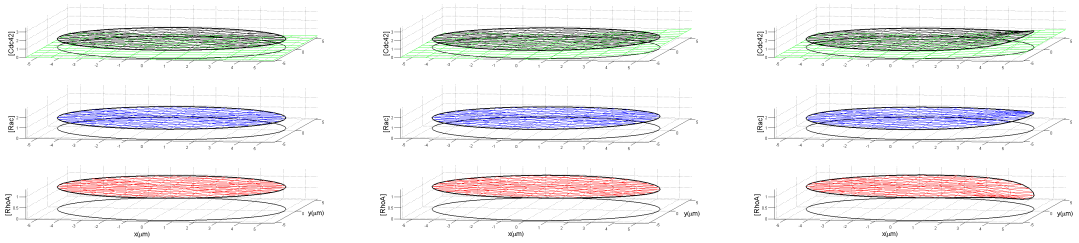

t=12.09s. t=27.05s. t=30.12s.

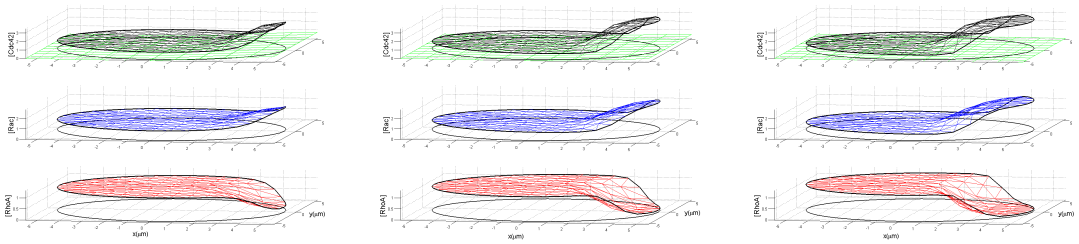

t=32.17s. t=35.04s. t=40.17s.

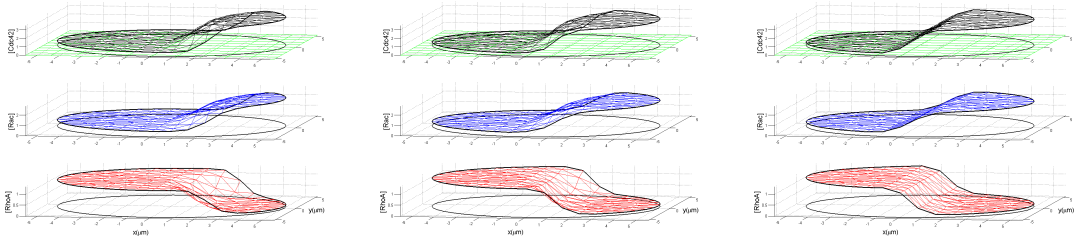

t=45.08s. t=60.05s. t=149.82s.

Figure 5.4: ⊗ Gradient stimulus and active concentration

and Rac_{GTP} at the cell front causes a local decrease of their inactive counterparts (not shown). Since transport of the inactive fraction in the Cytosol is very fast, this local drop is rapidly balanced by diffusion, resulting in a lower and quasi-homogeneous concentration of $Cdc42_{GDP}$ and Rac_{GDP} over the whole cell domain. The global decrease of the inactive fraction of Cdc42 and Rac also leads to a small decrease in their active fractions at the cell trailing edge, whereas the opposite holds true for Rho. Consequently, the inhibition of Rho by Cdc42 is weakened

at the cell rear of the cell and as a result the active concentration of Rho starts rising gradually at the cell back while decreases at the front. This trend is further reinforced by the mutual inhibition between Rho_{GTP} and $Cdc42_{GTP}$, which fuels the segregation of the areas of enhanced activation, with Cdc42 and Rac high at the cell front and Rho at the back. The appearance of these non overlapping areas of high activity is clear 20 seconds after the stimulus is fully activated. The polarization process is complete after approximately 1 minute, when the propagating fronts of active proteins that sweep the cell domain halt. In the final pattern, the concentration of active Cdc42 and Rac increases to 300% and 240% at the cell front, respectively, and decreases to 50% of the initial value at the cell rear. Conversely, the activation of Rho reaches 130% of its equilibrium value at the cell rear and 18% of at the front. In turn, the inactive fractions of the proteins reach an almost homogeneous distribution with Cdc42 and Rac down to 80% and Rho up to 120% of their initial values. This pattern is stable and the cell remains polarized after the stimulus is removed. Moreover, the final distribution of proteins is robust, in the sense that the final pattern is independent on the parameters that define the stimulus, such as the magnitude, the speed in which it is established or its characteristic length compared to the cell. The computational predictions derived from the Jilkine-Keshet model are in good qualitative agreement with the classical view on the spatio-temporal dynamics of RhoGTPase polarization process [135]. The time required to establish polarization on the scale of minutes is consistent with the experimental observations, and the distribution of the RhoGTPases qualitatively matches the compartmentalized distribution of the proteins found in migrating cells.

A descriptive explanation of the polarization process has been laid out in terms of the sign of protein crosstalk and the balance between the reactions taking place in the cell and diffusion. The mathematical basis of the mechanism of polarization is the existence of traveling wave solutions in the model equations, a well known property of nonlinear reaction-diffusion equations with bistable reaction terms[136, Chapter 3]. The external stimulus triggers a wave of excitation that advances trough the cell domain due to diffusion. Since the total amount of protein is conserved, the increase in the active fraction depletes the reservoir of inactive protein that fuels the advance of the activation front and the wave eventually stops. This mathematical behavior, well established in the field of excitable reaction-diffusion systems, has been named as ”wave-pinning” in the context of biological pattern formation [137]. However, as it shall be shown, the Jilkine-Keshet model also features another type of qualitatively different solutions associated with the existence of Turing instabilities. This solutions are not compatible with the observed features of cell polarization and suggest that the model should be modified.

5.1.2 Response to Reversals of Linear Stimuli

The second computational experiment consists in the study of a signal identical to the previous one followed after its decay at t_3 by the rise of a similar plane inclined in the opposite direction. This scenario allows to analyze the capacity of the model to remain sensitive an adapt to new stimulus.

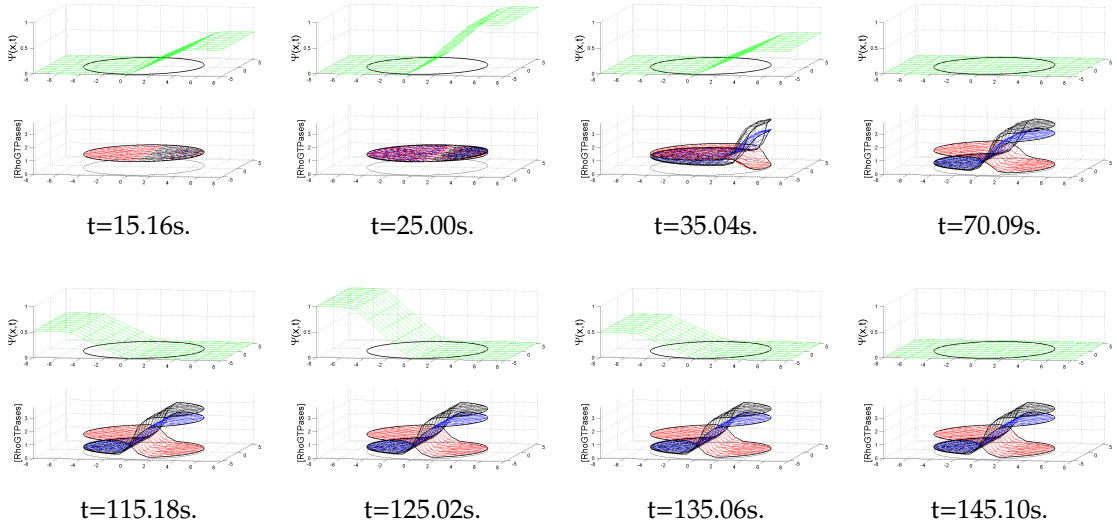

Figure 5.5: ⊗ No polarization switch after stimulus is reversed

The response to the first signal is identical to that encountered for the single Linear Stimulus: sensing of the external gradient, symmetry breaking and polarization (see first row in the simulation depicted in fig.5.5). However, after the gradient is reversed at $t_3 = 100$ seconds, the distribution of RhoGTPases is only slightly displaced during the time that the secondary stimulus is applied, but the direction of the polarization pattern does not change. Once the secondary stimulus is removed, protein concentrations simply return to the equilibrium values reached after the first polarization event. In other words, the cell is incapable of sensing the secondary stimulus once it is polarized, despite the fact that this stimulus is of the same magnitude that the original.
The lower limit of sensibility to the secondary stimulus can be found increasing the magnitude of the secondary signal until the inversion of the polarization axis occurs. For the Edelstein-Keshet model, the secondary signal must be approximately two orders of magnitude larger than the first signal in order induce the realignment of the polarization axis. The following simulation shows the inversion process produced by a signal 100 times bigger in maximum value than the

signal that induced the initial polarization :

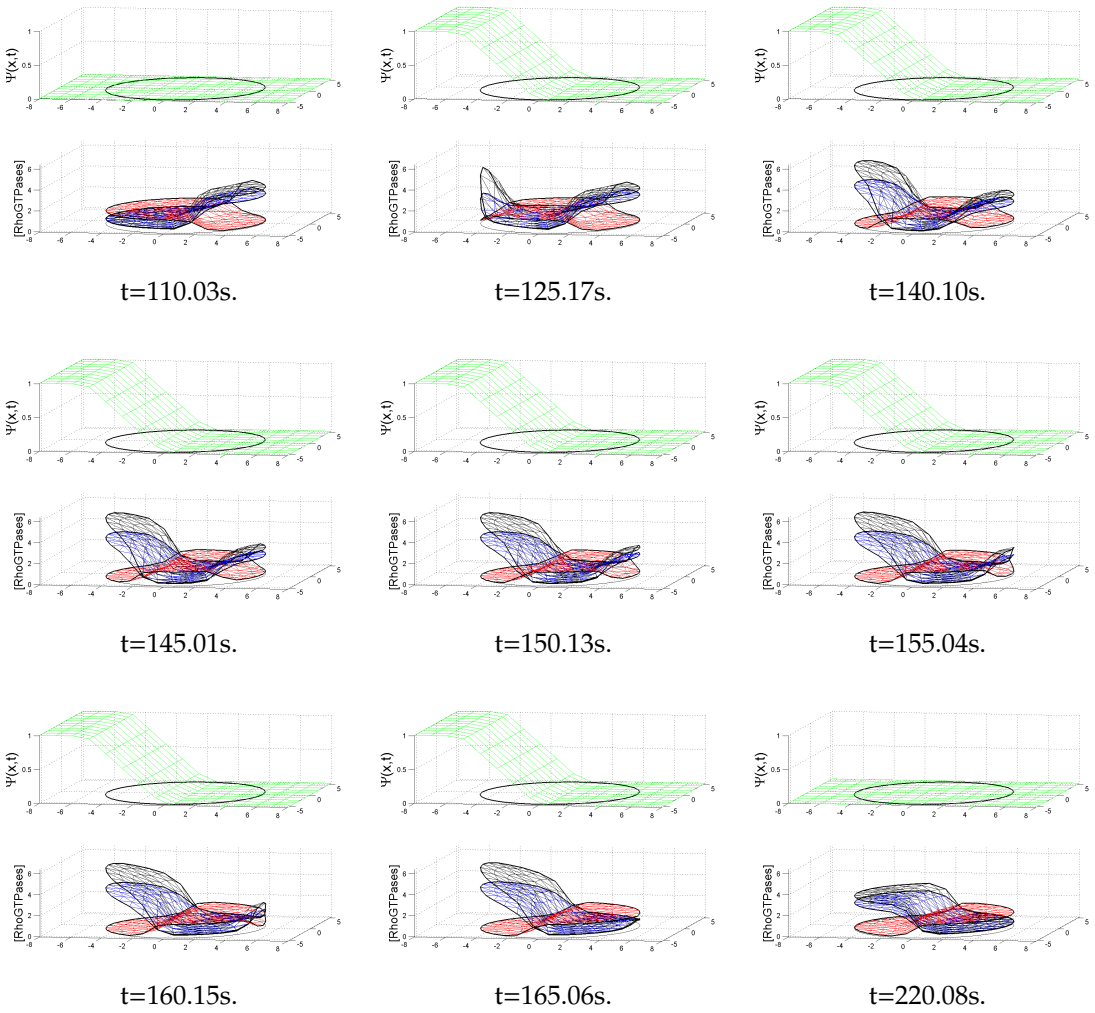

t=110.03s. t=125.17s. t=140.10s.

t=145.01s. t=150.13s. t=155.04s.

t=160.15s. t=165.06s. t=220.08s.

Figure 5.6: ⊗ Polarization switch after exposure to large secondary stimulus

Conceptually, this behavior is not satisfactory, as the cell should, as a 'good sensor' of external signals, be capable of inverting the polarization axis when the source of the external stimulus is changed. Indeed, this faculty is observed in experimental essays with chemotactic [3] as well as mechanotactic [28, 3] external cues. The cause of the lack of response of the model to secondary stimuli will be analyzed in the remaining of this chapter.

5.1.3 Response to a Localized Stimulus

The responses predicted by the regulatory model to signals of small spatial scale compared with the cell length are examined in this section. These type of stimuli, of the class depicted on right of figure5.1, are interesting because they resemble the signal profile that a cell would experience in a real experimental setting when exposed to a propagating front of diffusing biomolecules or small fluctuations of an external signal.
In experimental essays of chemotaxis, a common technique to generate spatially heterogeneous stimulus is to release a certain amount of a chemoattractant with the aid of a pipette or a small hole in the Petri dish where the cells are cultured. The spatio-temporal distribution of the biomolecule that results from this process can be modeled as the instantaneous release of a diffusible specie carrying the signal from a point-source. This is akin to the dispersion of a contaminant in a fluid or a drop of ink in a fluid tank, and the equation describing these processes has an analytical solution [138, chapter 6]. Thus, if a total concentration m_s of a biomolecule with diffusion rate d_s and decay rate k_s is released at time t_0 from a point r_0 (and uniformly along the z-axis), the concentration of the biomolecule in the in time t at a distance r from the source is given by :

$$\rho_s(r,t) = \frac{m_s}{\sqrt{4\pi d_s \cdot (t-t_0)}} e^{-\frac{(r-r_0)^2}{4\pi d_s \cdot (t-t_0)} - k_s \cdot (t-t_0)} \tag{5.1}$$

The cell receptors transduce a signal to the RhoGTPases when the molecules carrying the signal reach the membrane, and the stimulus function $\Psi(x,t)$ is assumed to be proportional to its concentration:

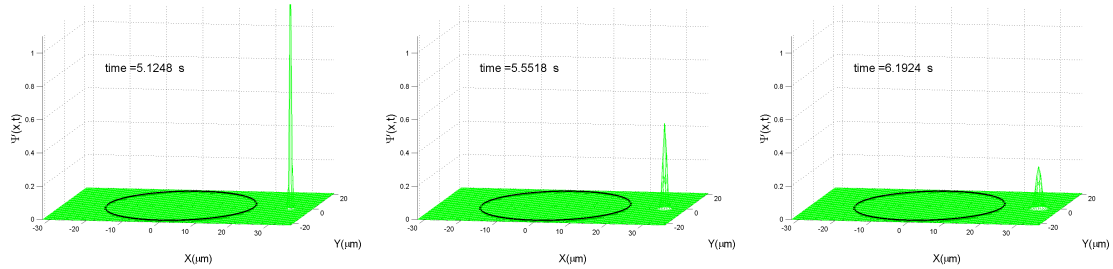

Figure 5.7: Dispersion of diffusible migration promoting agent

Different tests have been performed varying the parameters defining the gaussian stimulus function to evaluate the effects on the response of the regulatory

model. In addition, a series of stimulus functions characterized by being restricted to a small region of the cell, such as a sinusoidal pulse and a simple linear gradient defined so that it only excites a small area near the boundary, were also applied. The response of the RhoGTPase system is essentially the same given to the gradient stimulus of the previous section for all the cases, and the final polarization pattern is indistinguishable from that shown in figure 5.4. In this regard, the capacity of the Jilkine-Keshet model to reproduce RhoGTPase polarization is remarkably robust. Next, the focus is turned to evaluate this capacity when the cell geometry and size are changed.

5.1.4 Variations of cell size and shape

The simulations of the previous sections were repeated varying the size and geometry of the cell in order to check the effects in the response of the regulatory model. The goal is to test if polarization mechanism proposed by the Jilkine-Keshet model can operate in a realistic biological setting, given the fact that the size of different types of eukaryotic cells goes from $10 - 15\mu m$ for fibroblasts and neutrophiles to $100\mu m$ for neurons. In the context of migration, particularly, the polarization mechanism must also remain functional despite the dynamic changes in size and morphology undergone by the cell during their motion and deformation. RhoGTpases proteins, as stated previously, are contained in all eukaryotic cells and act as master regulators of cell migration in all of them. Therefore, the principles governing their organization in all these cell types must be common and any plausible theoretical model of RhoGTPase regulation should reflect this fact.
First, a circular cell of $20\mu m$ of radius is exposed to different types of stimulus. A simple linear gradient leads to the polarization pattern predicted before, with Cdc42 and Rac highly activated at the front and Rho at the back. However, as the spatial range of the stimulus function is restricted to a smaller region near the cell boundary, the polarization pattern that emerges changes.

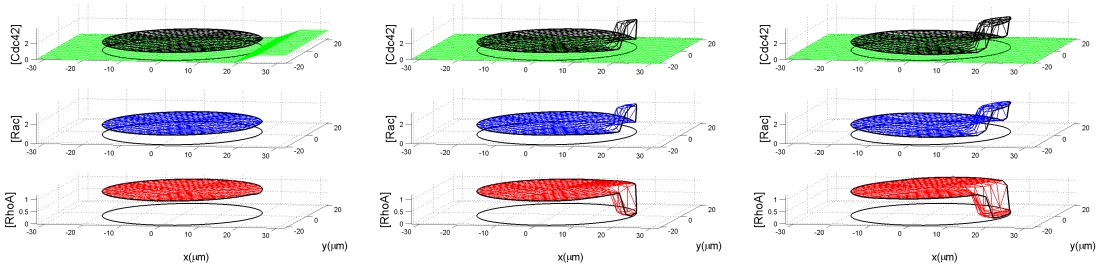

t=20.32s. t=50.05s. t=100.33s.

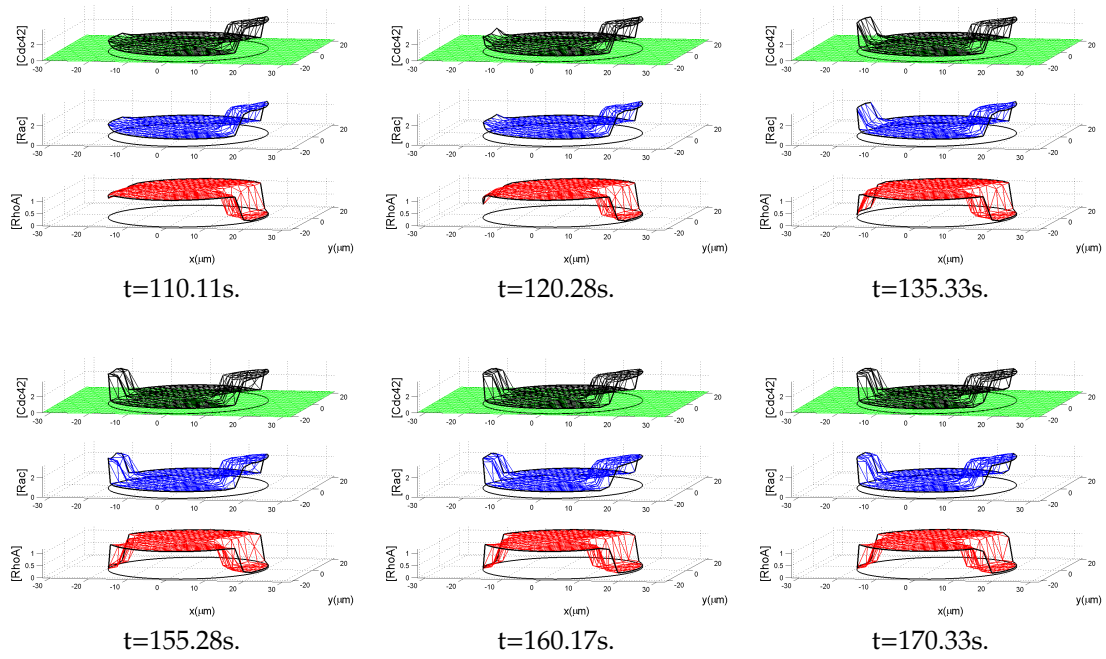

t=110.11s. t=120.28s. t=135.33s.

t=155.28s. t=160.17s. t=170.33s.

Figure 5.8: ⊗ Bipolar pattern after exposure to localized Stimulus

As the simulation shows, the localized stimulus leads to the appearance of a bipolar state. Initially, the response appears to be similar to that encountered for the Linear Stimulus, but after approximately 100 seconds, a second area of high Cdc42 and Rac activation appears at the end of the cell opposite to where the stimulus was applied. Further in time, a plateau of high $\rho_{\mathrm{GTP}}^{\mathrm{PM}}$ is formed inside the cell body, while $c_{\mathrm{GTP}}^{\mathrm{PM}}$ and $r_{\mathrm{GTP}}^{\mathrm{PM}}$ develop a symmetric pattern of high activation at the cell edges and low activation in the cell interior. This pattern is in clear contradiction with what is observed in biological cells and the underlying causes of these behavior must be investigated.

Next, a cell of the same size is exposed to a gaussian stimulus of the type described in the previous section. Again, the emergent pattern does not correspond to any distribution of the RhoGTPases proteins observed experimentally in cells. In this case, the emergent pattern is characterized by a quasi-periodic distribution of islands of high Cdc42 and Rac activation and low Rho activation. These islands appear successively in time, first at the edge reached initially by the propagating signal and then advancing to the distal end of the cell in a wave-like manner. The distribution of the islands of activation is symmetric across the x-axis, which is coincident with the direction of propagation of the front.

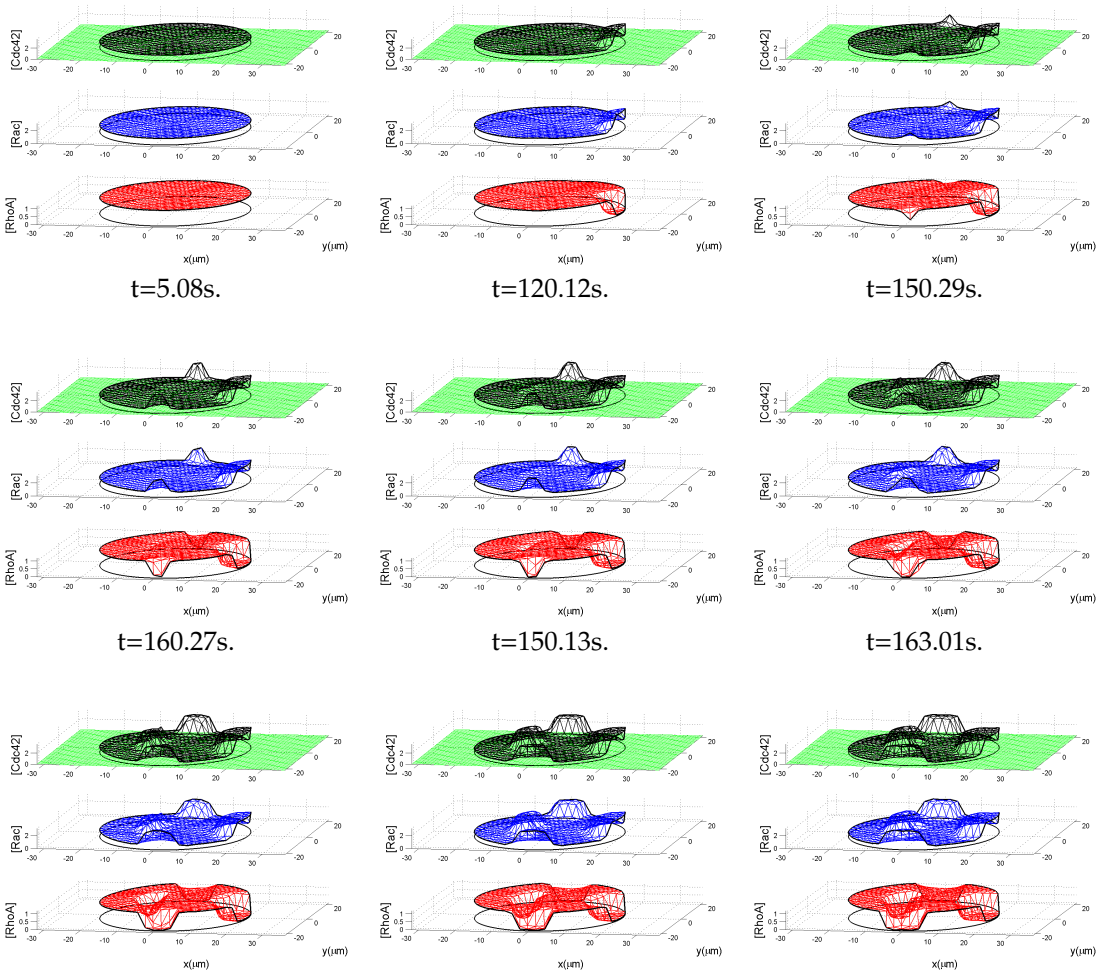

t=5.08s. t=120.12s. t=150.29s.

t=160.27s. t=150.13s. t=163.01s.

t=184.91s. t=198.95s. t=240.86s.

Figure 5.9: ⊗ Multipolar pattern after exposure to gaussian Stimulus

The quasi-periodic structure indicates the existence of a non-trivial mechanism of pattern formation entirely different from the traveling wave underlying apparition of the simple polar distribution.
The lack of robustness of the polarization mechanism in Jilkine-Keshet model is confirmed studying the distribution of RhoGTPase that emerges when the size of the cell is further increased. The last snapshot of the simulated responses given by cells of various sizes are shown in the following figure. The final steady pattern of protein distribution reached after the cells are exposed to simple linear gradients

features a clear scale dependency:

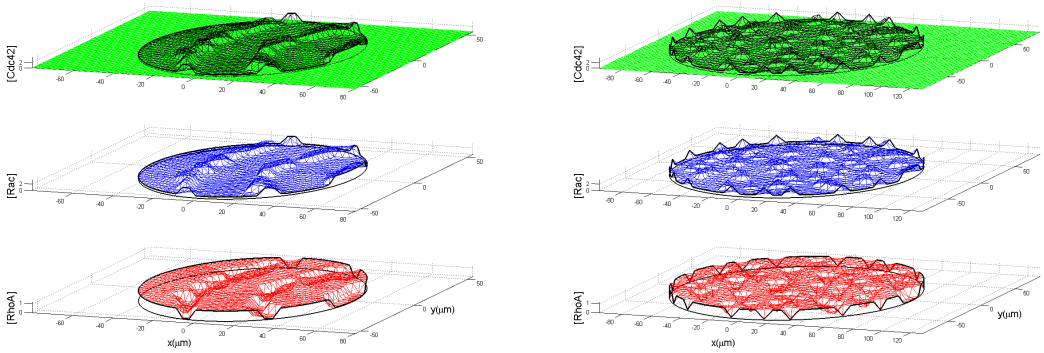

(a) Circular Cell R=50μm (b) Circular Cell R=80μm

Figure 5.10: $^{\otimes}$ Final RhoGTPases distribution in circular cells of increasing radius

As radius of a circular cell is increased to 50μm and 80μm, the pattern of RhoGTPAse displays an increasing number of non-randomly distributed structures of alternating high and low activation. The patterns evidences the existence of a characteristic length that determines the spacing between the zones of high and low activation. Variation of the cell shape and inclusion of the cell nucleus renders similar results:

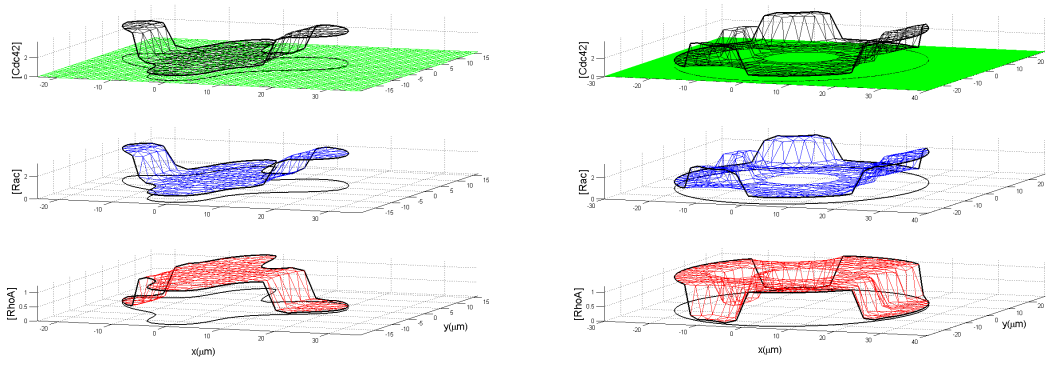

(a) Irregular cell (b) Cell with nucleus

Figure 5.11: $^{\otimes}$ Final RhoGTPases distribution in star-shaped cell and nucleus cell

An irregular cell exposed to external stimuli presents a robust pattern of polarization until bellow a certain cell size, suggesting that the morphology of the

cell is not a determinant variable of the final distribution of protein activation. However, if the cell size is increased, bipolar and multipolar patterns of activation emerge. Likewise, the inclusion of the cell nucleus, modeled as a circular void inside the cell where RhoGTPases can not propagate, does not hinder the establishment of the polar pattern, with Cdc42 and Rac highly activated at the cell front and Rho at the cell back. Again, the variable that triggers the appearance of distribution patterns with multiple areas of high activation is the cell size. These results lead to the conclusion that the Jilkine-Keshet model adequately captures the resilience of the mechanisms underlying cell polarization in cells of varying shape or where a nucleus is included, but that it is incapable of maintaining this robustness when realistic variations of cell scale are introduced.

5.2 Analysis of the response to external stimuli

The results of the previous section showed that the Jilkine-Keshet model of RhoGTPase regulation can in some instances reproduce qualitatively the process of cell polarization, but it also revealed important drawbacks that must be analyzed. More precisely, the failure to sense a signal of similar magnitude than a preceding signal that previously polarized the cell, and the unfitness of the model to describe the polarization process when the size is changed within a range of realistic biological values. The causes underlying this behavior are investigated in this section. First, phase plane analysis is used to understand the lack of response to secondary signals. Potential amendments to the RhoGTPase model are discussed. Second, linear stability analysis is performed to uncover the nature of the quasi-periodic patterns of RhoGTPase distribution. The analysis proves that the emergence of these solutions is associated to diffusion-driven instabilities and that the biologically meaningless distributions are Turing patterns. Arguments against Turing instability as a suitable mechanism to detect external signals or, more generally, to generate spatio-temporal order in the context of the cell regulatory system are presented next.

5.2.1 Lack of response to secondary signals

Phase plane analysis is an elementary technique of Dynamical systems theory that will be used to analyze the lack of response to secondary stimulus of the Jilkine-Keshet model. For the RhoGTPase system, the State space is the set of all the possible states, defined by the concentration of the proteins and the value of the stimulus function in every point of the cell. The Phase plane is the graphical portrait of the State space, so that every point in the plane corresponds to a par-

ticular state of the system. The initial state is then a point in the Phase plane, and the evolution in time of the system corresponds to a trajectory on the Phase plane determined by the governing equations. The trajectories on the Phase plane are tangent to a velocity field given by the derivatives of the system's variables. A closed trajectory on the Phase plane, for instance, represents a periodic solution, whereas a point where all the derivatives of the governing equations are zero is associated to an steady state.
The curves on the phase plane defined by the condition that the time derivative of one the variables vanishes are called nullclines. Hence, the trajectories of system on the phase plane do not cross the nullclines and are bounded by them. Intersections of all the nullclines correspond to isolated steady states of the system [139, chapter 6].
The complete RhoGTPase model requires considering the infinite State space of 6 protein concentrations and the stimulus signal Ψ in every point of the cell. However, since the focus of the analysis is to understand why the system does not react to a second signal once it has been polarized, it is only necessary to consider the trajectories of two representative points at the front and back of the cell, where the first and second stimulus are applied, respectively. If these points are sufficiently far from the transition zone of high and low activation in the polarized cell, it is a good approximation to neglect the diffusion term of the system of PDEs that governs the model and consider instead the associated Kinetic system 2.25. Due to the conservation of the total amount of Cdc42, Rac and Rho, only 3 equations in this ODE system and the 3 associated nullclines are independent. Thus, setting the left hand side of the system of ODEs 2.25 to zero, three nullclines curves are obtained in which the time derivatives of one pair of active-inactive proteins vanish simultaneously. From these expressions, the value of the active fraction of Cdc42, Rac and Rho along the curves can then be obtained as a parametric function of the concentrations of the other proteins and the value of the stimulus function:

$$x_{GTP} = f_{nlc}(\mathbf{r}_{GTP};\ x_{GDP};\ \Psi) \qquad x = c,\ r,\ \rho \tag{5.2}$$

The intersection of the three nullclines is the curve on the Phase Plane that contains the steady states of the system, obtained by introducing sequentially the expression from 5.2 for one protein along its nullcline into the next. In this way, substitution of the Rac nullcline into the Rho nullcline, and of the resulting expression into the Cdc42 nullcline leads to an implicit relationship between the value of the stimulus Ψ and the equilibrium concentration of Cdc42, given the

values of the inactive fraction at t_i:

$$\Psi = \frac{c_{\mathrm{GTP}}}{c_{\mathrm{GDP}}(t_i)} \cdot \mathrm{f}^B - \mathrm{f}^{\mathrm{A}}(c_{\mathrm{GTP}}; \mathbf{r}_{\mathrm{GDP}}(t_i)) \tag{5.3}$$

The ideas introduced previously are now applied to analyze the results of the simulation of the cell exposed to two consecutive and opposite linear gradients, which were shown in figure 5.5. The right edge of the cell was exposed to the first stimulus at time t_0 and removed in $[t_2, t_3]$. Another stimulus was applied to the left side of the cell in the interval $[t_4, t_6]$, while the cell had already polarized.
The following figure shows the bifurcation diagram of Cdc42-Ψ in the time interval corresponding to the application of first stimulus for a representative point on the left side of the cell and another at the right side. The steady-state curve Cdc42-Ψ is plotted with a continuous black line for time t_0, before the stimulus is applied, and with a discontinuous black line for time t_3, after the stimulus is removed. The trajectory followed by both points on the Phase plane are depicted with a discontinuous red line, with blue dots specifying the state at instants t_i:

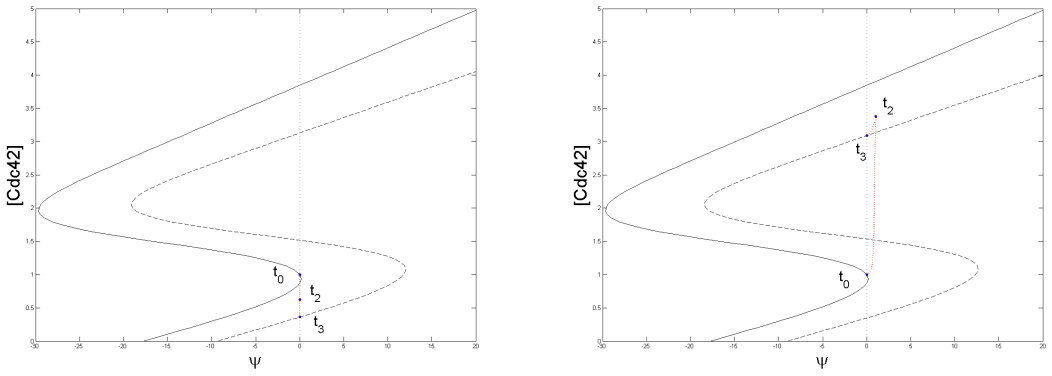

(a) Cell Left edge (b) Cell Right edge

Figure 5.12: Phase Plane trajectories during exposure to 1st linear gradient

Inspection of the bifurcation diagram shows that for a certain range of stimulus values $0 \leq \Psi < \Psi_m$, there are three possible values of $\mathrm{C}_{\mathrm{GTP}}$ on the steady state curve. The upper and lower branches are stable and correspond to equilibrium sates. The branch in the middle of the S-shaped curves is unstable. Initially, the cell is in the homogeneous state of low Cdc42 activation, and accordingly, at time t_0 the two representative points lay in the lower branch of the steady-state curve.

Application of the first stimulus drives the point at the right edge of the cell out of equilibrium and triggers the transition to the upper branch of the steady state curve, with higher equilibrium values of active Cdc42. Conversely, the point at the left edge of the cell is unaffected by direct application of the stimulus signal. The flow towards lower values of Cdc42 is caused by the rightward shift of the steady state curve. The rightward shift of the steady-state curve between t_0 to t_3 is driven by the decrease in concentration of the inactive fraction of Cdc42, which balances the increase in Cdc_{GTP} taking place at the other end of the cell. This effect is understood examining the structure of the steady-state curve in eq.5.3, that shows that a drop in concentration of Cdc_{GDP} results in a lower equilibrium concentration of Cdc_{GTP} for a fixed value of stimulus function. Even if the drop in concentration of the inactive fraction is localized at the right edge, where Cdc42 activation is taking place, the distribution of the inactive fraction is approximately equal at both points. This is due to the large diffusion constant of the inactive fraction, that ensures that its distribution becomes nearly homogeneous almost instantaneously. Hence, the profile of steady-state curves, determined by the concentration values of inactive proteins, is approximately the same for the point at the left and right edges of the cell. The differential application of the stimulus function is what determines the diverging trajectories followed by the two points on the Phase plane.
After the first stimulus is removed at t_3, the point at the right edge settles in upper branch of the steady-state curve and the point at the left edge in the lower branch, corresponding to the polarized state of the cell. Afterwards, the second stimulus is applied to the left side of the cell in the time interval $[t_4, t_6]$. The trajectories on the Phase Plane during the this time lapse are depicted in the next figure:

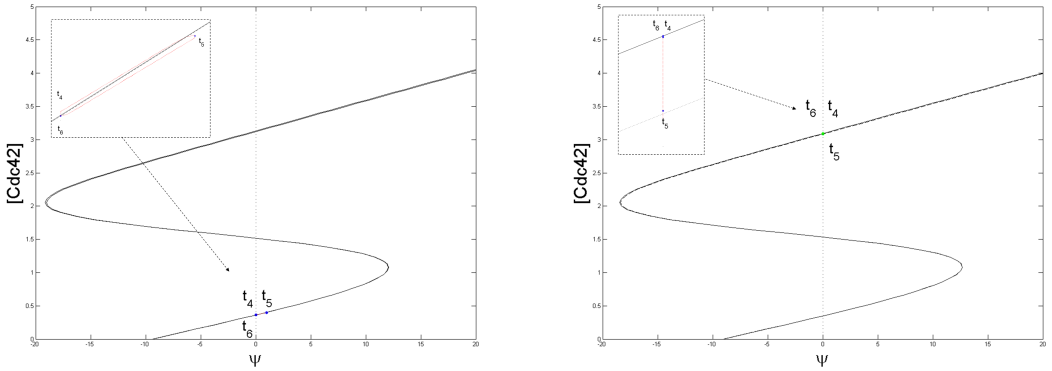

(a) Cell Left edge (b) Cell Right edge

Figure 5.13: Phase Plane trajectories during exposure to 2nd linear gradient

In this case, the increase of Ψ is not enough to overcome the barrier splitting the upper and lower nullcline branches and drive the point in the left edge of the cell to a state high activation. Thus, the underlying cause for the lack of response is clarified examining the trajectories of the two representative points on the Phase Plane. The S-shaped profile of the steady-state curve is determined by the structure of the governing equations, and in particular by the mutual inhibition interaction between Cdc42 and Rho. The position of the curve on the Phase Plane, on the other hand, depends on the concentration of inactive proteins $C_{GDP}(t)$. After the cell is polarized for the first time, C_{GTP} is locally increased, so that the overall concentration of inactive C_{GDP} decreases and the steady state curve is shifted. In addition, the concentration of Rho at the left edge of the cell, where the new stimulus will be applied, has risen and prevents Cdc42 activation. The combination of these two factors makes necessary a stimulus Ψ_m of bigger magnitude to trigger the transition between states. The results of the simulation in which the magnitude of the second signal was much bigger than the first, depicted in 5.6, where the cell was able to inverse the polarization axis, confirm this statement. The trajectories in the Phase plane of the two representative points show how the second stimulus, this time 100-fold larger than the first, is capable of driving the point on the left edge of the cell over the stability barrier and towards the branch of high active Cdc. Meanwhile, the point on the right is dragged towards the lower branch as the steady state curve is shifted due to the change in the inactive fraction of the proteins:

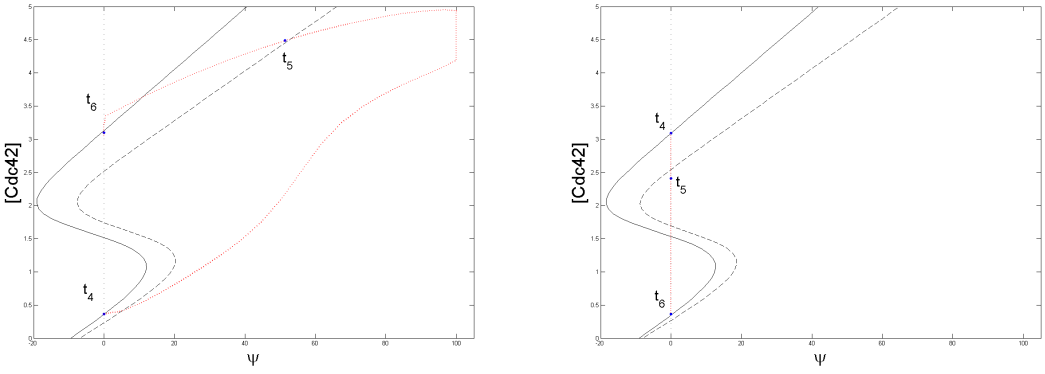

(a) Cell Left edge (b) Cell Right edge

Figure 5.14: Phase Plane trajectories during exposure to Large 2nd linear gradient

From a biological perspective, this behavior is caused by the fact that this model does not differentiate the sensing machinery of the cell and the crosstalk

mediators that generate the spatial and temporal organization. Hence, when the cell is polarized the RhoGTPase concentrations are substantially different from the homogeneous concentrations in the cell at rest, thereby distorting the cell's sensitivity. It remains a matter of experimental observation to determine if a cell requires a bigger stimulus to reverse its course of motion [3]. If the answer to that question were negative, it would point to the existence of a signal amplification mechanism in the RhoGTPase network or a different structure in which the regulation of the RhoGTPase organization and the sensing module are uncoupled. The notion that GAPs and GDIs might be targets of the sensing machinery or active players in the polarization process might be a part of the answer to this question.

5.2.2 Emergence of Turing patterns

Turing patterns are quasi-periodic solutions that emerge in reaction-diffusion systems that are stable under homogeneous perturbations, but become unstable under spatially heterogeneous perturbations. The proof that a reaction-diffusion system may feature Turing patterns uses linear stability analysis to study the evolution of the initial state after a heterogeneous perturbation is applied. The following analysis is based on the treatment of the topic found in [140, Chapter 2].
The system is initial in the homogeneous state $\mathbf{r_0}$, solution of 2.25. After the onset of the external signal, the system is perturbed into a state $\mathbf{r}(x,t) = \mathbf{r_0} + \delta\mathbf{r}(x,t)$ that no longer is in equilibrium nor homogeneous, since the perturbation is spatially dependent. The evolution of the system is found by substituting this state in the system of equations 2.22 and linearizing about the homogeneous state,

$$\frac{\partial \delta\mathbf{r}(x,t)}{\partial t} = \mathbf{J}^R(\mathbf{r_o})\delta\mathbf{r}(x,t) \; + \frac{1}{\Phi^2}\mathbf{D}\nabla^2\delta\mathbf{r}(x,t) \tag{5.4}$$

where $\mathbf{J}^R(\mathbf{r_o})$ denotes the Jacobian of the reaction term evaluated at the initial steady state.

$$\mathbf{J}^R(\mathbf{r_o}) = \left.\frac{\partial \mathbf{K}(\mathbf{r})\cdot\mathbf{r}}{\partial \mathbf{r}}\right|_{\mathbf{r}=\mathbf{r_0}} \tag{5.5}$$

The deviation from the initial state $\delta\mathbf{r}(x,t)$ is a solution of eq. 5.4 satisfying the problem's boundary conditions. The linearity and time-independence of the

operators $\mathbf{J^R}$ and $\mathbf{D}$ leads to solutions that can be expressed as linear combination of functions were the space and time variables are separable.

$$\delta\mathbf{r}(x,t)=\sum_q \delta\mathbf{r}_q = \sum_q \mathbf{v}_q\phi_q(x)\ e^{\lambda t} \tag{5.6}$$

Since $\mathbf{J^R}$ is by construction space independent, the solution can be constructed with functions ϕ_q belonging to the eigenspace of the Laplacian. The constants $\mathbf{v_q}$ are determined by the Fourier expansion of the initial state in terms of ϕ_q. The eigenfunctions must fulfill Neumann conditions to enforce that the solution of 5.4 complies with the no-flux condition at the boundary of the system.

$$\begin{aligned} \nabla^2\phi_q(x) &= -q^2\phi_q(x) \quad && x\in\Omega \\ \nabla\phi_q\cdot\hat{n} &= 0 && x\in\partial\Omega \end{aligned} \tag{5.7}$$

where Ω and $\partial\Omega$ represent the domain of the system and its boundary, respectively. In finite domains, the no-flux at the boundary condition in equation 5.7 implies that only a discrete set of eigenvalues are permitted.
Substitution of the tentative solution $\delta\mathbf{r}_q$ into eq. 5.4 transforms the dynamic problem into the following eigenvalue problem:

$$[\lambda\mathbf{I}-(\mathbf{J}^R(\mathbf{r_0})-(q/\Phi)^2\mathbf{D})]\delta\mathbf{r}_q(x,t)=0 \tag{5.8}$$

Non-trivial solutions exist provided that the determinant associated to the system of equations 5.8 vanishes. The matrix that defines the linear approximation of the reaction-diffusion problem is then:

$$\mathbf{F}^{RD}(\mathbf{r_o},\, q/\Phi)=[\mathbf{J}^R(\mathbf{r_o})-(q/\Phi)^2\mathbf{D}] \tag{5.9}$$

The determinant $P_{q/\Phi}(\lambda)=\det[\lambda\,\mathrm{I}-\mathbf{F}^{\mathrm{RD}}]$ is a polynomial of degree N equal to the number of reacting species in the system. The coefficients of $P_{q/\Phi}(\lambda)$ are

functions of the initial state $\mathbf{r_o}$ trough their dependency on jacobian of the reaction term $\mathbf{J}^R(\mathbf{r_o})$, and of the wave-number q through the diffusion term.

$$P_{q/\Phi}(\lambda) = \lambda^N + a_1(\mathbf{r}_0, q)\lambda^{N-1} + ... + a_{N-1}(\mathbf{r}_0, q)\lambda + a_N(\mathbf{r}_0, q) \tag{5.10}$$

The roots of the characteristic polynomial $P_{q/\Phi}(\lambda)$ for a particular wave-number give the eigenvalues associated to a mode ϕ_q.

$$P_{q/\Phi}(\lambda) = 0 \tag{5.11}$$

The relationship $\lambda(q)$ for which eq. 5.11 holds true is known as the Dispersion relation, and provides the eigenvalues as a function of the wave-number. The set of wave-numbers for which $\mathrm{Re}\,\lambda(q) > 0$ is the range of instability; if the real part of an eigenvalue is positive, the corresponding mode grows exponentially and the homogeneous steady state is unstable under heterogeneous perturbations. The system eventually reaches a new steady state, usually dominated by the non-linear evolution of the fastest growing mode, which is that with the maximum eigenvalue in the instability range of the dispersion relation . This state is known as Turing pattern and is stable to subsequent homogeneous or inhomogeneous perturbations.
A sufficient condition for the appearance Turing patterns is found in the change of sign in the determinant of the linearized equations. Diffusion-driven instabilities in reaction-diffusion system are determined by the existence of eigenvalues with positive real part for some $q > 0$ in the linear approximation of the governing equations. The following identity, based on the invariance of the determinant under similarity transformations, relates the product of the eigenvalues and the determinant of the linearized equations:

$$P_{q/\Phi}(0) = (-1)^N \det[\mathbf{J}^R(\mathbf{r_o}) - (q/\Phi)^2\mathbf{D}] = (-1)^N \prod_{i=1}^{N} \lambda_i(q) \tag{5.12}$$

By construction, the initial state is stable in the absence of diffusion. Therefore, the system is stable under homogeneous perturbations, characterized by $q = 0$,

and the eigenvalues fulfill the condition $\mathrm{Re}[\lambda_i(q=0)] < 0$. Consequently, a stable system is characterized by $P_{q/\Phi}(0) > 0$ for $q = 0$. The system undergoes a diffusion-driven instability when one of the eigenvalues turns positive for certain $q > 0$, leading to a sign change in $P_{q/\Phi}(0)$

$$P_{q/\Phi}(0) = (-1)^N \det\left[\mathbf{F}^{RD}(\mathbf{r_0}, q/\Phi)\right] < 0 \qquad \Rightarrow \quad \exists\ \lambda(q) \mid \mathrm{Re}\,\lambda(q) > 0 \tag{5.13}$$

Special consideration is required for systems with p conserved quantities, such as that of the RhoGTPases, because the rank of the reaction term jacobian is $\mathrm{rank}\,[\mathbf{J^R}(\mathbf{r_0})] = N - p$. It follows that there are p null eigenvalues at $q = 0$ associated to the conservation laws. If the $N - p$ non-vanishing eigenvalues fulfill $\mathrm{Re}[\lambda_i(q=0)] < 0$, stability at $q = 0$ is assumed to be guaranteed because growth of the neutral eigenmodes in the Center Manifold is precluded by the conservation laws. A practical illustration of this mechanism is found in [137, pag.1407]), but a more rigorous proof will be given in the next chapter. Still, emergence of a positive eigenvalue for $q > 0$ leads to the rise of diffusion-driven instabilities. Thus, in a system with conserved quantities, $P_{q/\Phi}(0)$ vanishes for $q = 0$, but the instability condition $P_{q/\Phi}(0) < 0$ for $q > 0$ still holds. This instability mechanism is not strictly the one described in Turing original paper, but rather the instability of Type II described in [141, pag.869].
In the language of dynamical systems, Turing instabilities correspond to a saddle node bifurcation, the crossing of a single real eigenvalue to the positive half of the real axis. Therefore, the existence of a range of wavenumbers q in which the sign of $P_{q/\Phi}(0)$ is negative is a sufficient condition to establish that the system can feature Turing patterns. Loss of stability associated to a pair complex-conjugate eigenvalues crossing the imaginary axis to the right half of the complex plane has not been considered. This type of instability corresponds to a Hopf bifurcation and gives way to time periodic oscillations. This behavior is not detected by a sign change in the determinant of the linearized equations .
The possibility of growth of an eigenmode q is subjected to an additional constraint, since the new solution has to fulfill the no-flux boundary conditions. In systems of finite size, only a discrete set of modes fulfills the boundary conditions, and these are the only modes that can emerge. This property plays an important part in the discussion on the suitability of a Turing-like mechanism for cell polarization, because the permitted patterns depend on the size of the system.
The Thiele modulus Φ ,the non-dimensional parameter that divides the wavenumber q in the linearized equations, is proportional to length of the domain. Thus,

if the length of the domain is scaled by a factor k, the Thiele modulus becomes $\Phi' = k \cdot \Phi$. The range of instability is given by the set of wavenumber $q\epsilon(q_1, q_2)$ for which $P_{q/\Phi}(\lambda) \leq 0$. It follows that the range of instability of a system k times the size of the original is shifted proportionally to:

$$P_{q/k\cdot\Phi}(\lambda) = 0 \qquad q \in (k \cdot q_1,\, k \cdot\, q_2) \tag{5.14}$$

Therefore, the dominating pattern depends also on the size of the system, because the wave-number q_M associated to the fastest growing mode is also shifted by a factor k.

$$q_M(k \cdot L_{cell}) = k \cdot\, q_M(L_{cell}) \tag{5.15}$$

More importantly, even the existence of diffusion-driven instabilities is dependent on the size of the system, because if the size of the domain is reduced enough, the instability range will be shifted bellow the smallest mode compatible with the boundary conditions. This property is reminiscent of the results of the computational experiments, where the quasi-periodic pattern only appeared for cells bigger than a certain size. As stressed previously, this makes Turing instabilities an inadequate mechanism to orchestrate protein spatio-temporal organization in biological cells, because the mechanism should be able to operate in cells of very different sizes and changing morphologies [142].
The theoretical framework introduced previously is general and gives sufficient conditions for the appearance diffusion-driven instabilities in reaction-diffusion systems. Now the focus returns to the analysis of the Jilkine-Keshet model of RhoGTPase regulation, to prove that the results of the simulations featuring quasi-periodic patterns of protein distribution are indeed Turing patterns. Linear stability theory predicts accurately the emerging patterns in one dimensional systems, particularly if the dominant unstable eigenmodes have large wavelengths, which usually dominate the nonlinear evolution of the system[140]. In two dimensional systems, the evolution of the system far from equilibrium is harder to predict. For this reason, the simulations of the previous section are reenacted in a 1-dimensional cell and the emerging patterns are compared with the predictions of the Linear stability analysis.
The simulations show that when the 10μm long 1-dimensional cell is exposed to

different types of stimulus of spatial range smaller than the cell length, in most cases the emergent pattern is the simple polar distribution of Cdc42 and Rac highly activated at the front, Rho is inhibited and the other way around at the back of the cell. However, depending on the specifics of the external stimulus, the simple polarization pattern is in some cases replaced by the emergence of a bipolar pattern.

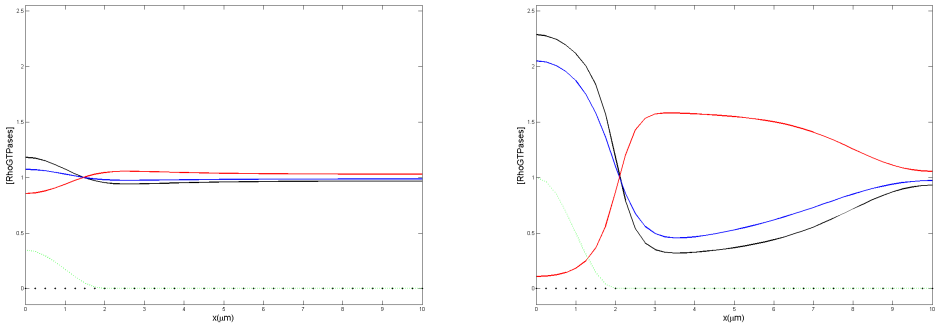

t=5.4s t=10.2s

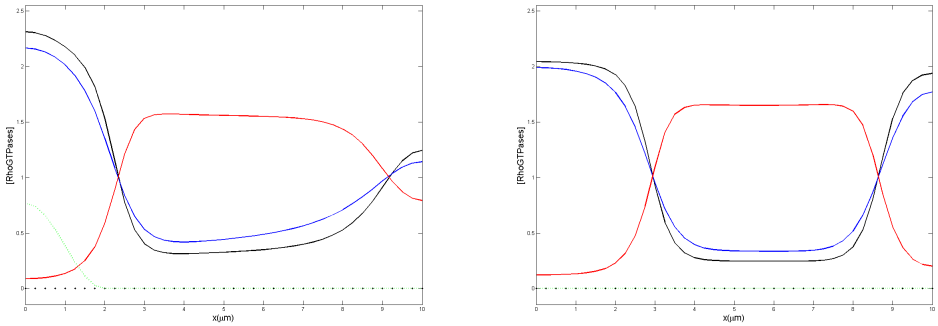

t=12.5s t=20.4s

Figure 5.15: ⊗ Emergence of Bipolar pattern in a 1d cell of L=10μm.

The simple polar distribution is the dominant final pattern,that is, the pattern most likely to emerge, as long as the cell length is smaller than 50μm. As the cell length is increased further, the simple polarization pattern is replaced as the dominant pattern by the emergence of the bipolar or multipolar protein distribution. These patterns are the one-dimensional counterpart of the final distribution found in the circular cell of 20μm radius exposed to linear stimulus. The characteristic wave-length of the bipolar pattern is approximately 10 μm, similar to the distance

between activation islands found in the 2D simulations.
The final state is highly dependent on the specific definition of the external stimulus. In order to remove this dependency, the response to a random stimulus was studied. The value of the signal function Ψ at every cell point is given by pseudo-randomly generated numbers drawn from a standard uniform distribution in the interval $[0, \Psi_m]$. This type of stimulus is also interesting because it mimics the noisy inputs that a cell experiences in real biological environment. It turns out that the final pattern of RhoGTPase distribution that is most likely to emerge is essentially determined by the cell length. As stated previously, in 10μm long cell, the pattern most likely to emerge when the cell is exposed to a random nosy stimulus is the simple polar pattern, although in some cases the bipolar pattern can also emerge, as shown in fig. 5.15. Doubling the cell length shifts the dominant pattern to a bipolar distribution with two maximums and two minimums of protein activation. This distribution has a similar wave-like profile than the bipolar pattern, with the same dimensional spatial period. The trend continues as the cell size is further increased, a pattern with the same characteristic wavelength is established and more maximums and minimums fit inside the larger cell.

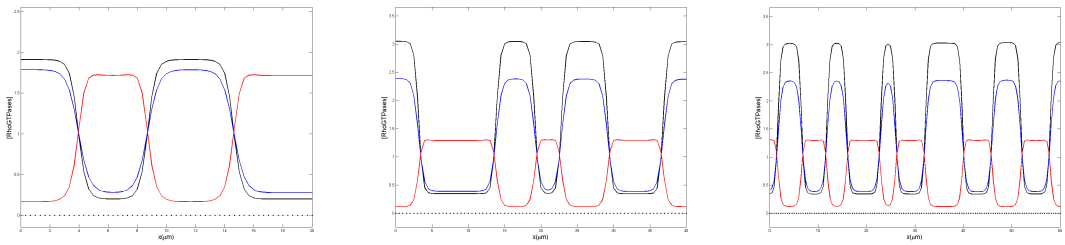

(a) L=20μm (b) L=40μm (c) L=60μm

Figure 5.16: $^{\otimes}$ Multipolar patterns in cells of increasing length.

This feature is characteristic of the patterns associated to diffusion-driven instabilities, and a clear indication that heterogeneous perturbations can lead Turing patterns solutions in the model. Application the theoretical framework presented above confirms that this is the case. For the 1-dimensional cell, the eigenfunctions of the reaction-diffusion system and the wave-numbers compatible with the boundary conditions can be found analytically:

$$\phi_n(x) = \cos(q_n x) \qquad q_n = n\pi \tag{5.16}$$

The final patterns of RhoGTPase distribution emerging in cell of increasing length show the sinusoidal profile of the eigenfunctions.
Indeed, numerical evaluation of the determinant of system's linearization shows that $P_{q/\Phi}(0) < 0$ for $q \sim (0, 4\pi)$. According to the condition given in eq. 5.13, the system becomes unstable for a discrete set of the modes in this range. The following figure presents the numerical evaluation of the $P_{q/\Phi}(0) = \det[-\mathbf{F}^{\mathrm{RD}}]$, which gives the range of instability, and the largest eigenvalue within the instability range:

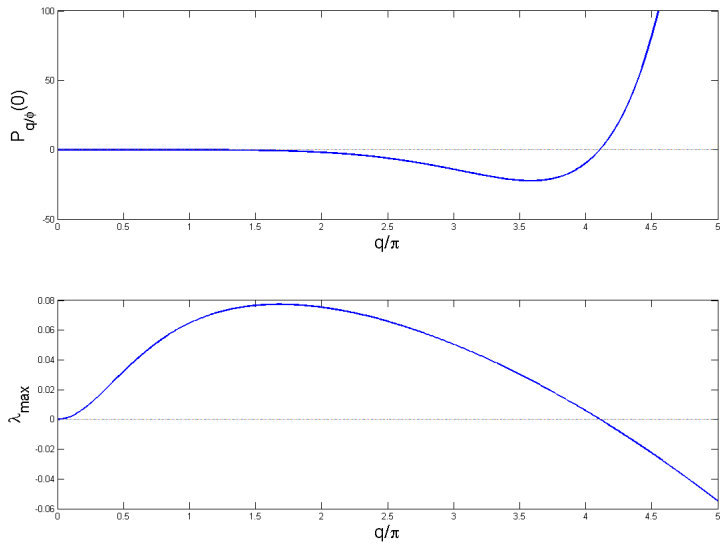

Figure 5.17: Up: $P_{q/\Phi}(0) = \det[-\mathbf{F}^{RD}(q/\phi)]$ for Φ(L = 10μm). Down: Maximum eigenvalue $\lambda_M(q/\pi)$.

Computation of the dispersion relation, depicted in fig.5.18, shows the existence of a single positive eigenvalue.

The existence of just one positive eigenvalue also rules out oscillations caused by a pair of complex eigenvalues crossing the imaginary axis. The three null eigenvalues at $q = 0$ stem from the conservation of the total amount of Cdc42, Rac, and Rho. Therefore, only the mode for which the positive eigenvalue is maximum can dominate the evolution of the system after an heterogeneous perturbation is applied. Specifically, the Dispersion relation reveals that in a cell of 10μm in length, $q = \pi$ and $q = 2\pi$ are the allowed modes in the instability range with the largest positive eigenvalue, with $\lambda_M(q = \pi)$ slightly larger. Hence, linear stability

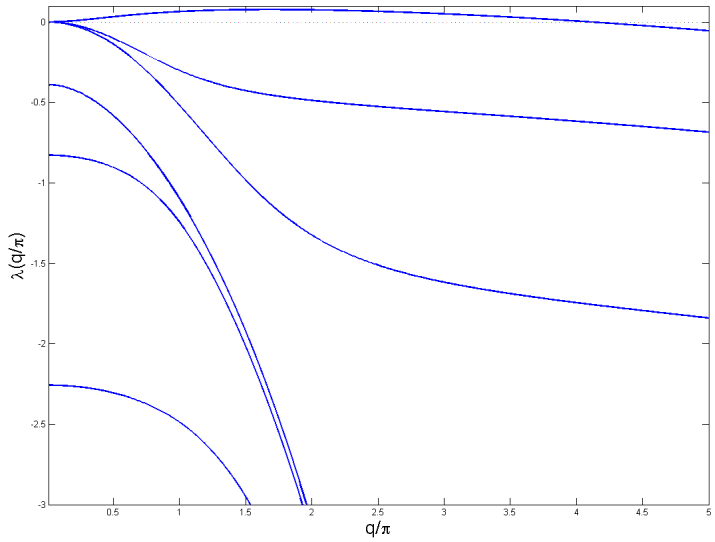

Figure 5.18: Dispersion relation for Jilkine's model. Eigenmodes $q = 1\pi,\ 2\ \pi,\ 3\pi$ have positive eigenvalues.

theory predicts that patterns of concentrations $\approx \cos(\pi x/\mathrm{L_{Cell}})$ or $\approx \cos(2\pi x/\mathrm{L_{Cell}})$ are expected to dominate after an stimulus is applied. Indeed, the prediction is confirmed by the results of the simulation in a 1D cell of this particular length, for the simple polarized state and the bipolar state are the nonlinear evolutions of the corresponding eigenmode. The fact that the eigenvalues of these two modes are almost equal, explains that the prevailing pattern is determined by the spatial profile of the external signal.
Increasing the cell length k-fold times displaces the fastest growing eigenmode by a factor k. Therefore, when the cell length is doubled, the largest eigenvalue is associated to the wave-number $q_M = 2 \cdot (\pi)$, when the cell length is tripled $q_M = 3 \cdot (\pi)$ and so forth. According to the theory, these eigenmodes shape the final distribution of proteins after the cell is perturbed, as confirmed by the simulation shown in fig.5.16 of cells of increasing length exposed to random noise.
In this way, the stability analysis proves that the patterns obtained in the simulations arise from diffusion-driven instabilities excited by heterogeneous external stimulus. I argue that Turing patterns are not a suitable mechanism to generate polarity in a migrating cell and, consequently, that a model of RhoGTPase regulation should not feature Diffusion-driven instabilities. First of all, Turing patterns are stable; if the cell reached such a state it would remain locked in it, rendering the sensibility to posterior stimulus completely impaired. More importantly, the existence of these solutions in the system depends not only on the parameters

at the molecular scale, but also at the cellular scale, such as size or morphology. RhoGTPases are ubiquitous in great variety of living organisms, from the most primitive unicellular yeasts to eukaryotic cells. The mechanism underlying their biological function should be independent of such variables, and remain operative despite the biological diversity amongst individual members, cell types, or changing environmental circumstances.

5.3 Crosstalk model and the dynamics of the RhoGTPase system

The preceding section proved that the RhoGTPase regulation model under analysis features diffusion-driven instabilities. Biological arguments against Turing instability as a plausible mechanism underlying cell polarization were presented. This section aims to identify the source of this behaviour. The analysis will reveal the crucial role played by feedback loops in the Interaction Scheme as the main determinants of the system's stability.

5.3.1 Interaction schemes: notation and definitions

A sufficient condition for a Reaction-Diffusion system to undergo Turing instabilities was presented in eq. 5.13 of the previous section. This condition is simply given by the sign of the determinant of the linearization of the governing equations $\mathbf{F}^{RD}(\mathbf{r_o}, q/\Phi)$:

$$P_{q/\Phi}(0) = (-1)^N \det[\mathbf{J}^R(\mathbf{r_o}) - \frac{q^2}{\Phi^2}\mathbf{D}] \tag{5.17}$$

The numerical evaluation of the corresponding determinant for the RhoGTPase model allowed to predict the existence of Turing instabilities and the dominating patterns. However, the numerical approach only allows to analyze a particular model, and the conclusions are dependent on the choice of parameters. In order to study the relationship between the basic hypothesis, the structure of the interaction scheme and the source of the undesired dynamics, the instability condition is studied analytically. The Jacobian of the reaction term of a system described by a set of Reaction-Diffusion with the structure of eqs. 2.22 can be split

in two parts, the Kinetic matrix itself $\mathbf{K}(\mathbf{r_0})$, and the Interaction matrix.

$$\mathbf{J}^R(\mathbf{r_o}) = \left.\frac{\partial \mathbf{K}(\mathbf{r}) \cdot \mathbf{r}}{\partial \mathbf{r}}\right|_{\mathbf{r}=\mathbf{r_0}} = \mathbf{K}(\mathbf{r_0}) + \mathbf{I}(\mathbf{r_0}) \tag{5.18}$$

The Kinetic matrix is the linear part of the reaction term. It has a bloc-diagonal structure, the coefficients of each block are the kinetic rates of transition between the states of activation of a particular protein. The Interaction matrix has been defined to include the off-diagonal terms in the Jacobian that result form the dependence of the kinetic rates on cross-interaction between the different proteins of the system.

$$\mathbf{I}(\mathbf{r_0}) = \left.\frac{\partial \mathbf{K}(\mathbf{r})}{\partial \mathbf{r}} \cdot \mathbf{r}\right|_{\mathbf{r}=\mathbf{r_0}} \tag{5.19}$$

The RhoGTPase model specified by the interaction scheme represented in figure 2.3, under the quasi-steady state approximation, is described by the reduced set of equations 2.29 and kinetic matrices of the type defined in 2.32. The corresponding Interaction Matrix takes the following form:

$$\mathbf{I}(\mathbf{r_o}) = \begin{bmatrix} 0 & 0 & f_r & 0 & f_\rho & 0 \\ 0 & 0 & -f_r & 0 & -f_\rho & 0 \\ g_c & 0 & 0 & 0 & g_\rho & 0 \\ -g_c & 0 & 0 & 0 & -g_\rho & 0 \\ h_c & 0 & h_r & 0 & 0 & 0 \\ -h_c & 0 & -h_r & 0 & 0 & 0 \end{bmatrix} \tag{5.20}$$

The structure of $\mathbf{I}(\mathbf{r_0})$ is consistent with the ordering of the concentration vector as defined in the QSS aproximation [1], and the notation used in its definition is derived from the notation adopted to define the kinetic rates. As previously, f^A and f^B, g^A and g^B, h^A and h^B denote the kinetic rates of activation and inactivation

[1]The concentration vector in the QSSA is defined as:

$$\mathbf{r}^{\mathrm{T}} = \begin{bmatrix} c_{\mathrm{GTP}} & c_{\mathrm{GDP}} & r_{\mathrm{GTP}} & r_{\mathrm{GDP}} & \rho_{\mathrm{GTP}} & \rho_{\mathrm{GDP}} \end{bmatrix} \tag{5.21}$$

associated to Cdc42, Rac and Rho, respectively. The entries k_{x} in the Interaction Matrix stand for the derivative of the kinetic rates with respect the concentration of protein x. Thus, the cases $k_{\mathrm{x}} = f, g, h$ correspond to the modulation of the kinetic rates of Cdc42, Rac and Rho, and $\mathrm{x} = c,\ r,\ \rho$ indicates which protein is the source of the interaction signaling. For instance, f_ρ is associated to the dependence of Cdc42 reaction rates on the concentration of active ρ_{GTP}, whereas g_C is associated to the modulation of Rac reaction rates on signalling from $Cdc42_{\mathrm{GTP}}$.
The precise definition of the coefficient in the Interaction matrix associated to the crosstalk from an active RhoGTPase x_{GTP} to some other RhoGTPase r is then given by:

$$k_{\mathrm{x}} = \frac{\partial \dot{\mathrm{r}}_{GTP}}{\partial \mathrm{x}_{GTP}} = \frac{\partial k^A}{\partial \mathrm{x}_{GTP}} \mathrm{r}_{GDP} - \frac{\partial k^B}{\partial \mathrm{x}_{GTP}} \mathrm{r}_{GTP} \qquad \mathrm{x} = x, r, \rho \tag{5.22}$$

Note that the assumption that crosstalk is mediated only by signalling from active RhoGTPases has been implicitly included, because the kinetic rates are considered function of x_{GTP} only.
According to this convention, $k_{\mathrm{x}} > 0$ represents activation signals from x_{GTP} to protein x , so that crosstalk from x_{GTP} displaces the equilibrium towards active r_{GTP} . Conversely, if $k_{\mathrm{x}} < 0$ the interaction is inhibitory, and crosstalk signals from x_{GTP} to protein r result in a increase of inactive R_{GDP}.

$$\begin{aligned} k_{\mathrm{x}} > 0 \qquad & \mathrm{r_{GDP}} \xrightarrow[k^B(-)]{k^A(+)} \mathrm{r_{GTP}} \\ k_{\mathrm{x}} < 0 \qquad & \mathrm{r_{GDP}} \xleftarrow[k^B(+)]{k^A(-)} \mathrm{r_{GTP}} \end{aligned} \tag{5.23}$$

In the specific RhoGTPase crosstalk scheme under study, Cdc42 is inhibited by Rho, Rac is activated by Cdc42, and Rho is activated by Rac and inhibited by Cdc42. Therefore, the sign pattern of the coefficients in the associated Interaction matrix are then given by:

$$\begin{aligned} f_{\mathrm{r}} = 0 \quad f_{\rho} < 0 \\ g_{c} > 0 \quad g_{\rho} = 0 \\ h_{c} < 0 \quad h_{\mathrm{r}} > 0 \end{aligned} \tag{5.24}$$

The interaction scheme also assumes that the kinetic rates of a protein are not modified by its own concentration. In biological terms, the model rules out autocatalytic interaction, and the mathematical implementation is then completed stating the zero value of the corresponding interaction terms:

$$f_{c} = g_{\mathrm{r}} = h_{\rho} = 0 \tag{5.25}$$

Before delving into the stability properties of the system, it is worth remarking certain properties of the equations that will be relevant in the analysis of the model. An interesting feature, which is made apparent by the structure of eqs. 5.22-5.23, is that there are two equivalent ways in which activation or inhibition interaction can be carried out. Theoretically, inhibition could be mediated by negative regulation of the GEF activity resulting in a reduction of k^{A}, or alternatively by a positive regulation of the GAP activity, with the ensuing increase of k^{B}. Both alternatives would effectively reduce the rate of activation of a protein, and the converse mechanisms hold for activation interactions. However, the model under study assumes that crosstalk signals modulates only GEF activity. In this case, the interaction terms are limited to:

$$k_{\mathrm{x}} = \frac{\partial k^{A}}{\partial \mathrm{x}_{GTP}} \mathrm{r}_{GDP} \tag{5.26}$$

Provided that the model included modulation of GDI or GDF activity, there would be a multiple number of alternatives channels to mediate inhibition or activation. Another important aspect is the direct relationship between the biological hypothesis on which the model is based and the structure of the Interaction Matrix. The assumption that crosstalk is mediated only by active RhoGTPases leads to kinetic rates that are independent of r_{GDP} concentrations, which is reflected in

alternating zero columns found in the Interaction matrix, associated to the lack of direct interactions between inactive RhoGTPases and other proteins.
Autocatalysis is the self-modulation of the production or activation rates of a protein by itself. In the model under study, the kinetic rates of activation of a particular RhoGTPase are not changed by its own signals . Thus, f_c, g_r and h_ρ being equal to zero is a consequence of the absence of auto-catalytic interactions in the model. This assumption is reflected in the mathematical formulation in the zero diagonal of the Interaction matrix.These structural traits will be important in the discussion of alternatives to the RhoGTPase regulation.

5.3.2 Feedback Loops, Turing Instability and adaptation

The definition, notation and interpretation of the entities that play a role in the analysis of the system's stability have been introduced. The instability condition in equation 5.17 can now be expressed in terms of the Reaction and Interaction matrix coefficients. For the specific RhoGTPase model under study, the analytical expansion of $P_{q/\Phi}(0) = (-1)^N \det[\mathbf{F}^{RD}]$ spans up to 720 terms, which after extensive algebraic manipulations of its factors [2] can be rearranged into a compact expression from which important insights on the system' dynamics can be gained.

$$\begin{aligned} P_{q/\Phi}(0) = \prod_{\mathrm{k}\,=\,\mathrm{f,g,h}} [q^2 d \cdot \mathrm{k}^{\mathrm{A}} + q^2 D(q^2 d + \mathrm{k}^{\mathrm{B}})] \; - \left[q^2 D\right]^3 \left[f_\rho \cdot g_c \cdot h_r\right] \\ - \left[q^2 D\right]^2 [\; q^2 d \cdot g^{\mathrm{A}} + q^2 D(q^2 d + g^{\mathrm{B}})] \left[f_\rho \cdot h_c\right] \end{aligned} \tag{5.27}$$

Three qualitatively distinct terms determine the sign of $P_{q/\Phi}(0)$. The first term contains only contributions from the Kinetic and Diffusion matrices, whose coefficients are positive by definition. This term is non-negative (strictly positive for $q > 0$) and, according to the stability condition, has a stabilizing effect on the system's dynamics. hence, the second and third terms in eq. 5.27 are the only possible sources of instability. These terms are formed by combinations of products

[2] $P_{q/\Phi}$ was computed using symbolic algebra software. In a general regulation model describing the dynamics of N proteins, the number of terms is $N!$. As the size of the systems grows, this type of analysis becomes rapidly unmanageable, and even if it can be done, it is increasingly hard to gain insight from it. For instance, the study of full RhoGTPase model, without the simplifying QSS approximation, requires dealing with an expression with 362.880 terms. This is one of the reasons to develop graph-theoretical tools to study reaction networks.

of the Interaction matrix coefficients with the Diffusion and the Kinetic matrices. Examination of their structure reveals that from all the possible products of coefficients in the I-matrix, only a very particular type contributes to $P_{q/\Phi}(0)$. These factors are combinations of coefficients associated to cyclic interactions between the variables of the systems. Indeed, $f_\rho \cdot g_c \cdot h_r$ represents the inhibitory interaction from Rho to Cdc42, which in turn activates Rac, which in turn activates Rho. Likewise, $f_\rho \cdot g_c$ is associated to the mutual inhibition between Cdc42 and Rho.

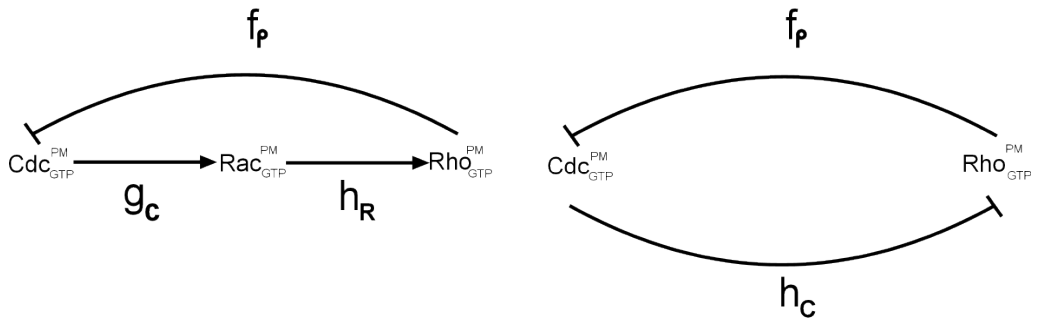

Figure 5.19: Interactions Cycles in Jiniker Crosstalk scheme.

The profound connection between the cyclical structures of the crosstalk scheme and the dynamics of the system is revealed in figure 5.19. The two possible sources of instability in the system correspond precisely to the only 2 cyclic chains of interactions that can be found in the crosstalk scheme. From here on cycles will be referred to as C_x , where x stands for the number of proteins involved in the cycle. In order to find out which of the network structures is causing the appearance of Turing patterns, the sign of the contribution of each cycle to the characteristic polynomial must be examined.

$$f_\rho \times g_c \times h_r = (-) \times (+) \times (+) \qquad f_\rho \times h_c = (-) \times (-) \tag{5.28}$$

Inspecting the preceding expression, it is readily seen that the two cycles have opposite effects on the stability of the system. C_3 is composed of 2 activation and 1 inhibitory interactions, so that the feedback carried through this channels drives the system towards stability. Conversely, C_2 is associated to the coupling of two inhibitory interactions, which results in double-negative feedback that effectively leads to $P_{q/\Phi}(0) > 0$. Therefore, c_2 is the only possible source of instability in the

system. In the limit of small wave-numbers, where instability occurs, $P_{q/\Phi}(0)$ is given by:

$$P_{q/\Phi}(0) \sim \left(\frac{q}{\Phi}\right)^6 D^3 \left(\prod_{k = f,g,h} k^B - \left[f_\rho \cdot g_c \cdot h_r\right] - g^B \left[f_\rho \cdot h_c\right] \right) \tag{5.29}$$

A change of parameter values could be a simple method to correct the model, so that C_2 does not dominate the system's dynamics in this range. However, weakening the mutual inhibition loop between Cdc42 and Rho possibly the eliminates the possibility of reproducing polarization. In addition, this strategy could only be applied to particular models and the conclusions would be of limited interest. Nevertheless, the goal of this section has been reached, since I aimed to establish a connection between the biological hypothesis and the dynamical response of the model equation. This result leads naturally to the following questions. Can this relationship be extended to other systems and other types of dynamical behavior? How can the RhoGTPase regulation model be modified in order to better describe the observations?

It is nice to know that the computer understands the problem. But I would like to understand it too.

Eugene Wigner, mathematical physicist

Chapter 6

Interaction Graph and Reaction Network Dynamics

This chapter presents the theoretical framework required to analyze the response of a regulatory model to external perturbations. Analytical tools required to systematically formulate alternative models capable of describing RhoGTPase polarization without featuring instabilities are developed. The results of the previous chapter suggest that feedback loops play a fundamental role in the dynamics of the RhoGTPase regulation model. This notion is extended to arbitrary Reaction Networks, laying out the framework in which the stability and dynamics of a general reaction-diffusion system can be studied. In remaining of the chapter, the relationship between the cyclic structure of the interactions in the network and the dynamics of the associated reaction-diffusion system will be explained using a Graph-Theoretical method.

6.1 General conditions for the Stability of RD systems

The starting assumption is that the biological regulatory network of interest can be modeled as a set of reaction-diffusion equations of N proteins. This is the general framework in which the RhoGTpases model was formulated:

$$\frac{\partial r_i}{\partial t} = F_i(\mathbf{r}) + \frac{d_i}{\Phi^2}\nabla^2 r_i \qquad i = 1, ..., N \tag{6.1}$$

The variations of concentration of a protein $r_i(x, t)$ are driven by the processes of Diffusion and Reaction. The dynamics of a protein are coupled to the other

members in the network if the reaction term is a function of the concentrations of the rest of proteins. This property is known as crosstalk. The steady states of the ODE system associated to the reaction-diffusion system, known as the kinetic system, provide the spatially homogeneous stationary states of the full system.

$$\frac{dr_i}{dt} = F_i(\mathbf{r}) \qquad i = 1, ..., N \tag{6.2}$$

The subset of steady states that are stable solutions of the kinetic system are equilibrium states denoted as $\mathbf{r_s}$. The assumption is that different biological or cellular functions are executed by the network in the different equilibrium states. The response of the cell to and external gradient signal is then determined by the stability and evolution of the state $\mathbf{r_s}$ under heterogeneous perturbations in the full PDE system 6.1.
The Hartman-Grobman Theorem states that a nonlinear dynamical system is topologically equivalent to its linear approximation near a hyperbolic steady state [143, pg. 13-14]. Hyperbolic steady states are those in which the eigenvalues of the linear approximation have non-zero real parts. Applied to the reaction-diffusion system of eqs. 6.1, this result implies that the response $\mathbf{r_s} + \delta\mathbf{r}(x, t)$ to perturbations in the nonlinear system is given by its linear approximation[1]:

$$\frac{\partial \delta \mathbf{r}}{\partial t} = [\mathbf{J}^R(\mathbf{r}_s) + (1/\Phi)^2 \mathbf{D}\nabla^2]\delta\mathbf{r} \tag{6.3}$$

It follows that the stability of a homogeneous steady states $\mathbf{r_s}$ with Neumann boundary conditions can then can be determined by the sign of the eigenvalues of the following matrix

$$\mathbf{F}^{\mathbf{RD}}_{ij}(\mathbf{r}_s) = \mathbf{J}^R_{ij}(\mathbf{r_s}) \; - (q/\Phi)^2 \, \mathbf{D}_{ik}\delta_{kj} \tag{6.4}$$

[1]The stability in a reaction-diffusion systems with conserved quantities requires particular considerations because each conserved quantity has associated an identically null eigenvalue and the Hartman-Grobman theorem can not be applied.

where **D** is a diagonal matrix with strictly positive coefficients. The matrix $\mathbf{J}^R(\mathbf{r_s})$ is the jacobian of the reaction term evaluated at a homogeneous steady state $\mathbf{r}_s$. The off-diagonal structure of the reaction term jacobian reflects the crosstalk between proteins of the network.

$$\mathbf{J}^{\mathbf{R}}_{ij}(\mathbf{r}_s) = \left.\frac{\partial F_i}{\partial r_j}\right|_{\mathbf{r}_s} \tag{6.5}$$

In particular, the interest lays in models in which external (heterogeneous) perturbations can trigger the transition from an initial homogeneous steady state to a polarized state featuring a non-homogeneous distribution of proteins. This requirement can be satisfied by the existence of traveling-wave solutions connecting different steady states in the phase plane of the reaction-diffusion system [136, chapter 3]. Recent work in reaction networks has connected the existence of multiple steady states with the cyclic structure of the interactions, more precisely, the existence of positive feedback loops [144]. However, the model is also required not to undergo diffusion-driven instabilities, independently of the choice of parameters or the size of the system. The previous analysis indicates that positive loops also have a crucial role in the appearance of Turing patterns. Therefore, the questions that must be addressed are: What structural properties must have a reaction network that guarantee that Turing instabilities do not occur? Are the conditions that rule out diffusion-driven instabilities compatible with multistationarity?

Turing instabilities stem from a saddle-node bifurcation. Generally, a bifurcation occurs when a change in a parameter value results in a qualitative change in the behavior of a system. In this case, the system is stable in the absence of diffusion ($q = 0$) and becomes unstable for heterogeneous perturbations ($q > 0$) as a real eigenvalue turns positive. Therefore, the requirement that Turing instabilities do not occur can be restated as a condition on the eigenvalues of $\mathbf{F}^{RD}$.

$$P_{q/\Phi}(\lambda) = \det\left[\lambda\,\mathrm{I} - \mathbf{F}^{\mathrm{RD}}(\mathbf{r_s})\right] = \sum_{k=0}^{N} a_k \lambda^{N-k} = \lambda^N + a_1\lambda^{N-1} + ... + a_{N-1}\lambda + a_N \tag{6.6}$$

The system will not feature Turing patterns if and only if the roots of the characteristic polynomial $P_{q/\Phi}(\lambda)$ have negative real parts for all $q > 0$.

6.1.1 Routh-Hurwitz conditions

The necessary and sufficient conditions for all the roots of a polynomial to lie in the left half of the complex plane are given by the Routh-Hurwitz criterion [145, pag 231]. The *N*x*N* Hurwitz matrix is defined in terms of the coefficients of the characteristic polynomial associated to $\mathbf{F^{RD}}$ as:

$$H = \begin{bmatrix} a_1 & a_0 & 0 & 0 & \dots & 0 \\ a_3 & a_2 & a_1 & a_0 & \dots & 0 \\ a_5 & a_4 & a_3 & a_2 & \dots & 0 \\ \vdots & \vdots & \vdots & \vdots & \dots & \vdots \\ \vdots & \vdots & \vdots & \vdots & \ddots & \vdots \\ 0 & 0 & 0 & 0 & 0 & a_N \end{bmatrix} \tag{6.7}$$

The Routh-Hurwitz criterion states that all roots of the characteristic polynomial $P_{q/\Phi}(\lambda)$ have negative real parts if and only if

$$\Delta(j) = \det[H(j)] > 0 \qquad j = 1, ..., N \tag{6.8}$$

where $H(j)$ is the submatrix obtained from taking the first j rows and columns of the Hurwitz matrix. A corollary of Routh-Hurwitz criterion is that the positivity of the a_k coefficients is a necessary conditions for stability.

$$a_k > 0 \qquad k = 1, ..., N \tag{6.9}$$

The condition $a_N = P_{q/\Phi}(0) = (-1)^N \det[\mathbf{F}^{RD}] > 0$ for $q > 0$, found in the previous section to be necessary for the stability of the system, is now revealed to be just a particular instance of the general Routh-Hurwitz criterion .

Application of this criterion in a reaction-diffusion system with conservation laws requires special considerations. Stability is studied near the homogeneous initial state $\mathbf{r_s}$, chosen amongst the equilibrium states of the system. By definition, equilibrium states are stable in the absence of diffusion, or equivalently, they are stable under homogeneous perturbations. Homogeneous perturbations are

characterized by a wave-number $q = 0$, which reduces $\mathbf{F^{RD}}(\mathbf{r_s})$ to $\mathbf{J^R}(\mathbf{r_s})$. The eigenvalues of $\mathbf{J^R}(\mathbf{r_s})$, however, are not all negative. Each local conservation law, as it is explained bellow, has associated the existence of an identically null eigenvalue. This prevents the direct application of the Hartman-Grobman theorem to study Turing instabilities, since $\mathbf{r_s}$ is not an hyperbolic equilibrium .

Local conservation laws are common in networks of reacting proteins. The RhoGTPase model, for instance, has 3 conservation laws associated to the conservation of the total amount of Cdc42, Rac and RhoA. Generally, conserved quantities are associated to a group of proteins $r_k, ..., r_m$ whose total amount does not change. In the reactions in which these proteins participate, an increase in concentration of the products of the reaction is balanced by the decrease in the concentration of the reactants, so that the net sum of their reaction rates vanishes.

$$F_k(\mathbf{r}) + ... + F_m(\mathbf{r}) = 0 \tag{6.10}$$

As a consequence of the existence of conserved quantities, the rows in the Jacobian corresponding to the reaction terms of these proteins are not independent.

$$\sum_{i=k}^{m} \mathbf{J}^{\mathbf{R}}_{ij}(\mathbf{r}_s) = \left(\frac{\partial F_k}{\partial r_j} + ... + \frac{\partial F_m}{\partial r_j}\right)\Bigg|_{\mathbf{r}_s} = 0 \qquad j = 1, ..., N \tag{6.11}$$

Consequently, if there are p locally conserved quantities in the reaction network, the rank of $\mathbf{J^R}(\mathbf{r_s})$ is equal to $N - p$. By the Rank-Nullity theorem, the dimension of the null space of $\mathbf{J^R}(\mathbf{r_s})$ and its rank must add up to N.

$$\text{rank}[\mathbf{J^R}(r_s)] + \ker[\mathbf{J^R}(r_s)] = N \tag{6.12}$$

It follows that there are p eigenvectors of $\mathbf{J^R}(\mathbf{r_s})$ whose eigenvalue is equal to zero, because the dimension of the null space is p. Therefore, a steady state $\mathbf{r_s}$ is not an hyperbolic equilibrium of $\mathbf{J^R}$ and the Hartmann-Grobmann theorem does not provide a information on the relationship between the full nonlinear system and its linear approximation. This point is generally overlooked in the literature, but can be partially bypassed invoking two results contained in the classic work

by Casten and Holland [146, pag. 356-358] on the stability of reaction-diffusion systems. The first theorem provides the stability properties of homogeneous steady states in the linear approximation 6.3 of the full problem.

Theorem 1. [Casten and Holland] Let **r** be a solution of the kinetic system 6.2. Then, the state **r** is:

(i) A globally asymptotically stable solution of the linear system 6.3 if for each non-negative q the eigenvalues of $\mathbf{J^R}(r) - (q/\Phi)^2\mathbf{D}$ have negative real parts.

(ii) A stable solution of the linear system 6.3 if for each non-negative q the eigenvalues of $\mathbf{J^R}(r) - (q/\Phi)^2\mathbf{D}$ have non-positive real part and those with zero real part have simple elementary divisors.

(iii) Unstable if for some $q \geq 0$ the eigenvalues of $\mathbf{J^R}(r) - (q/\Phi)^2\mathbf{D}$ have either positive real part or zero real part with non-simple elementary divisors .

Next, it is shown how this result can be used to establish the stability of $\mathbf{r_s}$ in a system with conserved quantities. The elementary divisors of a matrix are the characteristic polynomials of its Jordan blocks [147, Chapter VII]. An eigenvalue λ has simple elementary divisors if the order of its Jordan blocks is one. The number of Jordan blocks associated to λ is equal to the geometric multiplicity of λ, that is, the number of independent eigenvectors of the matrix with this eigenvalue. On the other hand, the sum of the orders of all the Jordan blocks of λ is equal to its algebraic multiplicity, that is, the multiplicity of the eigenvalue as a root of $P_{q/\Phi}$ [148]. It follows that if the geometric and algebraic multiplicity of λ are equal, the order of all of its associated Jordan Blocks is one, and therefore, the eigenvalue has simple elementary divisors.
In a reaction-diffusion system with p conservation laws, zero is indeed an eigenvalue at $q = 0$, and its algebraic multiplicity is exactly p. Since the dimension of the kernel of $\mathbf{J^R}(r_s)$ is equal to p , there are p independent eigenvectors associated to the 0 eigenvalue, and its algebraic and geometric multiplicity are equal. Therefore, a solution $\mathbf{r_s}$ fulfills the conditions of the second case of Theorem 1, as long as the remaining non-vanishing eigenvalues are negative. However, this result guarantees the stability of $\mathbf{r_s}$ in the linearized system, but it does not give information on the behavior of the solution on the full nonlinear system. This information is provided by a second theorem in [146]:

Theorem 2. [Casten and Holland] If $\mathbf{r_s}$ is an asymptotically stable solution of the linearized problem 6.3, then it is also an asymptotically stable solution of the nonlinear system 6.1.

According to this, the solution $\mathbf{r_s}$ falls short of the conditions that guarantee its stability in the nonlinear system 6.1, because Theorem 1 classifies is it as stable but not asymptotically stable. The difference between a stable and asymptotically stable solution lays in the upper bound that can be established to the departure of $\mathbf{r_s} + \delta\mathbf{r}(x,t)$ from $\mathbf{r_s}$ after it is perturbed. For general systems with zero eigenvalues, a less strict upper bound can be established because the decay of the neutral eigenmodes is less strong than it would be if all eigenvalues were negative. However, in the specific case that the zero eigenvalues stem from local conservation laws, such as those described previously, growth of the neutral eigenmodes is incompatible with the conservation laws themselves, so that they do not form part of the transient solution $\mathbf{r_s} + \delta\mathbf{r}(x,t)$ that emerges after $\mathbf{r_s}$ is perturbed. An example of this mechanism is found in [137]. It follows that the construction that establishes an upper bound for an asymptotically stable solution is also valid and Theorem 2 applies.

Consequently, $\mathbf{r_s}$ is a stable solution of the full nonlinear system if all the eigenvalues of $\mathbf{F^{RD}}(\mathbf{r_s})$ for $q > 0$ are negative, whereas for $q = 0$ the requirement is relaxed to the negativity of the $N - p$ non identically null eigenvalues. The Routh-Hurwitz criterion can be adapted to the modified stability conditions. In the next section, it is shown that for $q = 0$ the coefficients $a_k(\mathbf{r_s}, 0)$ of the characteristic polynomial are identically zero for $k > N-p$. Hence, $P_{q/\Phi}$ at $q = 0$ takes the form

$$P_{0/\Phi}(\lambda) = \sum_{k=0}^{N-p} a_k(\mathbf{r_s}, 0) \cdot \lambda^{N-k} = \lambda^p \sum_{k=0}^{N-p} a_k(\mathbf{r_s}, 0) \cdot \lambda^{N-p-k} = \lambda^p \cdot Q^{N-p}(\lambda) \tag{6.13}$$

where $Q^{N-p}(\lambda)$ is the polynomial of order $N - p$ in λ formed by the coefficients $a_1, ..., a_{N-p}$. The conditions that guarantee that the roots of $Q^{N-p}(\lambda)$ are negative are again given by the Routh-Hurwitz criterion, but with the general Hurwitz matrix defined in eq. 6.7 restricted to order $N - p$. Likewise, the necessary condition of the positivity of $a_k(\mathbf{r_s}, 0) > 0$ is also limited to coefficients $k = 1, ..., N - p$. For positive wave-numbers the symmetry of $\mathbf{J^R}$ is broken and the general Routh -Hurwitz conditions apply.

This result settles the necessary and sufficient conditions for the stability of a Reaction-Diffusion system with conserved quantities. Unfortunately, the conditions are of little practical value to suggest modifications in the Reaction scheme that lead to the desired dynamical properties of the Reaction-Diffusion system. The Routh-Hurwitz inequalities involve complex algebraic relationships between the a_k coefficients, so that the translation of these relationships into conditions to

impose on the Crosstalk scheme is not straightforward. As an illustration, the expansion Hurwitz determinants for $N = 6$ in terms of the coefficients of the characteristic polynomial is written explicitly .

$$\begin{aligned}
\Delta_1 &= a_1 \\
\Delta_2 &= a_1 a_2 - a_3 \\
\Delta_3 &= a_3 \Delta_2 + (a_5 - a_1 a_4) a_1 \\
\Delta_4 &= a_4 \Delta_3 + (a_1 a_6 - a_2 a_5) \Delta_2 - a_5 (a_5 - a_1 a_4) \\
\Delta_5 &= a_5 \Delta_4 - a_6 a_3 \Delta_3 + a_6 a_1 a_5 \Delta_2 - a_1^3 a_6^2 \\
\Delta_6 &= a_6 \Delta_5
\end{aligned} \tag{6.14}$$

Even for a simple model involving only 6 proteins, the complexity of the algebraic conditions makes them intractable. A slight improvement is found in the fact that the positivity of the a_k coefficients and of the Routh-Hurwitz determinants is not independent. This leads to a set of simplified conditions for stability, known as the Lienard-Chipart criterion:

$$a_N > 0, \quad a_{N-2} > 0 \,, ..., \qquad \Delta(1) > 0, \quad \Delta(3) > 0 \,, ..., \tag{6.15}$$

Lienard-Chipart involves half the number of determinants appearing in Routh-Hurwitz criterion. Still, this reduction does not result in a substantial improvement in the applicability of the constraints. A stronger limitation is that the conclusions reached on what properties make the system stable are dependent on the number of proteins and parameter values. This is an important drawback, because the goal is to find conditions that apply to a general biological networks, whose number of proteins may be huge or unknown. Nonetheless, the developments of this section are the theoretical basis upon which the alternative strategies developed in the remaining of this chapter will lead to establish the conditions that the Crosstalk scheme must fulfill, and form which useful biological insight is obtained

6.1.2 Expansion of the Characteristic Polynomial

In the previous chapter, the stability of the RhoGTPase system was investigated analyzing the structure of a_N, the independent term of the characteristic polyno-

mial. In that specific case, it was found that a_N is formed by a compact combination of the Cyclic interactions between the proteins in the networks. The definitions needed to develop the Graph-Theoretical tools to extend this notion systematically are introduced bellow. In addition, the algebraic manipulations of the characteristic polynomial allow to gain insight in to the source of the instabilities and possible modifications.

Let $\gamma_k = \{i_1, ..., i_k\}$ be a sequence of k distinct integers such as $1 \leqslant i_1 < i_2 .... < i_k \leqslant N$ and let S_k^N be the set of all the different γ_k sequences of k elements in $\{1, ..., N\}$. $\mathbf{F}^{RD}(\gamma_k)$ denotes the k-by-k principal submatrix of $\mathbf{F}^{RD}$ given by the coefficients with row and column indices equal to $\gamma_k = \{i_1, ..., i_k\}$. There are $N!/(N-k)!\,k!$ different k-by-k principal submatrices $\mathbf{F}^{RD}(\gamma_k)$, which are in a one-to-one correspondence with all the different sequences γ_k in S_k^N. The explicit reference to the state $\mathbf{r_s}$ at which the matrix $\mathbf{F^{RD}}(\gamma_k)(\mathbf{r_s})$ is evaluated is omitted to ease the notation. It is assumed that the matrix is evaluated at a steady states unless stated otherwise. The sum of the determinants of all the different k-by-k principal submatrices is denoted by E_k:

$$E_k(\mathbf{F}^{\mathrm{RD}}) = \sum_{\gamma_k \subseteq S_k^N} \det[\mathbf{F}^{\mathrm{RD}}(\gamma_k)] \tag{6.16}$$

The following identity, which can be verified using the Laplace expansion of the determinant [148], expresses the coefficients of the characteristic polynomial $P_{q/\Phi}(\lambda) = \det[\lambda \mathbf{I} - \mathbf{F}^{RD}]$ in terms of E_k :

$$a_k = (-1)^k E_k(\mathbf{F}^{\mathrm{RD}}) \qquad k = 1, .. ., N \tag{6.17}$$

In the case $k = 1$ the sum goes over the principal submatrices of order 1, which corresponds to the coefficients in $\mathbf{F^{RD}}$ diagonal. For $k = N$ the sum spans only the determinant of the complete matrix, for it is the only principal minor of order N . Hence, the equations 6.17 relate a_1 and a_N to the trace and determinant of $\mathbf{F^{RD}}$ [2]:

[2]The expression of $P_{q/\Phi}$ as a product of its roots $P_{q/\Phi}(\lambda) = \prod (\lambda - \lambda_i)$ relates its k-th coefficient to the sum of all the distinct k-fold products of eigenvalues. For $k = 1$ and $k = N$, $a_1 = (-1)^1 \sum \lambda_i$ and $a_N = (-1)^N \prod \lambda_i$. Combining this with eqs. 6.18, the well known identities between the trace and the sum of the eigenvalues and between the determinant and the product of the eigenvalues are recovered.

$$a_1 = (-1)^1 Tr[\mathbf{F}^{\mathrm{RD}}] \qquad a_N = (-1)^N \det[\mathbf{F}^{\mathrm{RD}}] \tag{6.18}$$

The first Routh-Huwitz condition requires $a_1 > 0$. Hence, the expression for a_1 in 6.18 shows that stability also imposes restrictions on the trace of $\mathbf{F^{RD}}$. This restriction will be important in the formulation of stable regulation models featuring bistability, because it sets a limit to the magnitude of Auto-catalysis.
In light of the explicit expression of the coefficients of $P_{q/\Phi}$, it is now trivial to show that conserved quantities imply that the coefficients of bigger order vanish at $q = 0$. As shown before, if there are p conservation constraints, the rank of $\mathbf{J^R}$ is $N - p$ and therefore all its minors of order larger than $N - p$ vanish. Since $\mathbf{F^{RD}}(\mathbf{r_s}, 0) = \mathbf{J^R}(\mathbf{r_s})$ at $q = 0$, all the terms in the expression 6.17 vanish for the coefficients $a_{N-p+1}, ..., a_N$, and consequently these coefficients are identically null.

Next, the attention is turned to transform the coefficients a_k into an expression where the contribution of the diffusion and reaction terms is partially uncoupled. This is convenient to identify possible sources of instability in the system. The coefficients a_k have been expressed as sum of principal minors of $\mathbf{F^{RD}}$:

$$a_k = (-1)^k \sum_{\gamma_k \subseteq S_k^N} \det[\mathbf{J}^{\mathrm{R}}(\gamma_k) - (q/\Phi)^2 \mathbf{D}(\gamma_k)] \tag{6.19}$$

Uncoupling of the Diffusion and Reaction contributions is achieved by expanding the minors of order k in eq.6.19 and grouping the resulting terms according to the number of entries from the Diffusion matrix. In this way, each minor $\det[\mathbf{F^{RD}}(\gamma_k)]$ is expressed as a summatory of products of all possible minors $\det[\mathbf{J^R}(\gamma_m)]$ of order $m \leqslant k$, given by the sequences $\gamma = \{i_1, ..., i_m\}$, multiplied by the $k - m$ coefficients $(d_{j_1} \cdot d_{j_2} ... \cdot d_{j_{k-m}})$ given by the complementary set $\bar{\gamma} = \{j_1, ..., j_{k-m}\}$ in $\mathbf{D}$. The subsets $\bar{\gamma}_m$ and γ_m are complementary sets in γ_k in the sense that $\gamma_m \cap \bar{\gamma}_m = \emptyset$ and $\gamma_m \cup \bar{\gamma}_m = \gamma_k$ [3]. Then, after some tedious algebra, the following expression is reached:

[3]Let γ_m and $\bar{\gamma}_m$ be complementary sets in γ_k with $0 \leq m \leq k$. Let γ_k be the set of k integers $\gamma_k = \{i_1, ..., i_k\}$ and γ_m a subset of m elements of γ_k. The complementary set $\bar{\gamma}_m$ is defined as $\bar{\gamma}_m = \{i_1, ..., i_k\} \setminus \gamma_m$, the set of elements in γ_k minus the elements in γ_m. Then, $\mathbf{A}(\bar{\gamma}_m)$ is the principal submatrix of order $k - m$ in $\mathbf{A}(\gamma_k)$ given by the coefficients with row and column index in $\{i_1, ..., i_k\} \setminus \gamma_m$ or , equivalently, the matrix obtained by deleting from $\mathbf{A}(\gamma_k)$ the rows and columns given by γ_m.

$$a_k = \sum_{\gamma_k} \Bigg\{ (-1)^k \det[\mathbf{J}^{\mathrm{R}}(\gamma_k)] + \sum_{m=1}^{k-1} (q/\Phi)^{2(k-m)} \sum_{\gamma_m \subset \gamma_k} (-1)^m \det[\mathbf{J}^{\mathrm{R}}(\gamma_m)] \det[\mathbf{D}(\bar{\gamma}_m)] + (q/\Phi)^{2k} \det[\mathbf{D}(\gamma_k)] \Bigg\} \tag{6.20}$$

The first and third summands in 6.20 stem exclusively from Reaction terms and Diffusion terms. The second is formed by minors of the Reaction Jacobian weighted by the complementary coefficients of the diffusion matrix. Examination of the expression of $a_k(q)$ in 6.20 provides insight into which interactions between the network proteins have more potential to lead to Turing instabilities. The system is stable by construction under homogeneous perturbations, characterized by wave-number $q = 0$. In this instance, the only terms contributing to $a_k(0)$ are the leading factors $\mathbf{J^R}(\gamma_\mathbf{k})$, so that these terms can be assumed to satisfy the stability conditions. As heterogeneous perturbations are considered, instabilities may arise as the value of the coefficients $a_k(q)$ departs from the values that fulfill the stability conditions. For the range of small wavenumbers $0 < q/\Phi < 1$, the change in $a_k(q)$ is dominated by the coupled term that grows as $\sim(q/\Phi)^2$, whereas the purely diffusive term only goes as $\sim(q/\Phi)^{2k}$. In the range of large wavenumbers $q/\Phi \gg q_M$, the purely diffusive term dominates over the rest, forcing the system into stability[4]. Thus, there is an intermediate band of wavenumbers in which the coupled term in 6.20 dominates over the rest an might lead to diffusion-driven instabilities. The coupled term is formed by pairs of reaction-like and diffusion-like factors: a factor $\mathbf{J}^{\mathrm{R}}(\gamma_k)$ stemming from crosstalk interactions between a subgroup of proteins, multiplied by a factor $\mathbf{D}(\bar{\gamma}_m)$ associated to the diffusion of the complementary subgroup of proteins. For given wave-number q, the dominant terms are those formed by strong interacting subgroups of proteins and fast diffusive subgroups of proteins. Systems containing strong interacting subgroups of proteins and fast diffusive subgroups of proteins are candidates to feature Turing instabilities. Indeed, the model of RhoGTPase regulation presented is of this type, as the crosstalk is carried locally by the slow-diffusive proteins inserted in the membrane and the inactive RhoGTPases diffuse fast. Interestingly, this suggest an alternative mechanism of crosstalk in which the mediators of fast diffusing proteins in the cytosol and the proteins embedded in the membrane

[4]For very large q/Φ, the matrix $\mathbf{F^{RD}}$ is diagonally dominant with negative diagonal entries and therefore stable by Gershgorin theorem [149]

interacted weakly. This fits precisely with the idea suggested early in Chapter 2 that active regulation and competition between RhoGTPases for GDIs binding, which sets the fraction of these proteins in the cytosol, might have an important role in crosstalk .

6.2 Reaction Graph

In previous chapters it was shown the need to modify current models of RhoGTPase regulation of cell polarization during migration, based on the discrepancy between its predictions and experimental facts. The source of this behavior was traced to the existence of a positive feedback loop in the interaction scheme which originated Turing instabilities. A Graph-Theoretical methodology is now introduced to study the connection between stability and the topology of the crosstalk scheme. The central result of this method is that it shows that the dynamical properties and stability of a general reaction-diffusion system are determined *only* by the cyclical structure of the network. Thus, the feedback structure of the Crosstalk scheme is the feature that determines the existence of oscillations and Turing Instabilities. In addition, this method allows to break down complex networks into smaller modules and provides a mechanism to relate the algebraic conditions of the previous section with intuitive biological implications.

The definition of the Reaction and Interaction graphs follows closely the definition of the Coates Graph of a general square matrix [150]. The Reaction Graph $G_R[\mathbf{J}^R(\mathbf{r_s})]$ is a labelled, weighted, directed graph associated to the linearization of the reaction-diffusion system. In a system with N interacting species, $G_R[\mathbf{J}^R(\mathbf{r_s})]$ is a graph with N nodes that has a directed edge from node j to node i if $\mathbf{J}^R_{ij}(\mathbf{r_s}) \neq 0$. The weight assigned to the edge is the coefficient $\mathbf{J}^R_{ij}(\mathbf{r_s})$. Note that according to this definition, the entries $\mathbf{J}^R_{ii}(\mathbf{r_s})$ in the diagonal of the Jacobian have associated an edge with i as the initial and terminal node. This type of edges are called loops and account for decay terms and autocatalysis in the reaction. A common convention to facilitate the visual interpretation of the Reaction graph is to draw an arrow or a bar at the end of an edge when the weight is positive or negative, respectively. In this way, an arrow edge associated to the coefficient $\mathbf{J}^R_{ij}(\mathbf{r_s}) > 0$ in the Jacobian represents positive crosstalk from protein j to protein i. Likewise, edges ended with a bar represent negative crosstalk. A node featuring a loop will be represented simply by a circle around the node, regardless of its sign. An important observation is that the sign of the entries in $\mathbf{J}^R(\mathbf{r_s})$ can depend on the state of the network, and consequently, the Reaction Graph also depends on the state $\mathbf{r_s}$ in which $G_R[\mathbf{J}^R(\mathbf{r_s})]$ is calculated. This is the case when there exist interactions between proteins that switch from inhibitory to activating (or the other

way around) depending on the concentrations of the proteins involved. Thus, even if the topology of the Reaction Graph is constant and independent of the state of the network, the sign of the edges might change if the nature of crosstalk depends on their concentrations. From now on, the explicit reference to the state $\mathbf{r_s}$ in which $G_R[\mathbf{J}^R(\mathbf{r_s})]$ is calculated will be dropped to ease the notation, but it must be remembered that the Reaction Graph is defined at a particular state of the network.
The interaction Graph $G_I[\mathbf{F}^{RD}]$ is the equivalent of the Reaction Graph including the diffusion term in $\mathbf{F}^{RD}$. If the Diffusion Matrix is diagonal, both graphs are topologically identical and the only difference lays in the weight of the loops.
The following 4x4 matrix $\mathbf{A}$ is used as an example to illustrate these definitions.

$$\mathbf{A} = \begin{bmatrix} l_1 & -b & +c & +d \\ 0 & l_2 & 0 & 0 \\ -e & 0 & l_3 & 0 \\ 0 & 0 & +f & l_4 \end{bmatrix} \tag{6.21}$$

Let $\mathbf{A}$ represent the Reaction term obtained from the linearization of a reaction-diffusion system. The coefficient $\mathbf{A}_{ij}$ is then associated to the variation of the reaction rate of protein i caused by the change in the concentration of protein j. The sign of $\mathbf{A}_{ij}$ determines the inhibitory or activating nature of the crosstalk signals from j to i. The sign of the interaction is reflected in the Reaction Graph by the type of edges between the nodes. According to the definitions given previously, $G_R[\mathbf{A}]$ is the 4-node graph shown in the following figure:

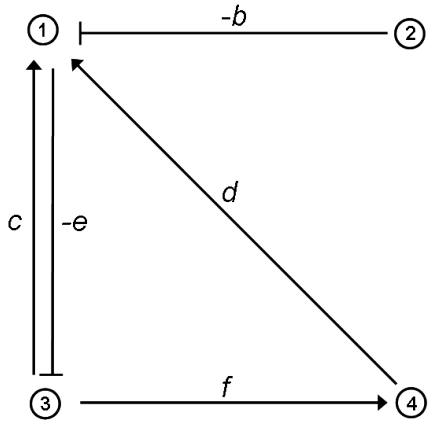

Figure 6.1: Interaction Graph associated to matrix $\mathbf{A}$.

$G_R[\mathbf{A}]$ is graphical counterpart to the reaction scheme of matrix **A**. The off-diagonal coefficients in row i of the matrix appear in the Reaction Graph as the edges carrying crosstalk signals to node i. The coefficients in column i correspond to the edges issuing from node i . For instance, node 1 receives negative signals from node 2 and positive signals from nodes 3 and 4; these edges correspond to the coefficients $-b$, $+c$ and $+d$ in the first row of matrix **A** , respectively. On the other hand, node 1 only sends inhibitory signals to node 3, corresponding to the single nonzero coefficient in column 1.
The definitions from Graph theory introduced next will be necessary to develop the framework for the analysis of the stability of a reaction-diffusion system. The indegree and the outdegree of a node are the number of edges that have this node as the initial or terminal node, respectively. A loop, defined as an edge that originates and ends at the same node, contributes 1 to both the indegree and the outdegree of that node. As an example, in the graph of 6.1, node 3 has indegree equal to 2, for it has an incoming edge from node 1 and the loop. The outdegree of this node is 3, because there are two edges going to nodes 1 and 4 plus the loop contribution.

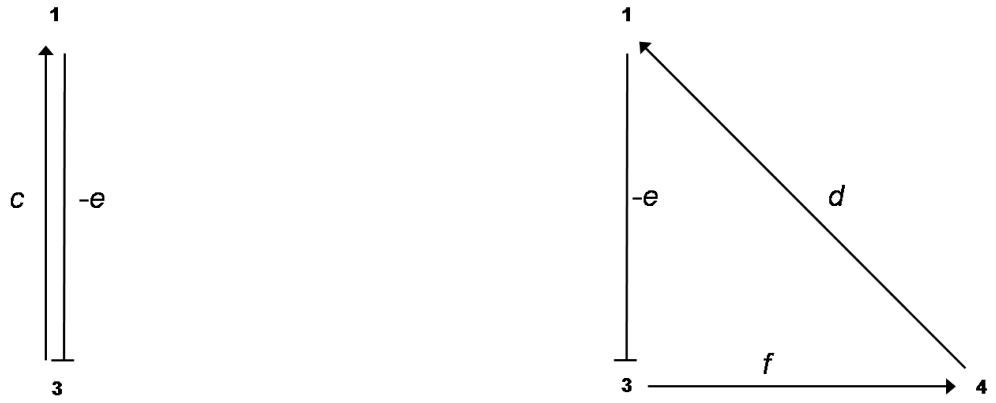

(a) Cycle C_2 (b) Cycle C_3

Figure 6.2: Cycles of length $m > 1$ in $G_R[\mathbf{A}]$

A cycle of length m is a subset of m distinct nodes and m distinct edges that join i_k to i_{k+1} for $k = 1, ..., m$ and an edge from i_m back to i_1 . By this definition, loops are also cycles of length one. The weight of a cycle $w(c)$ is the product of weights of the edges that form the cycle. Cycles are classified as positive or negative according

to the sign of its weight. The graph $G_R[\mathbf{A}]$ used as an example has, aside from the four loops associated to the diagonal terms in $\mathbf{A}$, a negative cycle of length 2 and a negative cycle of length 3. C_2 is negative and its weight is $w(C_2) = -e \cdot c$, whereas C_3 has weight $w(C_3) = -e \cdot f \cdot d$ and is also a negative cycle.
A subgraph of the Reaction Graph is a directed graph formed by a subset of edges and whose set of nodes are a subset $\gamma_k = \{i_1 ... i_k\}$ of those in G_R, with $\gamma_k \subset \{1 \dots N\}$. The Induced subgraph of γ_k , referred as the I-subgraph I_{γ_k} , is the subgraph of $G_R[\mathbf{A}]$ formed by the subset of nodes γ_k and all the edges that join nodes within this set. The induced subgraph I_{γ_k} is identical to the graph $G_R[\mathbf{A}(\gamma_k)]$ obtained by applying the definition of the Reaction Graph to the principal submatrix $\mathbf{A}(\gamma_k)$, so that all the definitions and properties of the Reaction Graph carry over its I-subgraphs. As an example, consider the 3-by-3 principal submatrix matrix $\mathbf{A}(\gamma_3)$ induced by the sequence $\gamma_3 = \{1, 2, 4\}$:

$$\mathbf{A}(\gamma_3) = \begin{bmatrix} l_1 & -b & d \\ 0 & l_2 & 0 \\ 0 & 0 & l_4 \end{bmatrix} \tag{6.22}$$

The I-subgraph associated to γ_k , shown in figure 6.3, is obtained by applying the definition of the Reaction graph to the matrix $\mathbf{A}(\gamma_3)$ or equivalently, by erasing from the complete graph $G_R[\mathbf{A}]$ the nodes that do not belong to γ_3 and the edges that do not start and finish in the nodes of γ_3 .

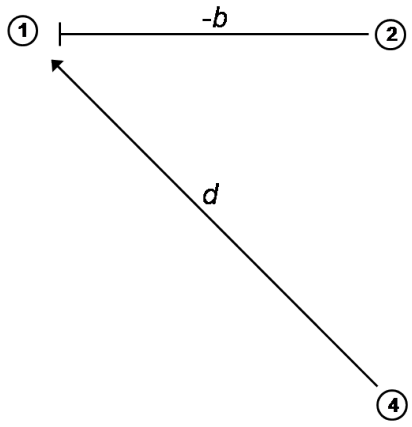

Figure 6.3: I-subgraph induced by $\mathbf{A}(\gamma_3)$.

Note that the Induced subgraphs of the Interaction Graph $G_I[\mathbf{F^{RD}}(\gamma_k)]$ obtained by considering all possible sequences γ_k are in a one-to-one correspondence with $\mathbf{F}^{\mathrm{RD}}(\gamma_k)$, the k x k principal submatrices appearing in the expansion of the k-th coefficient of the characteristic polynomial in eqs. 6.16 and 6.17. Likewise, all the terms $\mathbf{J^R}(\gamma_k)$ in the expression 6.20 of the coefficient a_k correspond to one and only one I-subgraph of the Reaction Graph $G_I[\mathbf{J^R}]$. Hence, the graph definitions introduced previously provide a method to associate a graph to each of the terms in the algebraic stability conditions.

A spanning subgraph is a subgraph that includes all the nodes in G_R, but not necessarily all edges. A linear spanning subgraph ℓ , also referred to as an L-subgraph, is a spanning subgraph of G_R in which each node has indegree 1 and outdegree 1. This definition implies that an L-subgraph is composed by a set of disjoint cycles and isolated loops, where the cycles are disjoint in the sense that each node belongs to one and only one cycle. The three different L-subgraphs contained $G_R[\mathbf{A}]$ are depicted in the following figure:

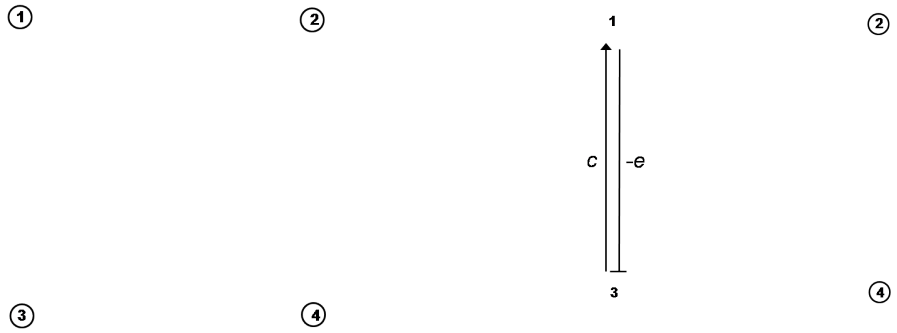

(a) L-subgraph ℓ_1 (b) L-subgraph ℓ_2

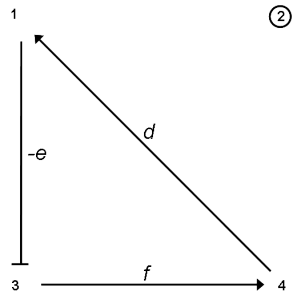

(c) L-subgraph ℓ_3

Figure 6.4: Linear spanning subgraphs of $G_R[\mathbf{A}]$

The number of cycles in a L-subgraph is denoted by $s(\ell)$. The weight of a L-subgraph is simply defined as the product of weights of the cycles contained in it.

$$w(\ell) = \prod_{c \subset \ell} w(c) \tag{6.23}$$

For the linear spanning subgraphs depicted in fig. 6.4 , the number of cycles and weights are:

$$\begin{aligned} s(\ell_1) = 4 \quad ; \quad w(\ell_1) &= (l_1) \cdot (l_2) \cdot (l_3) \cdot (l_4) \\ s(\ell_2) = 2 \quad ; \quad w(\ell_2) &= (l_2) \cdot (l_4) \cdot (-e \cdot c) \\ s(\ell_3) = 2 \quad ; \quad w(\ell_3) &= (l_2) \cdot (-e \cdot f \cdot d) \end{aligned} \tag{6.24}$$

The notion of linear spanning subgdigraph can be naturally extended to the I-subgraphs of $G_R[\mathbf{A}]$. The L-subgraphs contained in I_{γ_k} are all the different subgraphs of order k formed by a set disjoint cycles spanning the k nodes of the induced subgraph.

The L- subgraphs contained in the Reaction Graph of a matrix are the factors that determine the stability of the system. It has been shown that the Graph methodology provides a way to assign a I-subgraph to each of the terms appearing in the algebraic equations that determine the stability of the system. Particularly, these equations are expressed in terms of principal minors $\det[\mathbf{J^R}(\gamma_k)]$ of the reaction term Jacobian. Next, it will be shown that the value of each of these minors is determined *only* by the weights of the L-subgraphs contained in the associated I-subgraph I_{γ_k}. The intimate relationship between the dynamics of a reaction-diffusion system and the cyclical structure of the reaction network is explained by this fact.

The expression of the determinant of a N x N matrix $\mathbf{A}$ as a linear combination of the weights of the L-subgraphs in $G_R[\mathbf{A}]$ is known as the Coates formula :

$$\det[\,\mathbf{A}] = (-1)^N \sum_{\ell \subseteq G_R} (-1)^{s(\ell)} w(\ell) \tag{6.25}$$

where the sum goes through all the L- subgraphs in $G_R[\mathbf{A}]$. A sketch of the proof of the Coates formula is given following [151, pg. 143] and a more formal proof

can be found in [150, pg. 94]. The first part of the proof shows that there is a one-to-one correspondence between the non-vanishing terms in the determinant of a matrix and the linear spanning subgraphs in its associated Graph. The second part of the proof shows that sign of the contribution of the non-vanishing terms is also dictated by the structure the linear spanning subgraphs. The classical definition of the determinant of a N xN matrix is:

$$\det(\mathbf{A}) = \sum_{p} \varepsilon_{i_1 \ldots i_N} a_{1 i_1} \cdot \ldots \cdot a_{N i_N} \tag{6.26}$$

where the sum is over all the $N!$ permutations $p = \{1, ..., N\} \rightarrow \{i_1, ..., i_N\}$. The signature of the permutation is given by $\varepsilon_{i_1,\ldots,i_N}$ and it is equal to $+1$ if p is an even permutation and -1 if it is odd. All non-vanishing terms in eq. 6.26 are a product $a_{1 i_1} \cdot \ldots \cdot a_{N i_N}$ of N coefficients. Each index appears twice, one as a row index and one as a column index, so that each row and column contribute to the product with exactly one coefficient. Hence, the subgraph in $G_I[\mathbf{A}]$ defined by the entries $a_{1 i_1} \cdot \ldots \cdot a_{N i_N}$ has N edges, with exactly one edge coming into every node and one edge coming out of every node. Therefore, the subgraph associated to every term in eq. 6.26 is by definition a linear spanning subgraph in $G_I[\mathbf{A}]$.
Conversely, every linear spanning subgraph ℓ in $G_I[\mathbf{A}]$ has N nodes with indegree and outdegree equal to one. The N edges in ℓ are associated to N coefficients in $\mathbf{A}$, the edge directed to node j being the only one in the j-th row, and the edge coming out of node j being the only one in the j-th column. Arranging the indexes by increasing row order, the weight of ℓ becomes $w(\ell) = a_{1 i_1}, ..., a_{N i_N}$, showing the correspondence between each linear spanning subgraph in $G_I[\mathbf{A}]$ with one and only one of the permutations p in the definition of the determinant. In this way, a one-to-one correspondence has been established between the L-subgraphs in $G_I[\mathbf{A}]$ and the non-vanishing permutations terms in the $det[\mathbf{A}]$.
Explicit calculation of the determinant of the example matrix illustrates the first part of the proof, as det[$\mathbf{A}$] is proved to be a linear combination of the weights of the L-subgraphs ℓ_1 , ℓ_2 , ℓ_3 represented in figure 6.4.

$$\det(\mathbf{A}) = w(\ell_1) - w(\ell_2) + w(\ell_3) \tag{6.27}$$

The one-to-one correspondence provides a convenient way to label a particular L-subgraph by the associated permutation. The permutation $p = \{i_1, ..., i_N\}$ defines univocally the L-subgraph $\ell(p)$ as the subgraph of $G_I[\mathbf{A}]$ obtained by selecting the edge from node i_1 to node 1, from node i_2 to node 2 and generally from node i_k to

node k for $k = 1, ..., N$. In this way, the sign of the contribution of an L-subgraph to the determinant can be derived considering the signature of its associated permutation. The L-subgraphs ℓ_1 and ℓ_3 of the example correspond to the even permutations $p_1 = \{1, 2, 3, 4\}$ and $p_3 = \{4, 2, 1, 3\}$. Thus, the corresponding terms in the determinant must have positive sign, as it is confirmed examining the explicit expression in eq. 6.27. Conversely, ℓ_2 is associated to the odd permutation $p_2 = \{3, 2, 1, 4\}$ and consequently the sign of the corresponding term is negative. In the same way that permutations define univocally a L-subgraph, a cyclic permutation of k integers defines univocally a cycle passing through k nodes in $G_I[\mathbf{A}]$.
The second part of the proof shows how the signature of a permutation ε_p is related to the structure of the associated L-subgraph; more precisely, the number of cycles $s(\ell)$ contained in it. The parity of a permutation is the number of transpositions in which it can be decomposed. The decomposition is generally not unique, but the parity is invariant, so that permutations are classified as even or odd according to this number. The signature of a transposition is defined as -1, and by extension the signature of a permutation is given by the product of the signatures of its factors. Hence, the signature of even permutations is +1 , whereas the sign of odd permutations is -1. The theory of symmetric groups of finite degree establishes that for any permutation p there is a unique decomposition of p as a product of $s(p)$ cyclic permutations [152].

$$p = cp_1 \times cp_2 \times ... \times cp_s \tag{6.28}$$

In turn, any cyclic permutation of i objects can be written as the product of $i - 1$ transpositions . Hence, any permutation of N objects can be factorized as $s(p)$ cyclic permutations of $i, j, k, ...$, objects, with $i + j + k + ... = N$. The signature of the permutation, given by the product of the signatures of the cyclic factors is then $\varepsilon_p = (-1)^{i-1}(-1)^{j-1}(-1)^{k-1}... = (-1)^{N-S(p)}$. Rearranging , the following identity is obtained:

$$\varepsilon_p = (-1)^N(-1)^{s(p)} \tag{6.29}$$

It has been shown that a permutation p corresponds to an L-subgraph ℓ, and that the cyclic permutations in p correspond to the cycles in ℓ. Thus, replacing the permutation p for ℓ and the number of cyclic permutations in p for the number of cycles in $s(\ell)$ completes the proof of the Coates formula.
The expression of det$[\mathbf{A}]$ in equation 6.27 can now be derived strictly from the graphical structure of the associated Graph. Indeed, the sign of the contributions

of ℓ_1 and ℓ_3 are positive because they contain an even number of cycles (four loops in the former case, one loop and one cycle of length 3 in the latter case), whereas ℓ_2 contains an odd number of cycles (two loops and a cycle of length 2) and accordingly, its contribution is negative.
The Coates formula leads naturally to the definition of the weight of an Induced subgraph as the signed sum of the weights of the L-subgraphs contained in it. According to this definition, the weight of the I-subgraph I_{γ_k} is equal to the determinant of the principal submatrix $A(\gamma_k)$:

$$w(I_{\gamma_k}) \equiv \det[\mathbf{A}(\gamma_k)] = (-1)^k \sum_{\ell \subseteq I_{\gamma_k}} (-1)^{s(\ell)} w(\ell) \tag{6.30}$$

This definition is the last element required to reformulate the stability conditions for a Reaction-Diffusion system from a Graph theoretical point of view. The coefficient of order k in the characteristic polynomial was expressed in equations 6.16-6.17 as a sum over all the principal minors of order k in $\mathbf{F^{RD}}$. A method to associate a graph $G_I[\mathbf{F^{RD}}]$ to $\mathbf{F^{RD}}$ has been established. Particularly, each k x k principal submatrix $\mathbf{F^{RD}}(\gamma_\mathbf{k})$ corresponds to an Induced subgraph I_{γ_k} of order k in the Interaction graph. Furthermore, the associated principal minor $[\det \mathbf{F^{RD}}(\gamma_\mathbf{k})]$ is given by the weight $w(I_{\gamma_k})$ of the associated I-subgraph in G_I. Substitution of this identity restates the algebraic expression of a_k given in 6.19 as sum of weights of the Induced subgraphs as:

$$a_k = (-1)^k \sum_{I_{\gamma_k} \subseteq G_I} w(I_{\gamma_k}) \tag{6.31}$$

where the summation goes over all the I-subgraphs of order k in the Interaction Graph. Expanding the weight of the I-subgraphs in terms of the L-subgraphs according to eq.6.30 leads to:

$$a_k = \sum_{I_{\gamma_k} \subset G_I} \sum_{\ell \subseteq I_{\gamma_k}} (-1)^{s(\ell)} w(\ell) \tag{6.32}$$

Likewise, substitution of the weights of the I-subgraphs in the Reaction Graph in eq. 6.20 leads to the graphical counterpart of the uncoupled expressions of a_k:

$$a_k = \sum_{I_{\gamma_k} \subset G_R} \left\{ \sum_{\ell \subseteq I_{\gamma_k}} (-1)^{s(\ell)} w(\ell) + \sum_{m=1}^{k-1} (q/\varphi)^{2(k-m)} \sum_{I_{\gamma_m} \subset I_{\gamma_k}} \det[\mathbf{D}(\bar{\gamma}_m)] \sum_{\ell' \subseteq \gamma_m} (-1)^{s(\ell')} w(\ell') + (q/\varphi)^{2k} \det[\mathbf{D}(\gamma_k)] \right\} \tag{6.33}$$

Examination of these results provides an important insight on the relationship between the feedback structure of the Reaction scheme an the stability of the associated Reaction-Diffusion system. More precisely, the Graph-based expressions reveal that every cycle in the network has a defined role in the dynamics of the system. This allows to break down the complete network into smaller functional motives, thus providing a powerful tool to analyze general networks independently of their complexity or specific parameter values. The previous developments have established that cycles, through their weight contribution to L-subgraphs, are the structures that govern the stability of the network. A given cycle of the Reaction Graph might appear many times in the stability equations, because there might be several L-subgraphs that contain that particular cycle. However, its contribution to the weight of any L-subgraphs in which it appears remains constant: the weight of an L-subgraph ℓ formed by $s(\ell)$ cycles is given by the product of the cycles' weights and a factor (-1) for each of the $s(\ell)$ cycles contained in ℓ. Then, a particular cycle c always contributes a factor $(-1) \cdot w(c)$ to any of the L-subgraphs in which is found, and for this reason, its dynamical role can be assessed independently of the rest of the reaction scheme:

$$(-1)^{s(\ell)} w(\ell) = (-1) \cdot w(c) \prod_{c' \subseteq \ell \setminus c} (-1) \cdot w(c') \qquad \forall\, \ell \supset c \tag{6.34}$$

The expression above, defines the contribution of any L-subgraph containing the cycle c to the stability equations. Cycles were classified as positive or negative according to the sign of its weight, which defines its activating or inhibitory nature within a reaction network. It follows that negative cycles always contribute as a positive factor in every L-subgraph in which they are present, whereas positive cycles are the only possible source of a negative factor.

The Routh-Hurwitz criterion states that the positivity of a_k is a necessary condition for stability. Conversely, a negative coefficient is a sufficient condition for instability. This shows that positive cycles, for a certain range of parameter

values, are a sufficient element in a reaction network for Turing instabilities to occur.

This section has proved the central role of cycles in the stability of a reaction system. The value of the graphical methodology lays also in its power to break down a complex reaction network into smaller modules, enabling the analysis of their role in the dynamics of the whole system and identifying their function within the network. Moreover, the role of cycles in determining the dynamics of a dynamical system is actually broader than what it has been shown here. In the same way that Turing instabilities are associated to the existence of saddle-node bifurcations, other types of dynamical behavior, such as oscillating solutions, are associated to Hopf bifurcations and the conditions for its occurrence can be related to the cyclic structure of the reaction scheme. This topic is left for future work.

In the next section, results drawn from Matrix Theory will define a general class of Reaction Schemes that do not feature the shortcomings of existing models of RhoGTPase regulation discussed previously. Alternative models of RhoGTPase regulation will be formulated imposing the constraints required to belong to this class. The biological interpretation of these conditions, however, relies on the insights obtained from the graph-theoretical view.

6.3 Kinetic Matrix and stability

The former section analyzed the existence of diffusion-driven instabilities as a problem of locating the roots of a polynomial. The Routh-Hurwitz criterion provides sufficient conditions for the roots to lay on the left half of the complex plane, but their value to formulate alternative interaction schemes is limited. Explicit expression of the coefficients of the characteristic polynomial of $\mathbf{F^{RD}}(\mathbf{r_s})$ and separation of the Reaction and Diffusion contributions results in some progress in that direction, because it allows to identify the critical factors of the reaction scheme that may lead to the appearance of Turing patterns. An alternative approach, based on the notion of strong stability of matrix theory [153], might be more useful in suggesting modifications to the RhOGTPase regulation mode.

6.3.1 $\mathbf{P_0^+}$-matrices and Turing patterns

Let $\mathbf{A}$ be a real NxN stable matrix and $\mathbf{D} = \text{diag}[d_1, .., d_N]$ a diagonal matrix with nonengative entries.

Definition 1. The matrix $\mathbf{A}$ is said to be strongly stable if $\mathbf{A} - \mathbf{D}$ is stable for all $\mathbf{D} \geqslant 0$.

The property of strong stability , also referred as additive D-stability [154] , is directly related to the existence of Turing patterns. Provided that the reaction jacobian $\mathbf{J^R}(\mathbf{r_s})$ is strongly stable, the linearization of the reaction-diffusion equations $\mathbf{F}^{RD}(\mathbf{r_s}) = \mathbf{J}^R(\mathbf{r_s}) - (q/\Phi)^2\mathbf{D}$ remains stable for all wave-numbers $q > 0$. Hence, if $\mathbf{J}(\mathbf{r_s})$ is strongly stable, the system will not feature diffusion-driven instabilities. This notion leads to the following questions: Which structural properties guarantee that a matrix is strongly stable? How this structural properties translate into requirements for the Reaction scheme underlying $\mathbf{J^R}(\mathbf{r_s})$? A partial answer is provided by a classic result in matrix stability theory regarding the following subset of matrices:

Definition 2. The matrix $\mathbf{A}$ is said to be a P_0 -matrix if all the signed principal minors are nonnegative:

$$(-1)^k \det[\mathbf{A}(\gamma_k)] \geq 0 \qquad \forall\, \gamma_k \qquad k = 1, ..., N \tag{6.35}$$

The subset P_0^+ spans the P_0 -matrices that have at least one positive signed minor of each order for $k = 1, ..., N$. The central result of this section, proved in [153, pag. 255-256], states:

Theorem 3. [Cross] If $\mathbf{A}$ is strongly stable, then $\mathbf{A} \in P_0^+$

Conversely, the existence of a principal submatrix whose signed minor is negative guarantees that $\mathbf{A} - \mathbf{D}$ is unstable for some $\mathbf{D}$[5]. It follows that $\mathbf{J^R}(\mathbf{r_s}) \in P_0^+$ is a necessary condition for a reaction-diffusion system to not feature Turing instabilities.
In a system with p conservation laws, the Jacobian of the reaction matrix might be a P_0-matrix, but it can not be a P_0^+-matrix because the minors of order bigger than $N - p$ vanish. However, examination of the proof of theorem 3 reveals that the $\mathbf{A} \in P_0^+$ requirement can be relaxed to accommodate this type of systems. The first part of the proof shows that a strongly stable NxN matrix necessarily requires that the eigenvalues of every prinicpal submatrix are non-negative. Their

[5]In fact, the strong stability condition is too restrictive. It requires $\mathbf{A} - \mathbf{D}$ to be stable for all $\mathbf{D} \geq 0$, but for a particular network of proteins the diffusion constants are known experimental quantities and $\mathbf{D}$ is determined. Stability of $\mathbf{J^R} - q \cdot \mathbf{D}$ should be imposed for all $q > 0$ *and* $\mathbf{D}$ given and fixed. Indeed, the proof that the existence of a single negative signed minor in $\mathbf{A}$ is sufficient for Turing instabilities to occur is based on increasing the diffusion coefficients complementary to the negative minor until a positive eigenvalue is produced (see theorem 1 in [153, pag.255-256] or theorem 3.1 in [155, pag. 143]). Thus, it is theoretically possible that a system in which $\mathbf{J}^R \notin P_0^+$ does not feature diffusion-driven instabilities for a particular choice of $\mathbf{D}$. However, the aim is to keep the results as general as possible, in which case strong stability is close to the optimal stability requirement.

corresponding signed minors are given by the product of these eigenvalues and therefore are also non-negative. Thus far, strong stability only imposes $\mathbf{A} \in P_0$. The stricter condition $\mathbf{A} \in P_0^+$ stems from the starting assumption that $\mathbf{A}$ is stable, which according to the Routh-Hurwitz theorem entails that all the coefficients of the characteristic polynomial are strictly positive. This is fulfilled with the additional requirement that at least one minor of every order is positive, so that expansion of each of the coefficients a_k in equations 6.20 has at least one positive term . In a system with p conservation laws, it has been shown that stability is guaranteed if the matrix $\mathbf{A}$ is semistable: it has $N - p$ negative eigenvalues and p null eigenvalues. Thus, the positivity of the a_k coefficients is required *only* for the first $N - p$ coefficient. Consequently, the need for the existence of at least one positive minor of every order is restricted to the order $k = 1, ..., N - p$.

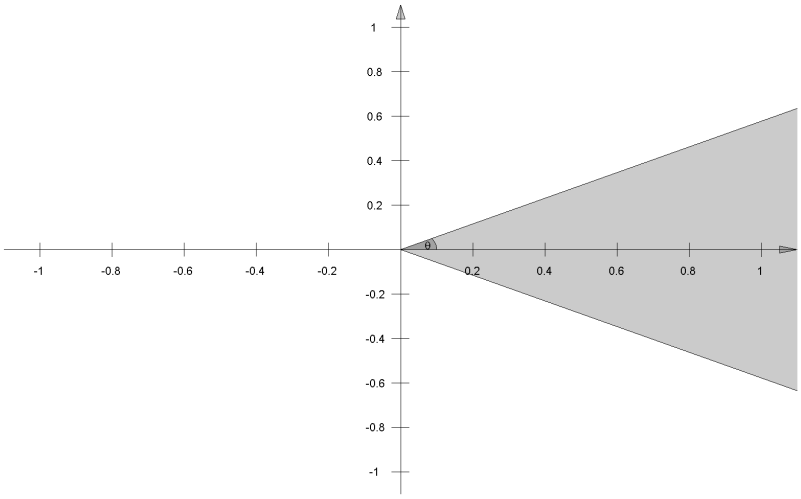

Figure 6.5: Exclusion wedge for the eigenvalues of a P_0-matrix $\mathbf{A}$ and $\mathbf{A} - q \cdot \mathbf{D}$. For $N = 6$, $\theta = 30°$

This argument can be recast in a more elegant way using the eigenvalue exclusion results found in [156]. In this work, it is proved that the eigenvalues of a P_0-matrix [6] are excluded from a wedge around the positive half of the real axis, as depicted in figure 6.5 . Let $\lambda = r\,exp(i\theta)$ be an eigenvalue of a NxN P_0-matrix,

[6]The definitions used in Kelloggs's paper [156] differ from those adopted here, which follow the definitions given in Cross paper [153]. The difference lays in a minus sign in the definition of a P, P_0 and P_0^+-matrices. The adaptation of the results to the alternative convention is straightforward, using the following property of the spectrum of a matrix $\sigma(-\mathbf{A}) = -\sigma(\mathbf{A})$

where θ is the polar angle measured form the positive real axis. Then:

Theorem 4. [Kellogg] $\lambda = r\exp(i\theta)$ is an eigenvalue of a NxN P_0-matrix if and only if

$$|\theta| \geqslant \pi/N$$

The strict inequality applies to P-matrices, those whose signed minors are all positive. The next step consists in showing that the eigenvalue exclusion region of a P_0-matrix $\mathbf{A}$ also applies to $\mathbf{A} - \mathbf{D}$. The key element for this is the following property of P_0-matrices, enunciated in Proposition 1 of [153, pag. 257].

Theorem 5. [Cross] If a matrix $\mathbf{A} \in P_0$ or $\mathbf{A} \in P_0^+$, the same is true of $\mathbf{A} - \mathbf{D}$ for all $\mathbf{D} \geq 0$.

This result is proved expanding a generic minor of order k of the matrix $\mathbf{A} - \mathbf{D}$ in terms of the minors of $\mathbf{A}$, as it was done for the coefficient a_k in eq.6.20. This shows that the minors of $\mathbf{A} - \mathbf{D}$ are minimal for $\mathbf{D} = 0$:

$$\begin{aligned}(-1)^k \det[\mathbf{A}-\mathbf{D}](\gamma_k) =& (-1)^k \det[\mathbf{A}(\gamma_k)] + \sum_{m=1}^{k-1} \sum_{\gamma_m \subset \gamma_k} (-1)^m \det[\mathbf{A}(\gamma_m)] \det[\mathbf{D}(\bar{\gamma}_m)] \\ &+ \det[\mathbf{D}(\gamma_k)]\end{aligned}$$

Every signed minor of $\mathbf{A} - \mathbf{D}$ is then a non-negative linear combination of the signed minors of $\mathbf{A}$. Hence, if $\mathbf{A} \in P_0$ every signed minor of $\mathbf{A} - \mathbf{D}$ is non-negative and increases with $\mathbf{D}$. In addition, if $\mathbf{A} \in P_0^+$ there is at least one positive signed minor of every order that guarantees that the same is true in $\mathbf{A} - \mathbf{D}$. These are precisely the definitions of a P_0 and a P_0^+ matrices, respectively, and therefore $\mathbf{A} - \mathbf{D}$ belongs to the same matrix class that $\mathbf{A}$. Consequently , the eigenvalue exclusion zone of $\mathbf{A}$, which only depends on the order of the matrix, is also valid for the eigenvalues of $\mathbf{A} - \mathbf{D}$ for any $\mathbf{D} \geq 0$. The relevance of these results regarding the existence of diffusion-driven instabilities in reaction-diffusion systems instabilities is now evident. Provided that the jacobian of the reaction term $\mathbf{J}(\mathbf{r_s})$ is a P_0-matrix, the eigenvalues of $\mathbf{J}(\mathbf{r_s}) - q \cdot \mathbf{D}$ can not cross to the positive half of the complex plane along the real axis, and Turing instabilities do not occur.
This result also shows why being a P_0^+-matrix is only a necessary condition for strong stability, as stated in Theorem 5: it does not prevent a pair of complex conjugate eigenvalues with $|\mathrm{Im}(\lambda)| > 0$ from crossing the imaginary axis for some $q > 0$. This type of behavior is associated to a Hopf bifurcation and leads to time-periodic

oscillations. For stable matrices of order $N \leqslant 3$, $\mathbf{A} \in P_0^+$ is also a sufficient condition for strong stability [153]. The connection between time-periodic solutions and the Reaction scheme structure is an extremely interesting topic, particularly in the context of cell migration, where the existence of an oscillating pattern of regulating signals could be at the root of the sequence of protrusion-adhesion-contraction phases that constitute the migration process. This topic, however, will not be pursued further, although possible lines of progress for establishing such a connection are mentioned to motivate future work. First, as originally noted by Clarke, Orlando's theorem [157] shows that Hopf bifurcations are related to the vanishing of the $N-1$ Hurwitz determinant; restating this conditions in Graphical terms using the methods developed here might uncover relationships between network structures and oscillations. Second, an original conjecture by Thomas, recently proved by Snoussi and Gouze [158], states that the presence of a negative cycle in the Reaction Graph is a necessary condition for stable periodic solutions. Thus, these results are a promising starting point to continue the study of the implications of the dynamical behaviour observed in experiments and the wiring of the regulatory networks of proteins underlying cell migration.
In the final section, the biological implications of imposing the P_0^+ form on the Reaction scheme are explained and related to the structure of the Reaction Graph.

6.3.2 $\mathbf{P_0^+}$-matrices and Reaction Graph structure

The biological implications of imposing that the Reaction scheme $\mathbf{J^R}$ has P_0^+ form are obtained examining the consequences on the structure of the associated Reaction graph $G_R[\mathbf{J^R}]$. The definition of a P_0-matrix, stated in def.6.35, requires that all the signed principal minors of $\mathbf{J^R}(\gamma_k)$ for $k = (1, ..., N)$ are non-negative. In addition, a P_0^+ matrix must have at least one positive signed minor of every order, although for our purposes this condition is limited to orders $k = (1, ..., N - p)$, where p is the number of conservation laws. The value of a principal minor determined by the sequence $\gamma_k = \{i_1, ..., i_k\}$ is given by the weight of the associated I-Subgraph I_{γ_k}, as defined in eq.6.30. Substitution of the Graph-based expression for $\det[\mathbf{J^R}(\gamma_k)]$ in the defining condition 6.35 of P_0-matrices leads to:

$$(-1)^k \det[\mathbf{J^R}(\gamma_k)] = (-1)^k w(I_{\gamma_k}) = (-1)^{2k} \sum_{\ell \subseteq I_{\gamma_k}} (-1)^{s(\ell)} w(\ell) = \sum_{\ell \subseteq I_{\gamma_k}} \prod_{c \subseteq \ell} (-w(c)) \geqslant 0$$

The inequality above applies to all possible sequences γ_k with $k = (1, ..., N)$. The interpretation in terms of the Graphical structure of the Reaction Graph is now straightforward. For every order k, a sequence $\gamma_k = \{i_1, ..., i_k\}$ determines

the I-subgraph that results from considering the $(i_1, ..., i_k)$ nodes of the Reaction Graph and all the interactions between nodes of this subset. Thus, in essence, for every γ_k considered, the network is being broken down to a subset of the proteins within it, and the analysis can be limited to the crosstalk interactions between these proteins. More precisely, the P_0 condition imposes the following restriction on the magnitude of the feedback structures of interaction between the proteins $(i_1, ..., i_k)$: the signed sum of the L-subgraphs contained in I_{γ_k} must be non-negative. The contribution of an L-subgraph containing $s(\ell)$ cycles is given by $[-w(c_1)] \times ... \times [-w(c_{s(\ell)})]$, the product of the weights of the $s(\ell)$ disjoint cycles in ℓ, plus a factor (-1) for each of the cycles. Thus, the P_0 condition can be simply restated in terms of the cycles in the Reaction Scheme as:

$$\sum_{\ell \subseteq I_{\gamma_k}} [-w(c_1)] \times ... \times [-w(c_{s(\ell)})] \geqslant 0 \qquad \forall\, \gamma_k \quad k = 1, ..., N \tag{6.36}$$

I-subgraphs of order $k = 1$ are formed by just one node of the Reaction Graph, and they include only one L-subgraph formed by the loop (cycle of order 1) around the node. Let the weight of the loop around node i be $w(l_i)$. The P_0 condition applied to I_{γ_1} with $\gamma_1 = \{i\}$ simply states $[-w(l_i)] \geqslant 0$; it follows that the weight of every loop in the Reaction Graph must be non-positive. The loops of the Reaction Graph are associated to the diagonal entries of the Kinetic Matrix, and correspond to the interactions of one proteins with itself, which include the decay terms and the autocatalytic terms of the kinetic rates.

For $k = 2$, the most general subgraph is composed by two nodes $\gamma_2 = \{i, j\}$ and the edges associated to crosstalk between them. Thus, this I-subgraph contains an L-subgraph formed by the two loops an another formed by the cycle of length 2 that comprises the interaction feedback between these two proteins:

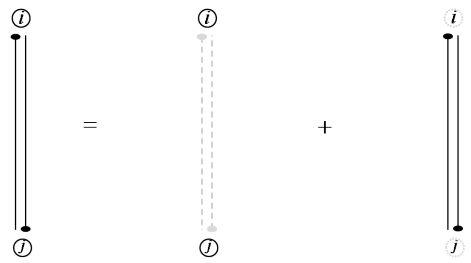

Figure 6.6: General I-subgraph of order 2

where the dots at the end of edges denote the unspecified sign of the interaction. The $\mathbf{P_0}$ condition applied to this I-subgraph leads to the following inequality:

$$\left[- \textcircled{\scriptsize i} \right] \times \left[- \textcircled{\scriptsize j} \right] + \left[- \overset{\bullet}{\underset{\bullet}{|}} \right] \geqslant 0 \tag{6.37}$$

Since the loops must be negative to fulfill the P_0-property in the corresponding I-subgraphs of order one, the minus signs can be inserted in the loops to clarify the meaning of this constraint:

$$\textcircled{+} \times \textcircled{+} \geqslant \overset{\bullet}{\underset{\bullet}{|}} \tag{6.38}$$

The implication for the 2-protein motif of fig.6.6 is that the magnitude of any positive feedback cycle in the network must be bounded by the decay terms. There are no constraints for negative cycles, although it must be noted that the P_0 property does allow to draw conclusions about oscillatory dynamics, for which negative cycles are known to be responsible.

In this way the analysis can be extended for larger subsets of the network. For instance, for $k = 3$ there is an important three-way interaction pattern, also known as the feed-forward motif[159], whose high statistical occurrence in real regulatory networks compared with a randomized networks indicates that it might constitute an important biological processing module [60]:

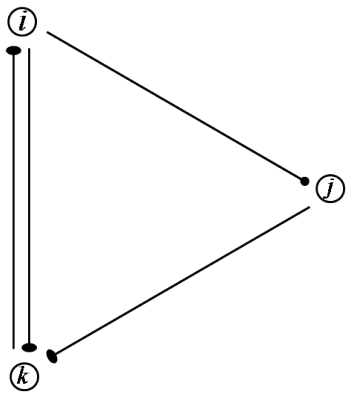

Figure 6.7: I-subgraph of order 3

This network motif has associated an I-subgraph that contains three L-subgraphs: the set of three loops, a cycle of order two with the disjoint loop, and the cycle of order three. The P_0 property leads to the following constraint on the feedback structures:

$$\left[-\textcircled{i}\right]\times\left[-\textcircled{j}\right]\times\left[-\textcircled{k}\right]+\left[-\textcircled{j}\right]\times\left[-\overset{\bullet}{|}\underset{\bullet}{|}\right]+\left[-\triangle\right]\geqslant 0 \tag{6.39}$$

This inequality has an structure identical to the stability condition stated in eq. 5.29 that was derived for the Jilkine-Keshet model in the previous chapter. This is no coincidence: if nodes i, j, k are made to represent *Cdc*42, *Rac*, and *Rho*, it can be seen that the I-subgraph of fig.6.7 has an identical structure to that of the Jiniger Regulation Scheme assumed for the RhoGTPase model. Hence, there is a one-to-one correspondence between the crosstalk terms in the stability condition stated in eq. 5.29 and the graph-based constraint. The i, j, k loops play the role of the kinetic rates of GAP hydrolysis f^{B}, g^{B} and h^{B} for *Cdc*42, *Rac*, and *Rho*, respectively. The 2-cycle corresponds to the term $f_\rho \cdot h_c$ that mediates the mutal inhibition crosstalk between *Cdc*42 and *Rho*, and the 3-cycle plays the role of the three-way negative feedback *Cdc*42 $\rightarrow$ *Rac* $\rightarrow$ *Rho* $\dashv$ *Cdc*42. Furthermore, rearranging the inequality 6.39, it also becomes trivial to identify the 2-cycle as the critical factor for the instability of the Jilkine-Keshet model:

$$\textcircled{+}\times\left[\textcircled{i}\times\textcircled{k}-\overset{\bullet}{|}\underset{\bullet}{|}\right]-\left[\triangle\right]\geqslant 0 \tag{6.40}$$

Since the 3-cycle is negative, it follows that the mutual inhibition cycle between *Cdc*42 and *Rho* is the source of Turing instabilities. Indeed, substitution of the parameter values given in [72] leads to $[f^{\mathrm{B}}\cdot h^{\mathrm{B}}]-[f_\rho\cdot h_c]=-1.4833$, confirming that the P_0-property is violated by the I-subgraph of order 2 associated to this term.

This shows the power of the Graph-based analysis, since the stability condition that was derived by *brute force* in the previous chapter can be readily obtained using this methodology. Moreover, the result stated in 6.39 applies to any network

containing this network motif, whereas the the stability condition derived laboriously in the previous chapter is only valid for that particular model. Finally, these results should also illustrate the power of this methodology to aid in the systematic formulation of regulation models that have the desired dynamical properties as pattern generators. This task is undertaken in the following Chapter.

For a joint scientific and geographical piece of organization, give me Scott; for a dash to the Pole and nothing else, Amundsen; and if I am in the devil of a hole and want to get out of it, give me Shackleton every time.

Apsley Cherry-Garrard, member of Scott's 1910-12 Antarctic Expedition

Chapter 7

A new class of RhoGTPase polarization models

A new class of RhoGTPase polarization models is postulated in this chapter. The new class is defined by a set of constraints derived from the previous results and experimental observations. The computational experiments of Chapter 5 are repeated adopting a particular Regulation scheme of this class, showing the improved polarization response of the new models. This model is then integrated with the Mechanical module developed in Chapter 3, without considering Focal Adhesions, and applied to simulate the migratory response of rapidly-moving cells of the type of keratocytes. Variations on the parameters and laws defining the relationship between force and RhoGTPase activation are tested to investigate the transition from amoeboid to mesenchymal modes of migration.

7.1 Theoretical framework: Reaction-Diffusion equations and waves

The idea that Turing's theory of pattern formation in biological systems [76] could be adapted to explain the emergence of cell polarity was first proposed by Meinhardt and Gierer [160]. In this seminal paper, they also suggested that the depletion of a substance could play the role of inhibitor in Turing's theory. More recently, Otsuji and coworkers [74] developed a model of RhoGTPase polarization based on these ideas. In this work, they identified Diffusion-driven instability and mass conservation as the essential elements common to their model and previous efforts to describe cell polarization. Thus, Turing instability was still a central ingredient of the model proposed to account for polarization. Later, Mori and coworkers [134] distilled a minimal model of an active-inactive RhoGTPase pair

and proved that Diffusion-driven instabilities were not necessary to account for polarization. In their conceptual model, the polarization mechanism is based on the existence of waves and the depletion of the protein that fuels the propagation of the wave. This mechanism, which they named *wave-pinning*, constitutes the basis upon which the new class of polarization mechanisms is built. A comprehensive review of alternative polarization models can be found here [1].

The starting building block are the pairs of Reaction-Diffusion equations developed in Chapter 2 to describe the concentration changes of a GTP-bound RhoGTPase and its inactive counterpart under the QSS approximation. The QSS approximation assumes that the flow of inactive RhoGTPases between the cell membrane and the cytosol is fast compared to the other kinetic transitions. Thus, for Cdc42, Rac and Rho there is a pair of equations of the type of sys.2.29 that describes their spatio-temporal dynamics in the cell. The goal is to formulate a model in this framework in which spatially heterogeneous external signals displace the system from an initial state of homogeneous concentration to a Polarized state with a high concentration of active Cdc42 and Rac at the cell front and of RhoA at the cell rear. The Reaction-Diffusion system that describes the RhoGTPases must have the following properties:

1. Conservation: the total amount of Cdc42, Rac and Rho is conserved.

2. Multistationarity: existence at least two or more equilibrium states in the Reaction system. These fixed points must be stable and correspond to the states of high and low RhoGTPase activation for a given concentration of inactive RhoGTPases.

3. P_0 -form of $\mathbf{J^R}(\mathbf{r_0})$: external perturbation of the initial RhoGTPase state $\mathbf{r_0}$ do not trigger the emergence of Turing patterns.

4. Reversible Polarization: a change in the source of the external signal is detected and leads to a realignment of the polarization axis.

Each of these properties has associated a constraint that must be fulfilled by the underlying Crosstalk Scheme. Property 1 is trivially fulfilled if the Reaction term of the active and inactive fraction of a RhoGTPase protein are equal and with opposite signs. Thus, the Reaction term has the following structure:

$$F = \mathbf{K}(\mathbf{r}) \cdot \mathbf{r} = \begin{bmatrix} f^{\mathrm{A}} \cdot c_{\mathrm{i}} - f^{\mathrm{B}} \cdot c_{\mathrm{a}} \\ -(\ldots) \\ g^{\mathrm{A}} \cdot r_{\mathrm{i}} - g^{\mathrm{B}} \cdot r_{\mathrm{a}} \\ -(\ldots) \\ h^{\mathrm{A}} \cdot \rho_{\mathrm{i}} - h^{\mathrm{B}} \cdot \rho_{\mathrm{a}} \\ -(\ldots) \end{bmatrix} \tag{7.1}$$

, where $\mathbf{r} = [c_a, c_i, r_a, r_i, \rho_a, \rho_i]$ denote the concentrations of active an inactive RhoGTPases [1] and the Kinetic rates k^{A} and k^{B} of activation and inactivation in the QSS approximation where defined in 2.32.

Property 2 requires that the ODE system 2.25 associated to the Reaction term, referred to as Kinetic system in Chapter 2, has two or more isolated steady states. This means that the Reaction term must have two or more different zeroes. As a consequence of Property 1, only half of the components of the Reaction term are independent, and the zeroes of $F(\mathbf{r})$ must be expressed as parametric functions of 3 of the concentration variables. Furthermore, the second property requires that these steady states correspond to different equilibrium values of the active fractions of RhoGTPases for a value of the inactive fractions. Therefore, $\mathbf{r}_i$ are taken as the fixed parameters and there must be at least two states $\mathbf{r}^- = \{\mathbf{r}_a^-; \mathbf{r}_i\}$ and $\mathbf{r}^+ = \{\mathbf{r}_a^+; \mathbf{r}_i\}$ that fulfill the following set of 3 algebraic equations:

$$F^a(\mathbf{r}_a^{\pm}; \mathbf{r}_i) = 0 \qquad \mathbf{r}_a^+ \neq \mathbf{r}_a^- \tag{7.2}$$

where F^a denotes the 3 components of the Reaction term associated to the active proteins. Let $\mathbf{J}_{\mathbf{a}}^{\mathbf{R}}(\mathbf{r}_a) = \partial F^a(\mathbf{r}_a; \mathbf{r}_i)/\partial \mathbf{r}_a$ denote the $3x3$ Jacobian of the reduced Reaction term. $\mathbf{J}_{\mathbf{a}}^{\mathbf{R}}(\mathbf{r}_a)$ is identical to the principal submatrix composed by the rows and columns associated to the active proteins in the complete Jacobian $\mathbf{J}^{\mathbf{R}}(\mathbf{r})$, as defined in eq.6.5 of the previous Chapter. In the general case, the reduced Jacobian, unlike the complete Jacobian, is non-singular, because in principle there are no additional symmetries in the Reaction network other than those associated to conservation laws. From condition 7.2, it follows that the Reaction term F^a can not be an injective function in the space of positive concentrations, since it has at least two isolated zeroes. This has important implications for the structure of the

[1] In Chapter 2, these variables were denoted as $c_{\mathrm{GTP}}, c_{\mathrm{GDP}}, \ldots, \rho_{\mathrm{GTP}}, \rho_{\mathrm{GTP}}$. The new definition is introduced just to ease the notation.

Crosstalk Scheme. A classic Theorem proved by Gale and Nikaido [161, see Theorem 4w, pag.89] shows that if the Jacobian of F^a is a non-singular P_0-matrix *for all* $\mathbf{r}_a$ in the space of positive concentrations[2], then F^a is injective in this space. Since F^a can not be injective by Property 2, it follows that $\mathbf{J_a^R}$ is not a P_0- matrix *for some* $\mathbf{r_a}$. Furthermore, under these conditions, a conjecture proposed by Thomas [162] and proved by Soule [144, Theorem 1, pag. 128] shows that this result implies that the Reaction Graph of $\mathbf{J_a^R}$ must contain a Positive Cycle *for some* state $\mathbf{r}_a$ in the space of positive concentrations.

Property 3 states that in the initial state $\mathbf{r_0}$, the Jacobian of the Reaction term must have P_0 form so that the system is not amenable to feature Turing Patterns. It must be stressed that this requirement is compatible with the previous condition. This property imposes P_0-form of $\mathbf{J_a^R}$ *at* the initial state $\mathbf{r_0}$, whereas Property 2 only demands that $\mathbf{J_a^R}$ is not P_0 *at* some other state $\mathbf{r_a}$ in the space of positive concentrations. Therefore, the combination of the constraints imposed by Properties 2-3 has important implications for the Reaction Graph: it must contain at least one Positive Cycle to account for multistationarity, and in turn this Cycle is subjected to the restrictions derived in Ch.6 to block the emergence of Turing patterns.

An important property of nonlinear parabolic systems is that they have traveling wave solutions, such as those describing combustion waves and propagation of electrical impulses in nerves [163, Chapter 9]. Imposition of Properties 1-2 on a Reaction-Diffusion equations of the type of 2.29 endows the system with traveling wave solutions that provide a mechanism that might account for polarization. The emergence of this type of solutions is explained following the treatment given in Grindrod's book [136, Chapter 1, sec. 1.5]. The wave-based polarization mechanism is compatible with Property 3 and suggests the additional features to be imposed on the Crosstalk Scheme to satisfy Property 4. The RD equations governing RhoGTPase dynamics were derived in the moving frame of the cell in terms of a generalized material derivative that included the volumetric deformation of the cell. The existence of traveling waves is illustrated in the simpler case of an immobile cell, but it carries over in general case. Consider the pair of reaction-diffusion equations describing the evolution of Cdc42:

$$\frac{\partial c_{\mathrm{a}}}{\partial t} = \frac{d}{\Phi^2}\nabla^2 c_{\mathrm{a}} + F_1(c_a, c_i) \tag{7.3a}$$

[2]Gale's theorem prescribes that these conditions must be fulfilled in a open rectangular set of $\mathbb{R}^n$. The Reaction term is defined for positive values of the proteins smaller than a certain bound imposed by mass conservation. Thus, the space in which F is defined is indeed an open rectangular set.

$$\frac{\partial c_{\mathrm{i}}}{\partial t} = \frac{D}{\Phi^2}\nabla^2 c_{\mathrm{i}} - F_1(c_a, c_i) \tag{7.3b}$$

The inactive fraction of the RhoGTPases diffuses very fast in the cytosol, so that their concentration becomes almost homogeneous rapidly compared to the timescales relevant to changes in the active fraction. Thus, the existence of waves solutions is shown taking c_i as a parameter in equation 7.3a. A traveling wave solution has the form $c_a(x,t) = w(z)$ where $z = x + v_c \cdot t$ and v_c is the wave speed to be determined later. Substitution of $\partial/\partial t = v_c \cdot d/dz$, $\partial/\partial x = d/dz$ and the test solution in 7.3a leads to the following ODE:

$$\frac{d}{\Phi^2}\frac{d^2w}{dz^2} - v_c \cdot \frac{dw}{dz} + F_1(w, c_i) = 0 \tag{7.4}$$

By Property 2, the reaction term F_1 has at least two zeroes $w = c_a^-$ and $w = c_a^+$ for a given value of c_i. The wave solution sought propagates throughout the cell replacing one state by the other. This solution represents an heteroclinic trajectory connecting the two equilibrium states on the phase space; if the solution is subjected to the conditions $w \to c_a^-$ as $z \to -\infty$ and $w \to c_a^+$ as $z \to +\infty$, the wave replaces the state c_a^- by c_a^+ as it advances over the cell. Note that it is possible to prescribe a solution that follows the opposite trajectory on the phase space by imposing $w \to c_a^+$ as $z \to -\infty$ and $w \to c_a^-$ as $z \to +\infty$; in this case the wave replaces c_a^+ by c_a^- as the wave sweeps the cell domain. This is an important property of the proposed mechanism, because the formulation of the complete RhoGTPase model relies on the existence of waves of Activation and Inactivation to generate reversible polar patterns. The wave velocity can be obtained multiplying eq.7.4 by dw/dz and integrating from $z = -\infty$ to $z = \infty$:

$$\begin{aligned} 0 &= \int_{-\infty}^{+\infty} dz \left(\frac{d}{\Phi^2}\frac{dw}{dz}\frac{d^2w}{dz^2}\right) - v_c \cdot \int_{-\infty}^{+\infty} dz \left(\frac{dw}{dz}\right)^2 + \int_{-\infty}^{+\infty} dz \frac{dw}{dz} F_1(w, c_i) \\ &= \frac{d}{2\Phi^2}\left(\frac{dw}{dz}\right)^2\Bigg|_{-\infty}^{+\infty} - v_c \cdot \int_{-\infty}^{+\infty} dz \left(\frac{dw}{dz}\right)^2 \pm \int_{c_a^-}^{c_a^+} dw\, F_1(w, c_i) \end{aligned} \tag{7.5}$$

where the ± sign in the second row results from the opposite limits of integration for Activating and Inactivating waves. The first term in 7.5 vanishes because the no-flux condition imposes that dw/dz is zero on the boundary. Hence, the wave velocity can the be expressed as:

$$v_c(c_i) = \pm \frac{\int_{c_a^-}^{c_a^+} dw\, F_1(w, c_i)}{\varphi} \tag{7.6}$$

where plus and minus signs correspond to Activating and Inactivating waves, respectively, and the denominator is the positive constant $\varphi = \int_{-\infty}^{+\infty} dz(dw/dz)^2$. The expression of $v_c(c_i)$ shows that the direction of propagation of a wave depends on the sign of the integral of the Reaction term, and that the wave speed is a function of the concentration of inactive proteins. The progress of a wave is stopped if the concentration of inactive protein, limited by the bounds imposed by conservation of the total amount of protein, reaches a critical value in which $v_c(c_i)$ vanishes. As the wave freezes, a fraction of the cell is left in the state c_a^+ of high activation and the other at state c_a^- of low activation. This process constitutes the nucleus of the polarization mechanism that Mori and coworkers [134] named wave-pinning and incorporated in their conceptual model adopting a cubic Reaction term, similar to those found in the Cable equation and the FitzHugh-Nagumo model of electrical pulse propagation in nerve cells [164, Chapter 7]. A cubic form of $F_1(c_a, c_i)$ is

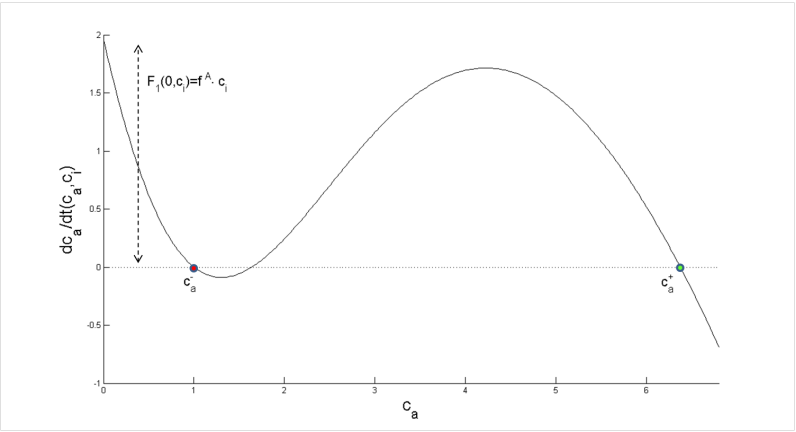

Figure 7.1: Phase plane with cubic Reaction term. High an low activation states correspond to stable zeroes of $F_1(c_a, c_i)$.

obtained assuming a constant rate of inactivation and a sigmoidal rate of activation

in $dc_a/dt = F_1(c_a, c_i) = f^A(c_a) \cdot c_i - f^B \cdot c_a$, which endows the system with two stable and one unstable steady states. Initially, the concentration of active and inactive protein is homogeneous over the cell, and the total concentration is given by $c_T \cdot L_{\text{cell}} = c_a \cdot L_{\text{cell}} + c_i \cdot L_{\text{cell}}$. An Activation wave emerges when an external signal displaces one of the edges of the cell from the state of low activation c_a^- to c_a^+ (marked with a red and a green dot in fig.7.1). As the Activation wave advances, switching an increasing area of the cell to the state of concentration c_a^+, the reservoir of inactive protein decreases because the total amount of protein is conserved. Due to the decrease in c_i, the rate $F_1(c_a, c_i)$ of conversion of inactive protein to the active state is reduced, and as a consequence the velocity of propagation of the activating wave diminishes. Eventually, the progress of this process depletes the

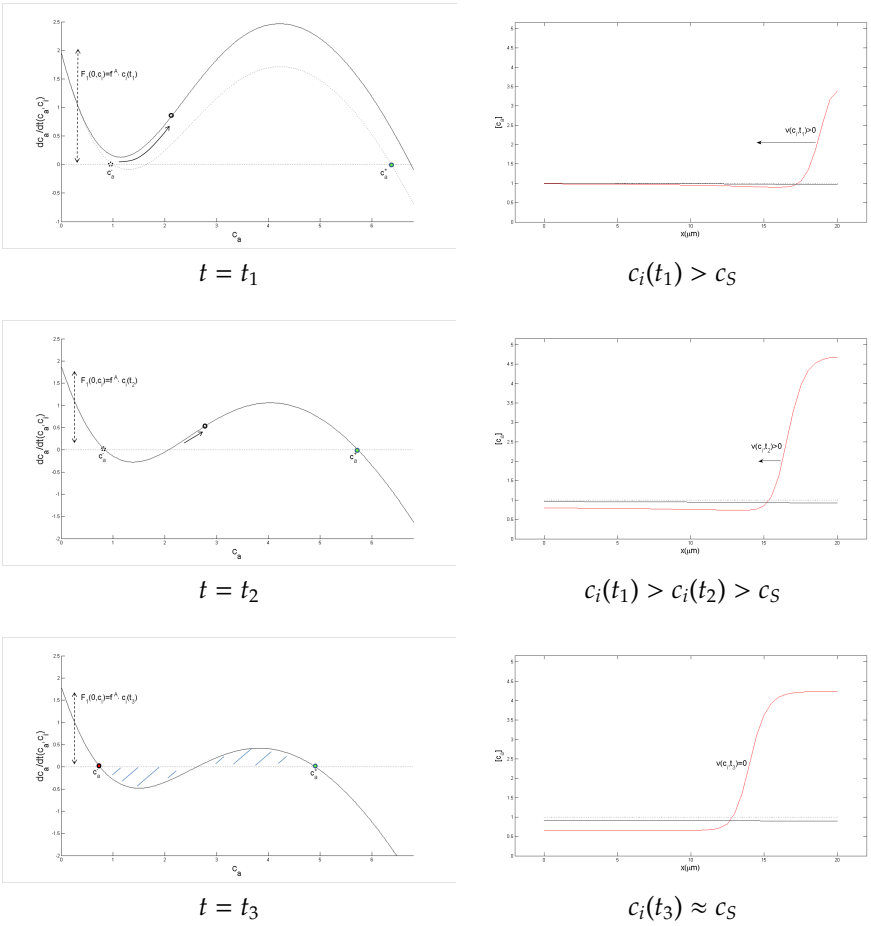

$t = t_1$ $c_i(t_1) > c_S$

$t = t_2$ $c_i(t_1) > c_i(t_2) > c_S$

$t = t_3$ $c_i(t_3) \approx c_S$

Figure 7.2: Right: Wave-pinning of an Activation wave. Left: Heteroclinic trajectory on the Phase Plane of Activated points

concentration of inactive protein to a value $c_i = c_i^S$ in which $v_c(c_i^S)$ vanishes and the activation wave stops. The condition for wave-pinning is that the integral of the Reaction term in eq.7.6 vanishes, which occurs when the positive and negative area between dc_a/dt and the abscissa are equal.
The existence of Inactivation waves is supported by the opposite process: the wave advances switching an growing fraction of the cell from c_a^+ to c_a^-, so that the concentration of inactive protein increases until reaches c_i^S and the wave stalls:

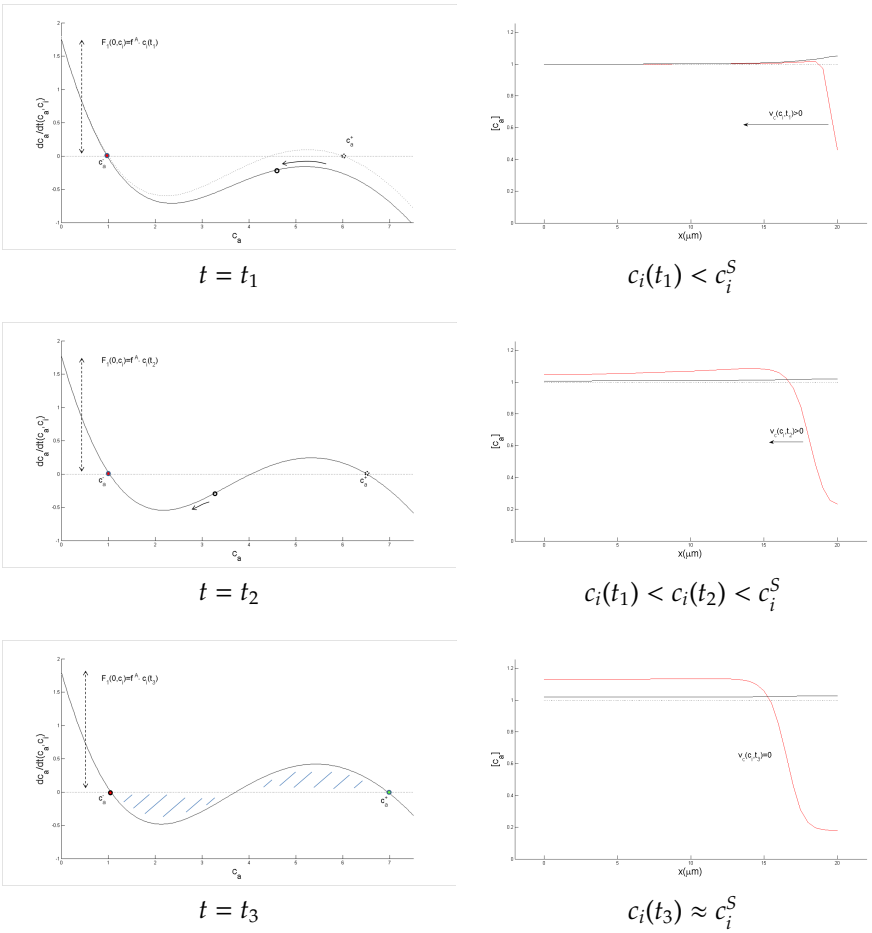

$t = t_1$ $c_i(t_1) < c_i^S$

$t = t_2$ $c_i(t_1) < c_i(t_2) < c_i^S$

$t = t_3$ $c_i(t_3) \approx c_i^S$

Figure 7.3: Right: Wave-pinning of an Inactivation wave. Left: Heteroclinic trajectory on the Phase Plane for inactivated points

Note that the Inactivation wave also affects the fraction of the cell that has not been driven to c_a^- by the wave; in this part of the cell the final concentration c_a^+ is higher than it was initially, because the concentration of c_i has increased.

Another important feature of the wave-based mechanism of polarization, not

shared by Turing-based mechanisms, is that the activated fraction of the cell is independent of the size of the cell. Let θ and $(1-\theta)$ be the fractions of the length of the cell L_{cell} having a high concentration and low concentration activated protein. The concentration of inactive protein at which the wave stalls is $c_i = c_i^S$, and the total concentration of protein is denoted by c_T. Assuming that the transition between the two cell areas is sharp, the conservation of protein imposes the following constraint:

$$c_T \cdot L_{cell} \approx c_i^S \cdot L_{cell} + c_a^+ \cdot \theta \cdot L_{cell} + c_a^- \cdot (1-\theta) \cdot L_{cell} \tag{7.7}$$

It follows that the fraction of the cell activated by the wave only depends on the total concentration of protein c_T, the concentration c_i^S at which the wave stalls, and the roots $c_a^+(c_i^S)$, $c_a^-(c_i^S)$ of the Reaction term.

$$\theta \approx \frac{c_T - c_i^S - c_a^-}{c_a^+ - c_a^-} \tag{7.8}$$

This feature is important because it shows that the wave-based mechanism of polarization can remain functional in cells of different types and shapes. The values of c_i^S and $c_a^\pm$ are determined by kinetic parameters of molecular origin in the Reaction term. Consequently, these parameters should be independent of the cell type, since the proteins and reactions involved are the same. The concentration c_i^S , in turn, depends on the total quantity of protein expressed and on the size of the cell. Under the plausible assumption that the total quantity expressed is proportional to the size of the cell or nucleus, the activated fraction θ would remain approximately equal in cells of different types. In addition, this result suggest a simple mechanism that cells could use to control their polarization state. Expression 7.7 shows that there is a minimum value of the total concentration $c_T = c_{\min} \mid \theta < 0$ bellow which polarization can not occur. Thus, modulating the expression of the protein, cells could allow or block the establishment of polarization in response to external stimuli.

7.2 A new class of RhoGTPase polarization models

The new class of RhoGTPase polarization models is formulated using pairs of Reaction-Diffusion equations of the type described in the previous section as the basic building blocks. The spatio-temporal evolution of the RhoGTPases will be determined by traveling wave fronts and wave-pinning, but the Reaction terms include an additional dependency on the concentration $\mathbf{r}(x,t)$ of the other RhoGTPases to incorporate Crosstalk:

$$\frac{\partial c_{\mathrm{a}}}{\partial t} = \frac{d}{\Phi^2}\nabla^2 c_{\mathrm{a}} \quad + \quad [f^A(c_a,\mathbf{r})\cdot c_i - f^B\cdot c_a] \tag{7.9a}$$

$$\frac{\partial c_i}{\partial t} = \frac{D}{\Phi^2}\nabla^2 c_{\mathrm{i}} \quad - \quad [f^A(c_a,\mathbf{r})\cdot c_i - f^B\cdot c_a] \tag{7.9b}$$

$$\frac{\partial r_{\mathrm{a}}}{\partial t} = \frac{d}{\Phi^2}\nabla^2 r_{\mathrm{a}} \quad + \quad [g^A(r_a,\mathbf{r})\cdot r_i - g^B\cdot r_a] \tag{7.9c}$$

$$\frac{\partial r_i}{\partial t} = \frac{D}{\Phi^2}\nabla^2 r_{\mathrm{i}} \quad - \quad [g^A(r_a,\mathbf{r})\cdot r_i - g^B\cdot r_a] \tag{7.9d}$$

$$\frac{\partial \rho_{\mathrm{a}}}{\partial t} = \frac{d}{\Phi^2}\nabla^2 \rho_{\mathrm{a}} \quad + \quad [h^A(\rho_a,\mathbf{r})\cdot \rho_i - h^B\cdot \rho_a] \tag{7.9e}$$

$$\frac{\partial \rho_i}{\partial t} = \frac{D}{\Phi^2}\nabla^2 \rho_{\mathrm{i}} \quad - \quad [h^A(\rho_a,\mathbf{r})\cdot \rho_i - h^B\cdot \rho_a] \tag{7.9f}$$

The Reaction terms have the same structure $F_{\mathrm{r}}(\mathrm{r}_a,\mathrm{r}_i,\mathbf{r}) = k^A(\mathrm{r}_a,\mathbf{r})\cdot \mathrm{r}_i - k^B\cdot \mathrm{r}_a$ for all the proteins. The kinetic rates of GAP hydrolysis, which determine the inactivation rate, are assumed to be constants $k^B = \delta_{\mathrm{r}}$. The kinetic rates of activation k^A are assumed to follow Michaelis-Menten dynamics with Hill coefficient $nH = 2$:

$$k^A(\mathrm{r}_a,\mathbf{r}) = [1 + \gamma_{\mathrm{r}}(\mathbf{r})\frac{\mathrm{r}_a^2}{\kappa_{\mathrm{r}}^2(\mathbf{r}) + \mathrm{r}_a^2}] \tag{7.10}$$

for $\{k^{\mathrm{A}},\mathrm{r}_a\} = \{f^{\mathrm{A}},\mathrm{c}_a\};\ \{g^{\mathrm{A}},r_a\};\ \{h^A,\rho_a\}$[3]. The key parameters in the activation are

[3] k^A and k^B are given in adimensional form. The dimensional form with units s^{-1} is recovered multipliying them by the reference rate k_o used in the definition 2.15 of the Thiele Modulus

the Michaelis-Menten constant κ_r, the Maximal velocity γ_r, and the Hill coefficient nH. These type of sigmoidal kinetic laws fit the experimentally observed dynamics of many reactions catalyzed by regulatory enzymes. Hence, the meaning of these parameters depends on the detailed reaction mechanisms underlying the biochemical reactions [165, Chap.6]. For the particular case of RhoGTPase activation, it is important to remember that the kinetic rates of activation are a compound $k^A = k^{GEF} \cdot k^I$ of the rates k^{GEF} of GDP-GTP exchange by GEFs and the rates of insertion of RhoGTPases in the plasma membrane $k^I = k^{GDF}/(k^{GDF} + k^{GDI})$, which are catalyzed by GDIs and possibly some still to be identified GDFs. Thus, assuming Hill-type kinetics for the activation rates of the RhoGTPases must be interpreted in terms of the mechanisms controlling the activity of these enzymes. Generally, a Hill coefficient $nH > 1$ results from cooperative interactions between proteins and enzymes: the binding of a protein to an enzyme alters the enzyme conformation and enhances the binding to subsequent proteins [165], suggesting that either GEFs, GDIs or GDFs could act as homotropic allosteric enzymes. However, the ultra-sensitivity associated to sigmoidal kinetics can arise from alternative mechanisms, such as the existence of zero order or intermediate biochemicals steps, the presence of additional enzymes participating in the biochemical reactions [166] or biological noise[167]. In the RhoGTPase case, particularly, the auto-catalytic loops could reflect the dependence of GDIs or GEFs activity on the local availability of active and inactive proteins. Independently of its biochemical root, sigmoidal kinetics endow the system with a positive loop for each protein in the Reaction Graph, in fulfillment of Property 2 necessary for the multistationarity of the network. The Reaction terms have the cubic form shown in fig.7.1, so that there is a range of concentrations of inactive proteins $r_i^m(\gamma_r, \delta_r, \kappa_r) < r_i < r_i^M(\gamma_r, \delta_r, \kappa_r)$ for which there are two concentration values of active proteins $r_a^-(c_i)$ and $r_a^+(r_i)$ that are stable equilibrium states. Following the beautiful treatment of the cubic found in [168], it can be shown that the existence of 3 roots requires $\gamma_r > \gamma_{3R} = 8$ and that the concentration of inactive protein is found within the bounds given by:

$$r_i^{M/m}(\kappa_r, \gamma_r, \delta_r) = \kappa_r \sqrt{r_{3R}^2(\gamma_r, \delta_r) \pm \Delta r_{3R}^2(\gamma_r, \delta_r)}$$

$$r_{3R}^2(\gamma_r, \delta_r) = \frac{\delta_r^2}{\gamma_r} \frac{(\gamma_+^{-1} - \gamma_r^{-1})(\gamma_r^{-1} - \gamma_-^{-1})}{(1+\gamma_r^{-1})^3} \qquad \Delta r_{3R}^2(\gamma_r, \delta_r) = \frac{\delta_r^2}{\gamma_r} \frac{\sqrt{2^3(\gamma_{3R}^{-1} - \gamma_r^{-1})^3}}{(1+\gamma_r^{-1})^3} \tag{7.11}$$

where the constants $\gamma_\pm^{-1} = (5 \pm 3\sqrt{3})/4$ have been introduced to simplify the expression. The dependency of the limits of $r_i \in (r_i^m, r_i^M)$ that permit the existence

of two activation states on kinetic parameters γ_r and δ_r is plotted in the following figure. The dependency of $r_i^{M/m}$ on κ_r is simply linear and is not represented.

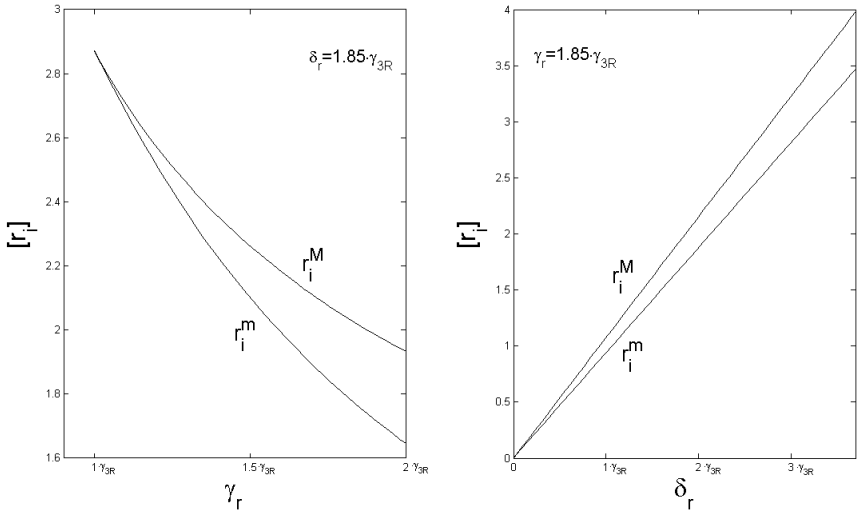

Figure 7.4: Inactive concentration bounds for multistationarity

This figure shows that for a given concentration of inactive protein r_i, a small modulation of the kinetic parameters can drive this protein outside the multistationarity regime. Thus, an increase in γ_r, or a decrease in κ_r or δ_r, forces a transition to the state of high activation of r_a^+ . Conversely, a reduction of γ_r, or an increment in κ_r or δ_r, renders the state of high activation unstable and triggers a transition to the state r_a^- of low activation.

The new class of models is based on the hypothesis that Crosstalk between RhoGTPases is executed by the controlled modulation of the Michaelis-Menten constant or the Maximal activation Velocity of the reactions that govern the activation of the proteins. Crosstalk signals emanate from activated RhoGTPases inserted in the Plasma membrane and regulate the kinetic parameters of other RhoGTPases localized in the same area. Thus, for a given concentration of the inactive form of a RhoGTPase r_i, approximately homogeneous in the cell, localized signaling activity from another RhoGTPase x_a can induce a local change of $\gamma_r(x_a)$ or $\kappa_r(x_a)$ that switches the activation level of r_a in this area of the cell. Since the diffusiveness of the activated proteins embedded in the Plasma Membrane is very small, the switch in the activation level is local, but the emergence of waves of activation or inactivation propagates the transition according to the mechanism described in the previous section.

The strength of the Crosstalk signals sent by a RhoGTPase x_a are assumed to

be a sigmoidal function of the increment from the activation level relative to the initial equilibrium state x_a^0:

$$s(x_a) = \begin{cases} 0 & x_a < x_a^0 \\ \frac{(x_a - x_a^0)^2}{s_0^2 + (x_a - x_a^0)^2} & x_a \geqslant x_a^0 \end{cases} \tag{7.12}$$

where s_0 is a constant that controls the concentration threshold at which Crosstalk signals are emitted. The kinetic parameters of the target RhoGTPase are assumed to have a simple linear dependency on the strength of the Crosstalk signals:

$$\gamma_r(x_a) = \gamma_0 \cdot [1 + \phi \cdot s(x_a)] \tag{7.13a}$$

$$\kappa_r(x_a) = \kappa_0 \cdot [1 - \eta \cdot s(x_a)] \tag{7.13b}$$

where $\left|\phi\right| < 1$ and $\left|\eta\right| < 1$ are small constants that control the maximum magnitude of the modulation exerted by x_a. The sign of these constants determines if Crosstalk carries inhibitory or activating signals from the effector RhoGTPase to the target RhoGTPase. If $\phi > 0$, the signals increase the Maximal activation Velocity and enhance activation, whereas $\phi < 0$ is associated to inhibition. Likewise, $\eta > 0$ leads to a Crosstalk-mediated decrease in the Michaelis-Menten constant and activation, whereas $\eta < 0$ promotes inhibition.

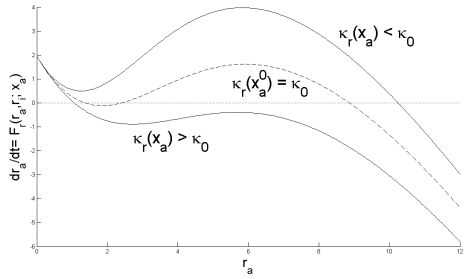

(a) Modulation of κ_r by x_a for $\eta > 0$ (upper curve) and for $\eta < 0$ (lower curve)

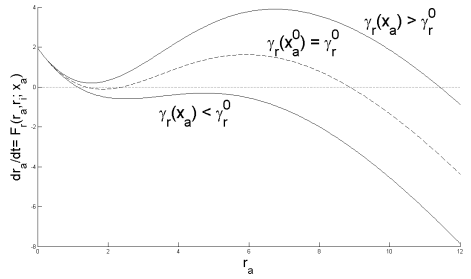

(b) Modulation of γ_r by x_a for $\phi > 0$ (upper curve) and for $\phi < 0$ (lower curve)

Figure 7.5: Variation of the Activation rate due to Crosstalk

There are several biochemical processes that could support the proposed mech-

anism of Crosstalk between RhoGTPases. Generally, the Michaelis-Menten constant κ reflects the affinity of an enzyme for its substrate, and the Maximal activation Velocity γ is a function of the total enzyme concentration and the limiting reaction rate in the biochemical steps underlying the reaction. Usually, modulation of the Michaelis-Menten constant of a biochemical reaction arises from competitive inhibition between the molecules involved, associated to two proteins competing to bind the same enzymes as catalyst of their reactions. Modification of the Maximal activation Velocity γ is associated to non-competitive regulation, stemming from the modification by other molecules of the activity of the enzymes that catalyze the biochemical process [169, Chapter 5].

For the reactions involving RhoGTPases, an increase in the Michaelis constant $\kappa_{\mathrm{r}}(x_a)$ could indicate the existence of competitive inhibition between the two proteins, meaning that RhoGTPases x and r compete for binding the same GEFs, GDIs or GDFs enzymes. Recent experimental data reviewed in section 7.2.2 and in [6] supports the existence of such a crosstalk mechanism via competition to bind GDIs. Conversely, positive Crosstalk associated to a decrease of $\kappa_{\mathrm{r}}(x_a)$ could be mediated by signals from RhoGTPase x that enhanced the affinity of the enzymes for r, particularly GEFs and GAPs, boosting its activation levels. Modulation of the Maximal velocity $\gamma_{\mathrm{r}}(x_a)$ is usually related to uncompetitive regulation of a protein-enzyme reaction. This occurs when a third regulatory molecule binds the enzyme-protein complex at a site different from where the enzyme-protein form a bond, altering the rate of reaction. This mechanism of Crosstalk has been observed experimentally in the stimulation of the activity of GEFs or GAPS specific for a RhoGTPase by other RhoGTPases [6]. The experimental data indicates that this is one of the main mechanisms that mediate activation and inhibition between RhoGTPases. From a mathematical standpoint, introduction of crosstalk via modulation of γ or κ is nearly equivalent, and the choice must be guided by experimental evidence.

An important consequence of the postulated mechanism of Crosstalk is that any Reaction scheme defined within this Class fulfills Property 3 stated in the previous section, which ensures that no Turing patterns emerge from external perturbations. The functional form of the Crosstalk signal strength $s(x_a)$ has the implicit assumption that interaction between RhoGTPases is only switched on far from the initial equilibrium state.

$$\left.\frac{\partial s(x_a)}{\partial x_a}\right|_{x_a^0} = 0 \tag{7.14}$$

Consequently, since Crosstalk signals at the initial equilibrium state are turned off, the change in the kinetic rates associated to Crosstalk is null:

$$k_{\mathrm{x}} = \left.\frac{\partial F_{\mathrm{r}}(\mathrm{r}_a, \mathrm{r}_i, x_a)}{\partial x_a}\right|_{\mathbf{r^0}} = \frac{\partial s(x_a)}{\partial x_a}\frac{\partial}{\partial s}\left.\left(k^A[\mathrm{r}_a, s(x_a)] \cdot \mathrm{r}_i - k^B \cdot \mathrm{r}_a\right)\right|_{\mathbf{r^0}} = 0 \tag{7.15}$$

For this reason, in the initial equilibrium state $\mathbf{r^0}$, the Cycles of length greater than one in the Reaction Graph have a vanishing weight. Indeed, the Reaction Scheme can contain any number of feedback Cycles, such as the terms $f_\rho \cdot g_c \cdot h_r$ or $f_\rho \cdot h_c$ of the Reaction scheme discussed in the previous Chapter. As long as the strength of Crosstalk signals has a quadratic (or superior) decay near the equilibrium state, interaction through feedback Cycles is weak and does not endanger the P_0-property of the Reaction scheme in the initial state. The only potentially problematic Cycles are the autocatalytic loops $k_{\mathrm{r}} = \partial F_{\mathrm{r}}(\mathrm{r}_a, \mathrm{r}_i, x_a)/\partial \mathrm{r}_a$, which correspond to the diagonal entries in $\mathbf{J^R}(\mathbf{r_0})$. However, in both possible initial states $\mathbf{r^0} = (\mathrm{r}_a^-, \mathrm{r}_i)$ and $\mathbf{r^0} = (\mathrm{r}_a^+, \mathrm{r}_i)$, since they are stable steady states, these loops are necessarily negative for all the proteins. It follows that $\mathbf{J^R}(\mathbf{r^0})$ is a P_0-matrix and that no Turing instability can occur, independently of the number or sign of the crosstalk interactions postulated in a particular model within this Class.

This concludes the definition and interpretation of the new Class of RhoGTPase polarization models. Alternative schemes within this Class result from different assumptions on which protein crosstalks with which other protein, and the detailed mechanism that mediates the interaction. The keys to interpret these assumptions in terms of the underlying biochemical mechanisms have been introduced and can be used to analyze the predictions in the context of the available experimental data. The next section shows the improved polarization response of one particular scheme of this class to external signals.

7.2.1 Polarization response to external stimuli

A RhoGTPase Crosstalk scheme of the Class defined previously is presented to illustrate its improved polarization response. The computational experiments performed in Chapter 5 are repeated and reveal that the polarization mechanism is robust and remains functional independently of the morphological features of the cell or the profile of the external signal.

The external signal is defined as in Chapter 5 by a function $\Psi(x, t)$ that represents the spatial concentration of a chemo-attractant or some other generic cue

registered by the sensing machinery of the cell. The signal is registered by a first layer of receptors embedded in the membrane that recruit and turn on GEF enzymes that directly activate a specific RhoGTPase. This protein will be referred as the *sensor* RhoGTPase, it acts as the link between the primary layer of receptors in the membrane and the rest of the RhoGTPase network and its enzymes. The intermediate biochemical steps in Chemotaxis are believed to involve lipid receptors known as phosphoinositides (PIs), their kinases (PI3k and PI5k) and phosphatases (PTEN) [170, 171], although the identity of the *sensor(s)* protein(s) and the complex feedback loops between RhoGTPases, PI3k and PTEN, and PIs are far from being understood and their role in the polarization process remains highly controversial[172, 173]. In the case of Mechanotaxis, the process of mechanosensing necessarily involves Integrin receptors, but the nature of the transduction process from mechanical cues to the RhoGTPases is even less clear. For this reasons, the detailed transduction process is not modeled explicitly; instead, the underlying biochemical steps are lumped into a final signal received by the *sensor* RhoGTPase following a rationale analogous to that used to derive the functional form of Crosstalk in the previous section. Thus, the strength of the modulation from the primary layer of receptors to the *sensor* RhoGTPase is assumed to be a sigmoidal function of the actual concentration of the external cue

$$s_\Psi(x,t) = \frac{\Psi(x,t)^2}{\Psi_0^2 + \Psi(x,t)^2} \tag{7.16}$$

where Ψ_0^2 sets the concentration of stimulus at which the signal strength from the receptors to the RhoGTPases is half of its possible maximum value. The Michaelis-Menten constant of the *sensor* RhoGTPase is modified by this signal according to:

$$\kappa_r(\Psi) = \kappa_0 \cdot [1 - \eta \cdot s_\Psi(x,t)] \tag{7.17}$$

where $\eta > 0$ represents activation. Generally, Cdc42 has been accepted to be the master regulator of polarity and that Cdc42-specific GEFs interact with PIP3 to initiate polarization[55]. However, recent experimental evidence [174, 175], also suggest that it is in fact Rac-specific GEFs that are upregulated by PIs. For this reason, there are as many theoretical models that assume that Cdc42 is the protein *sensor*, such as the Jilkine-Keshet model[72] or examples found here[176, 177] as

models proposing Rac [178, 179]. The reality is more likely a complex combination of the two hypothesis, but for the purpose of illustrating the polarization response of the new Class models, it will be assumed that the *sensor* is Cdc42. The consensus on the nature of the Crosstalk interactions between RhoGTPases and the specific wiring of the network is hardly any stronger. Therefore, the Reaction scheme is formulated adopting the minimal complexity to support polarization as the guiding principle. In addition, this choice will show that it is possible to formulate a model that can reproduce polarization without mutual inhibition feedback, proving that one of the guiding principles of the Jilkine-Keshet model discussed earlier is not accurate. A minimal Reaction scheme assuming Cdc42 as the sensor RhoGTPase has associated the following reduced Reaction graph $G_R[\mathbf{J_a^R}]$[4]:

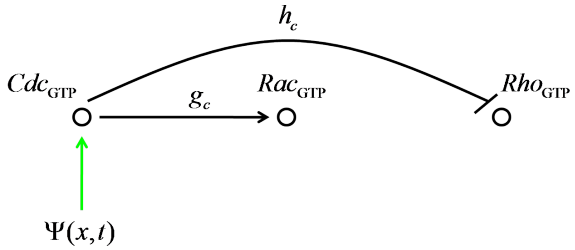

Figure 7.6: Reaction Graph of the minimal Reaction scheme that supports polarization

The non-dimensional values of the kinetic parameters defining a Reaction scheme based on the Reaction Graph of fig.7.6 are set according to theoretical requirements: the sign of the coupling constants ϕ and η that determine the modulation of the kinetic parameters by crosstalk interactions are determined by the Reaction Graph, and the Maximal velocities of autocatalysis γ_{r} must induce at least an 8-fold increase of the activation rate so that the multistationarity condition $\gamma_{\mathrm{r}} > \gamma_{3R}$ is fulfilled. The following table summarizes the values for a particular model of the new class, which will be referred as Model A:

Table 7.1: Model A: Non-dimensional kinetic parameters

Model A	γ_0	ϕ	κ_0	η	δ
*Cdc*42	12	–	1	0.5	10
Rac	10	–	1	0.5	10
RhoA	10	−0.5	1	–	10

[4]The complete Reaction Graph is $G_R[\mathbf{J^R}]$, but $G_R[\mathbf{J_a^R}]$ fully determines the Reaction scheme and is the relevant subgraph for the P_0 structure of the scheme

Aside from the theoretical constraints, the model is remarkably robust to changes in the rest of the parameters, and the choice of their values is guided by experimental facts and mathematical simplicity. Thus, the kinetic rates of GAP hydrolysis δ_r are assumed to be of the same magnitude than the rates of GTP exchange by GEFs, and the coupling constants are set to 0.5 to limit the maximum modulation of γ_r and κ_r induced by crosstalk to a 50% change of their intrinsic value. Interestingly, the theoretical constraint of $\gamma > 8$ is consistent with reported values of a 10-fold increase in the reaction rates induced by these enzymes [180, 181]. The dimensional forms of δ and γ_0 in units of $[s]^{-1}$ are recovered multiplying them by the reference reaction rate k_0 of the RhoGTPases, , which sets the time scale of the RhoGTPase reactions and is assumed to be equal for the three proteins. The initial concentrations of *Cdc*42 and *Rac* are set to homogeneous values of the equilibrium state $\mathbf{r^0} = (r_a^-(r_i), r_i)$ with $r_i^S < r_i < r_i^M$. In this way, the initial concentration of inactive protein is smaller than the value that permits the existence of two stable states but bigger than the value at which waves stall, allowing the emergence of Activation waves. Conversely, the initial concentration of *RhoA* is set to the equilibrium value $\mathbf{r^0} = (r_a^+(r_i), r_i)$ with $r_i^S > r_i > r_i^m$, so that the protein is in the multistationarity regime and Inactivation waves can emerge.

Protein concentrations are left in adimensional form using the Michealis-Menten of each RhoGTPase as the scaling unit of concentration, but measurements of RhoGTPase concentration in living cells could be used to recover units of $[\mu M]$ amenable to be compared with experimental values. The reference reaction rate is set to $k_0 = 0.1\, s^{-1}$ for Model A. The experimental and theoretical reasons to adopt this and other values of the kinetic parameters will be discussed after the polarization response of Model A is demonstrated. To that end, two consecutive linear stimulus of the type described in Chapter 5 are prescribed to study the polarization response of this model. Both stimulus gradients have the same spatial profile and magnitude, set to reach a value $\Psi_{max} = 10 \cdot \Psi_0$ and are hold for a period of 30 seconds:

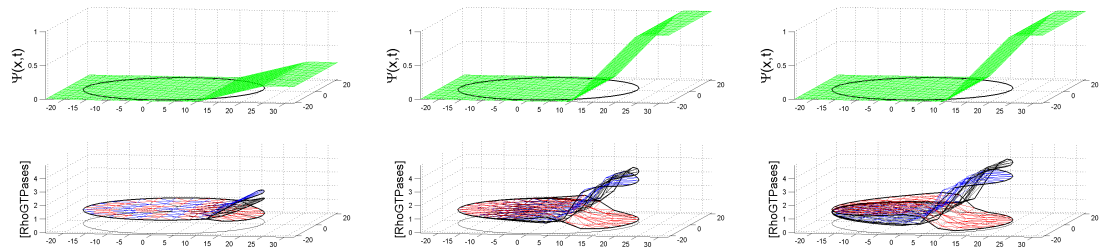

t=12.46s. t=20.17s. t=40.36s.

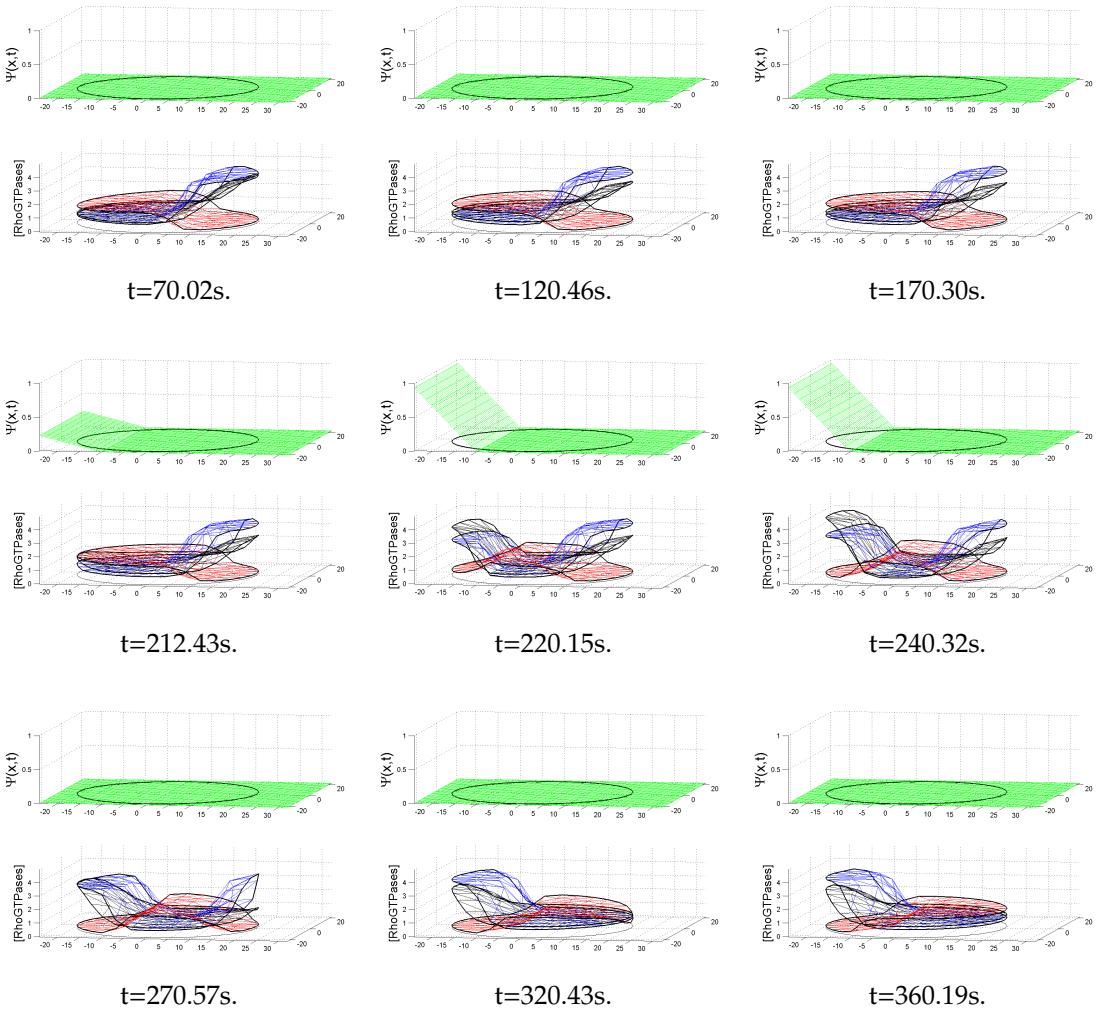

Figure 7.7: ⊗ Polarization switch after exposure to reversal of stimulus

The simulation illustrates the key features of the polarization response of the new model. After the first stimulus is applied, *Cdc*42 is upregulated at the area of the cell with bigger exposure to the gradient, eventually reaching a 4-fold increase in the activation level. Concomitant *Cdc*42 crosstalk signalling induces a similar increase in *Rac* activation in this area and a decrease in *RhoA* to a 10% of its initial activation level. Wave propagation drives the distribution of *Cdc*42 and *Rac* activation toward the cell interior until they are self-arrested by the depletion of inactive protein. *Rho* undergoes the opposite process, as the Inactivation wave advances inwards, the amount of inactive proteins is increased and supports a

2-fold increase in the activation level at the opposite side of the cell. It also should be noted that polarization is *persistent*, meaning that the asymetric protein distribution remains after the stimulus is removed, as the snapshots correspondint to $t \in [70, 170]$ sec. and $t \in [270 - 360]$ sec. attest.

A salient property of the model is that the polarization response amplifies shallow gradients and is reversible: after the secondary stimulus is applied, the opposite process takes place and the polarization axis is inverted. The improvement in the sensitivity is substantial and emerges naturally from the assumptions on how the external signal is transduced to the RhoGTPAses (amplification) and the reversibility of the trajectories corresponding to wave-solutions in the phase plane (reversibility). In fact, polarization reversibility does not depend on the magnitude or spatial profile of the stimulus $\Psi(x, t)$: the key variable that determines the switch is the span of time during which the cell is exposed to an stimulus. The secondary stimulus initiates a new polarization event independently of the magnitude of the stimulus, but the completion of the realignment process requires that the stimulus is hold during a minimum period of time that allows the switch in the polarization axis to conclude. The parameter that sets the characteristic time scale of the kinetic reactions is the reference reaction rate k_0. For Model A, the adopted value is $k_0 = 0.1s^{-1}$, which sets the minimum time of exposure to a secondary stimulus required to complete the inversion of the polarization axis in approximately 20 seconds. If k_0 is increased, the dynamics of the kinetic reactions are speeded and the time threshold is lowered, and if k_0 is decreased the polarization process is slowed down and reversibility requires longer exposure times. The value of k_0 adopted in Model A is twice the value used in Mori's model [134] for the intrinsic rate of activation. As mentioned earlier, this choice only affects the characteristic times of polarization and is not an essential feature of the model. Due to the great discrepancies in reported values of the GEF and GAP baseline kinetic rates[180, 182, 181, 183], the choice is made to speed up the sensibility of the cell to short-lived stimulus[5]. A more interesting aspect of this issue is that experimental values of kinetic rates are obtained from biochemical essays in test tubes, which differ greatly from the effective kinetic rates governing the same reactions inside living cells. Reactions in the interior of a living cell take place in an environment densely filled with macromolecules and architectural barriers, which result in alterations of the nominal kinetic rates due to the under-appreciated phenomena of molecular crowding, molecular confinement and adsorption[184]. Theoretical predictions and experimental measurements estimate the an alteration of the kinetic rates in more than one order of magnitude[185].

The next set of computational experiments were designed to demonstrate the

[5] Alas, this also reduces the simulation time required to reproduce the polarization event!

robustness of the polarization response and to confirm that the defining properties of the New Class of Reaction schemes blocks the emergence of Turing patterns. To this end, the size of the cell was increased up to $80\mu m$ in radius and no occurrence of Diffusion-Driven instabilities was found. In addition, these results show that the size of the high activity zones scales with the size of the cell, as explained in the exposition of the theoretical foundations of the model.

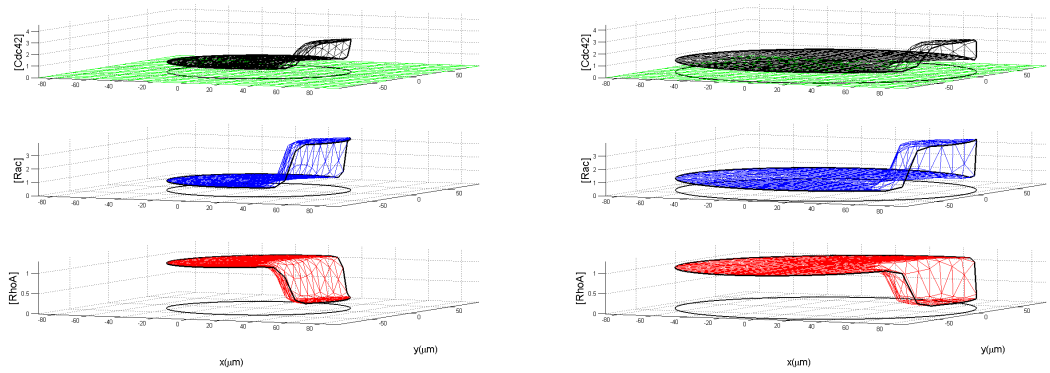

(a) $R_{cell} = 50\mu m$ (b) $R_{cell} = 80\mu m$

Figure 7.8: $^{\otimes}$ Robust Polarization in cells of increasing size

This is a desirable property in a model of cell polarization if it has to remain functional in cells of various type. Related to this issue is the question of the robustness of the polarization response in front of changes of cellular morphology. To illustrate that this is indeed the case, the following simulation of the polarization process uses a fibroblast-like geometry, showing that the functionality of the polarization mechanism remains intact, even in the extreme case of a non-convex geometry featuring thin protrusions resembling filopodia:

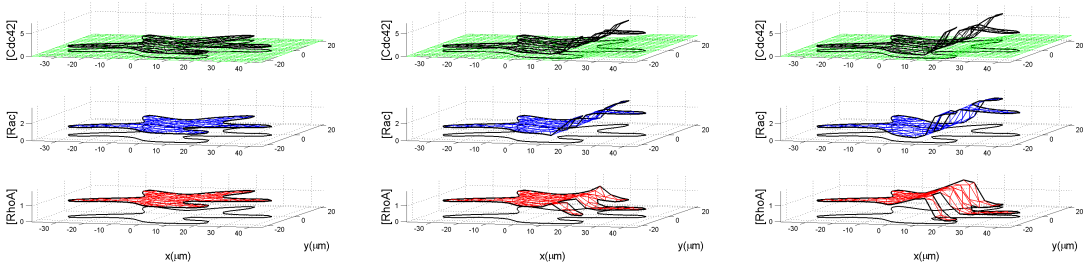

t=10.46s. t=23.17s. t=30.36s.

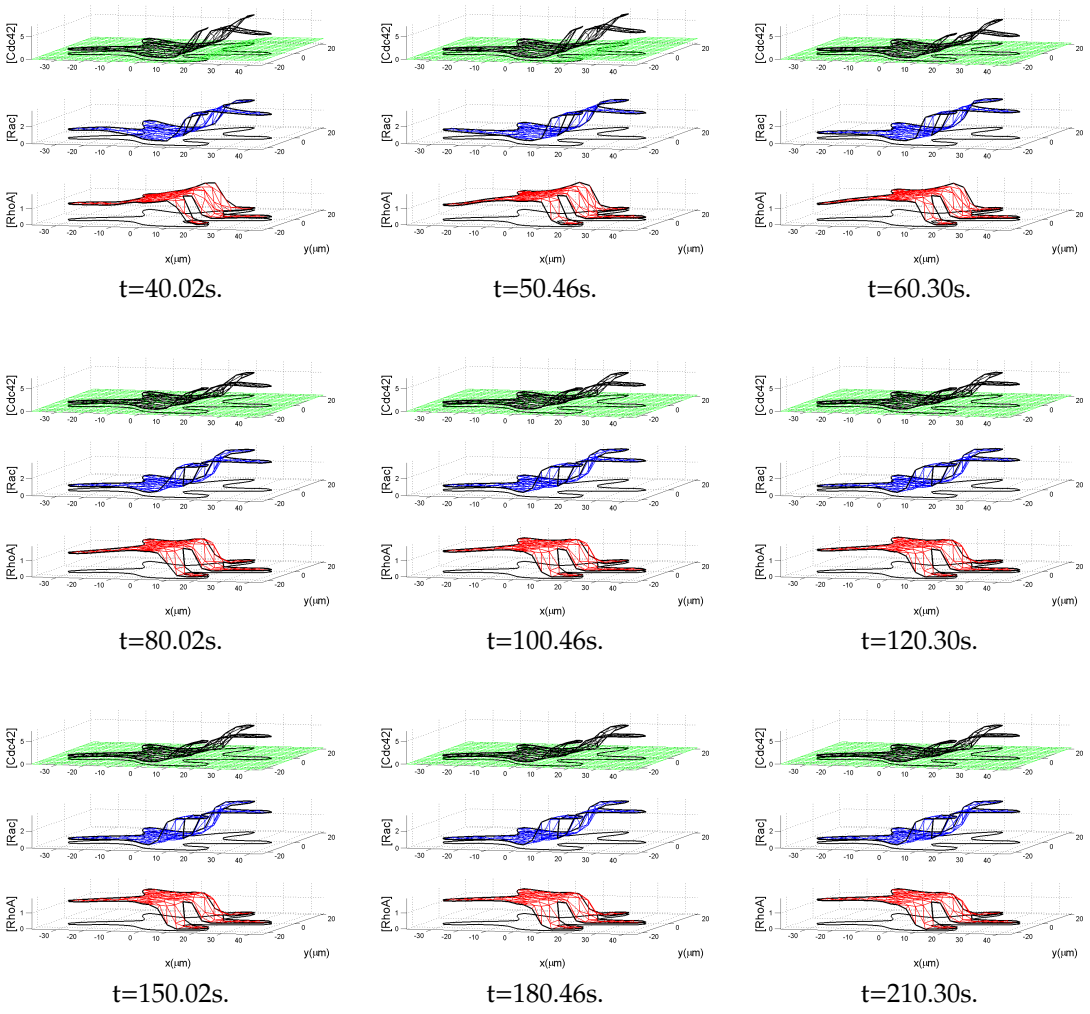

Figure 7.9: ⊗ Polarization reponse in a Fribroblast-like cell geometry

Another important feature is the remarkable robustness of the model against parameter changes. The final polarization pattern is independent of the specific form of the stimulus $\Psi(x,t)$, whereas variations of the kinetic parameters affect primarily the extent of the activation zones and the magnitude of the increase in activation. For instance, increasing the value of γ_0 for *RhoA* enhances the level of activation of this protein. Furthermore, Crosstalk interaction between RhoGTPases can be included either through modulation of the Maximal reaction velocity or the Michaelis-Menten constant without substantial changes in the polarization response. The qualitative features of the polarization response are also preserved against changes in the Reaction Graph. The following Graph is an alternative

Crosstalk scheme to Model A that presents a similar behavior:

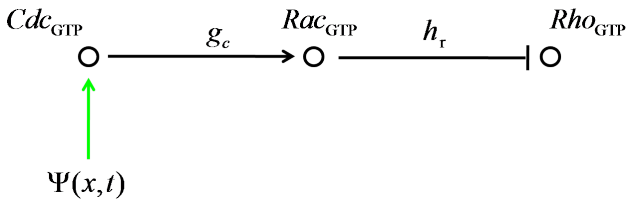

Figure 7.10: Alternative Reaction Graph

Interestingly, this is a Reaction Scheme derived from experimental observations that was discarded in the paper by Jilkine and coworkers [72] on the basis that it could not support polarization. It follows that reformulating other schemes proposed in the experimental literature and discarded on these grounds within the theoretical framework derived here could made them suitable candidates to describe RhoGTPase crosstalk. Another important property of the New class of Schemes is the scope of cellular behaviors that can be reproduced. The simulation depicted in fig. 7.7 shows that the polarized state emerging from the application of an heterogeneous stimulus is maintained after the stimulus is removed; this is a property of a polarization model named *maintenance*, according to the classification found in a recent comprehensive review on mathematical models of polarization [1][6]. A variation of the Maximal Velocity of the *sensor* protein *Cdc*42 results in a qualitative change in the polarization response that has interesting implications related to this property: reducing its value from $\gamma_0 = 12$ to $\gamma_0 = 10$, the polarization state is *transient* and the cell returns to the initial state after the stimulus disappears:

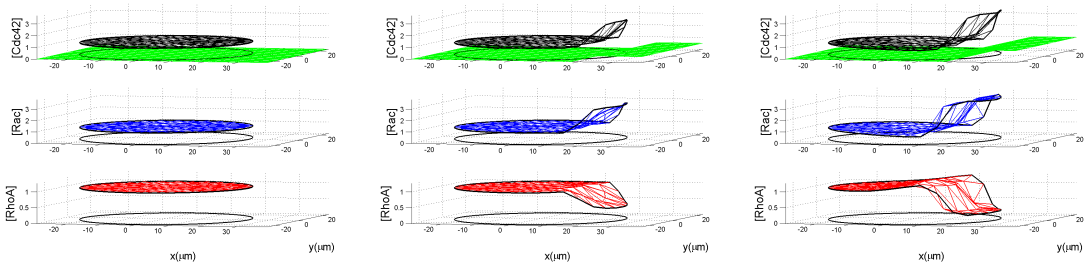

t=9.00s. t=15.03s. t=39.01s.

[6]The property of reproducing a transient polarization to a uniform stimulus is named *adaptation* by the authors of this review. This behavior is also reproduced by all schemes in the New class of polarization models

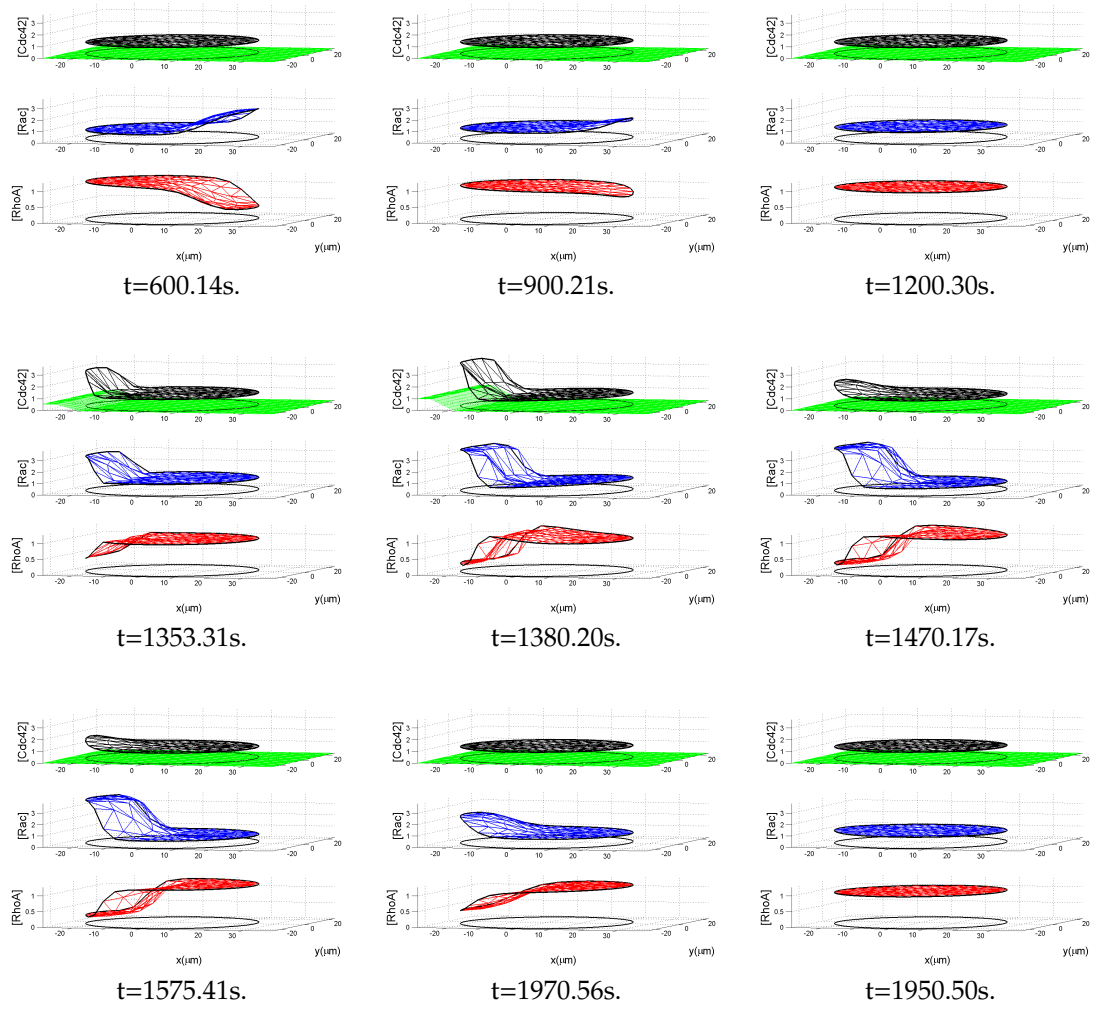

Figure 7.11: $^{\otimes}$ Transient Polarization switch

The change in the polarization response from Permanent to Transient is produced by the reduction of the Maximal Velocity γ of the sensor protein to a value close to the γ_{3R}, the minimum value that allows the existence of multiple equilibrium states. Thus, a continuum variation of one of the parameters allows to reproduce two distinct modes of polarization and migration, used by different types of cells or suited for different physiological conditions. Furthermore, the model reproduces another feature of polarization defined in [1] as *adaptation*, which consists in the generation of persistent polarization response to gradients of stimulus, but a transient response to uniform stimulus. Indeed, the simulations

show that after a uniform stimulus is applied and removed, the cell returns to its initial homogeneous state (not shown). This illustrates the flexibility of the new Class of models: as it is remarked in the previously cited review [1], there is an abundance of theoretical models to describe cell polarization and they are generally appropriate to describe the migration behavior of only one particular cell type. The important point is that in actuality, the existence of different migration phenotypes and strategies in biological cell is most likely the result of an adaptable modular apparatus that is shared by cells from different types. By tuning the activity of the molecular regulators that control and couple the different modules, cells are able to adopt a particular motility mode [58]. A particularly striking example is the transition from mesenchymal to amoeboid migration modes, which can be induced by externally modifying the relative strength of *RhoA* and *Rac* signaling[20, 186]. These two types of motility modes differ primarily in the size and strength of the adhesions and forces developed by cells to move on a substrate; crucially, the switch between mesenchymal an amoeboid modes of migrations is an important strategy used by malignant cells for dissemination during the metastasis stage of cancer [187]. This example illustrates the importance of an aspect of cell migration that has not been addressed by other theoretical models and that might have important clinical implications. The New class of polarization models proposed in this Thesis represents a promising step in the direction of understanding the plasticity of the migration process. Indeed, the mechanisms governing the mesenchymal to amoeboid transition (MAT) and the ensuing unrestricted migratory behavior of malignant cells have been related to the unregulation of signaling pathways associated to RhoGTPase, but identification of the underlying molecular processes is still at its infancy[66]. It is thus tempting to draw a connection between the observed plasticity of the cell migration process and the prediction that a variation in a molecular parameter that determines kinetic rate of activation results in a qualitative change in the polarization response from transient to persistent characteristic of amoeboid migration. Furthermore, the theoretical model suggests that specific mechanism underlying this process is related to an alteration of the activity of GEFs or GDIs enzymes, a prediction that could be explored experimentally.

7.2.2 Experimental evidence on RhoGTPase regulation and the New Class of models

A survey of some of the most recent and conclusive experimental observations suggesting that our understanding of the RhoGTPase cycle is incomplete is given in this section. These experimental evidence, in fact, provides compelling support for the hypothesis underlying the formulation of the new Class of RhoGTPase reg-

ulation models, which was been developed on theoretical grounds. RhoGTPase regulation of the Actin cytoskeleton was discovered in the early nineties by Ridley and coworkers [188]; since then, biochemical studies have revealed the role played by GEFs, GAPs and GDIs in their activation cycle, and a great number of their downstream targets and their functions have been identified. These studies have shown the central part played by RhoGTPases in fundamental processes common to all eukaryotic cells, such as division, adhesion and migration. This data has been integrated in a standard model of RhoGTPases regulation, in which modulation of GEF activity by GTP-bound RhoGTPases is the central channel of crosstalk[189], as described in the first section of Chapter2.

However, a growing body of experimental evidence points to a more complex scenario, in which GAP and GDI activity are also actively regulated during the RhoGTPase cycle. GAPs and GDIs have been found to be downstream targets of GTP-bound RhoGTPase signalling, in what could constitute additional mechanisms of crosstalk between proteins, in addition to those controlling GEF activity. An intriguing possibility is suggested by a few observations of GDI bound RhoGTPases not being biologically inert, so that they could trigger signals to actively regulate the RhoGTPase cycle[190, 6]. RhoGTPases can also modulate GAP and GDI activity of its own regulators, which would provide the means for positive or negative autocatalytic signals, necessary in sustained locomotion and to terminate a particular process during migration, respectively [191, 68]. There is also evidence that the specificity of GEFs, GAPs, and GDIs for a particular RhoGTPase can be altered by their own signals, and furthermore, that they can act as activators for a certain protein and as inhibitors for another [192]. Thus, the relevance of these observations to provide an experimental basis for the New class of models is double: self-regulation of the enzymes associated to a RhoGTPAse by itself provide a plausible biochemical mechanism from which the functional form of the Kinetic rates in the New Class of regulation could be derived. During the development of the model, it was mentioned that the adopted Hill-type form of k^A could be a product of GEFs or GDIs acting as homotropic enzymes for the RhoGTPases, meaning that upon binding between them, a conformational change of one of the proteins takes place and modulates the affinity to bind third molecule. Such a mechanism has indeed been reported for the two *Cdc*42 and *Rac*-specific GEFs *Pix* and *Tiam*1 [186] and two RhoGTPase effectors *PAK* and *Wave*2, respectively. *PAK* and *Wave*2 act as scaffold proteins that promote the recruitment of the aforementioned GEFsm, but they also are molecules targeted by the RhoGTPases and activated to perform important functions in cell migration. Thus, this form of 3-way interaction constitutes a form of self-activation that facilitates the activation of the RhoGTPases, but also provides a mechanism to select which of the myriad of RhoGTPase targets is activated.

Second, the strong evidence summarized above of an active involvement of GDIs and GAPs in RhoGTPase regulation, auto-catalysis, and competition to bind common regulatory enzymes, supports the existence of alternative Crosstalk mechanisms, such as those considered in the development of the New model Class due to strictly theoretical grounds.

Certainly, these observations suggest a more complex RhoGTPase cycle, but the void in our understanding of their regulation may be even more profound. The results of experiments with recently available RhoGTPase Knockout Mice are often contradictory to those obtained from studies based in over-expression of exogeneous RhoGTPases mutants [65]. Over-expression experiments consists in the transfection of cellular lines with Double-Negative or Constitutively Active RhoGTPases, which inhibit or overstimulate RhoGTPase signalling, respectively. The observation of how a particular RhoGTPase mutant affects cell behaviour and the activation levels of other proteins is then used to infer its function and interaction partners. Conversely, in Knockout Mice experiments, iRNA is employed to silence the genes associated to the expression of an individual protein. A recent study using this technique to block *RhoGDI*1 expression showed that in the absence of this protein, the fraction of RhoGTPases in the cytosol is targeted for rapid degradation [78]. This result suggests that the conclusions drawn from over-expression studies may be flawed, because indirect crosstalk between RhoGTPases is overlooked. The amount of RhoGDI1 in the cell is approximately the same as the sum of the total amount of *Cdc*42, *Rac*, and *RhoA*, so that RhoGTPases have to compete to bind GDI. Therefore, over-expression of an exogeneous mutant of one of them prevents the others from binding the limited amount of RhoGDI and promotes degradation of their cytosolic fraction and a reduction of the concentration of the active fraction inserted in the membrane. Consequently, the effects of over-expressing a single RhoGTPase would not only be associated to this particular protein, but also to coupled variation of activity levels and concentration of the rest. This form of indirect crosstalk through competitive interaction compromises the interpretation of over-expression studies, from which much of our knowledge of RhoGTPase function has been gained in the past. Particularly, some of the inhibiting or activating interactions forming proposed Reaction Schemes might be an artifact, while the real underlying channels of Crosstalk are overlooked. More importantly for the purposes of this Thesis, this experiment provides strong evidence of a specific biochemical mechanism of Crosstalk based on competitive interactions between RhoGTPases, which is one of the proposed mechanisms of RhoGTPase interaction in the New Class of Regulation models.

Further exploration of the ideas discussed in this Thesis to interpret the data obtained from new experimental techniques [186], which allow the observation of RhoGTPase signaling with spatio-temporal resolution, might aid to extend our

understanding of the mechanisms underlying RhoGTPase regulation and address the current difficulty in integrating the observations from over-expression studies and knockout mice.

7.3 Migratory Response to external stimuli

In this section, a member of the new Class of RhoGTPase polarization models is integrated with the mechanical module developed in Chapter 3 to describe cell migration. Discrete adhesive contacts are not considered: the external stimuli represent a chemotaxis-inducing gradient and the predicted migratory response will be compared with qualitative features of cells using amoeboid motility. This mode of migration is typically used by keratocytes, leukocytes and neutrophiles; is characterized by the absence of mature adhesions from which cells pull on the substrate and a characteristic cell-type dependent shape. The movement is powered by propulsive o pushing forces and the cells adopt a rounded, fan-like morphology during their gliding motion[58].

The coupling between the Regulatory and Mechanical model occurs through the determination of the protrusive and contractile forces by the RhoGTPAses as explained in Chapters 2-3. The strength of RhoGTPase signaling setting the magnitude of the forces is described using a functional form similar to that used in eq.7.12 to model the strength of Crosstalk. According to the experimental evidence, the protein assumed to control the level of contraction force is *RhoA*, whereas the protein that determines the protrusion force is *Rac*. Therefore, at any point inside the cell body in which the activation level of *RhoA* is higher than the equilibrium concentration, the force contraction force is switched on. The mathematical description of the contraction law $\tau^{cont}(\mathbf{r})$ was given in 3.23. Assuming that the contraction force is isotropic, the general law is then reduced to $\tau^{cont} = \tau^{cont}(\rho) \cdot [\ 1 \quad 1 \quad 0\ ]$.

$$\tau^{cont}(\rho) = \tau_0^{prot} \cdot \frac{(\rho_a - \rho_a^0)^2}{\alpha_P^2 + (\rho_a - \rho_a^0)^2} \tag{7.18}$$

The protrusion force $\mathbf{t}^{prot}(\mathbf{r})$ described by the law given in eq.3.24 results in a force normal to the plasma membrane triggered at those points on the cell boundary where the concentration of *Rac* is higher than the equilibrium concentration.

$$\mathbf{t}^{prot}(r) = P_0^{prot} \cdot \frac{(r_a - r_a^0)^2}{\alpha_C^2 + (r_a - r_a^0)^2} \cdot \hat{n} \tag{7.19}$$

The parameters τ_0^{cont} and P_0^{prot} set the maximum magnitude of the stresses exerted by the cell. According to experimental evidence, they are of the order of $\sim 1 - 10 nN/\mu m^2$, depending on the cell types and migration mode [193].

The parameters defining the constitutive equation of the cell cytoskeleton 3.22 and the cell substrate interaction are taken from the values adopted in the 1-dimensional models by Gracheva-Othmer[95],and Larripa-Mogilner[96], and experimental references therein.

Table 7.2: Cell constitutive parameters

Parameter	Physical Meaning	Value
E_0	Cytoskeleton elastic modulus	$\sim 10\, nN/\mu m^2$
μ_0	Cell viscosity	$\sim 1 - 10\, nN \cdot s/\mu m^2$
β	Cell-substrate friction	$\sim 0.5 - 1\, nN \cdot s/\mu m^3$
h_0	Cell height	$0.1\ \mu m$
P_0^{prot}	Protrusion stress	$\sim 10 nN/\mu m^2$
τ_0^{cont}	Contraction stress	$\sim 10 nN/\mu m^2$

For the first set of simulations, the cell cytoskeleton is described as an isotropic viscoelastic solid, and consequently the stiffness matrix is defined by the elastic modulus given in the previous table and the isotropic stiffness matrix 3.17.

Interestingly, the simulations show that a variation of the ratio of τ_0^{prot} to P_0^{prot}, crosstalk, and the rheological properties of the cell, allows to predict qualitatively different morphologies adopted by the cell that have a remarkable resemblance to the characteristic shapes featured by cells of different types during migration.

In addition, the cell is assumed to be totally incompressible, so that in expanding (contracting) areas the cell height is reduced (increased) to conserve the volume. As a consequence of this choice, the dilution term in the Reaction-Diffusion equations describing RhoGTPase distribution vanishes. The fundamental difference is that in the incompressible case the concentration of proteins is not altered

by volumetric changes in expanding or contracting areas, while in the compressible case the expansion (contraction) has associated a small decrease (increase) in the concentration, but otherwise the results are qualitatively similar. Finally, the migration model is fully defined assuming Model A as the Reaction scheme for the RhoGTPases. The predicted migration response of this model to a transient linear stimulus is shown in the following figure. For each time-frame, the stimulus profile, cell shape, and polarization forces are depicted in the upper windows, and the RhoGTPase distribution is depicted in the lower windows:

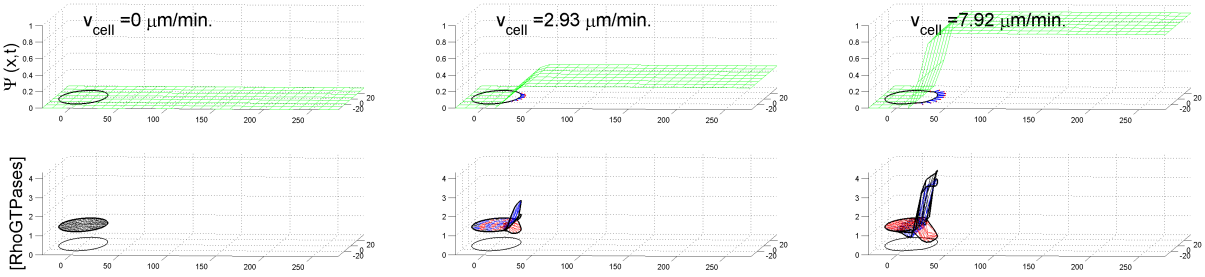

$t = 0.3$min. $x_{\text{cell}} = 0\mu m$ $t = 0.4$min. $x_{\text{cell}} = 0.1\mu m$ $t = 0.6$min. $x_{\text{cell}} = 1.6\mu m$

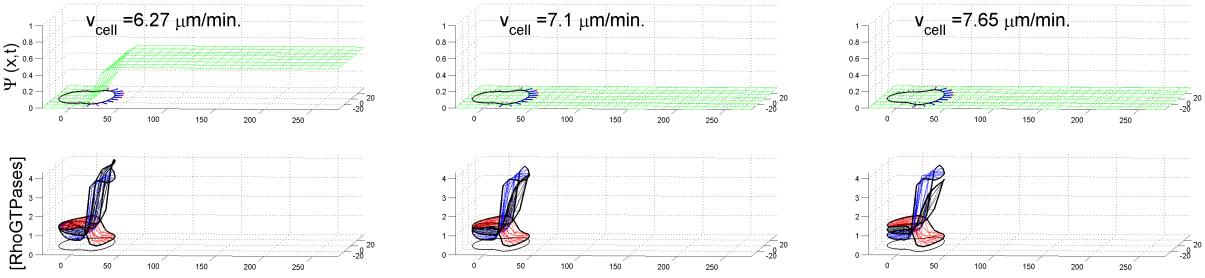

$t = 0.9$min. $x_{\text{cell}} = 4.3\mu m$ $t = 1.2$min. $x_{\text{cell}} = 5.7\mu m$ $t = 1.5$min. $x_{\text{cell}} = 8.2\mu m$

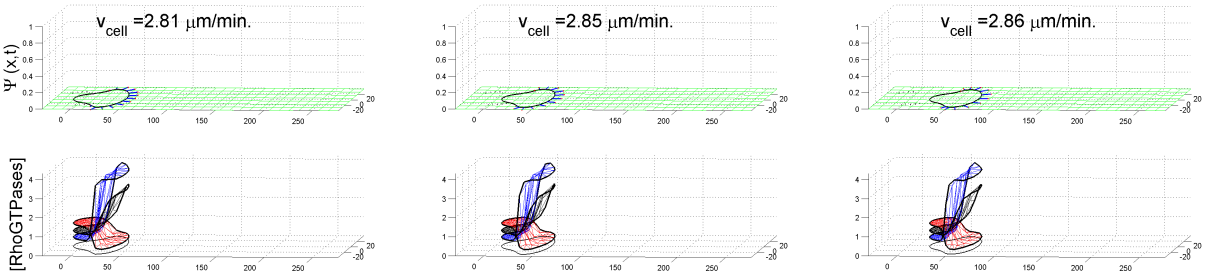

$t = 5.0$min. $x_{\text{cell}} = 21.0\mu m$ $t = 10.0$min. $x_{\text{cell}} = 35.2\mu m$ $t = 15.0$min. $x_{\text{cell}} = 49.4\mu m$

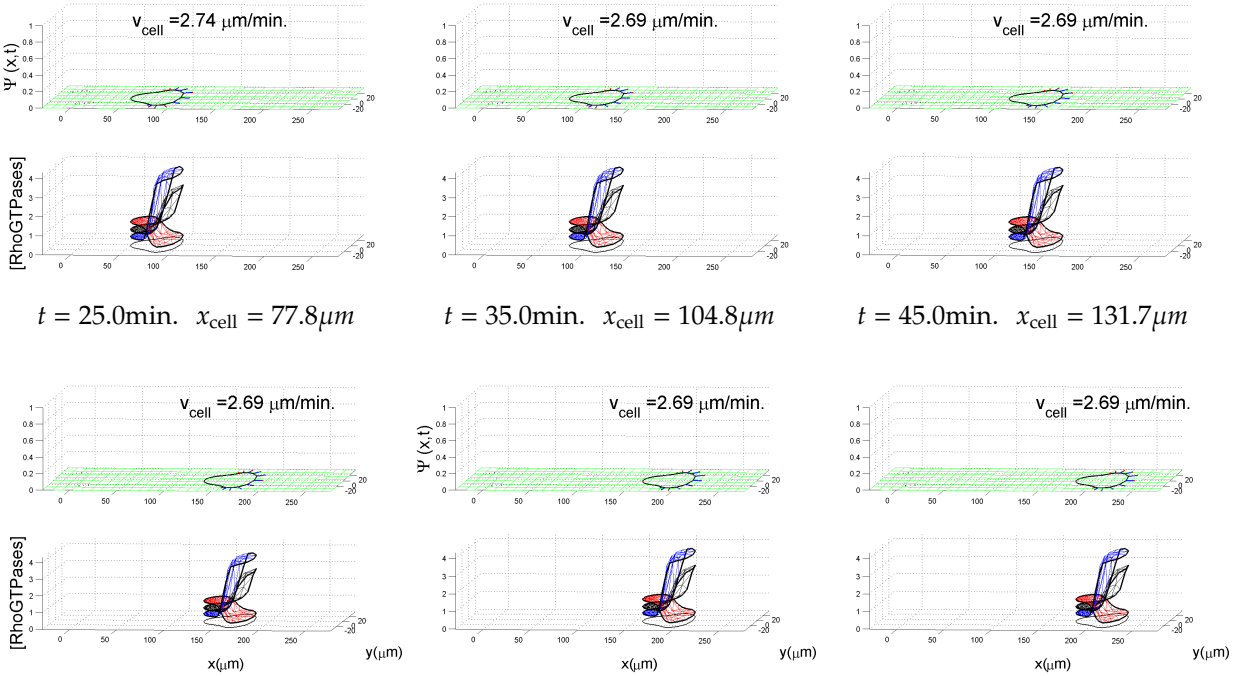

Figure 7.12: ⊗ Persistent amoeboid motion

The polarization process occurs analogously to the examples in which movement was not considered. In this case, however, as the RhoGTPases become asymmetrically distributed and their activation levels overcome the equilibrium values, protrusion and contraction forces are developed at the areas where *Rac* and *Rho* are higher, respectively. The polarization process is completed after approximately 2 minutes, corresponding to the first 6 snapshots of figure 7.12. During this process, the area that will become the cell front, where *Cdc*42 and *Rac* are activated, is extended due to the development of protrusion forces, whereas the opposite end, which will become the trailing edge, starts retracting due to rise of contraction forces associated to *RhoA* activation. After approximately 5 minutes, the cell reaches a steady state morphology characterized by a broad, fan-like front and a smaller rounded trailing edge. The shape adopted by the cell during its movement has a remarkable resemblance with the *teardrop* morphology adopted by *Dyctioselium* cells [3], neutrophiles and other cell types that use an amoeboid-based mode of migration[7]. The migration speed has been approximated as the velocity of the cell centroid. The high initial velocities are a product of the cell being deformed, which leads to an advance of the centroid but little net forward movement. However, as the cell reaches the final equilibrium shape, the velocity

is stabilized at $\sim 3\mu m/min.$, in agreement with reported values of fast migrating amoeboid cells[46]. The cell-substrate friction and protrusion force magnitude are the key variables that determine migration speed. Since Model A is the underlying Reaction scheme, the polarization state is persistent, and consequently, the cell maintains its direction of motion after the stimulus is removed. Reduction of the value of *Cdc*'s Velocity of autocatalysis given in 7.1 to $\gamma_C = 10$ results in a Reaction scheme that produces transient states of polarization. In this case, under the same stimulus and using the same values for the rest of the parameters, the migration response is accordingly transient:

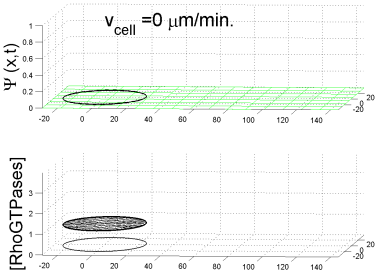

$t = 0.26$min. $x_{\text{cell}} = 0\mu m$

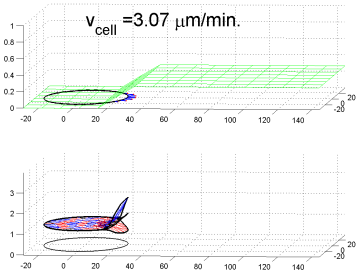

$t = 0.4$min. $x_{\text{cell}} = 0.1\mu m$

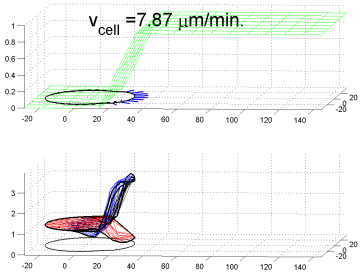

$t = 0.56$min. $x_{\text{cell}} = 1.6\mu m$

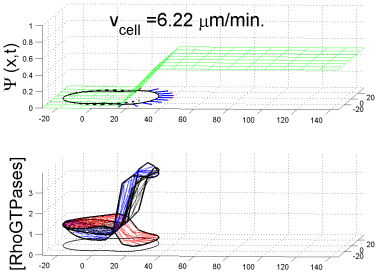

$t = 0.96$min. $x_{\text{cell}} = 4.3\mu m$

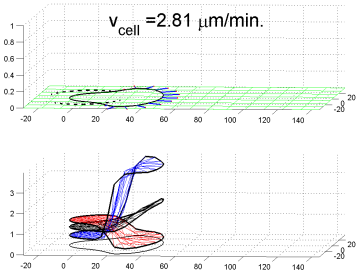

$t = 5.0$min. $x_{\text{cell}} = 20.9\mu m$

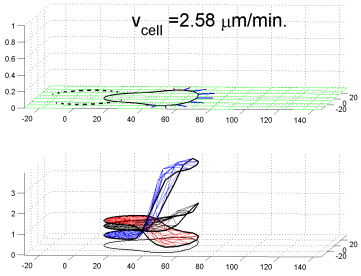

$t = 12.0$min. $x_{\text{cell}} = 40.1\mu m$

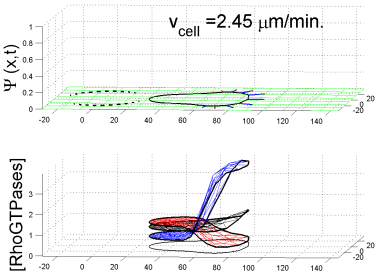

$t = 19.0$min. $x_{\text{cell}} = 57.7\mu m$

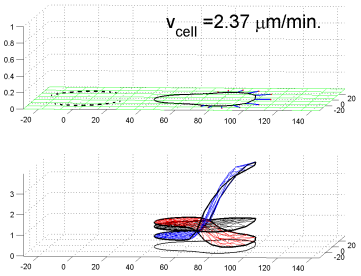

$t = 25.0$min. $x_{\text{cell}} = 72.2\mu m$

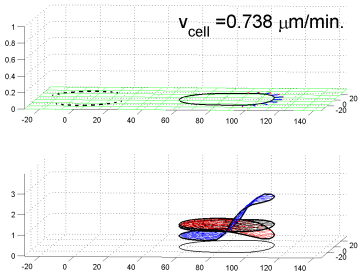

$t = 33.0$min. $x_{\text{cell}} = 82.3\mu m$

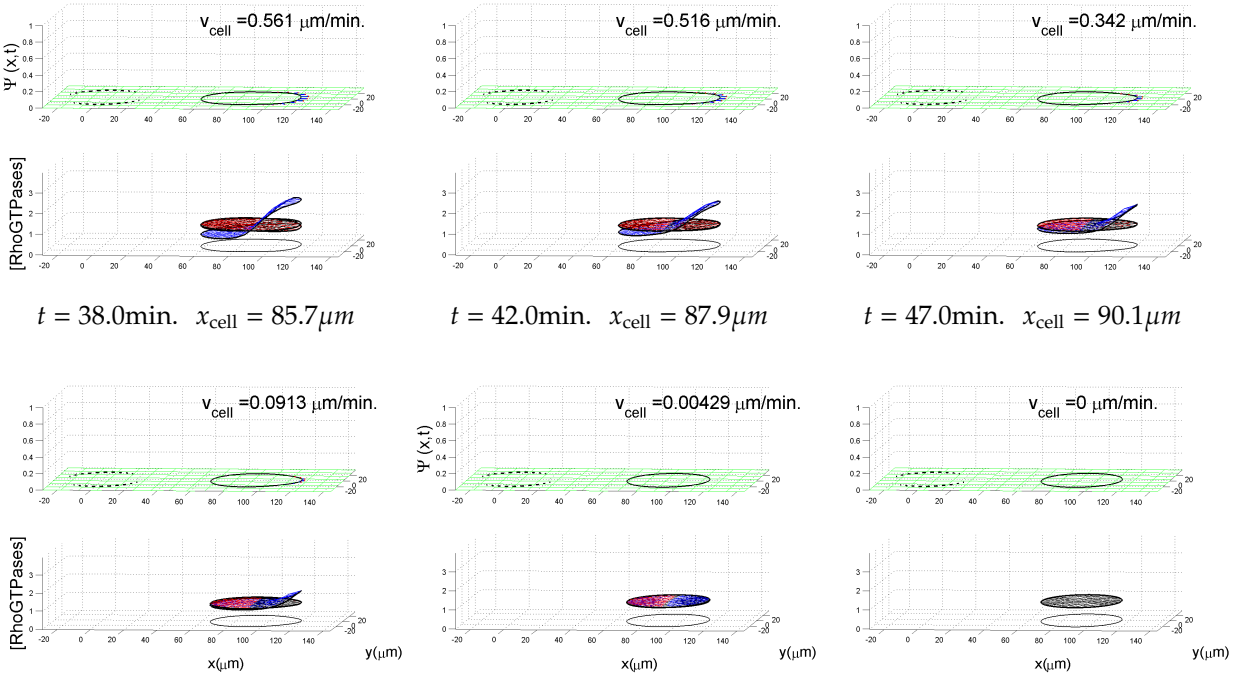

Figure 7.13: ⊗ Transient amoeboid motion

Again, it must be emphasized that the variation in the migratory response results form the continuous variation of a single parameter. Moreover, the last two simulations represent only two extremes amongst the possible forms of polarization and movement that can be captured by the model. For instance, if the Velocity of autocatalysis of *Cdc*42 is kept at $\gamma_c = 10$ but the values for *Rac* and *RhoA* are increased to γ_r, $\gamma_\rho > \gamma_{3R}$, hybrid *persistent-transient* state of polarization response are obtained. For instance, setting $\gamma_r = 12$ and keeping the rest of the autoctalysis constants at values close to γ_{3R} results in a reaction scheme in which only the polarization of *Rac* is *persistent*. If the Maximal Velocirty of autocatalysis of *RhoA* is also increased to $\gamma_r = 20$, *Cdc*42 protein returns to the homogeneous initial state after the stimulus vanishes, but the proteins controlling the level of forces, *Rac* and *Rho*, remain in the polarized state. The possible interest of this hybrid states of protein distribution lays in that a cell featuring such a polarization state would be able to sustain its direction of motion indefinitely if no other stimulus were applied, but since the *sensor* protein would return to its initial state, the cell sensing machinery would maintain its power to detect new stimuli completely

unaltered[7].
The instantaneous velocity of the *persistent* and *transient* forms of cell movement are compared in figure 7.14. The velocity profile of the two modes of migration is almost identical in the initial migration stage. The two peaks in the velocity profiles are artifacts caused by the advancement of the cell centroid as a result of the cell being deformed by protrusion and contraction forces, as mentioned earlier. The first peak is associated to the extension of the leading edge after *Rac* is activated and protrusion forces are developed at the cell front. The establishment of the polar pattern of *RhoA* lags behind, and once it is established it triggers the contraction of the trailing edge of the cell, which explains the second peak. Shortly after the cell adopts its equilibrium shape, a constant migration speed is attained, although in the transient mode of migration the velocity starts decaying when the polarized state fades (after approximately 15 minutes.).

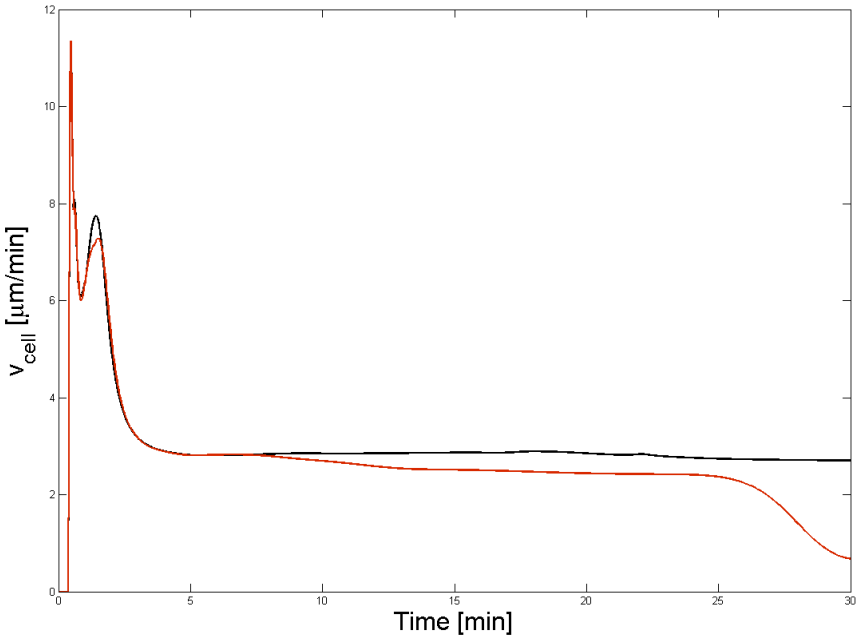

Figure 7.14: Migration speed approximated as the velocity of the cell centroid. Black: Persistent migration. Red: Transient migration

In both cases, the migration speed is an increasing function of the magnitude protrusion force P_0^{prot} and a decreasing function of the cell-substrate friction β.

[7]The simulation displaying this form of migration is not shown in the main text, but can be found in the movies of the accompanying CD

This result is not in agreement with the observed biphasic relationship between speed and adhesion strength featured by many cell types. It is a well established experimental fact that cell speed is fastest at intermediate levels of cell-substrate adhesion strength, and it decays for very large or very low adhesive strengths [194, 195]. This limitation of the model was entirely expected, since in this chapter only a continuous drag between the cell membrane and the substrate has been considered, without including the adhesion apparatus of the cell. The biphasic relationship between migration speed and cell-substrate adhesion strength stems from the balance between the need to establish sufficiently strong attachment points to exert traction and protrusion forces in order to pull the cell body forward, and the increasing difficulty of releasing these contacts as the cell-substrate adhesion strength is high. In a seminal paper that represented one of the first attempts to formulate a detailed model of cell migration, DiMilla an coworkers [94] predicted the existence of the biphasic relationship using a simplified version of this "physical" principle, which was later confirmed in experimental essays. More recent experiments, however, have shown that the underlying mechanisms are more complex and involve also the RhoGTPases and differential activation of myosin contraction [196, 197]. In addition, the simple yet insightful 1D model of DiMilla, in which no regulatory network was considered, movement was in fact a result of prescribing an asymmetry in the adhesion strength along the cell (either assuming an increasing concentration or increasing strength of receptors toward the cell front), which combined with uniform contraction leads of course to forward advancement of the cell center of mass. These important aspects of cell migration will discussed in more detail later in section 7.4 and in Chapter 8, where Focal adhesions are incorporated into the model.

7.3.1 Simulation of Chemotaxis essays

The focus is next turned to recapitulate the migratory response of cells in realistic chemotaxis essay conditions. A classic chemotaxis experiment, as discussed in section 5.1.3, consists in the release of a certain a diffusible chemoattractor with a pipette or from punctual hole in the chamber where the cells are cultured. As the molecule spreads over the chamber, the cells detect the gradient and start migrating towards the source. The spatio-temporal concentration of such a molecule is given analytically in eq.5.1 and corresponds to a gaussian that decays over time with its maximum centered at the release point. The amount of m_s chemoattractor released is set so that if it were homogeneously distributed over a $200\,\mu m\,x\,200\,\mu m$ square containing the cell, the concentration would be 10-fold times the parameter Ψ_0 that sets the sensitiveness in eq. 7.16. The diffusion and decay constants of the chemoattractor are set in the range of $d_s = 1 - 100\,\mu m^2 \cdot s^{-1}$

and $k_s = 0.1 - 0.01s^{-1}$. The value of d_s determines how fast the concentration of the chemoattractor becomes homogeneous, and hence the steepness of the gradient that reaches the cell. The values studied range from the small diffusion constant of the RhoGTPases in the membrane to the large values characteristic of a small protein in water, without significantly affecting the capacity of the cell to detect the gradients and polarize along the direction of steepest growth. The next simulation shows the response to 3 consecutive releases from sources separated approximately $100\mu m$ from the cell. The Reaction Scheme is again a *persistent* form of Model A and the chemottractant parameters correspond to the values in the lower bounds given above.

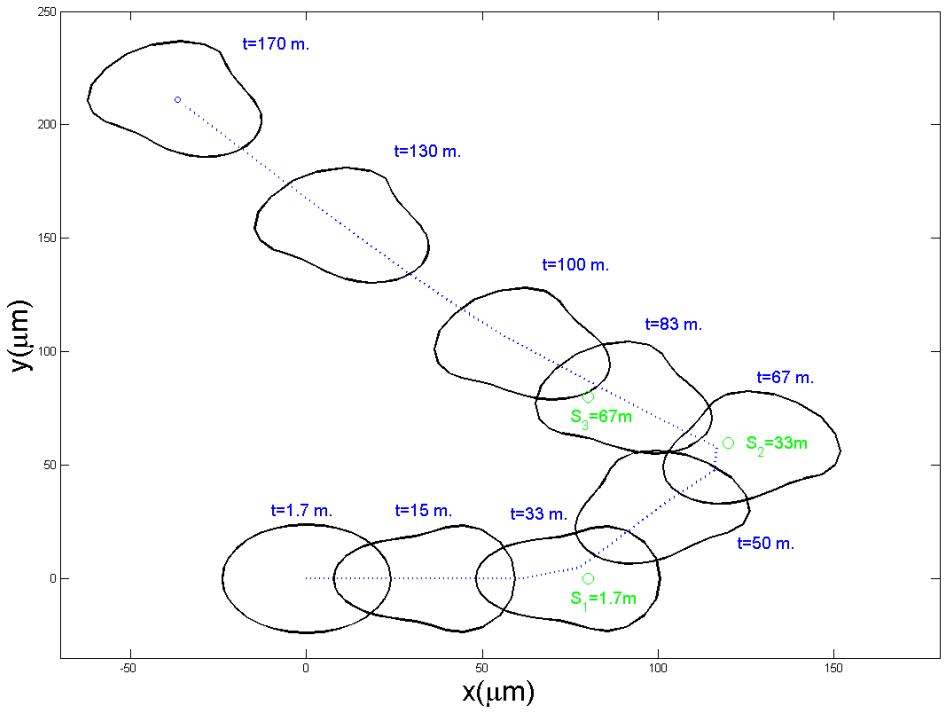

Figure 7.15: ⊗Persistent migration following chemoattractant releases at t_1 = 1.7min. , t_2 = 33.3min. and t_3 = 66.6min. from different point-sources.

Several features of the simulated response stand out for their qualitative faithfulness with the observed behavior of chemotactic cells. First, the remarkable capacity of the *computational cells* to pick up shallow gradients and align the polarization axis in the direction of the source. This feature has been tested performing multiple simulations with variations in the distance to the point-sources

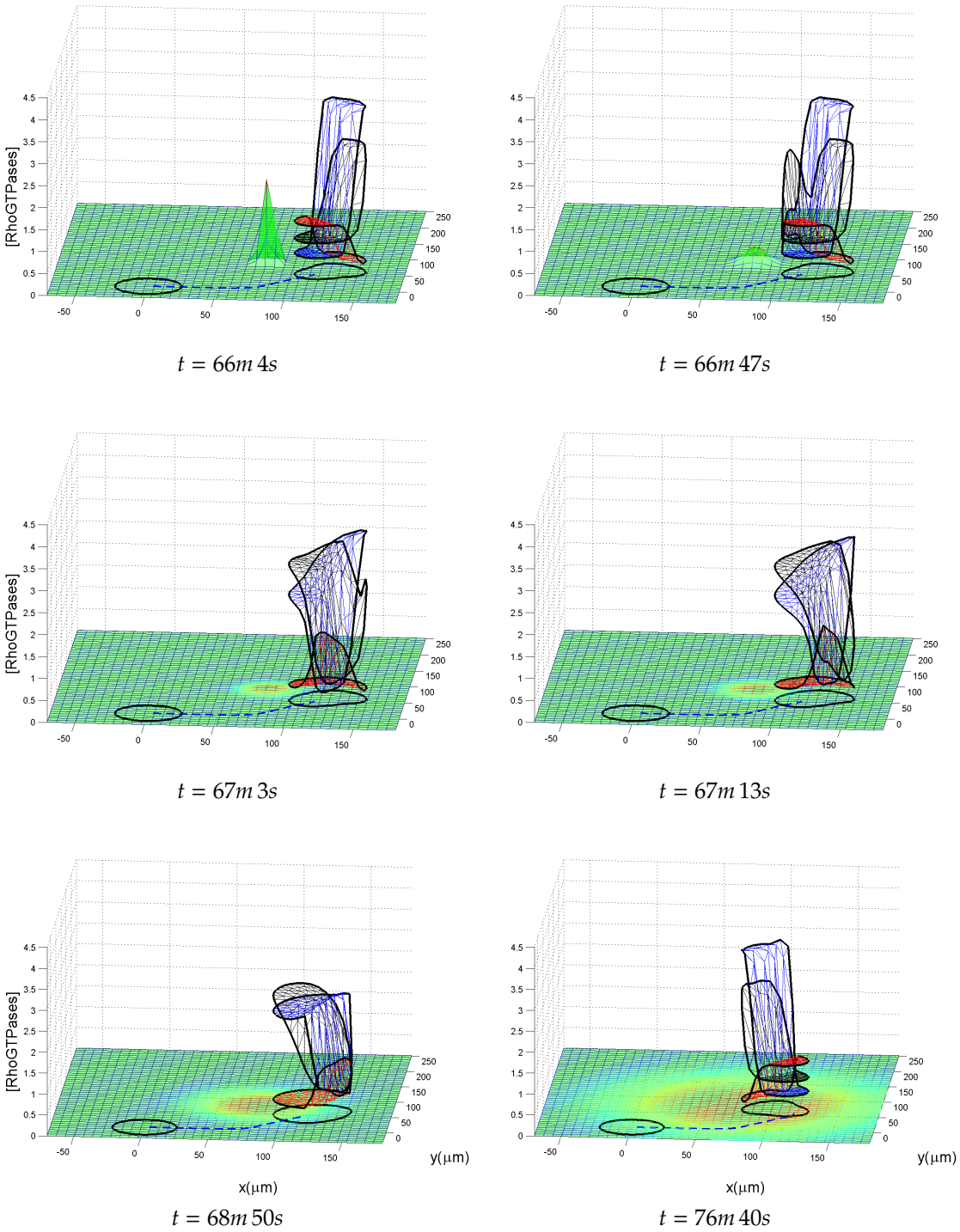

$t = 66m\,4s$ $t = 66m\,47s$

$t = 67m\,3s$ $t = 67m\,13s$

$t = 68m\,50s$ $t = 76m\,40s$

Figure 7.16: $^{\otimes}$ Realignment of polarization axis after new stimulus S_3

and chemoattractant parameters; the animation of this and similar computational experiments not shown in the main text can be found in the accompanying CD. Second, the process of realignment of the axis of polarization when a new stimulus release occurs and reaches the cell moving away from the new source. This process occurs twice during the simulation shown in figure 7.15, first at $t_2 = 33$ min when S_2 is released while the cell is moving rightwards and later at $t_3 = 66.6$ min. as the cell is moving diagonally to the upper-right corner of the domain and S_3 is released. The realignment event corresponding to this last switch is shown in detail in figure 7.16. As the front of the new stimulus S_3 hits the side of the cell, relative to the current axis of polarization, a new area of high *Cdc*42 activation is developed and coexists with the preexisting one. Gradually, the new zone of high activation grows, depleting the reserve of inactive protein that sustains the zone of high activation of the area that marked the old cell front, so that as the new zone is reinforced the preexisting one is weakened. Simultaneously, crosstalk signaling triggers an increase in *Rac* activation and a decrease in *RhoA* in the newly excited area, which by the same depletion mechanism that applies to *Cdc*42 also leads to the reinforcement of the new activation zones of *Rac* and *RhoA*. This process is completed after approximately 3 minutes, when the old areas of high activity are suppressed and the new areas of high and low activation are established. Concomitant to this process, the protrusion and contraction forces evolve according to changing distribution of the RhoGTPases and the old areas of protrusion and contraction fade away and are replaced by a new lamellipodium and contractile tail. Once the realignment of the polarization axis is completed and the level of force reaches a steady state, the cell recovers the *teardrop* shape and resumes its motion toward the source of the new stimulus.

Indeed, this is the way in which this process takes place in most types of real cells [5, 3, 4], as opposed to performing U-turns or maintaining the coexistence of several activated zones. This result is particularly relevant to interpret the experimental findings of a recent and fascinating study of the mechanisms of *Cdc*42 polarity in buddying yeast [4], which in turn provide convincing support for the ideas presented in this Thesis. Before entering in the discussion of these experimental observations, the results of another computational experiment are shown in figures 7.17-7.18 to better illustrate the dynamics of the process of polarization realignment. In this case, the spatial source of the consecutive stimulus is prescribed so that the second stimulus hits the cell from behind and the third laterally. The cell first detects and follows a trajectory towards stimulus S_1, retracing its path after S_2 reaches the cell from behind and then making a diagonal turn to the right in pursue of S_3.

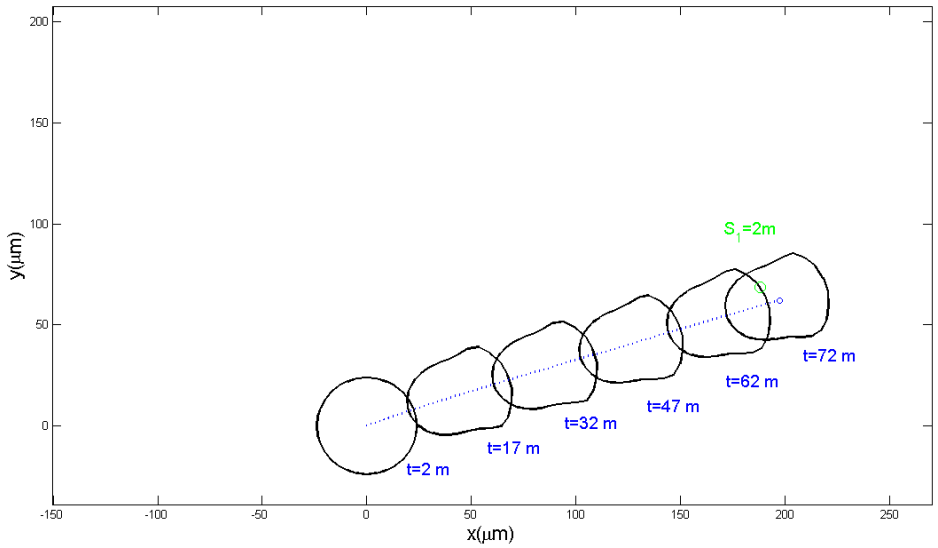

(a) Cell Trajectory between release of S_1 and release of S_2

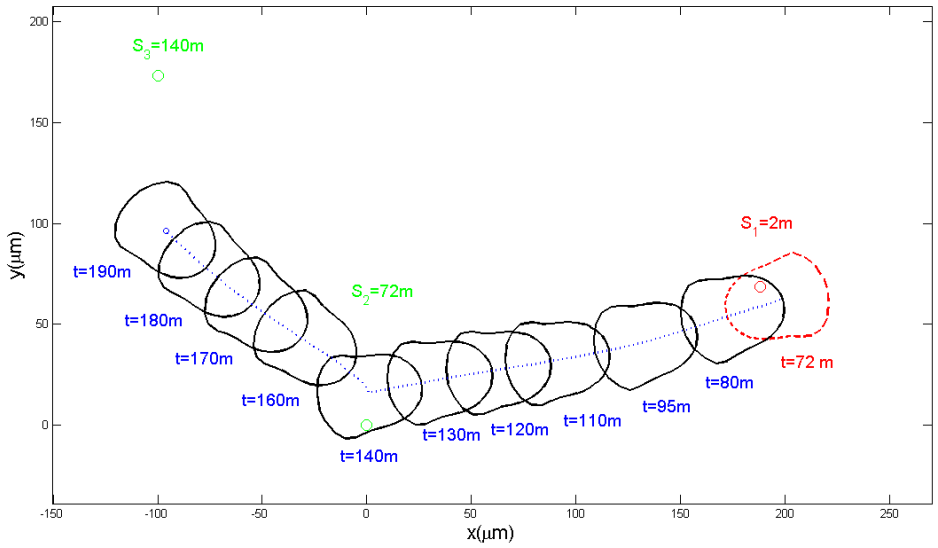

(b) Cell Trajectory between release of S_2 and release of S_3

Figure 7.17: ⊗Persistent migration following chemoattractant releases at t_1 = 2min. , t_2 = 72min. and t_3 = 140min. from different point-sources.

The dynamics of the RhoGTPases during the timespan between the discharge of S_2 and the realignment event is completed are shown in detail in figure 7.20.

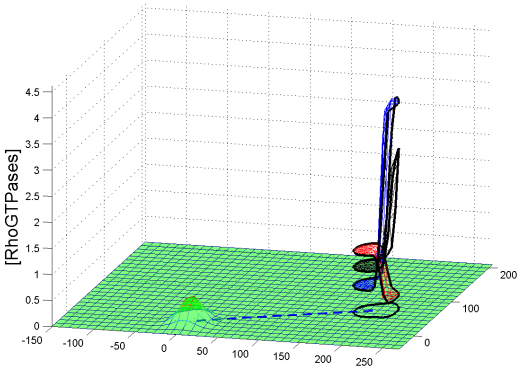

$t = 72m\,6s$

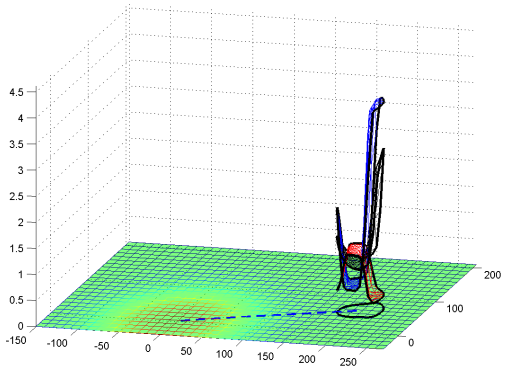

$t = 72m\,22s$

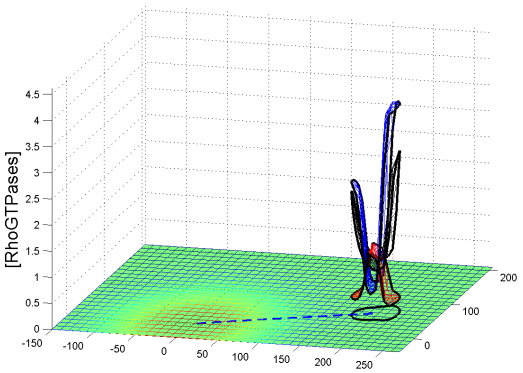

$t = 72m\,25s$

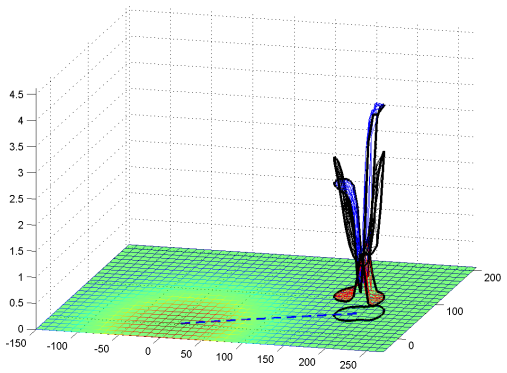

$t = 72m\,30s$

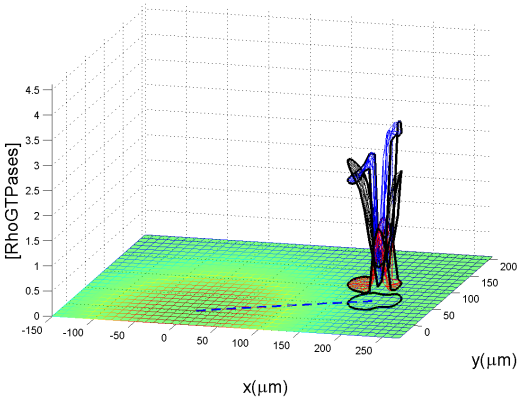

$t = 73m\,0s$

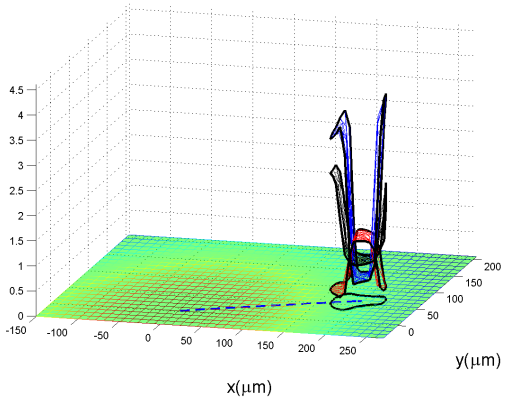

$t = 74m\,0s$

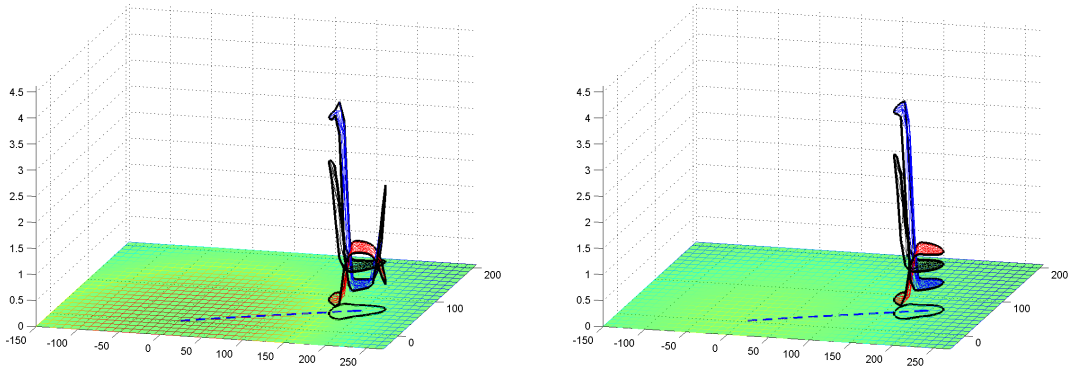

$t = 55m\,0s$ $t = 76m\,1s$

Figure 7.18: $^{\otimes}$ Realignment of polarization axis after release of stimulus S_2

In the previous simulation it can be appreciated how the new zones of activation grow at expense of the old ones. A central question in cell polarization is related to the mechanisms that control the establishment of a single zone of growth. In a recent and exceedingly interesting study of *Cdc*42 polarization in *Saccharomyces cerevisiae*, conclusive evidence was found that cell might initiate several clusters of high *Cdc*42 activation, but competition between the distinct zones for a limiting factor eventually produces a single winner and suppresses the rest [4]. Moreover, they found that the growth of the different *Cdc*42 clusters is fueled by an autocatalytic loop and describe the underlying biochemical process, which provides an interesting interpretation of the RhoGTPase model proposed in this Thesis in terms of experimentally observed molecular mechanisms. The autocatalytic loop comprises the scaffold protein *Bem*1*p* binding a *GEF* specific for *Cdc*42 to the kinase *PAK*. This $Bem1p - GEF - PAK$ complexes diffuse fast in the cytosol, but since *PAK* is a molecule with a strong affinity to bind active *GTP*-bound *Cdc*42 inserted in the membrane, the complexes are recruited in the preexisting clusters of high concentration of $Cdc42 - GTP$ and the *GEF* in the complex promotes further activation of neighboring GDP-bound *Cdc*42. Thus, this process constitutes the basis for both the autocatalytic loop that allows the emergence of clusters of high *Cdc*42 activation and a mechanism to enforce the "*singularity of cell polarization*"[4], because competition for the limited amount of $Bem1 - GEF - PAK$ complexes ensures that a single winning cluster emerges. Certainly, there might be other biochemical processes involved, but this mechanism provides an exciting interpretation of the Reaction term of the RhoGTPase model derived at the beginning of this Chapter on purely theoretical grounds. Particularly, it provides a biochemical basis to support the proposed form of the kinetic rates of activation

given in eq.7.10. The sigmoidal form of $k^A = k^{\text{GEF}} \cdot k^{\text{GDF}}/(k^{\text{GDF}} + k^{\text{GDI}})$ would stem from the GEF mediated autocatalytic loop. In addition, the mechanism of competition for limited resources of regulatory enzymes between different zones of high activation of *Cdc*42 suggests that this mechanism might also operate to mediate Crosstalk between RhoGTPases. Two mechanisms of Crosstalk have been considered in the model, one channeled through variations of the Michaelis constants κ_r that would result from this type of competitive interactions; and another included through variations in the autocatalysis velocities γ_r that could result from non-competitive interactions and for which there is also substantial evidence.

Even though the changes in concentration and limited amount of *GEFs* and the rest of the regulatory enzymes has not been considered, the model reproduces the coexistence, competition and eventual survival of a single activation zone through the related mechanism of depletion of inactive RhoGTPases. The timescales predicted by the model to resolve the conflicts between coexisting zones of activation are of the order of a few minutes, consistent with the reported experimental values in this [4] an similar studies of polarity reversal [5, 3]. However, depending on the specifics of the stimulus, such as the distance from the source of release to the cell, or the amount of chemoattractant discharged, interesting variations in the dynamics of polarization predicted by the model can be observed. For instance, when the amount of chemoattractant deployed is very large or the source of release is very close to the cell, the stimulus still reaches first the edge closer to the point of release, but as it propagates it floods the whole cell, which is temporarily exposed to a large an almost uniform concentration of stimulus. In this case, it can be observed that the cell first polarizes towards the stimulus source, but then it is transiently left in a state of nearly homogeneous high activation for *Cdc*42 and *Rac* and low activation of *RhoA* when the whole cell is saturated by the large stimulus. Shortly after, the cell returns to a polarized state pointing towards the source of the stimulus in timescales of the order of minutes and resumes its motion in its direction. This behavior is enabled by the property of *adaptation* featured by this model, which is defined as the generation of a transient state of global activation under the exposure to a uniform stimulus that disappears after the stimulus is removed[1]. In this case, however, the stimulus is not perfectly uniform, and as the chemoattractant propagates the cell is able to differentiate the small concentration gradient and instead of returning to the initial homogeneous state, it returns to the correct polarized state.

This process can be seen in figures 7.19-7.20, showing the result of a simulation in which migration was triggered by discharges of a large amounts of chemoattractant released from a distance close to the cell.

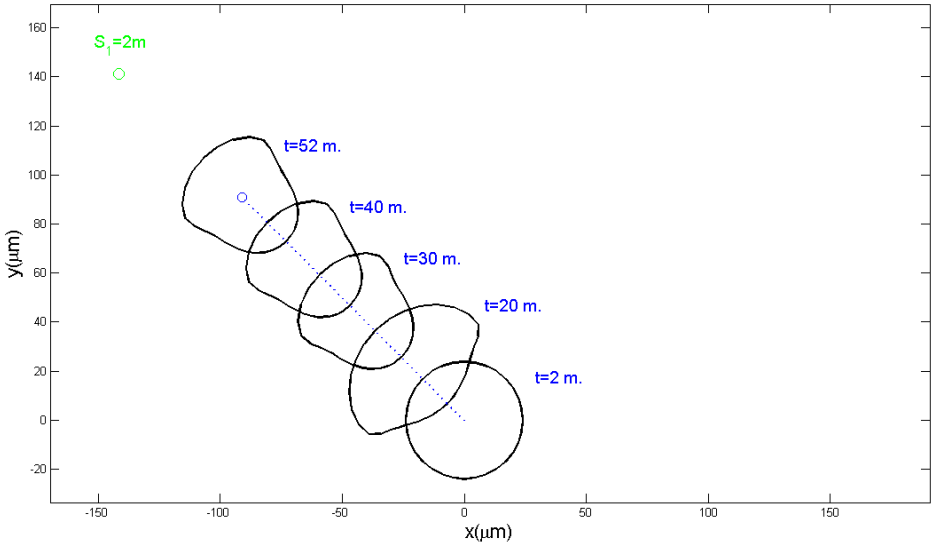

(i) Cell Trajectory between release of S_1 and release of S_2

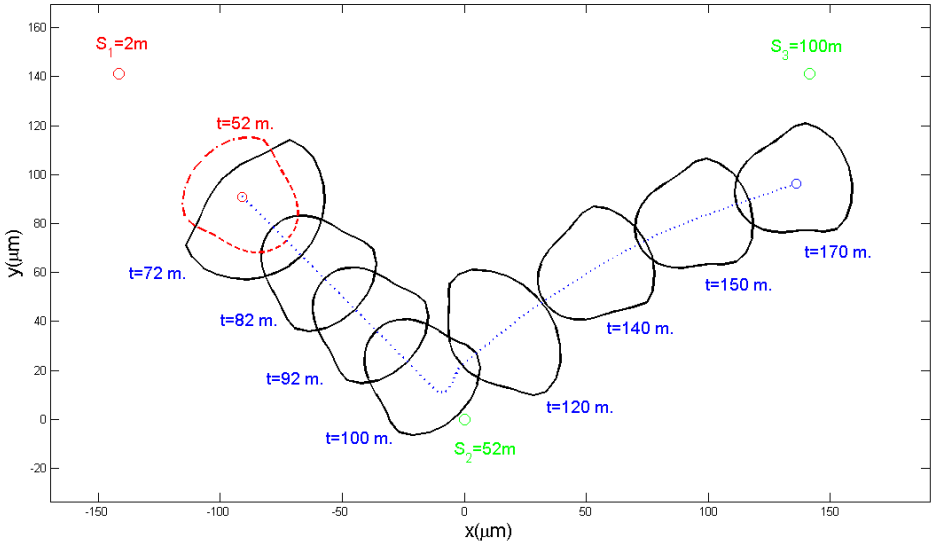

(j) Cell Trajectory between release of S_2 and release of S_3

Figure 7.19: ⊗Migration triggered by large chemoattractant discharges at t_1 = 2min. , t_2 = 52min. and t_3 = 100min.

The detailed dynamics of RhoGTPases polarization, saturation and recovery of the polarization state directed towards the source of S_2 are shown in the following

figure:

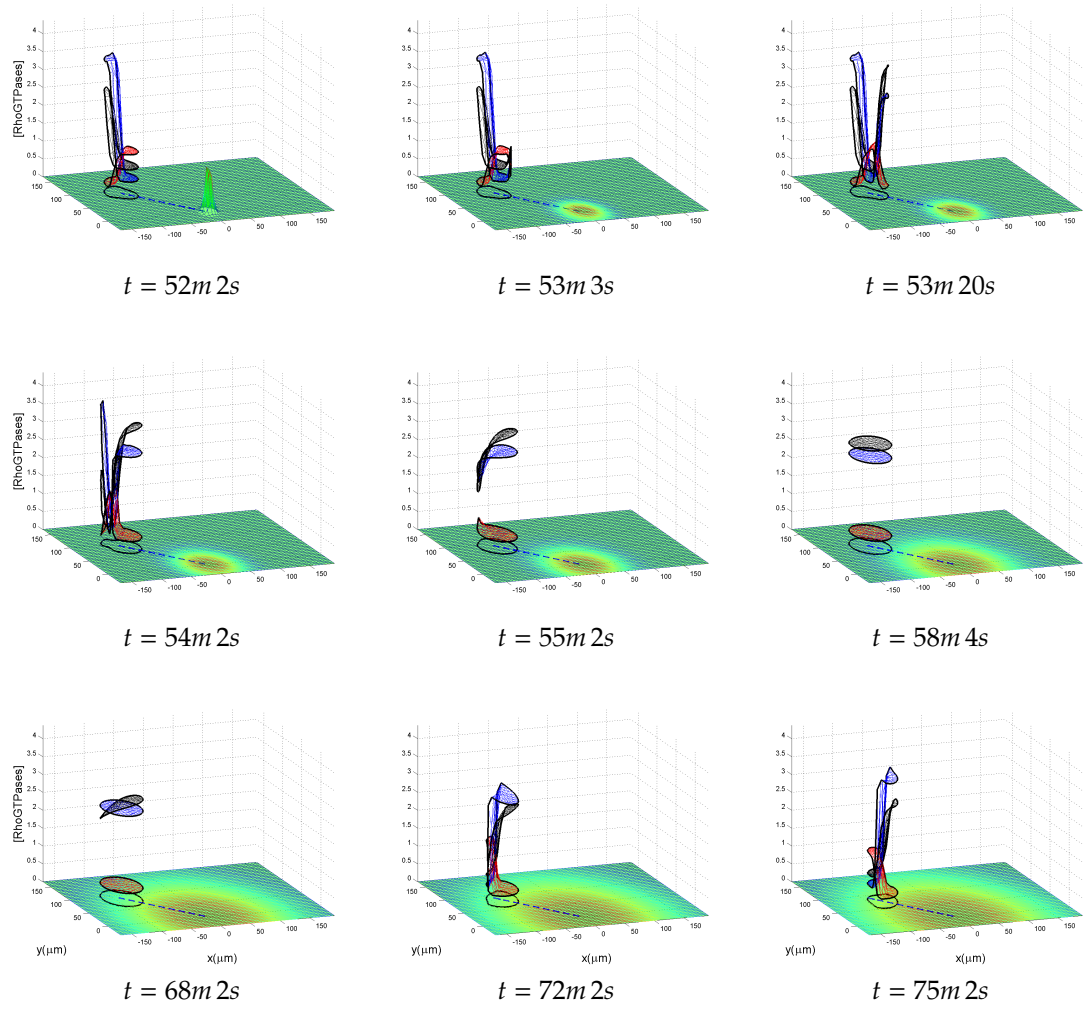

$t = 52m\,2s$ $t = 53m\,3s$ $t = 53m\,20s$

$t = 54m\,2s$ $t = 55m\,2s$ $t = 58m\,4s$

$t = 68m\,2s$ $t = 72m\,2s$ $t = 75m\,2s$

Figure 7.20: $^{\otimes}$ Sequence of polarization, saturation and repolarization after release of stimulus S_2

Interestingly, a similar behavior was observed in another study of cell chemotaxis with *Dictyoselium Discoideum* cells subjected to changing concentrations of *cAMP* chemoattractant released from a micropippette[5]. In this experiment, the authors studied the dynamics of polarization of PIP_3, *PI3K* and *PTEN*, which is a lipid receptor and an associated kinase and phosphatase that are believed to act upstream of the RhoGTPases in chemotaxis. Exposing the cells to a stimulus gradient with a temporal component, they observed that "*an entire response ensued*

along the entire perimeter and then PIP_3 gradually polarized at the side of the cell facing the micropipette." When they brought the micropippete very close to the cell and quickly discharged the chemoattractant, "*to produce a transient bolus of cAMP, which saturated cAMP receptors and then allowed the generation of a steady state gradient at a lower midpoint concentration, PIP_3 accumulated throughout the membrane in response to the uniform stimulus, then disappeared and gradually reappeared as a crescent on the side of the cell facing the micropipette*." This is indeed the response predicted by the model, as shown in the figure above. Other observations described in that study are recapitulated as well: the response to a stimulus depends on the steepness of the gradient rather than the absolute value of the chemoattractant concentration; when a cell is exposed to two simultaneous stimulus, it is able to respond on both ends; and cells described by this model have also been shown to respond to rapidly changing stimulus. In fact, the authors of the study had previously proposed a popular theoretical model known as LEGI (Local Excitation-Global Inhibition) [198] to describe PIP_3, *PI3K* and *PTEN* polarization in chemotaxis, and argue against alternative mechanisms on the basis that they can not account for all the aforementioned observations. The LEGI model is based on the idea that the occupancy of chemotactic receptors controls two opposing processes: a fast an localized (slow-diffusing) activation signal proportional to the local fraction of occupied receptors and a global (or fast diffusing) inhibitor which is proportional to the global fraction of occupied receptors. The response is then proportional to the ratio of activator to inhibitor. Thus, gradients of varying slope and midpoint concentration are detected because activation exceeds inhibition at the cell front, whereas at the rear the opposite applies. In this way, this elegant mathematical model also leads to perfect *adaptation* to uniform stimulus, can reproduce the response to multiple stimulus and is very robust against parameter changes. However, as pointed out by Jilkine and Edelstein-Keshet [1], LEGI models can not easily reproduce *persistence* of polarization and lack the capacity to amplify gradients. Finally, experimental evidence has cast some doubt on the necessity of the molecular players proposed to mediate polarization which, perhaps from a more aesthetic point of view, makes the notion of finding a molecular target whose activation is proportional to the concentration of an activator and an inhibitor somewhat doubtful.

In their comparison of alternative models of cell polarization[1], Jilkine and Edelstein-Keshet also indicate a number of limitations in models using a wave-based mechanism to reproduce polarization. First, they note that in wave-based models the activation at the front is independent of the strength of the stimulus. This is true for Mori's conceptual model of a single RhoGTPase [134] and in Jilkine's model of the three proteins[72], but not for the model presented in this Thesis. The external signal $\Psi(x,t)$, representing in this Chapter the actual con-

centration of a chemoattractant $\rho_c(x,t)$, is transduced to the RhoGTPase signaling network through the sigmoidal input function $s[\rho_c(x,t)]$ defined in eq. 7.16. It models the strength of the modulation of RhoGTPase activation by a primary layer of cell receptors and is assumed to follow Hill-like kinetics. In Mori's and Jilkine's models, the activation rate of the RhoGTPAse is increased proportionally to the magnitude of the external signal without further amplification, and the response is essentially independent of its strength. Conversely, in the model presented here the signal is amplified by the input function, but in addition it is assumed to enter into the RhoGTPase pathway through a modification of either the Maximal Velocity of autocatalysis γ_r or the Michaelis-Menten constant of the *sensor* protein. Hence, this hypothesis leads to both amplification of the external signal and a nonlinear response that increases with its strength. The increase is bounded due to the functional form of $s[\rho_c(x,t)]$, which could be easily amended by changing the ratio of the exponents in its definition; however, it seems reasonable to assume that the capacity of the cell receptors to transduce external signals of increasing strength saturates above a certain threshold. The second drawback is related to the long time taken by the wave-based models to resolve multiple peaks of activation. They notice that this process can be accelerated by including additional components in the network. Since Mori's model describes a single protein, Crosstalk is not considered. In Jilkine's model, the existence of Turing solutions and the form of the Reaction scheme interfere to slow down transition between states. In the model proposed in this Thesis, the amplification mechanism and Crosstalk consistent with the P_o structure of the Reaction Graph lead to the faster resolution of multiple zones of activation. Related to this point, it can be shown that alternative Reaction Graphs with additional interactions between the proteins can boost this process.

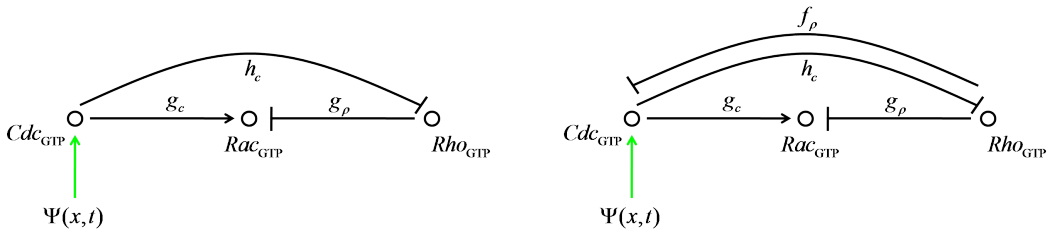

Model B Model C

Figure 7.21: Alternative Reaction Schemes for the RhoGTPases with additional inhibitory interactions from RhoA

The Graphs depicted above, which include inhibitory interactions from *RhoA* to the other proteins, maintain the qualitative behavior of the scheme labeled

as Model A and shown in fig.7.6. Both schemes polarize and resolve multiple zones of activation faster than Model A. An important difference is that Model C displays a slightly reduced sensitivity to secondary stimulus reaching the cell from the rear because the *sensor* protein *Cdc*42 is inhibited by *RhoA*. Also, the existence of a direct mutual inhibition cycle in Model C abolishes the capacity to produce *transient* polarization states. The Jacobian associated to this Reaction scheme is P_0 despite containing a positive feedback cycle, and hence Turing Patterns do not emerge. Under some combinations of stimulus releases from different spatial sources, however, complex spatio-temporal patterns of activation and oscillations of the proteins emerge, although the polarized state is eventually reached as well. As stated in Chapter 6, it would be interesting to pursue in the study of the relationship between the Reaction Graph structural properties and complex dynamics of the reaction-diffusion network such as oscillations and activations pulses. This might be particularly fruitful to interpret the wealth of data obtained from new imaging technologies that allow to observe the spatio-temporal dynamics of RhoGTPase signaling in real time with micrometer scale resolution, from which a more dynamically rich scenario than the classic view of *Cdc*42 and *Rac* activated at the front and RhoA at the rear is emerging[186]. This section concludes with a computational experiment performed to demonstrate the capacity of the model to discriminate conflicting gradients. This time, two slightly different amounts of chemoattractant are discharged simultaneously from two points situated at angles of 45° and the same distance from the cell. The quantity of chemoattractant released only differ in 10%, the diffusion and decay constants of the molecule are set to $d_s = 100\mu m^2 \cdot s^{-1}$ and $k_s = 0.05s^{-1}$, so that the resulting gradients are very shallow. The dynamics of RhoGTPase polarization are shown bellow.

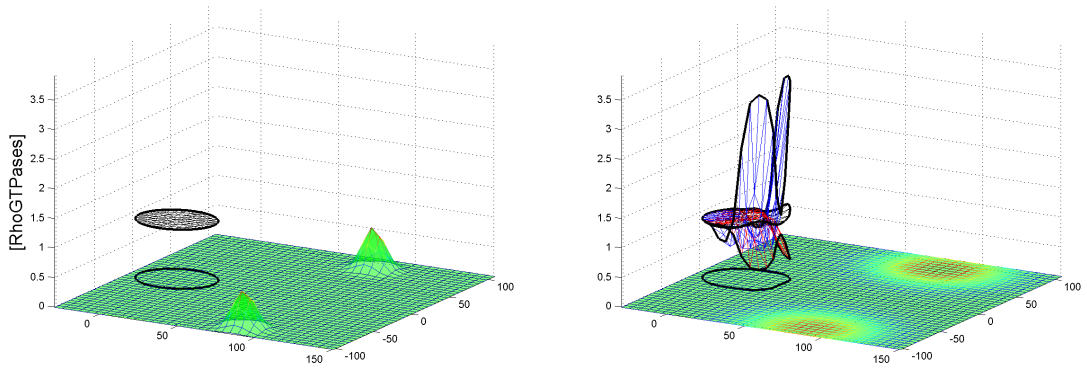

$t = 3m\,32s$ $t = 4m\,15s$

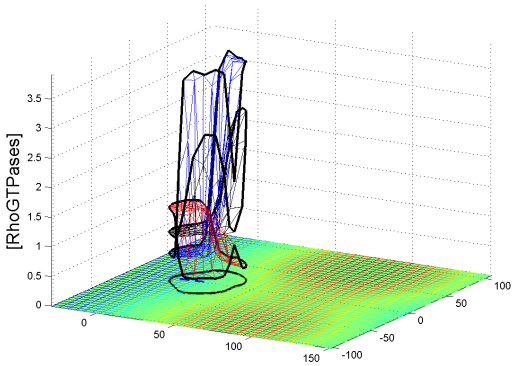

$t = 10m\,1s$

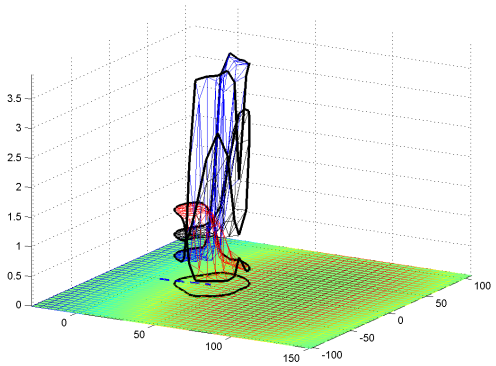

$t = 15m\,1s$

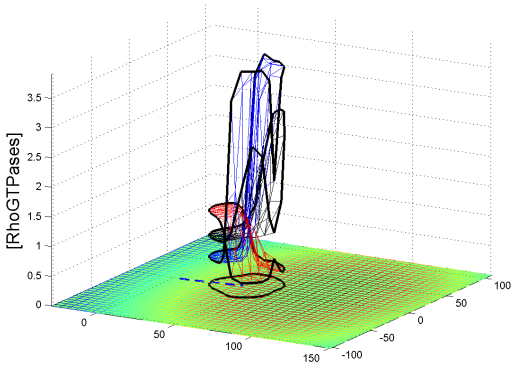

$t = 18m\,0s$

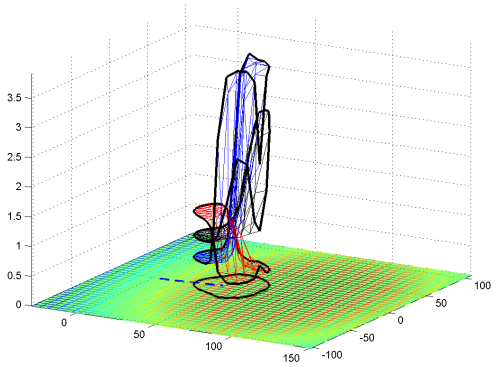

$t = 19m\,0s$

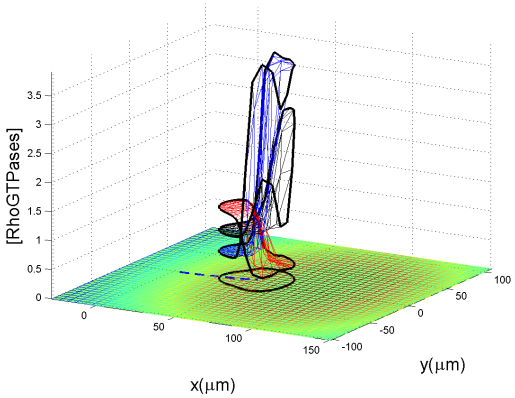

$t = 20m\,0s$

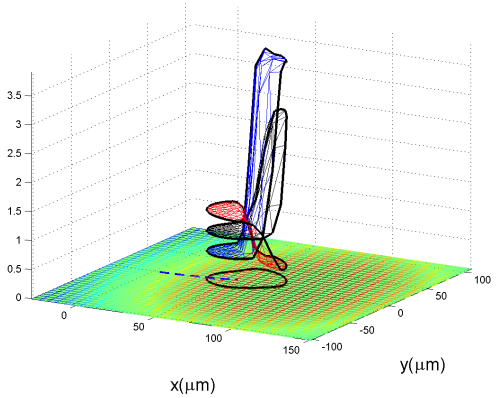

$t = 22m\,1s$

Figure 7.22: ⊗ Y-shaped extension and subsequent dominance of pseudopod closer to larger stimulus

The release of the two stimulus triggers the emergence of two symmetric zones of activation of *Cdc*42 and *Rac* at the cell front. Protrusion forces developed at these sites result in the cell forming two symmetric extensions of the leading edge pointing at the two stimulus sources, reminiscent of the shape of pseudopodia. The bipolar pattern reflects the two conflicting signals detected by the cell, and during the first 10 minutes the cell advances along the straight line equidistant from the sources of the stimulus. Eventually, the process of competition between activation zones leads to the gradual reinforcement the activation area closer to the stronger stimulus and suppression of the other. Thus, the pseudopodia-like extension associated to the weaker stimulus retracts and the cell follows an arching trajectory towards the source of the stronger signal.

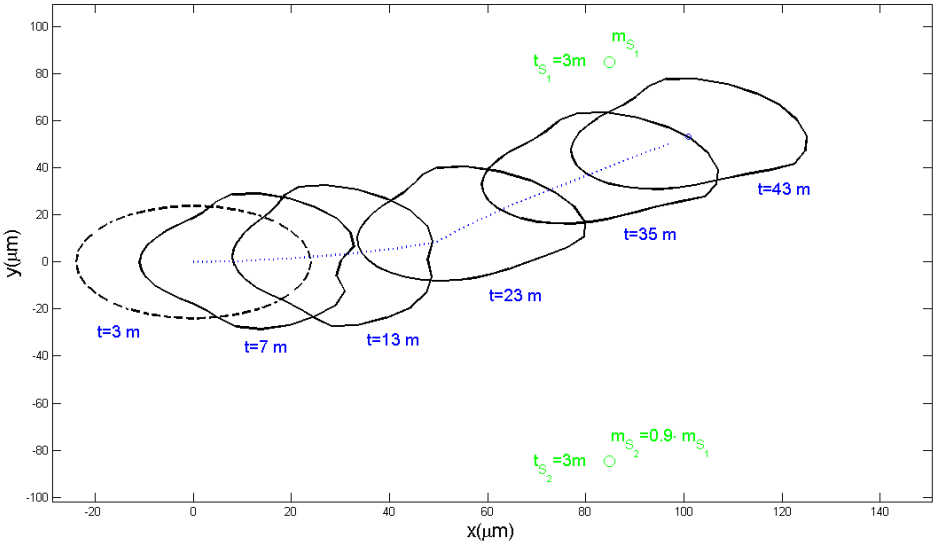

Figure 7.23: ⊗ Cell Trajectory after discharging simultaneously two stimulus with only a 10% difference in chemoattratant amount

The former computational experiment illustrates the outstanding capacity of the model to discriminate shallow gradients. It must be noted that as the chemoattractants spreads, the relative difference in steepness of the concentration gradients decreases over time. This result is particularly interesting in the context of another experimental study that aimed to asses the role pseudopodia in non-stimulated cell migration[199]. Pseudopodia are actin-rich protrusions formed randomly at the periphery of migrating cells in the absence of stimulation, but whose size and dynamics of formation becomes biased in the presence of chemoattractants or other external cues. In this study, the authors developed a novel tool

to track the position, size and frequency of formation of pseudopodia and studied the correlations with the direction of movement of starved *Dictyoselium Discoideum* cells. They observed the formation of two type of extensions in the absence of external signals: *de novo* pseudopods, which form randomly throughout the periphery of the cell, and pseudopods formed by a 60° split from the base of an existing pseudopods.

One of the main conclusions of this experiment is that there is a correlation between the ratio of the two types of pseudopods and the persistence of migration in a fixed direction. *De novo* pseudopods are associated with sudden switches of direction, whereas a high proportion of pseudopods formed from existing ones are associated to straight runs in one direction. Even though the study did not deal with gradients of chemotaxis inducing factors, this result lead them to raise an interesting question related to the mechanisms underlying this form of migration: is the biased migration along a chemoattractant gradient related to a shift in the frequency an location of pseudopod formation or is it related to some other alternative mechanism?

The results of this Chapter allow to suggest an alternative scenario: Chemotaxis could be attained without biasing the basal random rate or location of pseudopod formation, but simply by inducing the repression, by the mechanism of depletion described previously, of those extensions that are not favored by the external gradient. The coincidence of the direction of migration and the location of splitting pseudopodia would stem from the fact that the sustained extension of the surviving pseudopods gives enough time to the actin-filaments that constitute them to undergo the process of filament branching that is intrinsic to their polymerization dynamics. Consistent with this idea, well established experimental facts[47, 200] and biophysical models [201] show that actin-filament branching occurs at orientations of ±35°, which is indeed similar to the observed orientation of pseudopod splitting reported in [199]. Furthermore, the idea proposed is backed by the observations reported in [2] that the location and direction of pseudopods is not oriented nor biased by chemtacttracctants in cells migrating along a gradient, and that "*directional sensing is mediated by maintaining the most accurate existing pseudopod, rather than through the generation of new ones*"[8]. A plausible mechanism to achieve exactly that, by repression of the unfavorable extensions at the expense of those closer to the chemoattractant source, is suggested by the predictions of the model presented.

[8]In addition, they found that *PI3K* affects the frequency of pseudopod formation but not the accuracy of pseudopod selection and thus is not necessary for chemoattractant gradient sensing. This reinforces the notion that LEGI models[198, 5], while being an elegant gradient sensing model, relay on an hypothetical diffusible inhibitor whose existence is doubtful. After decades of research, it remains elusive[202]

7.4 A short digression on Cell Polarization and the Physics of Cell Migration

7.4.1 On cell polarization and gradient sensing models

The predictions and properties featured by the model derived in the present Chapter are discussed in the context of other proposed theories of cell polarization and gradient sensing. It has been shown that the model can reproduce all but one of the properties characteristic of most forms of cell migration, as defined in a comprehensive comparison of theoretical models of polarization found in [1]. The scope properties that can be recapitulated is not equaled by any other class of the models analyzed. Particularly, the model presented in this Thesis can reproduce *persistent* and also *transient* migration by a simple shift of the parameter that sets the magnitude of the autocatalytic loop of the protein controlling the emergence of polarity. This is an attractive feature, in line with the notion of plasticity of cell migration that states that different types of movement form part of a continuum powered by the same underlying mechanisms[58]. The model is also endowed with the property of *high amplification* of external signals, which combined with the fact that wave-based models do not require feedback loops to maintain polarity result in the model also featuring *reversible polarization* when new stimulus are applied and high sensitivity to rapidly changing signals. The model has also been shown to feature *multi-stimuli response* and *adaptation* to uniform stimulus. Intriguingly, the last property is not assigned to wave-based models in the comprehensive classification of theoretical models of cell polarization by Jilkine and Edelstein-Keshet [1]. This is most likely due to the fact that they analyze the behaviour of the model's by Jilkine[72] and similar models [176] as representative of the rest of models of this class. In the case of Jilkine's model, lack of *adaptation* is associated to the fact that polarization is sustained by the existence of strong feedback interactions between the proteins, which tend to lock the system when it reaches a polarized or excited state. Direct, mutually inhibiting strong interactions also account, as discussed in Chapter5, for the defective *reversible polarization* showed when new stimuli are applied. The model derived in this Thesis bypasses this requirement by assuming autocatalytic loops in the kinetics of each RhoGTPase, for which there is compelling experimental evidence. In addition, Jilkine's model is not strictly a wave-based model, because the form of Crosstalk proposed allows the emergence of Turing patterns that might interfere with the dynamics of the system. The last property defined in [1] is that of *spontaneous polarization*. Many cell types are known to polarize in the absence of external cues, whereas the model presented in this Thesis remains in the initial unpolarized state in these conditions. Spontaneous polarization is likely to stem from an stochastic

element in the cell polarization process, such as small fluctuations in the kinetic rates of the molecules involved in the underlying biochemical reactions[167]. The model presented here does not contain any stochastic ingredient, admittedly an important element of biophysical systems at the cellular scale. However, if such an ingredient were introduced in the model, *spontaneous polarization* can be readily accounted for in the framework of the New Class of polarization models. Introducing a random noise in the kinetic rates at every cell point, to represent the aforementioned fluctuations in the biochemical reactions, it can be shown that the cell switches from the initial state to an state featuring multiple and randomly distributed peaks of activations.

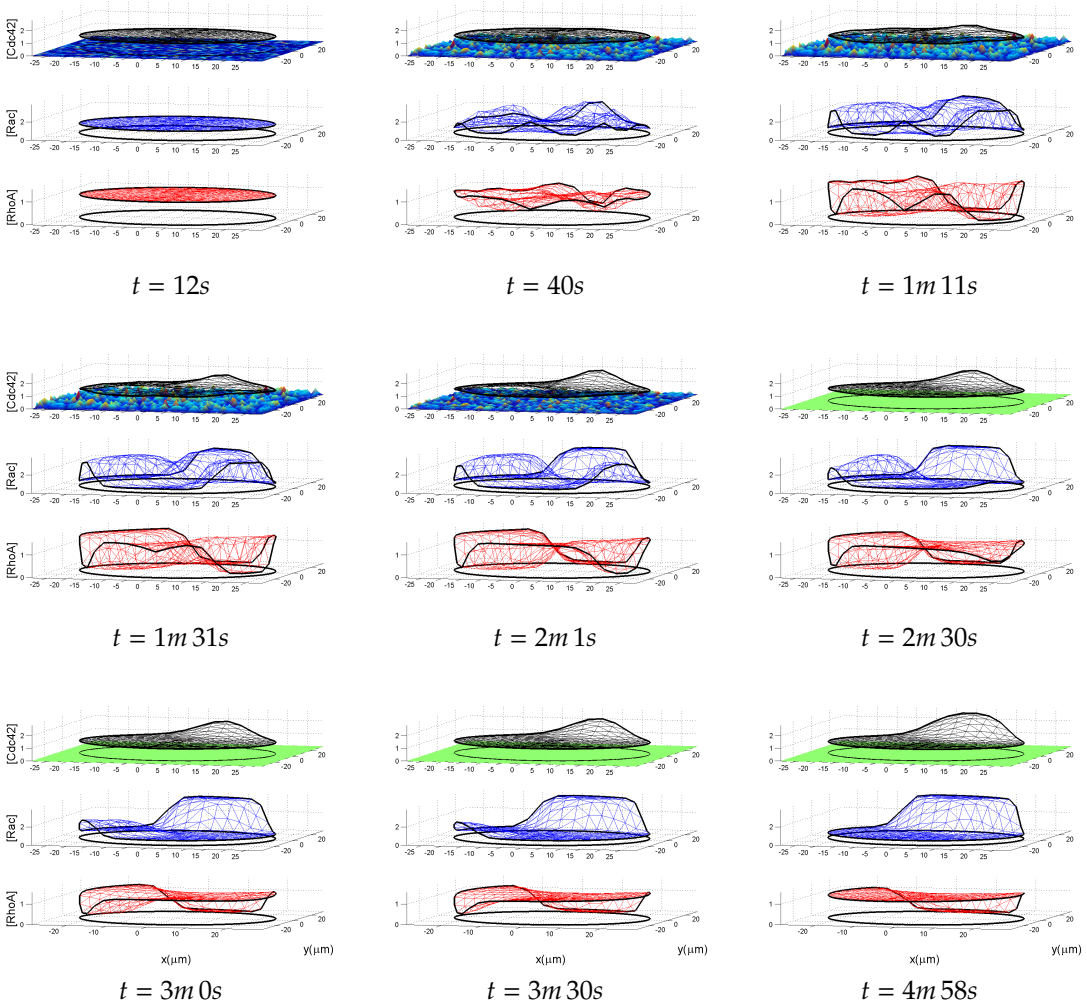

Figure 7.24: ⊗ Spontaneous polarization induced by noise

The maximum amplitude of the fluctuations was set at a tenth of the parameter Ψ_0 that sets the sensitivity scale to external signals. Amplification of the noise forces the transition to a state with multiple peaks of activation, but shortly after the competition process between activation spikes takes over and they coalesce until a well defined polar pattern emerges. Thus, in the framework of the New Class of polarization models presented, *spontaneous polarization* emerges if biological noise above a certain threshold is amplified.

7.4.2 On the physics of migration and cell shapes

The theoretical foundations to develop a regulatory network that features desired properties as spatio-temporal organizer of cellular activity during migration have been throughly discussed. Important insights for the interpretation of recent experiments of cell Chemotaxis have been discussed [2, 3, 4, 5]. Three topics, however, haven been given little attention: the shape adopted by the cell during its movement, the inclusion of protrusion as a force- boundary condition, and the differences between assuming that cells behave as an incompressible or compressible material during its movement. They shall be discussed briefly next.
Regarding cell morphology, it has been shown that the shape adopted by the cell during its movement has a remarkable resemblance with the tear-like adopted by neutrophile cells. The key hypothesis that lead to such result are the assumption of isotropic cell material properties and contraction, and the hypothesis that protrusion forces are normal to the membrane. A conceptual model of shape formation known as Graded Radial Extension model (GRE) proposes that the fan-shaped morphology adopted by migrating *fish keratocytes* can be recapitulated prescribing a normal maximum extension at the central point of the leading edge that continuously decreases toward the sides. Likewise, the shape at the rear is explained prescribing a maximum contraction at the central point that decays laterally[7]. Interestingly, the model provides a plausible explanation to such a spatial dependence: since forces are assumed to be proportional to the concentrations of proteins and they continually decay from the zone of high to low activation in the polarized state, such a force profile is obtained naturally. The only additional assumption is that forces are normal to the cell membrane, which is justified by the orientation of actin-fibers at the leading edge. Moreover, a variation between the relative of parameters that control the magnitude of protrusion and contraction forces (P_0^{prot} and τ_0^{cont}), the degree of anisotropy of the cell cytoskelton (given by the ratio of E_{xy}/E_{yx}, see eq. 3.15) allows to recapitulate different shapes characteristic of other types of cells. Furthermore, the assumed RhoGTPase crosstalk scheme has also interesting effects on the shape adopted by the cell as it migrates. It has been mentioned earlier that size of the activation

and inactivation zones and the level of activation of the proteins at this zones depends on the assumed crosstalk scheme between the proteins. For instance, the reaction schemes labeled as Model B and Model C (see fig.7.21), which both include indirect mutual inhibition between Rac and Rho, lead to sharper transitions between activation and inactivation zones and higher increase of protein activation relative to the equilibrium levels, which results in more defined zones of protrusion and contraction. Surprisingly, as the strength of the inhibition between proteins is increased this effect is reinforced and allows to recapitulate a continuous transition from the tear-like shape of *neutrophiles* to the fan-like shape of *keratocytes* (see third row):

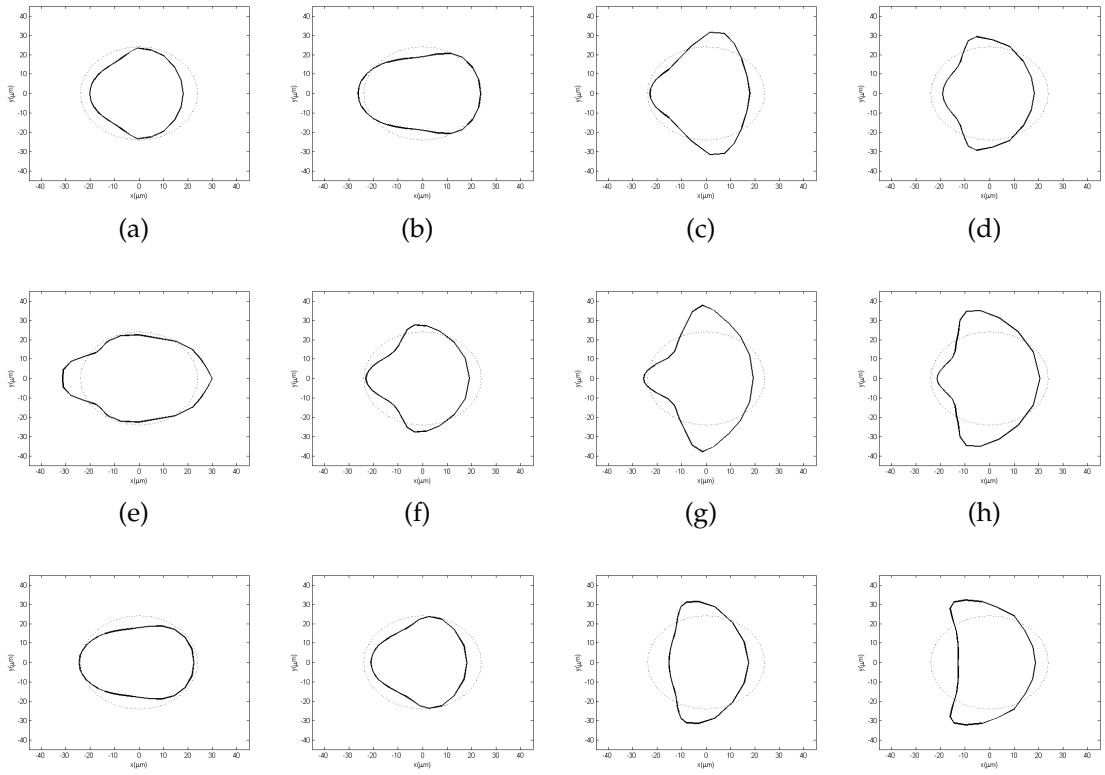

Figure 7.25: Cell morphologies recapitulated varying force parameters (first row), cytoskeleton anisotropy (second row), and Cdc42-Rho mutual inhibition strength (third row)

This result is exceedingly interesting for two reasons. First, showing that the shapes characteristic of different migrating cell types can be recapitulated by

modulating (only) the magnitude of crosstalk between RhoGTPases suggests, to my knowledge for the first time, an alternative explanation to the one generally accepted; that is, that the differences result from different levels of protrusion and contraction forces. The latter is in fact, more an observation than an explanation[9]: fan-like cells such as *keratocytes* and tear-like cells such as *neutrophiles* are known to develop different distribution and magnitude of forces during their movement; the differences in shape are then a consequence of them. But, what about the underlying cause of the difference in forces developed by different cell types?

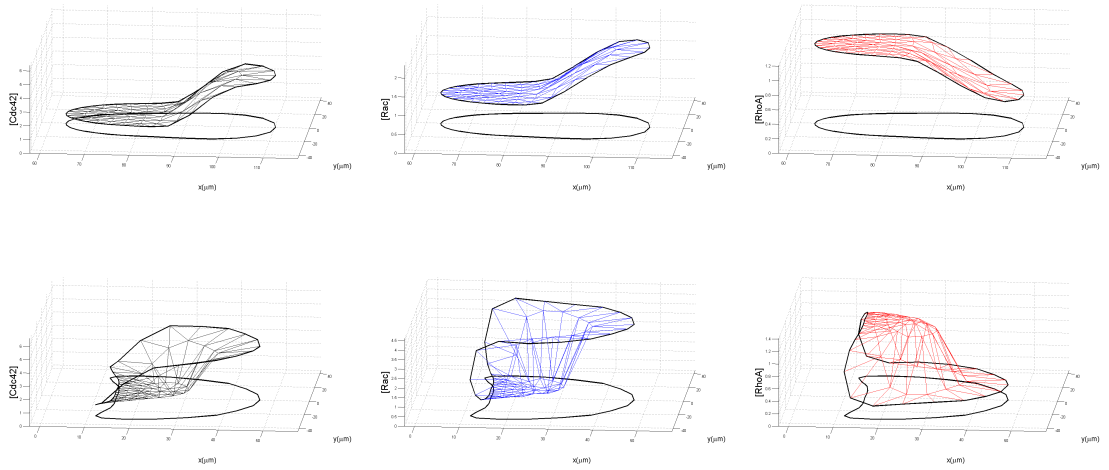

Figure 7.26: Crosstalk strength determines RhoGTPase distribution and cell morphology. Shapes characteristic of *neutrophiles* (upper row) and *keratoctyes* (lower row) are obtained for strong and weak crosstalk between proteins.

The result under discussion suggests a plausible mechanism: tuning the strength of crosstalk between RhoGTPases alters the spatial extent and relative increase of the activation zones, which in turn results in different distribution and magnitude of forces developed. This can be appreciated comparing the upper and lower rows of fig.7.26, where the two markedly different distribution of RhoGTPases lead to the *keratocyte* and *neutrophile* shapes depicted in fig.7.25 (i)

[9] A result of this type between forces and shapes was obtained by Vanderlei and coworkers in [203]. They relay on an altogether different description: the membrane is modeled as tension bearing structure that interacts with a fluid cytosol and a fluid environment, without including the cytoskeleton. Experimental evidence does not support such a mechanical role of the plasma membrane. The second important difference is that the regulatory module consists of a single protein (i.e no crosstalk) which prevents them to capture the perhaps more interesting relationship between the RhoGTPase crosstalk and cell shape.

and (l), respectively. Note that the only parameter changing is the maximum modulation of the Maximal activation velocities and Michaelis-Menten constants by Crosstalk[10]. Differences in the strength of the crosstalk between RhoGTPases could be mediated by differences between the enzyme activity or concentration of GEFs, GAPs and GDIs between different cell types; it would be interesting to explore this idea experimentally. Certainly, there might be additional mechanisms by which some cell types can develop strong forces that result in high speeds and fan-like shapes during migration, while others adopt the slow-moving tear-like shapes characteristic of *neutrophiles*, but the mechanism discussed entails a plausible and intriguing possibility.
The second reason why this result is interesting is because it connects with the notion of *plasticity* [58] that has been emphasized previously: that the observed variations in motility mode, morphology, adhesivity and other properties that define the migration of different cell types[11] might simply result from the variation in the relative magnitude of parameters controlling the different modules of a common underlying machinery.

The next aspect that is discussed is the introduction in the model of protrusion forces as a prescribed (RhoGTPase dependent) stress boundary condition. A fair criticism is that adding them in this way is an artifact because in essence amounts to add an external force, and that it does not consider the reaction forces that must be sustained by adhesion contacts at the back while actin-filaments push at the front. This is true, although it can be argued they can be neglected using the following argument. These reaction forces are channeled by a dense network of cytoskeleton filaments at the lamellipodia that physically connects the leading front with adhesion contacts. Hence, as the cytoskeleton becomes more dense an interconnected towards the rear of the cell, where its linked to adhesion sites, the reaction forces are effectively distributed amongst many contacts and therefore, as a first approximation, can be neglected. In any case, a more realistic description would require a description of the cytoskeleton to a level of detail beyond the focus of this Thesis. This issue is related to the fact that the model does not capture the biphasic relationship between cell velocity and adhesiveness of the substrate discussed previously. It must be said, however, that such a relationship should be expected of any system relaying on adhesion or friction with surface to move. For low adhesiveness, rearward traction forces produce small forward reaction forces required to advance; for high adhesiveness, forward reaction forces are high but the strong adhesion to the substrate hinders the release of adhesion points. It fol-

[10]Precisely, shifting the values of $|\eta| = |\phi|$ from 0.125 to 0.75 in eq.7.13 leads from *neutrophile* to *keratocyte* characteristic shapes

[11]The addition of Focal adhesions, providing points of strong anchorage to the substrate at the rear of the cell, leads elongated triangular shapes characteristic of fibroblasts.

lows that there is a optimum range of adhesiveness in between where maximum velocities are achieved. However, the existence of this biphasic relationship can be recapitulated once Focl adhesions are added to the description of cell migration in the next chapter. Further, it will be shown that this relationship does not arise from simple mechanical principle, but from the complex interplay between the adhesion an regulatory machinery; a notion that is supported by experimental evidence [204, 196].

Finally, a brief discussion of the effects of considering the cell an compressible or incompressible material. It has been said that the results obtained with one or the other alternatives are qualitatively similar. This, however, does not hold for high levels of protrusion and contraction forces. In this case, the compressible assumption leads to interesting behaviors associated to the effective dilution of RhoGTPase concentration when the cell extends and the increase in concentration when the cell contracts. This coupling between the geometrical and regulatory modules can lead to complex dynamics, such as waves and oscillations of RhoGTPase concentration and forces. This complex dynamics have not been investigated further, although they could indeed have an important role in cell migration. Generally, all the models of cell migration assume the more simple incompressible assumption, arguing that since the cell is basically a water container, it should be nearly incompressible. This is however not necessarily true, because variations of osmotic pressure and flow of cell content through the permeable plasma membrane can certainly lead to volumetric changes. In fact, such changes have been proved to be relevant for at least two cell processes in recent studies. The movement of *Euglenoids* cells, a type of primitive bacteria, relays on periodic changes of volume and shape to swim at low Reynold numbers[205]. The coupling between cell shape changes and pulsating forces is also central in the process of dorsal closure during the development of *Drosophila* embryo[206]. Hence, it would be interesting to further investigate the possible role that this might have in migration, a topic that, to my knowledge, has been so far largely neglected.

I think I must have another go at the Matterhorn. I have got a most original idea which I should like to try.

Edward Whymper, illustrator and explorer

Chapter 8

A new view on cell durotaxis

Any cell type, other than neurons, when cultured on a substrate with a gradient of rigidity, will migrate in the direction of higher stiffness. This principle, known as Durotaxis, operates in physiological conditions and has also important implications in disease[29, 30]. For instance, the elasticity of the extracellular matrix has recently been found to be a crucial factor specifying the lineage fate of stem cells [207] and is a central element in the orchestration of embryo morphogenesis [208, 209]. Regarding pathologies, numerous observations demonstrate that the influence of the matrix mechanical properties on growth, apoptosis[41] and motility [42] of cancer cell is different than in normal cells, which has important implications for their metastasic potential [32, 43, 44, 45]. New experimental setups are providing increasingly precise data on the different aspects of the process, from the relationship between gradient strength, migration speed and phenotype[13, 37]; the role of adhesions and cytoskeleton dynamics[56, 57]; to the genes and molecular players involved[210, 38]. Yet, the underlying mechanism of mechanosensing and durotaxis remains largely unknown.

The evidence gathered proves that Focal Adhesions are the main actors in the first stage of cell response to stiffness, and a number of different theoretical models have been proposed to explain how they act as local mechanosensors. However, independently of the physical or biochemical principle at play, a fundamental question has not been addressed either from a theoretical or experimental perspective: detecting a gradient, mechanical or otherwise, requires by definition measuring *differences* in the property being sampled. For the particular case of cell durotaxis, let this point be made more clear with an idealized depiction of the process. A cell is plated on a substrate featuring a stiffness gradient, and the gradient results strictly from mechanical properties; there is no other anisotropy in the topography or the density of ligands on the surface. Two Focal Adhesions have been formed at each extreme of the cell body, so that FA_1 lays on a position

of higher stiffness than FA_2. The cell tests the substrate by an unspecified process and each adhesion, by an unspecified mechanosensing process, transduces the local mechanical information into two signals[1] s_1 and s_2 that elicit a cell response: migration in the direction of higher stiffness.

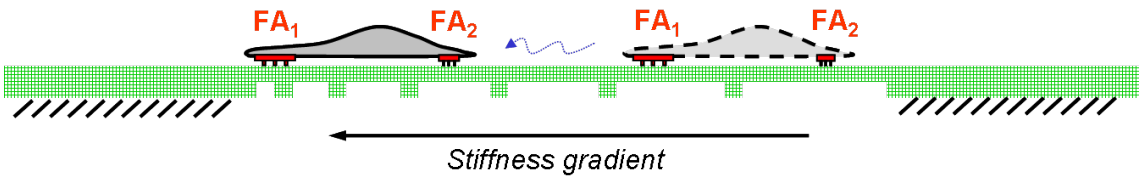

Figure 8.1: Detection of a stiffness gradient requires integrating the mechanical information gathered locally at FAs

Eventually, as the cell moves forward, it reaches a position in which a new FA_2' lays on the spot where FA_1 was before. Again, each Focal adhesion reports the local mechanical information, but the signal emitted by FA_2' must be exactly the same sent by FA_1 in the previous migratory step. However, since FA_1' has been formed in a region of higher stiffness than FA_2' , the cell detects the *difference* in signals emitted and resumes its motion along the gradient. It follows that Durotaxis requires *comparing* the response of Focal adhesions to the mechanical properties of the substrate, which is precisely the point that was meant to be emphasized: sensing a rigidity gradient and follow the direction of increasing stiffness necessarily requires *integrating* the mechanical information gathered by the mechanosensors.

Note that this account rests on the following assumptions: Focal adhesions *are* the mechanosensors; the signal emitted is determined, at least initially, only by the substrate mechanical properties *and* the pulling force exerted by the cell to test the substrate; and Focal adhesions have no memory. Ample experimental evidence supports the first hypothesis, as reviewed in [59, 211, 104, 212, 50] and references therein. The second hypothesis is based on the fact that Focal adhesions are the link between the cell and the substrate, while the experimental setups used in Durotaxis essays guarantee that the substrate is homogeneous in any property aside from stiffness. In addition, the fast characteristic times of FA adaptation to changes in stiffness of the order of seconds[213, 11] supports that the response,

[1]The word signal is used as an abstraction of an undetermined reaction undergone by a Focal adhesion to the mechanical test that allows the cell to determine the local stiffness. It is not meant to imply any specific form of FA-cell communication, such as a biochemical signal or adhesion remodeling, since the actual mechanism is not known.

at least initially, is of purely mechanical nature. During this short time-scale, the experimental evidence also shows that the process of mechanically proving the substrate involves a tight spatio-temporal control of the force applied by the cell at individual focal adhesions [9, 10, 14]. Regarding memory, the assumption rests simply on the fact that FAs are broken and reassembled as cells move.

Hence, understanding cell durotaxis involves two fundamental questions: How do Focal Adhesions act as mechanosensors? How do cells integrate the mechanical information to measure a gradient and migrate along it? A new hypothesis, based on a simple physical principle, is proposed that might address them.

8.1 Durotaxis: A simple physical mechanism?

The starting point to introduce the hypothesis is the description of a single Focal Adhesion developed in section 3.3 of Chapter3. The mechanical state of a contact is defined by the number of receptors $N(t)$ bound to substrate ligands, the total force $F(t)$ applied by the cell onto the adhesion, and the stiffness $k_s(E_s)$ of the anchorage point. The total force, as derived in eqs.3.37-3.39, determines the force $f(t) = F(t)/N(t)$ withstood by each receptor, the displacement of the Focal adhesion $u - u_0^{FA}$ from the anchorage point, and energy $e_R(f)$ stored by each receptor due to the mechanical stretch. In turn f, u, and e_R determine the rates of bond formation and rupture and thereby the dynamical evolution of the number of bound receptors $N(t)$ in the Focal Adhesion, according to the governing equation 3.34. The hypothesis on how cell test the mechanical properties of the substrate

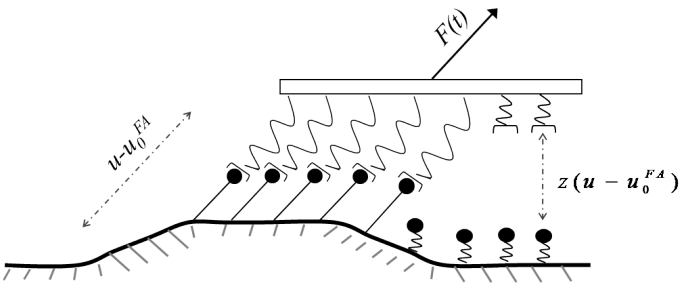

Figure 8.2: Schematic description of FA mechanics

is postulated as follows: *Cells probe the substrate at each FA independently and investing a constant power per bound receptor to pull on the substrate*. The underlying molecular process that could bring about such a mechanism can be envisaged in the following way: in the neighborhood of a Focal Adhesion there is an excess

of energy-storing molecules, namely *ATP*, which are consumed at a constant rate by a contractile structure, namely actin-myosin-II filaments, which are anchored at the intracellular domain of every receptor engaged to a ligand. Thus, the mechanosensing hypothesis contains an implicit assumption; that upon the formation of every new pair of ligand-receptor bonds, a traction-bearing structure is either activated or anchored at the intracellular domain of the receptor in a short timescale of the order the binding events. Then, this structure initiates an uptake of energy-storing molecules at a constant rate, determined by the kinetics of the molecular motor-filament system, and as the filament contracts, a pulling force is developed. This hypothesis was formulated as plausible theoretical mechanism that could explain Durotaxis with no regard to experimental evidence. However, a set of recent experimental studies provide convincing support to its assumptions. First, a remarkable study using time-lapse traction force microscopy, published during the completion of this Thesis, has demonstrated that centripetal cell generated forces pull on each adhesion repeatedly and autonomously, and that this sampling process is required for Durotaxis[14]. Regarding filament attachment and force control at the short time-scales required by the hypothesis, the support can be found in different studies focused on the characterization at single FA level of force development and myosin-II recruitment in real time. Cell force is found to adapt to stiffness changes in times samller than 1 second [8, 213, 11], whereas the rates of recruitment of myosin-II and actin [9, 10] to Focal adhesion sites is modulated in short-timescales that are also consistent. Time-scales and magnitudes of the force ramps in these studies are central to the theory of Durotaxis developed here and will be discussed later. First, it will be shown that the simple hypothesis proposed promotes faster and stronger maturation of adhesion sites on stiffer anchorage points.

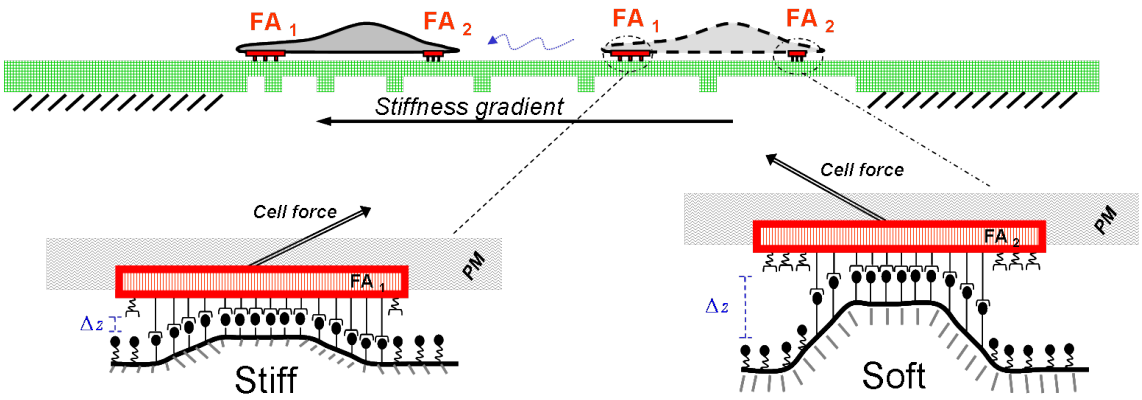

Figure 8.3: Focal adhesion nucleation is favored at the stiffer edge of the cell

Intuitively, this principle can be explained by the fact that the hypothesis proposed leads to faster force build-up, higher energy storage, and smaller separation from the substrate at the receptors of the Focal adhesion at the stiffer end of the cell. The proposed hypothesis is expressed mathematically as follows:

$$p_0 = \frac{de}{dt} = \frac{d}{dt}\left[\frac{f(t)}{2\bar{k}}\right] = \frac{f(t)}{\bar{k}}\dot{f}(t) \tag{8.1a}$$

$$F_{FA}(t) = N(t) \cdot f(t) \tag{8.1b}$$

The first equation states that the energy spent to pull on each ligand-receptor pair per unit of time during the mechanical sampling process is constant, with p_0 being the intrinsic power defined by the kinetics of the molecular motor-filament system, $\bar{k} = k_P \cdot k_S(E_S)/(k_P + k_S(E_S))$ the compound spring constant of the ligand-receptor-substrate[2], and $f(t)$ the force produced on the ligand-receptor pair. The second is a consequence of the hypothesis, stating that the total resultant force applied on each FA is maintained proportional to the number of engaged receptors, which in turn sustain the loading force determined by the postulated principle. The time-evolution of force build-up on each ligand-receptor pair is found integrating equation 8.17a.

$$f(t) = \sqrt{2 \cdot \bar{k} \cdot p_0 \cdot t} \tag{8.2}$$

Given $f(t)$, the displacement from the point where the FA is initially forming can be derived from eq.3.38 as $u(t) - u_0^{FA} = \sqrt{2p_0 \cdot t/\bar{k}}$, and the mechanical energy stored on each ligand-receptor pair can be calculated as $e_P(t) = \bar{k} \cdot p_0 \cdot t/k_P$ from 3.39. This result already shows that force is built faster and that energy storage increases with stiffness, whereas the displacement from the substrate induced by the loading force, which hinders the formation of bonds, is lower with higher $\bar{k}$.

[2]Introduction of typical values of E_S for the Young's modulus of the substrate and the radius of an integrin receptor [214, 215] in eq.3.35 to estimate $k_S(E_S)$ and comparison with measured values for k_P [216] leads to $k_P >> k_S$. Since the compound spring constant of two springs in series is determined by the weaker link, $\bar{k} \approx k_s(E_s)$ largely reflects the stiffness of the substrate.

The variables defining the mechanical sampling process are scaled using the following argument. In the study of Durotaxis cited previously[14], characterizing experimentally for the first time the actual process of fibroblasts sampling the stiffness of the extracellular matrix by repeatedly tugging on individual adhesions, it was observed that the force on each adhesion follows a sequence of periodic increases in tension and subsequent relaxation. The period of force oscillation is approximately of $30 - 50$ seconds, which suggests that the tugging process has characteristic duration t_{cont} that may depend on the type of cell. On the other hand, different cell types are known to thrive in a particular range of substrate stiffness[217, 218, 219, 220], but when they are cultured in too compliant substrates, Focal adhesions can not form and the rate of apoptosis is increased[8, 122]. This suggests that for each cell type there must be a characteristic range of stiffness where cells can develop an adequate level of tension for the maturation of their contractile machinery. Let $\bar{k}_{ref}$ be the stiffness at the lower end for viable Focal adhesions to form in an specific cell type. According to the tugging process described above and the constant power hypothesis, during the sampling period t_{cont}, the cell would develop a force $f_g = (2 \cdot p_0 \cdot \bar{k}_{ref} \cdot t_{cont})^{1/2}$ per ligand-receptor pair, sufficient for Focal Adhesions to grow and stabilize. The displacement and energy stored per ligand receptor pair reached at the end of the sampling process are then given by $u_g = f_g/\bar{k}_{ref}$ and $e_g = f_g^2/2k_P$. The temporal evolution of $f(t)$, $u(t) - u_0^{FA}$, and $e_R(t)$ can then be expressed in terms of these parameters as:

$$\frac{f(t)}{f_g} = \sqrt{\frac{\bar{k}}{\bar{k}_{ref}} \frac{t}{t_{cont}}} \qquad \frac{u(t)-u_0^{FA}}{u_g} = \sqrt{\frac{\bar{k}_{ref}}{\bar{k}} \frac{t}{t_{cont}}} \qquad \frac{e_P(t)}{e_g} = \frac{\bar{k}}{\bar{k}_{ref}} \frac{t}{t_{cont}} \tag{8.3}$$

The expression summarizes the core of the Durotaxis principle. The ratio of these variables at Focal adhesions formed at anchorage points with a difference of stiffness results in a shift in the rates of bond formation and rupture and thereby their maturation and stability. It is now possible to return to the conceptual scenario introduced at the beginning of this chapter and depicted in fig. 8.3 to illustrate Cell Durotaxis. Indeed, the displacement induced by the pulling force on FA_1 is smaller than in FA_2, which results in a higher the rate of bond formation (see eq.3.31 for $W_f(u - u_0^{FA})$ and its derivation). The mechanical energy stored in the receptor is also higher, so that the level required to trigger the inside-out mechanism of valency regulation that controls the number of available receptors at FA_1 is reached faster (see eq.3.33 for $N_T(e_P)$ and its derivation) . Finally, the loading force per receptor in FA_1 is higher than in FA_2, which increases the rate of bond rupture (see eq.3.30 for $W_r(f)$ and its derivation); however, since the force

scale f_0 required to break the molecular bonds is presumably an order of magnitude bigger than the force f_g required to trigger their activation, these effect is largely offset by the boost in growth associated to the others. Thus, ratio of $f(t)$, $u(t) - u_0^{FA}$, and $e_R(t)$ at FA_1 and FA_2 is given by eq.8.3 as:

$$\frac{f^{FA_1}(t)}{f^{FA_2}(t)} = \sqrt{\frac{\bar{k}_1}{\bar{k}_2}} > 1 \qquad \frac{u^{FA_1}(t) - u_0^{FA_1}}{u^{FA_2}(t) - u_0^{FA_2}} = \sqrt{\frac{\bar{k}_2}{\bar{k}_1}} < 1 \qquad \frac{e_P^{FA_1}(t)}{e_P^{FA_2}(t)} = \frac{\bar{k}_1}{\bar{k}_2} > 1 \tag{8.4}$$

In addition, the hypothesis leads to the prediction that a cell laying on a very soft substrate, so that $\bar{k} << \bar{k}_{ref}$ would develop a small force $f(t_{cont}) << f_g$ insufficient to promote FA growth, as the experimental evidence proves[8, 122]. Note that this result has been derived assuming the mechanical description of a Focal adhesion introduced in Chapter3, but it is nonetheless general. The constant power hypothesis postulated, even in a more complex description, including a viscoelastic resistance to the pulling force from the membrane or other structures interacting with the adhesion, leads to the same principle: force and energy storage are favored at stiffer anchorage points, displacement is smaller. In fact, the prediction of the constant power hypothesis is also independent of the Kinetic description of a FA, as long as displacement from the anchorage point reduces the rate of bond formation, and the scale of the force per receptor that leads to bond rupture is larger than the force that promotes growth.

8.2 Is cell mechanosesning controlled by strain or stress? Neither

The notion that Focal Adhesion maturation is promoted by stiffness has been explained qualitatively. Next, it will be demonstrated analytically studying the solution of the equation 3.34 governing the dynamics of the number of closed bonds $N(t)$ in a FA. The results of this section provide a plausible answer to the first of the fundamental questions stated earlier: How do Focal Adhesions act as mechanosensors?

The theoretical predictions that result from this analysis are important because they can be compared with experimental measurements contained in recent studies [8, 9, 10, 11] of real-time area growth and force development in Focal Adhesions, including their dependence on substrate rigidity. More precisely, the predictions will be compared to measurements of Focal adhesion area growth in real time $A^{FA}(t)$ in [10, 11], total force per focal adhesion in real time $F(t)$ in [9, 11] and

its dependence on the substrate stiffness[9, 11], traction stress in real time $\sigma^{FA}(t)$ [10, 11], and its dependence on stiffness [8, 11] and finally, the dependence of the saturation force $F_{sat}(t_{cont}, \bar{k})$ per Focal adhesion on the stiffness[8, 11]. A point that must be emphasized beforehand: the predictions match remarkably the experimental data gathered from different techniques, substrate elasticity ranges and cell types. Thus, the mechanosensing hypothesis provides a unifying principle that allows to explain a wide range of allegedly conflicting data. The disparity of data has been attributed to differences in experimental set-ups and cell types, but it also has fueled an ongoing controversy on how cell test the mechanical properties of the substrate, with essentially two opposing camps defending that cells either exert a constant displacement-strain[221, 11, 222] or stress [8, 49, 223] to assess the mechanical properties of the environment. The scope of observations that can be explained by the hypothesis proposed here, to wit, that cells in fact spent a constant amount of energy per time pulling on the substrate, has important implications for this issue.

The equation derived in section 3.3 for $dN(t)/dt$ is now restated introducing the force f_g, displacement u_g and energy e_g characteristic of the mechanical sampling process as the scales for the corresponding parameters determining the rates of bond rupture and formation. As a reminder, f_o is the force scale that determines the rate of rupture events, u_o is the displacement scale that determines the rate of binding events and e_0 sets the energy scale of receptor activation by the postulated inside-out mechanism of valency regulation[3].

$$f_o = \lambda_1 \cdot f_g \qquad u_0 = \lambda_2 \cdot u_g \qquad e_o = \lambda_3 \cdot e_g \tag{8.5}$$

The parameters f_0, u_0, and e_o were derived in terms of the energy landscape of the ligand-receptor potential and molecular properties of the receptors and can be estimated from experimental observations[120, 119, 121]. The important point is their proportionality λ with the characteristic values reached during the mechanical testing process.

[3]Adhesion avidity (i.e. strength) is likely controlled by an additional channel of inside-out signaling to modulate receptor affinity[215, 121], which is assumed to occur downstream of RhoGTPase signaling. See section3.3 for the discussion of the molecular mechanisms postulated that result in a dependence of $f_o(\mathbf{r})$ and $u_o(\mathbf{r})$ on RhoGTPase signaling. This process, however, takes place on a longer time-scale than that of the mechanical sampling process and is not necessary to demonstrate the principle. Modulation of integrin affinity by inside-out signaling will have an important role as a mechanism to *amplify* rigidity gradients, as shown in the next section where the mechanosensing hypothesis is implemented in the migration model to investigate Cell Durotaxis.

Introduction of these definitions in the equation governing the evolution of $N(t)$ leads to[4]:

$$\frac{dN(t)}{dt} = -w_0\, e^{\frac{f(t)}{\lambda_1 f_g}} \cdot N(t) + w_0'\, e^{-(\frac{u(t)}{\lambda_2 u_g})^2}[N_T \frac{e_P(t)}{e_P(t) + \lambda_3 e_g} - N(t)] \tag{8.6}$$

As explained earlier, a condition for the Durotaxis principle to work is that $\lambda_1 >> 1$, so that the force required to break a ligand-receptor bond is larger than the forces reached during the mechanical test. λ_2 and λ_3 are assumed to be close to ~ 1, so that the cell is sensitive to the dispalcements and forces developed during the mechanical sampling process. The intrinsic rate of bond formation is expressed in terms of the intrinsic rate of bond rupture as $w_0' = w_0 \cdot \alpha$; where $\alpha \sim 1$ but is kept to maintain the analysis as general as possible. The analysis of eq.8.6 is divided in three timescales defined by $1 \sim w_0 \cdot t << w_0 \cdot t_{cont}$, $1 < w_0 \cdot t < w_0 \cdot t_{cont}$ and $w_0 \cdot t \sim w_0 \cdot t_{cont}$. The first two time-intervals correspond to an intermediate period, longer than the time required for rupture and binding events to occur but smaller than the characteristic time of the mechanical sampling process, so that $f(t) < f_g << \lambda_1 \cdot f_g$, $u(t) < u_g$ and $e_P(t) < u_g$. Conversely, for $t \sim t_{cont}$ the mechanical sampling process is near its end and the variables fulfill $f(t) \sim f_g << \lambda_1 \cdot f_g$, $u(t) \sim u_g$ and $e_P(t) \sim e_g$.

The analysis starts in the intermediate time-scale of the sampling process, in which the variables that determine FA dynamics are small, so that according to equations 8.3 the terms in eq. 8.6 that modulate the kinetic rates can be approximated as:

$$e^{\frac{f(t)}{\lambda_1 f_g}} \approx 1 \qquad e^{-(\frac{u(t)}{\lambda_2 u_g})^2} \approx 1 \qquad \frac{e_P(t)}{e_P(t)+\lambda_3 e_g} \approx \frac{1}{\lambda_3}\frac{\bar{k}}{\bar{k}_{ref}} \cdot \frac{t}{t_{cont}} \tag{8.7}$$

Introduction of this approximation in eq.8.6 leads to:

$$\frac{dN(t)}{dt} \approx -w_0 \cdot N(t) + \alpha \cdot w_0 (N_T \frac{1}{\lambda_3}\frac{\bar{k}}{\bar{k}_{ref}}\frac{t}{t_{cont}} - N(t)) \tag{8.8}$$

[4]The point of formation of the FA has been considered to take place at $u = 0$ to alleviate the notation, so that $u(t) - u_0^{FA} = u(t)$.

This equation has the following analytical solution[127, see chapter 8]:

$$\frac{N(t)}{N_T} \approx \frac{1}{\lambda_3}\frac{\bar{k}}{\bar{k}_{ref}}\frac{\alpha}{(1+\alpha)^2}\frac{1}{w_0 t_{cont}}(w_0(1+\alpha)\,t + e^{-w_0(1+\alpha)\,t} - 1) \tag{8.9}$$

which already shows that the number of closed bonds is an increasing function of the stiffness of the substrate. Particularly, for the time-scales $1 \sim w_0 \cdot t << w_0 \cdot t_{cont}$ and $1 < w_0 \cdot t < w_0 \cdot t_{cont}$, the number of closed bonds goes as:

$$\frac{N(t)}{N_T} \sim \begin{cases} \frac{1}{\lambda_3}\frac{\alpha}{2}\frac{\bar{k}}{\bar{k}_{ref}}\frac{w_0 \cdot t^2}{t_{cont}} & 1 \sim w_0 \cdot t << w_0 \cdot t_{cont} \\ \frac{1}{\lambda_3}\frac{\alpha}{(1+\alpha)}\frac{\bar{k}}{\bar{k}_{ref}}\frac{t}{t_{cont}} & 1 < w_0 \cdot t < w_0 \cdot t_{cont} \end{cases} \tag{8.10}$$

The ratio in the number of closed bonds between two adhesions anchored at points with different stiffness can be calculated from this result, which in both the short and intermediate time-scale of FA maturation goes like:

$$\frac{N_1(t)}{N_2(t)} \approx \frac{\bar{k}_1}{\bar{k}_2} \tag{8.11}$$

It follows that if $\bar{k}_1 > \bar{k}_2$ then $N_1(t) > N_2(t)$, that is, the adhesion at the stiffer spot grows faster. This prediction is consistent with the long established observation that cells develop bigger FAs in rigid substrates and that for very soft substrates they can not be formed. The governing equation $N(t)$ can not be solved analytically for the longer time-scale $w_0 \cdot t \sim w_0 \cdot t_{cont}$, but this notion can be substantiated analyzing its steady state solutions. Setting $dN/dt = 0$ in eq. 8.6 allows to express the number of closed bonds at the equilibrium state at $t = t_{cont}$ as:

$$\frac{N_{eq}(t_{cont},\ \bar{k})}{N_T} = \frac{a(\bar{k})}{[a(\bar{k}) + \lambda_3]}\frac{\alpha}{[\alpha + e^{1/[\lambda_2^2 \cdot a(\bar{k})]}]} \tag{8.12}$$

where the relative stiffness is defined as $a(\bar{k}) = \bar{k}/\bar{k}_{ref}$. Thus, $N_{eq}(t_{cont}, \bar{k})$ is an increasing but bounded function of the stiffness that fulfills $N_{eq}(t_{cont}, \bar{k}) \to 0$ for

$\bar{k} \rightarrow 0$. The equilibrium solution is only reached in a substrate with stiffness comparable to $\bar{k}_{ref}$. For soft substrates, $\bar{k} << \bar{k}_{ref}$ implies $u(t \rightarrow t_{cont}) >> u_g$, so that the displacement induced by the force developed during the pulling process results in a vanishing rate of bond formation. After a transient increase in the number of bonds, the displacement from the anchorage point leads to exponential decay and rupture of adhesion formed in soft substrates.

8.2.1 Area of Focal Adhesions in real time: theory and measurements

The number of closed bonds can be used as an estimation of the area $A^{FA}(t)$ of a Focal adhesion during the intermediate time-scales of maturation. The relationship is based on the observation [224] that the density ρ_I of integrin receptors in a FA remains approximately constant after the nucleation phase; it must be remembered that this part of the process is outside the range of the analysis. This leads to the simple relationship $A^{FA}(t) = N(t)/\rho_I$. The predicted evolution of $N(t)$ for the initial phase of Focal Adhesion maturation given in 8.10 can then be compared with the measurements in real time of area growth of Focal adhesions from two recent experimental studies. In [11], the area of fluorescently

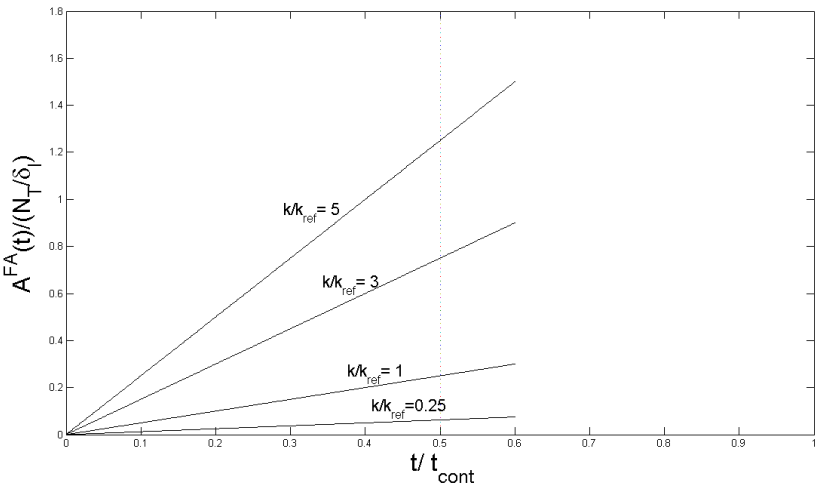

Figure 8.4: Predicted Initial regime of stiffness-dependent Focal adhesion Area growth. Compare to fig. 2B in [11]

.

tagged Focal adhesions of *REF*52 Fibroblasts was measured culturing the cells on substrates featuring micron-sized pillars of various diameters to obtain different

effective stiffnesses. The area of focal adhesions was found to grow linearly in time for a timespan of the order $5 - 8$ minutes followed by a saturation phase to a size of approximately $5\mu m^2$ after 10minutes. The slope of the curves $A^{FA}(t)$ was found to increase with stiffness, and although the functional dependency in $A^{FA}(t, \bar{k})$ was not calculated, the data is consistent with a linear dependence in $\bar{k}$ in the initial phase of FA growth. The theoretical prediction given in eq. 8.10 and depicted in fig.8.4 captures the linear growth in time in this initial phase, and predicts also a linearly increasing rate of area growth with stiffness, which could be confirmed experimentally. This result has been obtained with $\alpha = 1$ and $\lambda_3 = 1$; note that changing the ratio of the activation and inactivation rates by varying α or the receptor activation energy λ_3 only shifts the slope of area growth but the dependency in $\bar{k}$ and t is preserved. A similar behavior was observed in another experiment [10] tracking the growth of Focal adhesions in $3T3$-Fibroblasts and Osteosarcoma cells: an initial regime of linear growth in time of $A^{FA}(t)$ for 5 minutes followed by the stabilization of the adhesion size at $1.6\mu m^2$ and $3.0\mu m^2$ for $3T3$-Fibroblasts and Osteosarcoma cells, respectively. In this essay no attempt was made to characterize the dependence of FA growth with $\bar{k}$ by using different substrates. Therefore, the interpretation of the measurements of $A^{FA}(t)$ from both

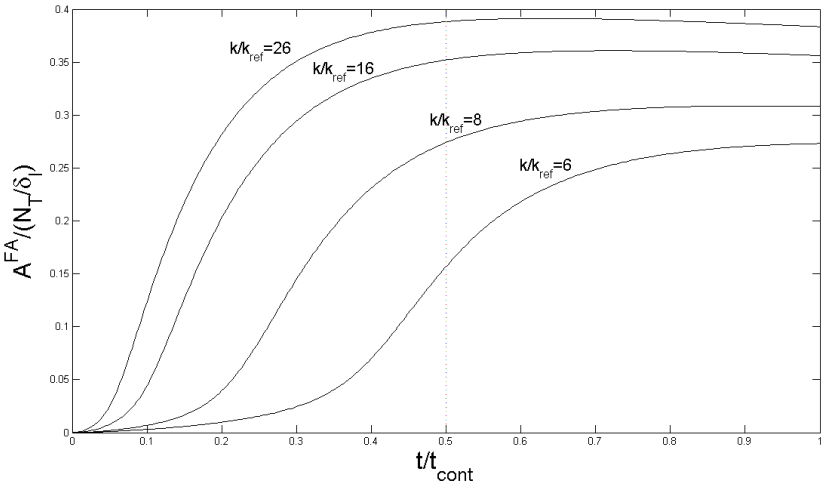

Figure 8.5: Predicted Focal adhesion growth and saturation for $t \in [0, t_{cont}]$. Compare to fig. 2B in [11] and figures 3a(top) and 4b(top) in [10]

.

studies is straightforward within the framework of the mechanosensing theory: FA maturation is promoted by the postulated pulling force, which initially leads to a linear increase of $A^{FA}(t)$ in both time and substrate stiffness. The linear regime only applies to $t < t_{cont}$; for $t \to t_{cont}$ the approximations $e_P(t) << e_g$ and $u(t) << u_g$

and are no longer valid and the decrease in the binding rate leads to the saturation phase. Numerical solution of the fully non-linear equation for $dN(t)/dt$ allows to predict the complete dynamics of Focal adhesion area growth. This result, depicted in fig.8.5; shows that the theory captures the observed evolution of $A^{FA}(t)$ from an initial rate of linear growth in time to a saturation phase (compare with figures 3a(top) and 4b(top) in [10]). Moreover, it also matches the reported increase in the rate of area growth with the stiffness of the substrate(compare with fig. 2B in [11]). Again, the qualitative agreement of the solutions with the observations has been obtained by just using plausible values from a theoretical standpoint[5] for the non-dimensional parameters λ_i and α; a close fit with the reported data could be obtained by adopting values estimated from experimental measurements at the single receptor level (using Atomic Force Microscopy [119]) or Focal Adhesion level (using FRAP [225]) of the kinetic rates of bond formation and rupture and structural properties of the receptor molecules. The theory allows to predict the dependence of the area of saturation of Focal adhesions with the stiffness of the substrate considering eq.8.12 and assuming as previously the relationship between FA area and number of bonds:

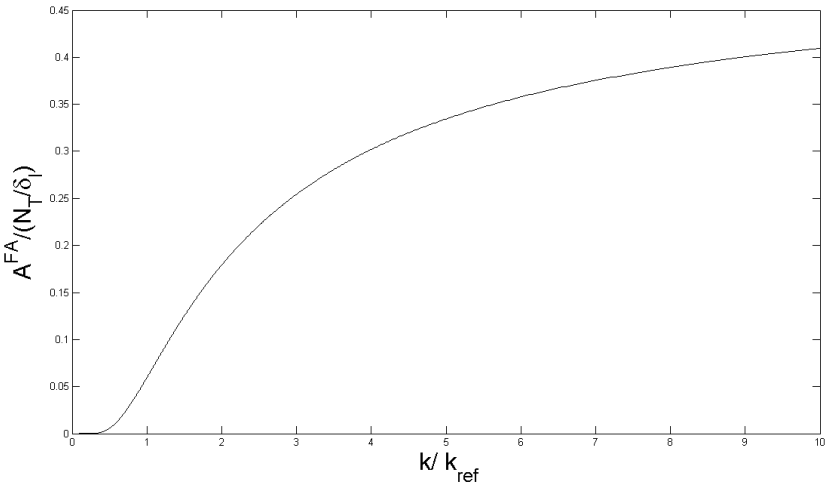

Figure 8.6: Theoretical prediction of the saturation area of Focal adhesion as a function of the stiffness

.

[5]The values adopted are: $\alpha = 1$, from assuming similar intrinsic rates of activation and inactivation; $\lambda_1 = 100$, so that the forces developed during the sampling process are smaller than the characteristic forces of bond rupture; $\lambda_2 = 0.5$, so that $\bar{k}_{ref}$ is the characteristic range of sensitivity to substrate stiffness; $\lambda_3 = 1.0$, so that energies developed during the sampling process for $\bar{k} \sim \bar{k}_{ref}$ promote receptor activation.

This result is consistent with the well known experimental fact that cells laying on very soft substrates develop small and poorly defined focal adhesions, and that the contacts become bigger and more stable in stiffer substrates[27, 122]. No quantitative assessment of this relationship can be found in [11], but the prediction could be tested experimentally. For $\alpha = 1$ the prediction of the relationship between FA equilibrium area and stiffness can be expressed in a compact fashion, more amenable to analytical treatment and comparison with measurements:

$$A^{FA}(t_{cont},\ \bar{k}) \sim \frac{1}{2}\frac{a(\bar{k})}{[a(\bar{k}) + \lambda_3]}\frac{e^{-1/[2\cdot a(\bar{k})\lambda_2^2]}}{\cosh[1/(2\cdot\lambda_2^2\cdot a(\bar{k})]} \tag{8.13}$$

Reported lateral spacing of integrin receptors in Focal adhesions[224] of $30nm$ results in a value of integrin density $\delta_I \approx 10^3\mu m^{-2}$, which combined with an estimated value of $N_T \sim 10^3 - 10^4$, leads to predict dimensional values of $A^{FA}(t)$ of the order of $1 - 10\mu m^2$, consistent with the order of magnitude of the values observed in the experiments discussed[10, 11]. Measurements of the intrinsic rates of integrin-ligand binding of $w_0 \sim 10^{-1} - 10^{-2}s^{-1}$ lead to an estimation of the characteristic times for initial the nucleation phase of the order $t \sim w_0^{-1} \sim 10-100s$, which are bellow the resolution of the data published in both studies. Hence, the predicted initial quadratic regime of Focal adhesion growth for $w_0 \cdot t \sim 1$ can not be compared to the experimental data; in addition, in this timescale, stochastic dynamics associated to the small number of bonds during the nucleation phase make the deterministic description no longer valid[226]. This timescale allows also to estimate a lower bound for the characteristic time t_{cont} of the postulated process of cell tugging on FAs as $t_{cont} > w_0^{-1}$ of the order of minutes, consistent with the characteristic times of Focal Adhesion maturation observed in both studies. This time scale is longer than the period $\sim [30 - 50]s$ of force oscillation in FAs reported in [14]; note however, a critical difference between the cells in this study and the cells in [10, 11]: in the former case cells were cultured in substrates featuring a *gradient* of stiffness and cells were *migrating*, whereas the results discussed from the latter studies are associated to adherent *non-migrating cells* cultured in different substrates but with a spatially homogeneous rigidity. This suggests that existence of the stiffness gradient interrupts the mechanical testing process, triggers cell polarization and leads to directed migration. This notion will be central in the model of Durotaxis presented in the next section; interestingly, it is consistent with the observations in the study reporting for the first time the sampling process at individual FAs [14] but also with a recent the observation that fibroblast polarization requires and is preceded by Focal adhesion mechanosensing[210].

8.2.2 Force at Focal adhesions: theory and measurements

Measurements of the time-evolution of the total force per Focal adhesion and its dependene on substrate stiffness found in [11] and [9] are compared with the predicted $F(t)$ in the intermediate time-scale. The latter study used optical tweezers to trap micron-size beads functionalized with fibronectic ligands so that individual focal adhesions of $3T3$ fibroblasts could attach to them and exert forces. Varying the intensity of the laser traps they were able to mimic anchorage points with different effective stiffness at individual contacts. The effective stiffnesses in this study are an order of magnitude smaller than in the studies discussed previously, and the same applies to the forces developed by the cell. In both cases, the observations show that the total forces exerted by cells at individual contacts increased with time, and that the rate of $dF(t)/dt$ increased with the stiffness of the substrate. The theoretical prediction of the evolution of this variable is given by $F(t) = N(t) \cdot f(t)$, which according to eq. 8.10 for the approximation of $N(t)$ in the linear regime and eq.8.3 for the postulated force per receptor leads to:

$$\frac{F(t)}{N_T \cdot f_g} \sim \frac{1}{\lambda_3} \frac{\alpha}{(1+\alpha)} \left(\frac{\bar{k}}{\bar{k}_{ref}} \cdot \frac{t}{t_{cont}} \right)^{3/2} \qquad 1 < w_o \cdot t < w_o \cdot t_{cont} \tag{8.14}$$

Hence, the approximation of $F(t,k)$ obtained from the mechanosensing theory predicts that Force at individual FAs grows in the initial maturation phase as $F(t,\bar{k}) \sim \bar{k}^{\beta} \cdot t^{\gamma}$ with $\beta = \gamma = 1.5$. The data found in figure 2 of [9], showing the curves $F(t)$ for three different laser traps allows to estimate the exponents. Fitting the time exponent for the two larger rigidities as $\gamma = \ln[(F_{\bar{k}}(t_i)/(F_{\bar{k}}(t_j)]/\ln[(t_i/t_j)]$ for the three combinations of 3 time-points, leads to $\gamma = [1.7203, 1.6902]$ for the softer and the stiffer trap, in close agreement with the theory. The data reported in figure 2a of [11] does not allow to make a fit, but is also consistent with the prediction. Regarding the dependency in $\bar{k}$, the exponent is fitted to the data in the study with optical tweezers as $\beta = \ln[(F(t_i,\bar{k}_1)/(F(t_i,\bar{k}_2)]/\ln[(\bar{k}_1/\bar{k}_2)]$ for three time points, leading to a consistent value of $\beta = [1.0882, 1.0911, 1.1594]$. The study with the micropatterned substrate reports a linear dependency of $dF(t)/dt$ in stiffness (see figure 2D in [11]), which implies a value of $\beta = 1$. Hence, the experimental data suggests a slightly weaker dependence in stiffness than the predicted by the theory. This can be explained as follows: there are two contributions to the dependency of $F(t,\bar{k}) = N(t,\bar{k}) \cdot f(t,\bar{k})$ in $\bar{k}$ that lead to the prediction $\beta = 1.5$, one associated to the dependency in stiffness of the force developed for each receptor that goes $\bar{k}^{0.5}$ and the other to the increase in the number of closed bonds with $\bar{k}$ that goes as $\bar{k}^{1.0}$. This last dependency; however, stems from the approximation of $N(t)$

in the initial range of maturation, which neglects variations in the binding ($\downarrow$) rate due to the increase in displacement caused by the low rigidity of the laser traps. Hence, the small disagreement is caused by the overestimation of $N(t)$ and not by the rate of force development that stems from the mechanosensing hypothesis. Numerical solution of the full equation 8.6 for $t \in (0, t_{cont})$ demonstrates how the theory matches the observations. Note that in the study with optical tweezers, as

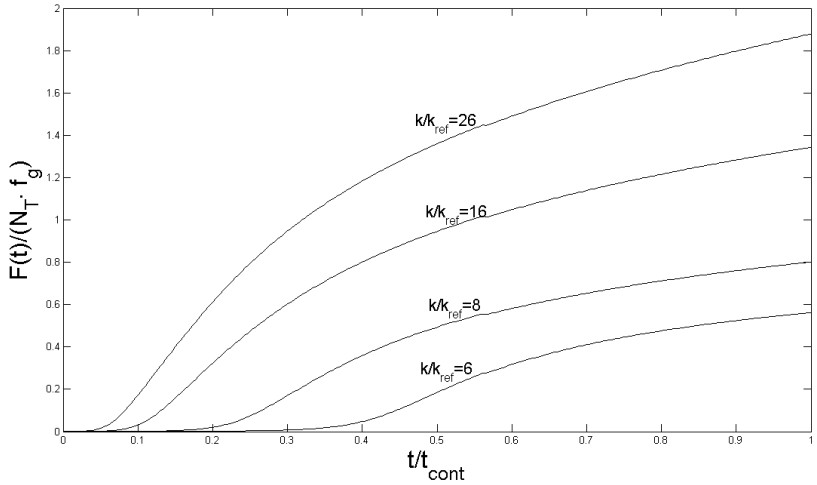

Figure 8.7: Force developed per Focal adhesion during mechosensing test . Compare to fig. 2A in [11] and figure 2 in [9]

.

mentioned earlier, the stiffness traps are an order of magnitude smaller than those found in the study with micro-pillars, which are closer to physiological conditions. The curves $F(t)$ reported with the optical traps (see fig. 2 in [9]) do not reach the saturation phase predicted by the theory and also reported in [11] (see figure 2A), despite the fact that the measurements are performed for similar periods of 10 minutes and in both experiments the cells used were Fibroblasts. The interpretation within the framework of the theory is straightforward: the stiffness of the laser traps in [9] is an order of magnitude smaller than the stiffness of the micro-pillars used in [11], which implies that $\bar{k}_{laser} \cdot t/(\bar{k}_{ref} \cdot t_{cont}) << \bar{k}_{pillar} \cdot t/(\bar{k}_{ref} \cdot t_{cont})$. In the former case, according to the theory, both development of force per receptor (see eq.8.3) and the increase in the number of closed bonds (see eq. 8.10) are much slower, which leads to a build-up of the total force per focal adhesion that takes a much longer time (see eq. 8.14). Remember that the measurements of $F(t)$ in both studies were performed for similar time-windows of 10 minutes. Hence, the study with optical tweezers[9] only captured the first stage of the cell

mechanosensing process observed in the essay with micro-pillars, which corresponds to the initial evolution of $F(t)$ measured experimentally and reported in figure 2A of [11] and also to the theoretical prediction of $F(t)$ near the origin of the time axis in figure 8.7. This interpretation of course rests on the fact that both studies used Fibroblasts, which means that the cells should invest a similar power p_0 to pull on the substrate for the similar time-periods of the measurements.

A crucial measurement providing conclusive support for the mechanosensing theory proposed is found in the data of force saturation at individual Focal adhesions reported in the study using micro-pillar patterned substrates. This experiment assessed the quantitative relationship between the saturation force $F^{FA}_{sat}(\bar{k})$ developed at individual FAs with the stiffness $\bar{k}$ of the pillar in which it was formed, finding a linear relationship between them "*within our range of rigidities*"[11]. In fact, close examination of the data reported (see fig. 2C in [11])) shows that the linear relationship does not hold for larger rigidities, and that the poor correlation coefficient obtained is associated to the Force data points in the larger rigidity range being bellow the stated linear relationship. It will be shown that the mechanosensing theory proposed does explain this discrepancy. The prediction of the saturation force per Focal adhesion for $t \to t_{cont}$ is given by equations 8.12 and 8.3 as $F^{FA}_{sat}(t_{cont},\ \bar{k}) = N_{eq}(t_{cont},\ \bar{k}) \cdot f(t_{cont},\ \bar{k})$.

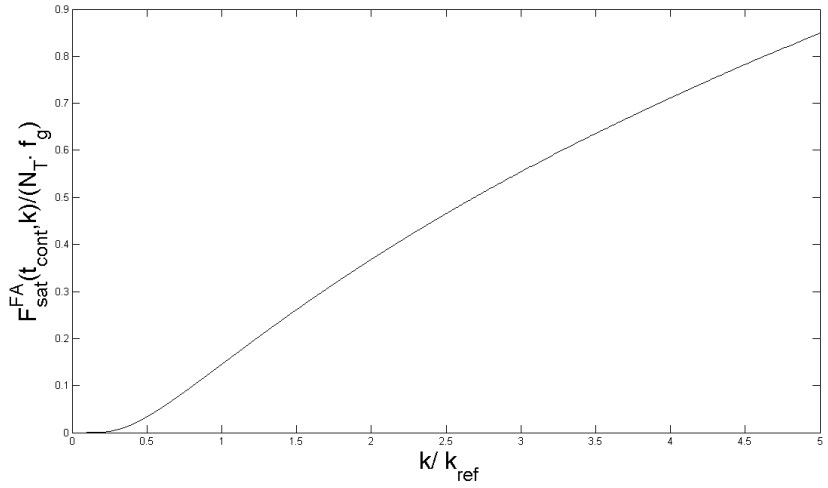

Figure 8.8: Theoretical relationship between stiffness and saturation Force developed by Focal adhesions. Compare to fig. 2C in [11] and note the decay of the experimental data of $F^{FA}_{sat}(\bar{k})$ bellow the linear regime for large rigidities

The predicted dependency between saturation force and substrate stiffness does indeed feature a small deviation from linearity for higher rigidities. This

behavior is preserved against parameters changes. Variation of the parameter λ_3 associated to the energy required to activate receptors, the length scale λ_2 that controls the modulation of bond formation by displacement, or the ratio between intrinsic rate of bond rupture and formation only shifts the magnitude of the decay and the range of rigidities in which the deviation takes place. The following figure illustrates this feature, with the dotted line representing the dependency of F_{sat}^{FA} with $\bar{k}$ for reference values $\alpha = 1.0$, $\lambda_2 = 0.5$ and $\lambda_2 = 1.0$ shown in the previous figure:

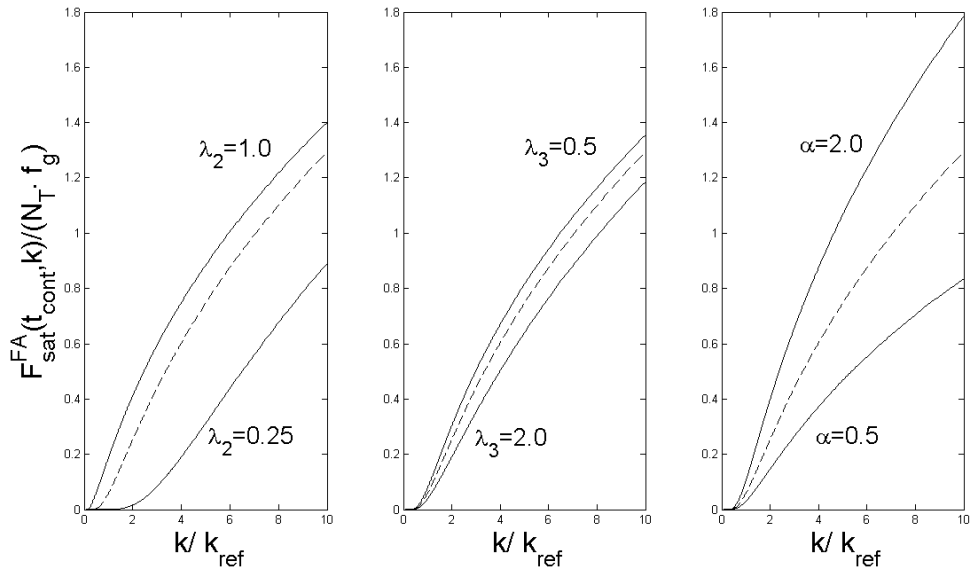

Figure 8.9: Predicted dependency of F_{sat}^{FA} with $\bar{k}$ in terms of receptor kinetic and molecular parameters. Weakening in the dependency of $F_{sat}^{FA}(\bar{k})$ with $\bar{k}$ for large rigidities is conserved

Further insight can be gained considering the analytical expression of the saturation force. The prediction of the mechanosensing theory proposed for $F_{sat}^{FA}(t_{cont},\ \bar{k})$ is given by:

$$F_{sat}^{FA}(t_{cont},\ \bar{k}) \sim \left[\frac{a(\bar{k})}{[a(\bar{k}) + \lambda_3]} \frac{\alpha}{[\alpha + e^{1/[\lambda_2^2 \cdot a(\bar{k})]}]}\right] \cdot \sqrt{a(\bar{k})} \tag{8.15}$$

where it must be remembered that the relative stiffness has been defined simply to alleviate the notation as $a(\bar{k}) = \bar{k}/\bar{k}_{ref}$. Thus, the saturation force predicted by

the theory has two contributions, the first associated to the equilibrium number of closed bonds (see eq. 8.12) and the other associated to the force developed per receptor due to the pulling process postulated (see eq. 8.3). Since the force that stems from the hypothesis of cells investing a constant power to mechanically test the substrate goes as $f(\bar{k}) \sim \bar{k}^{1/2}$, it follows that the small decay of $F_{sat}^{FA}(t_{cont}, \bar{k})$ from the linear dependency observed in [11] is accounted for by a dependency of the number of bonds with $\bar{k}$ weaker than $N_{eq}(t_{cont}, \bar{k}) \sim \bar{k}^{1/2}$. Interestingly, the authors of the study discussed stated that "*[...] in contrast to the force, the dependency of FA growth (area) was less obvious although the saturation size depended on the stiffness of the pillars*"[11]. Indeed, the theory proposed predicts a saturation size of FA that does depend on the stiffness of the substrate. The exact relationship[6] predicted by the theory is given in eq.8.12. It would be interesting to obtain the data for which no obvious dependency could be found and compare it with this prediction.

Two important implications follow from the last result. First, the authors of the experiment, accepting a linear relationship between $F_{sat}^{FA}(\bar{k})$ and $\bar{k}$, reach the conclusion that cells exert a constant deformation on the substrate, which "*suggests the existence of a mechanosensing mechanism that is regulated by substrate deformation*". The experimental data, however, casts some doubt on the validity of the premise that leads to this conclusion[7]. Second, the alternative mechanosensing theory proposed seems to provide a better fit by predicting the observed weakening of the dependence of $F_{sat}^{FA}(\bar{k})$ for large rigidities. Further experimental data of this relationship could provide the definitive evidence required to corroborate or disregard the alternative hypothesis.

8.2.3 Stress at Focal Adhesions: theory and measurements

Another observation that finds a simple explanation in the context of the mechanosensing theory proposed is the measurement of the time evolution of traction stresses at individual Focal contacts. The predictions of the theory are compared to the time-dependent stress curves found in [10], its dependence with the stiffness of the substrate [11] and its relationship with Focal adhesion area[8]. These studies

[6] Note that Focal adhesion area and number of closed bonds are related by a simple proportional relationship given by the density of receptors in the adhesion. The less scary expression for A_{sat}^{FA} given in 8.13 is found by assuming $\alpha = 1$, i.e, equal intrinsic rates of bond formation and rupture

[7] The authors also cite two of their earlier studies [221, 227] as evidence of a linear relationship between Focal adhesion force and stiffness. Strangely enough, the experimental data found in the first provides a linear relationship between the *logs* of the variables $\ln(F^{FA}(\bar{k})) \sim \beta \ln(\bar{k})$ (see fig. 2 in [221]), which hardly allows to conclude nothing more than a dependency $F^{FA}(\bar{k}) \sim \bar{k}^{\beta}$, given the experimental error bars. In the second, the weakening in $F^{FA}(\bar{k})$ for larger rigidities can be noticed even more clearly (see figs 2C, 2D in [227])

obtained the stresses using radically different techniques[8], and to my knowledge, there is not a satisfactory explanation reconciling the different types of observation. Next, it will be shown that the mechosensing hypothesis proposed in this Thesis provides a unifying and simple interpretation for them. This has important implications for the related to question of how cells sense mechanical properties: the observations in [8] are representative of the type of essays that have supported the hypothesis that cells apply a constant stress at Focal adhesions to infer the mechanical properties of the substrate; conversely, the observations in [11] have lead others to conclude that cells attempt to exert a constant displacement on the substrate.

The stress, by definition, is the total force applied at a Focal adhesion divided by the total area of the contact. Since according to the mechanosensing hypothesis stated in eq. 8.1, both the total force $F(t)$ and the area $A^{FA}(t)$ of a focal adhesions are proportional to the number of receptors, the stress predicted by the theory can be derived from the force $f(t)$ sustained per ligand-receptor pair as:

$$\sigma^{FA}(t) = \rho_I \cdot f(t) = \rho_I \cdot f_g \sqrt{\frac{\bar{k}}{\bar{k}_{ref}} \frac{t}{t_{cont}}} \tag{8.16}$$

Note that $f(t)$ is completely determined by the hypothesis that cells invest a constant energy per time $p_0 = f_g^2/(2 \cdot \bar{k}_{ref} \cdot t_{cont})$ for each receptor during a mechanosensing sample; where $\bar{k}_{ref}$ and t_{cont} are characteristic of each cell type. Hence, the observations of stress at individual focal adhesions provide a direct test of the hypothesis. Experimental measurements of stress development at individual FAs in real time are found in [10]. The stress *in newly formed* adhesions for both $3T3$ fibroblast and *USOS* osteosarcoma cells showed a strong increase in time for a certain period and then tended to stabilize in a timespan of similar duration (see figs. 3b-bottom and 4b-bottom in [10] for each type of cells). Interestingly, the authors found that this evolution only applies to *newly formed* contacts, but not to

[8]The earlier study of Balaban, Schwarz, Geiger and coworkers [8] represented a milestone because it provided the experimental set-up that has become the staple of cell traction force microscopy. Briefly, they patterned an elastic substrate with micro-dots as fiducial markers, so that measuring the displacement of the micro-dots caused by the cell forces allowed to reconstruct the strain field and obtain the associated stress field. In addition, they used a Green-Fluorescent-Protein fusioned with vinculin to tract Focal adhesion area in real time. A refinement of this method is also used in[10]. In contrast, the study using substrates featuring arrays of micro-pillars [11] measured the deflection of the pillar tips produced by the cells traction forces, thus obtaining directly the total forces exerted by individual FAs. Simultaneously measuring the area of these Focal Adhesions allowed them to calculate the stresses

older contacts after the phase of assembly. This observation is consistent with the mechanosensing hypothesis, since according to the theory, this time-dependence of stress growth should be observed during FA maturation; no statement has been made about the dynamics of older contacts.

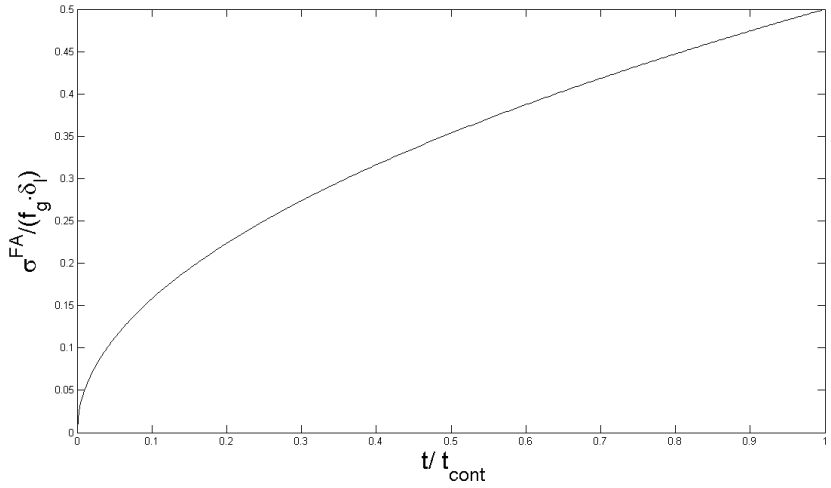

Figure 8.10: Predicted time-course of normalized stress at FAs. Compare to fig. 3b(bottom) and 4b(bottom) in [10]

The time-course reported is consistent with the evolution $\sigma^{FA}(t) \sim (t/t_{cont})^{1/2}$ predicted by the theory. Note that the authors state that in the initial regime of FA maturation there is a linear correlation between the stress developed and Focal adhesion length (i.e area), but in fact the correlation coefficient is only $r = 0.76$. Therefore, it would be interesting to check if the relationship that stems from the theory using the predicted values for $\sigma^{FA}(t)$ and $A^{FA}(t)$ provides a better fit.
Interestingly, the reported data for the different cell types is qualitatively similar, but the time-course of stress development appears to be shifted, with stress build-up and stabilization occurring more slowly in osteosarcoma cells. The second difference observed is that the magnitude of the saturation stresses is higher for fibroblasts than for osteosarcoma cells; more precisely, the magnitude of observed stresses at the plateau is $\sim$ 1nN$\cdot\mu$m^{-2} for fibroblasts, whereas for osteosarcoma cells is $\sim$ 0.5nN$\cdot\mu$m^{-2}. Can the mechanosensing theory proposed explain these differences between cell types?

Crucially, all the data for osteosarcoma cells was obtained in substrates of Young's modulus $E_{S1} = 2.8$ kPa , whereas the stress curves of 3T3 fibroblast were obtained in stiffer substrates of $E_{S2} = 16$ kPa Young's modulus, which leads to

effective stiffnesses[9] $\bar{k}_1 < \bar{k}_2$. The dimensional value of the stress that stems from the constant power hypothesis for each cell type is then:

$$\sigma^{osteo}(t) = \rho_I \cdot \sqrt{2 \cdot p_0^{osteo} \cdot \bar{k}_1 \cdot t} \tag{8.17a}$$

$$\sigma^{fibro}(t) = \rho_I \cdot \sqrt{2 \cdot p_0^{fibro} \cdot \bar{k}_2 \cdot t} \tag{8.17b}$$

Hence, the first difference has in fact already been given a simple explanation within the theory proposed: since the stiffness of the substrates where fibroblasts were cultured was higher, stress build-up is faster. Note that no assumption has been made yet as to the values of p_0 for the different cells; they could be different as long as p_0^{osteo} is not much bigger than p_0^{fibro}. This leads to second difference observed: that the stresses developed by fibroblasts at any given time, and in particular at the saturation phase, were higher than those developed by osteosarcoma cells. Again, since the substrates for osteosarcoma cells were softer than those used for fibroblasts, the observed differences in stresses for $t \to t_{cont}$ are readily accounted for examining eqs. 8.24, as long the characteristic contraction times of osteosarcoma cells t_{cont}^{osteo} are not much longer than t_{cont}^{fibro}.

What about the variables t_{cont}^{cell} and p_0^{cell} that define the mechanical sampling process executed by each cell type? The authors of [10] state in the Methods section that the choice of substrates was made "*to accomodate differences in cell contractility*"[10]. Now, the initial question and this observation bear to the following, seemingly obvious but more interesting thought: Why are some cells more contractile than others? Can the mechanosensing theory proposed tell us something about it? There are two alternative possibilities to answer these question within the framework of this theory: more contractile cells could either invest a higher p_0^{cell} to develop forces during the contraction process or they could contract for longer times t_{cont}^{cell}. The foundational hypothesis was based on the idea that the

[9] Reminder: the stiffness of a substrate is related to its Young's Moudulus by eq.3.35 as $k_S(E_s) = (4/3)^2 \cdot E_s \cdot r_P$, where r_P is the characteristic radius of a receptor or ligand. Then, the compund stiffness fullfills $\bar{k}_1 = k_P \cdot k_S(E_{S1})/(k_P + k_S(E_{S1})) < k_P \cdot k_S(E_{S2})/(k_P + k_S(E_{S2})) = \bar{k}_2$.

[10] Most likely, the choice was made to avoid the large displacement that fibroblasts would induce if they were cultured in the substrate used for osteosarcoma cells, which would possibly invalidate the calculation of the stresses based on linear elasticity or even wrinkle the substrate. Or the other way around, if osteosarcoma cells were cultured in the substrate used for fibroblasts they would develop such as small displacements that would probably fall bellow the experimental resolution.

power constant p_0 is a quantity defined by the kinetics of the molecules involved in generating pulling forces, prominently *F-actin* and *myosin-II*, which are shared by all types of cells. It follows that p_0 should then be independent of the cell type, and that the fact some cells are more contractile should explained by the fact they contract for longer times t_{cont}^{cell} [11]. Let's see where this assumption takes us.

In the statement of the mechanosensing hypothesis, $\bar{k}_{ref}$ was introduced as a reference stiffness where a particular cell type would develop a force per receptor $f(t_{cont}^{cell}) = f_g$, comparable to those required for its Focal adhesions to mature. This force is given by the conditions $e_g(f_g) > e_0$ and $u_g(f_g) < u_0$, so that the energy stored per receptor is of the order required to activate them and the displacement induced between ligand-receptor pairs is small compared to those associated to thermal fluctuations. In turn, e_0 and u_0 are determined by molecular properties of the receptors[12] and for this reason, are characteristic of the receptors expressed by a cell, not of the cell type. Hence, the force/energy required to form mature adhesions based on a given type of receptors should be independent of the cell type. To develop such a force, it follows that the stiffness $\bar{k}_{ref}$ required by different cell types, contracting during a period t_{cont}^{cell} characteristic of the cell type but with an energy per time p_0 similar for all of them, is given by:

$$\bar{k}_{ref} > \frac{f_g^2(e_0, u_o)}{2p_0 \cdot t_{cont}} \tag{8.18}$$

Sticking to the premises of the view presented, a highly contractile cell, namely a fibroblast, is associated to t_{cont}^{fibro} longer than the contractile t_{cont}^{osteo} characteristic of a less contractile cell such as an osteosarcoma. It then follows that a osteosarcoma cell requires a much stiffer substrate than a fibroblast to establish mature contacts and adhere to a substrate[13]. This view is consistent with the fact that the tissue

[11] A simple experiment can be proposed to validate one of the alternatives and discard the other: culture two different cell types with different characteristic contractility (for instance fibroblasts and osteosarcoma cells) on the same substrate and measure the rates of force build-up. If the rate of force increase is the same for both cell types, this means that there is indeed an $p_o[energy/time]$ parameter that is intrinsic to the contractile apparatus of these cell types, and the more contractile type should be observed to apply traction forces for longer times t_{cont}. Conversely, if the rate of force increase is higher in one of the cell types, the energy per time invested pulling on FAs by this cell type should be higher, with no implications for the time of contraction.

[12] See section 3.3 for the derivation in terms of the LR energy landscape potential and receptor molecular properties

[13] For the study under discussion [10], both osteosarcoma cells and fibroblasts were cultured on a substrate coated with fibronectin; thus it is reasonable to assume that both cell types were using similar receptors to engage the ligands.

were osteosarcoma cells are found *in vivo* are bones, much stiffer than the connective tissues were fibroblasts are found. Thus, the mechanosensing hypothesis proposed suggests a mechanism that would define the range of appropriate stiffness for a cell to thrive, depending on the characteristic contractility and receptors expressed by its cell type.

The p_0-hypothesis can be further validated using experimental measured values for the parameters to compare the predictions with dimensional values of the experiments. Precisely, p_0 is approximated using only one data point $(t_i, \sigma^{FA}(t_i))$ in the fibroblasts stress-time curve of fig. 3b-bottom of [10]. Note the remarkable match with the experimental data without the need to use a more accurate fit. The intrinsic contraction power is then estimated according to eq. 8.24 as:

$$p_0 = \left[\frac{\sigma^{fibro}(t_i)}{\rho_I}\right]^2 \frac{1}{2 \cdot \bar{k}_2(E_{S2}) \cdot t_i} \tag{8.19}$$

The data point from fig. 3b-bottom in[10] used is $(t_i, \sigma^{FA}(t_i)) = (0.88\text{kPa}, 10\text{min})$, hence, the coincidence of the prediction with this time point should not be considered when assessing its accuracy. The values of the parameters required to evaluate $k_2(E_{S2})$ and p_0 are:

Table 8.1: Adhesion receptor parameters

Parameter	Physical Meaning	Value
ρ_I	Integrin density	$10^3 \mu\text{m}^{-2}$ [224]
r_p	Integrin radius	1nm [215]
k_p	Integrin spring constant	$5\text{pN}\cdot\text{nm}^{-1}$ [216]

The estimated value of p_0 [14] is then used to predict the *entire* time-stress curves developed at *FAs* for *both* fibroblasts and osteosarcoma cells. Note that the match of the prediction with experimental data is above 90% for the entire time-course

[14] A change of 1 order magnitude in the adopted value of ρ_I and r_P leads to a change of 2 and 1 orders of magnitude in the estimated p_0. Considering the experimental uncertainty in the reported values of these parameters, p_0 should only be considered a rough estimate of the [*energy*/*time*] consumed by receptor. The point is to prove that there *is* such a p_0 independent of the cell type that defines the mechanosensing process

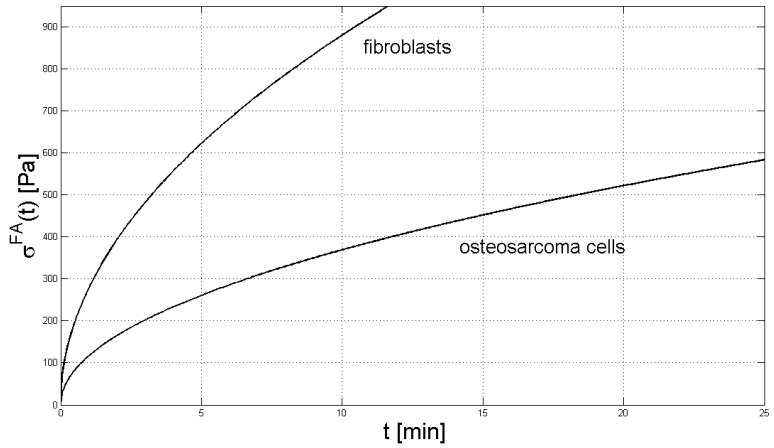

Figure 8.11: Stress time-course for two cell types in [10]. Compare fibroblasts prediction to fig. 3b(bottom) and osteosarcoma's with 4b(bottom) in[10]

of the measurements for both types of cells. In fact, the fact that both cell types change the contraction regime after a certain time t_{cont}^{cell} has not even been considered; cutting off the accepted time-range of predictions improves the match dramatically. Further, the value of p_0 estimated from this experiment[10] can be used to predict the observations in [11], an altogether different set-up using micro-pillars to study the dependence of FA forces with stiffness.

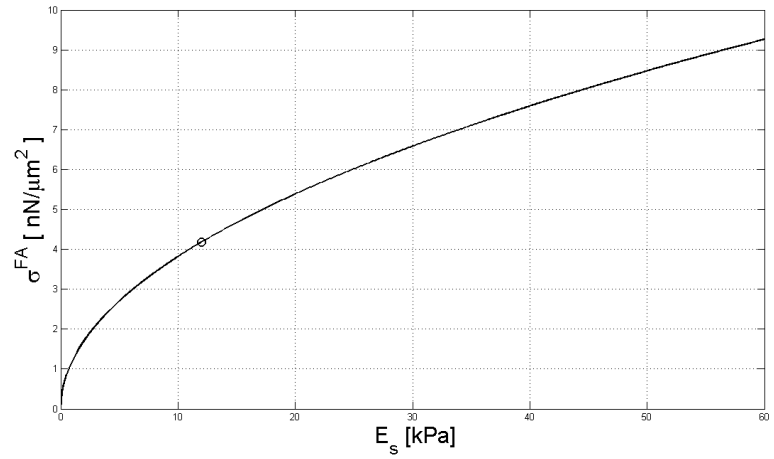

Figure 8.12: Stress dependence with stiffness for large times at FAs. Compare data in fig. 3B of in[11]. Compare prediction of $\sigma^{FA} = 4.2\text{nN}\cdot\mu\text{m}^{-2}$ for $E_S = 12\text{kPa}$ (highlighted with a circle) with fig.5e in [8].

Precisely, the prediction is compared to the observed dependence of saturation stress $\sigma^{FA}(t_{cont}, \bar{k})$ at FAs with $\bar{k}$ (see fig. 2B in [11]). The actual value of the contraction time required by the cells to develop these stresses was not reported, the only data provided is that cells were allowed to adhere to the substrate for 5 hours, which is the estimation used for t_{cont}. Again, the accuracy of the prediction is above 90%. Finally, the reader is invited to check in fig.8.12 (see highlighted circle) that the prediction for the stress that would be developed at a Focal adhesion on a substrate of 12kPa in Young's modulus is 4.2 nN$\cdot\mu$m^{-2}. The grounbreaking study of Balaban and coworkers[8], described at the introduction of this section, lead many to believe that cells test the substrate by developing a constant level of stress because they indeed found a constant value for fibroblasts cultured on an elastic substrate. The value measured was of 5.5 ± 2 nN$\cdot\mu$m^{-2}. And the Young's modulus of the substrate used, 12kPa.
As the authors of [11] rightly point out, changing the rigidity of the substrate would have shown that this conclusion does not hold. However, the alternative explanation, that cells exert a force proportional to the stiffness, so that a constant displacement is induced, is not supported by the full range of experiments discussed here either.

8.2.3.1 Constant power hypothesis: final considerations

Up to the present, allegedly conflicting observations have sustained an ongoing controversy on how cells test the mechanical properties of the substrate, with two opposing views supporting that cells apply a constant stress or a constant strain and *measure* the conjugate property There might be an alternative answer: cells spend a constant amount of energy per time to test de substrate. As shown throughout the preceding discussion, there is a number of observations that are consistent with this principle, but to my knowledge no direct measurement of energy consumption at Focal adhesion has been performed, which is the core of the principle proposed. However, a study of muscle contraction [228] estimated ATP consumption in the scale of mili-seconds by measuring P_i release associated to ATP hydrolysis; this suggests that such a measurement is possible, and that the hypothesis proposed can be subjected to direct experimental validation. Considering that the energy released from the hydrolysis of ATP in cellular conditions is $e_{ATP} \sim 57$ kJoule/mol [229] and that p_0 is the energy consumed per time and receptor during the mechanosensing process, the number of ATP consumed per second and receptor can be estimated as $r_{ATP} = p_0/e_{ATP}$. Perhaps, a more accessible experimental quantity would be the rate of ATP consumption for a given area of Focal adhesion, which considering the receptor density ρ_I and eq.8.19 is then given by:

$$R_{ATP} \approx \left(\sigma^{cell}(t_i)\right)^2 \frac{1}{\rho_I} \frac{1}{2 \cdot \bar{k}_2(E_{S2}) \cdot t_i} \tag{8.20}$$

where R_{ATP} is the rate of ATP consumption per unit of time and Focal adhesion area. Thus, this relationship could probably be tested measuring simultaneously the stress developed at a single Focal adhesion for a time of contraction t_i, the rate of P_i release, and the density of receptors ρ_I in this FA. The prediction could be further tested measuring R_{ATP} against variations in the stiffness of the substrate and cell type. To conclude, I'd like to stress an important aspect of the theory presented. The predictions stemming from the p_o-hypothesis have been obtained in the framework of the mechanical and kinetic description of a Focal Adhesion developed in section 3.3. However, the conclusions do not depend on the details of these descriptions. As to the mechanical description, the crucial point is that pulling on substrate-adhesion contacts with p_0 leads to less ligand-receptor separation and larger energy storage on stiffer substrates. As to the kinetic description, an extension of Bell's theory of force influence on cell receptor bonds, the fundamental element is that the kinetic rate of formation decreases with receptor-ligand separation and that activation of adhesion receptors is promoted by energy storage. Thus, the predictions of the p_0-hypothesis are quite robust to refinements in the description of FAs[15][16], which supports the idea that it represents a universal

[15]George Irving Bell worked throughout his career in Los Alamos Scientific Laboratory in Santa Fe, New Mexico. Around 1978, he switched his line of of work from neutron transport in thermonuclear weapons to cell biology. Then, he produced a theory on how cell receptors bonds should be affected by mechanical forces; later proven to be accurate [82]. This would have been remarkable enough without adding the fact that at that time, cell adhesions and receptors had barely been observed. Incidentally, and possibly due to his influence, the idea of the existence of catch bonds, postulated by Micah Dembo[230], emerged from the same lab. Bonds that increase their lifetime and activation with force could be an important ingredient in the mechanosensing process, amplifying the sensitivity of cells to stiffness

[16]In 1953, the 3*rd* American expedition lead by Charles S. Houston tried to climb *K*2 in Karakorum. They were forced to retreat near the summit after one of the members of the party, A. Gilkey, became critically ill. During their heroic descend along nearly vertical ice faces, lowering Gilkey with an improvised stretcher, one of the climbers slipped and dragged the whole team down. They would have found their death 2000 meters bellow if Pete Schoening would not have quickly coiled the rope around his body and belayed the whole team, including Gilkey, with his ice axe. Later, however, while waiting anchored to the mountain face for the rest of climbers to set up camp, Gilkey disappeared never to be found. Fact and myth next become blurry, but some of the members of this legendary expedition believed that Gilkey, realizing that his companions would not make it out of the mountain with him, sacrificed himself. This is however true, amongst the men that survived this fall, was George I. Bell. As a matter of fact, he is the one who slipped[231].

principle underlying cell mechanosensing.

8.3 How cells integrate mechanical information to detect stiffness gradients?

The preceding section has given a plausible answer to the first fundamental question required to understand cell Durotaxis: how Focal adhesions act as mechanosensors? Next, it is turn to address the second question, as stated in the beginning of this chapter: how cells integrate the mechanical information gathered locally to sense a *gradient* of mechanical properties? The mechanosensing theory proposed directly suggest a mechanism by which cells could integrate this information and migrate along gradients of stiffness.

The proposed mechanism is based on the broad evidence supporting that Focal adhesions, besides acting as mechanosensors, are signaling centers that initiate a cascade of regulatory events that elicit the cellular response to mechanical cues [100, 50]. Particularly, signalling events originated at Focal adhesions trigger the recruitment of proteins and enzymes such as *FAK*, *GEFs* and *GAPs* that mediate the activation of the RhoGTPases, which in turn are the central regulatory node from which the main biochemical networks associated to migration are coordinated [56]. The precise mechanism of transduction of mechanical inputs into biochemical signals is not known, although the most likely candidates involve conformational changes induced by force on integrin receptors or some other mechano-responsive element of adhesion sites [101, 102, 103], exposing cryptic sites that are recognized by other molecules[105]. Independently of the detailed mechanism, this evidence suggests that the level of loading of adhesion receptors is transduced into biochemical signals to the regulatory machinery of the cell. Thence, the hypothesis on how mechanical inputs are transduced into biochemical signals is postulated as follows: *the state of mechanical loading of adhesion receptors in a Focal Adhesion is transduced into a biochemical signal that is determined by the mechanical energy stored per receptor and proportional to the number of receptors in the adhesion*.

The intermediate biochemical steps that most likely separate integrin signaling from RhoGTPases activation are lumped into a transduction signal of strength s_{FA} that directly modulates the activation of one of the RhoGTPases. The predictions that follow from this hypothesis will show that differential signaling at Focal adhesions along a stiffness gradient can lead to cell polarization and directed movement. The hypothesis relays on the principle that energy storage and receptor binding are faster at FAs on stiffer anchorage points, as demonstrated

previously. There is more than one definition of s_{FA} consistent with this hypothesis in the theoretical framework developed; but this principle is independent of its particular form[17]:

$$s_{FA}(x_{FA}, t) = \int_t \frac{N(t')}{N_T} \frac{e_P(t')}{e_P(t') + e_T} \, dt' \tag{8.21}$$

where the mechanical energy per receptor $e_P(t)$ and $N(t)$ are determined by the stiffness of the anchorage point $E_s(x_{FA})$ and the pulling process with power p_0 introduced previously. The energy level that sets the scale of transduction events is defined as $e_T = \lambda_4 \cdot e_g$ to relate it to the characteristic energies per receptor developed during mechanical samples. In the context of Cell Durotaxis, s_{FA} plays an analogous role to the signal $s_\Psi(x, t)$ that triggers the activation of a *sensor* RhoGTPase in the description of Chemotaxis, as seen in eq.7.16 of chapter 7. Following the reasoning to derive the activation rate modulation of the protein targeted by the Chemotactic receptors, the signal transduced from mechanical cues is assumed to modulate the Michaelis-Menten constant of *Cdc42* as:

$$\kappa_c(s_{FA}(t)) = \kappa_0 \cdot [1 - \eta \cdot s_{FA}(E_s, t)] \tag{8.22}$$

where the decrease of the Michaelis-Menten constant of *Cdc*42 is assumed to be bounded. Hence the activation rate of the *sensor* protein is locally modulated by Focal adhesion signaling as $\Delta\kappa_c(s_{FA}(t)) \propto s_{FA}(E_S, t)$, which in turn depends on the stiffness of the anchorage point. After a certain time t_{FA}^{wa}, modulation of the kinetic rate of the *sensor* protein will reach a critical level $\Delta\kappa_c^{crit}$ and trigger the emergence of an activation wave originated at the location of the adhesion site[18]. Since the time-scale of cell polarization is longer than the characteristic time-scale

[17] An alternative definition considered is $s_{FA}(x_{FA}, t) = (N(t)/N_T) \cdot (e_P(t)/e_P(t) + e_T)$. In this case the transduction signal sent by a FA depends on the present mechanical state of the contact, whereas in definition 8.21 it depends on the loading-history during the period of mechanical sampling t_{cont}. In the history-dependent case, if a cell maintains the contractile state reached at t_{cont}, any contact that reaches a stable state (i.e anchored at a spot above minimum stiffness threshold) will *eventually* trigger a signaling event and cell polarization. In the alternative choice, a FA might mature but transduce a signal so weak that does not affect the target regulatory pathways. The implications of the choice will discussed later in the context of experimental observations.

[18] The mechanism of wave-activation and its interpretation in terms of underlying biochemical processes was shown in fig. 7.5

of Focal adhesion formation [210], suggesting that t_{FA}^{wa} can be estimated assuming that the activation event occurs after adhesion sites have reached its equilibrium size at t_{cont}[19]. Introduction of $N(t) \approx N_{eq}(\bar{k})$ as given in eq.8.12 and the expression 8.3 for $e_P(t_{cont})$ in the equation 8.21 for s_{FA} leads to:

$$t_{FA}^{wa}(\bar{k}) \propto (1 + \frac{\lambda_3}{a(\bar{k}_1)})(1 + \frac{\lambda_4}{a(\bar{k}_1)})(\frac{\alpha + e^{\frac{1}{a(\bar{k}_1)}\frac{1}{\lambda_2^2}}}{\alpha}) \tag{8.23}$$

where $a(\bar{k}) = \bar{k}/\bar{k}_{ref}$ is the ratio of substrate stiffness relative to the characteristic rigidities on which the cell can develop mature adhesions. This result shows that the signaling emitted by FAs anchored on a stiffer point ($a(\bar{k}) \uparrow$) will require shorter times ($t_{FA}^{wa} \downarrow$) to trigger the emergence of an activation wave. Intuitively, this is explained by the fact that equilibrium size of adhesion and energy stored by receptors increases with $\bar{k}$. Further, t_{FA}^{wa} must be a limiting factor for the time t^{pol} required to polarize in response to mechanical properties: since ($t_{FA}^{wa} \downarrow$) is a decreasing function of the absolute rigidity of the substrate, cells should polarize faster on stiff substrates. This prediction will be shown to be confirmed by observations. The dependence of t_{FA}^{wa} with the stiffness of the substrate can be quantified as follows: let two Focal adhesions FA_1 and FA_2 be located at the opposite ends along the cell axis defined by a stiffness gradient, so that the stiffness of their anchorage points is given by $\bar{k}_1$ (soft end) and $\bar{k}_2 \approx \bar{k}_1 + \Delta\bar{k} \cdot L_{cell}$ (stiff end).

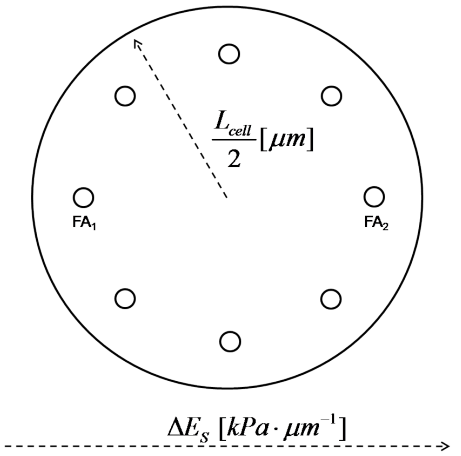

Figure 8.13: Cell geometry and symmetric Focal Adhesion distribution adopted to illustrate gradient sensing and durotaxis

[19]The alternative assumption, that mechano-transduction parallels FA maturation, has interesting implications for experimental observations to be discussed later.

The relative increase in stiffness between FA_1 and FA_2 is then given by $x_1 \approx (\Delta\bar{k}/\bar{k}_1) \cdot L_{cell}$. From expression 8.23, it can be shown that the time required to trigger an activation event by FA_1 and FA_2 follows the ratio:

$$\frac{t^{wa}_{FA_2}}{t^{wa}_{FA_1}} \sim \frac{1}{(1+x_1)^2} e^{-\frac{1}{\lambda_2^2}\frac{x_1}{a(\bar{k}_1)}} \quad \ll 1 \qquad \bar{k}_1 < \bar{k}_{ref} \tag{8.24a}$$

$$\frac{t^{wa}_{FA_2}}{t^{wa}_{FA_1}} \sim [1 - \frac{x_1}{ctt_1}] \quad < 1 \qquad \bar{k}_1 \sim \bar{k}_{ref} \tag{8.24b}$$

$$\frac{t^{wa}_{FA_2}}{t^{wa}_{FA_1}} \sim [1 - \frac{x_1}{ctt_2}\frac{1}{a(\bar{k}_1)}] \quad \sim 1 \qquad \bar{k}_1 > \bar{k}_{ref} \tag{8.24c}$$

where $ctt_1(\lambda_i, \alpha)$ and $ctt_2(\lambda_i, \alpha)$ are constants that decrease with λ_2, α and increase with λ_3, λ_4. This result is important: since $t^{wa}_{FA_2} < t^{wa}_{FA_1}$, it follows that FA_2 signaling promotes the activation of *Cdc*42 faster and that the emergence of a activation waves will reflect the asymmetry in the mechanical properties of the substrate. This will lead to the alignment of the axis RhoGTPase polarization with the rigidity gradient and eventual movement in the $FA_1 \rightarrow FA_2$ direction. Further, it shows that the delay in the emergence of activation waves is an increasing function of the *relative* magnitude of the gradient $\Delta\bar{k}/\bar{k}_1$ *and* of the range of absolute rigidity relative to the characteristic stiffness $\bar{k}_1/\bar{k}_{ref}$. Precisely, for a given gradient slope, the time-window separating the emergence of activation waves is maximized at the low range of rigidities relative to $\bar{k}_{ref}$. In other words, the theory predicts that the sensitivity to stiffness anisotropies is optimal in the range of rigidities where the cell has more difficulty to establish mature adhesions.

This leads to the core of the mechanism of stiffness gradient sensing proposed. The delay in the onset of RhoGTPase activation at the region of the cell on the softer part of the substrate is the crucial element that allows to integrate the mechanical information. Cells establish numerous adhesion sites near the membrane and therefore a similar process of mechcanotransduction is undergone by all of them. However, if the cell is cultured on a substrate featuring a gradient of stiffness, the emergence of activation waves occurs faster in those contacts anchored at points in the stiffer area and blocks the emergence of activation zones at the area of the cell on the softer part of the substrate by the mechanism of competition between activation zones described thoroughly in chapter 7. Concomitant crosstalk between the RhoGTPases leads to the simultaneous establishment of a polarized pattern of activation for the rest of the proteins. Therefore, the condi-

tion cell polarization induced by mechanical anisotropies is that the time-window $\Delta t^{wa} = t^{wa}_{FA_1}(\bar{k}_1/\bar{k}_{ref}) - t^{wa}_{FA_2}(\bar{k}_1/\bar{k}_{ref}, \Delta\bar{k}/\bar{k}_1 \cdot L_{cell})$ separating the occurrence of activation events must be longer than the time required by the wave of RhoGTPase activation to propagate a cell length from the region on the stiffer end of the gradient, thereby blocking the emergence of activation-waves at the soft end:

$$\Delta t^{wa}(\bar{k}_1/\bar{k}_{ref}, \Delta\bar{k}/\bar{k}_1 \cdot L_{cell}) \;>\; \frac{L_{cell}}{\bar{v}_{Rho}} \tag{8.25}$$

where $\bar{v}_{Rho}$ is the mean speed of wave propagation[20]. Conversely, if this condition is not fulfilled the activation events occur almost simultaneously and the gradient will not be resolved. The time-delay between activation events can be obtained from eqs. 8.23 and 8.25 as a function of the gradient slope and the absolute rigidity of the substrate. From this relationship, it is possible to derive analytically the minimum threshold bellow which mechanical anisotropies can not be detected:

$$\frac{\Delta\bar{k}}{\bar{k}_1} > \frac{\varphi_1(\lambda_i, \alpha)}{v_{Rho}} a^3(\bar{k}_1) e^{-\frac{1}{a(\bar{k}_1)}\frac{1}{\lambda_2^2}} \qquad a(\bar{k}_1) < 1 \tag{8.26a}$$

$$\frac{\Delta\bar{k}}{\bar{k}_1} > \frac{\varphi_2(\lambda_i, \alpha)}{v_{Rho}} \qquad a(\bar{k}_1) \sim 1 \tag{8.26b}$$

$$\frac{\Delta\bar{k}}{\bar{k}_1} > \frac{\varphi_3(\lambda_i, \alpha)}{v_{Rho}} a(\bar{k}_1) \qquad a(\bar{k}_1) > 1 \tag{8.26c}$$

This theoretical development reveals important properties of the mechano-sensing mechanism proposed that can be contrasted with experimental observations. First, the rigidity threshold to detect mechanical anisotropies is independent of the cell size. This result follows from the simple fact that the offset between activation events is proportional to the difference in stiffness along the gradient $\Delta\bar{k} \cdot L_{cell}$, but since the time required by the activation wave to travel a cell length

[20]Note that the instantaneous wave-speed v_{Rho} is a non-tivial function of the concentrations of the RhoGTPases (see eq.7.6), but that once an activation event occurs, it is approximately independent of the mechano-transduced signal and hence a mean velocity of wave-propagation can be defined.

is also proportional to L_{cell}, its dependence cancels out. This is an attractive property from a theoretical perspective: as stated repeatedly throughout this Thesis, the principles underlying cell function must remain operative against biological diversity. Mechanosensing and Durotaxis are no exception, the experimental evidence shows all types of cells feature a similar preference to migrate along stiffness gradients and that this capacity is certainly robust against variations in cell size.

Another important prediction that stems from the previous result is that the sensitiveness to mechanical anisotropies is a function of the absolute rigidity of the substrate, which in turn has interesting implications for the biological function of cell Durotaxis. Equation 8.26, shows that from a soft substrate where Focal adhesion maturation is hindered ($a(\bar{k} < 1)$) to a substrate where formation of contacts is optimal ($a(\bar{k} > 1)$), the sensitivity to mechanical anisotropies decreases:

$$\left.\frac{\Delta \bar{k}^D}{\bar{k}_1}\right|_{\bar{k}_1 < \bar{k}_{ref}} << \left.\frac{\Delta \bar{k}^D}{\bar{k}_1}\right|_{\bar{k}_1 \sim \bar{k}_{ref}} << \left.\frac{\Delta \bar{k}^D}{\bar{k}_1}\right|_{\bar{k}_1 > \bar{k}_{ref}} \tag{8.27}$$

where the superscipt D has been added to denote the lower bound of the anisotropies that bias cell polarization and durotaxis. Essentially, for very soft substrates, this bound vanishes and any anisotropy will trigger polarization and directed migration along a gradient. This response is limited only at the extreme range of soft rigidities, where establishment of Focal adhesions fails[21]. Therefore, this result shows that for substrates of stiffness bellow the range rigidities suited for a particular cell type to develop strong Focal adhesions (i.e $\bar{k} < \bar{k}_{ref}$), its capacity to detect stiffness gradients and migrate toward a region more appropriate to adhere is maximized, whereas for substrates above this range (i.e $\bar{k} > \bar{k}_{ref}$) its sensitiveness to mechanical gradients is weakened. Interestingly, this suggests a plausible biological function of Durotaxis: to provide different cell types with an additional mechanism to locate their appropriate position in an organism. According to this idea, a cell in a tissue alien to its function would have high sensitivity to stiffness gradients and start durotaxing until it reached and environment matching the mechanical properties characteristic of its type. At that point, the combined effects of reduced sensitivity to stiffness gradients and the development of firm FAs would lead the cell to adhere and remain in

[21]Mathematically, this is explained by the onset of a bifurcation in the eq.8.6, the governing equation for FAs. Bellow $\bar{k}_{ref}$, the only steady state that can be reached is $N(t) = 0$, i.e FAs fail. Intuitively, $\bar{k}_{ref}$ is determined by the ratios of energy stored to receptor activation energy and of ligand-receptor distance induced to distance scale for bond formation

the *correct* location according to its physiological role. Further, this interpretation also suggests a biological function of mechano-induced *apoptosis*, the well documented observation that cells cultured on very soft substrates compared to the environments in which they are found *in vivo* can not establish focal adhesions and are programmed to die[8, 122]. Indeed, the theory presented predicts that Focal adhesions can not mature bellow a certain rigidity; it follows from the present discussion that the biological function of mechano-induced apoptosis could be to prevent cells to proliferate in tissues where they not belong. Consistent with this idea is the observation that malignant cells have their sensitivity to mechanical properties altered[41, 42], which allows them to proliferate and colonize foreign tissues where cell in normal conditions would undergo apoptosis. This functional interpretation of cell Durotaxis is directly suggested by the mechano-sensing theory presented and, to my knowledge, has not been proposed before.

8.3.1 Stiffness Gradient sensing: the mechanism

The biophysical principles underlying the theory of cell mechanosensing have been laid out in the previous section. It is turn to demonstrate that this theory, combined with the model of RhoGTPases polarization presented in chapter 7, provide an interpretation for available experimental observations and insight into the process of Durotaxis. To that end, a circular cell shape featuring a symmetric distribution of Focal adhesions is adopted, as sketched in fig.8.13, in order to prevent any prescribed asymmetry to aid the computational cell to detect the stiffness gradient. In the initial state, RhoGTPases are distributed homogeneously in an equilibrium concentration and Focal adhesions have no receptors engaged with ligands on the substrate. A mechanical sampling process is initiated by the cell investing a constant power p_0 at each Focal adhesion, which in turn will locally transduce the mechanical information into an input for the RhoGTPases system as described previously. The adopted RhoGTPase Crosstalk scheme features mutual inhibition between *Cdc*42 and *RhoA* and activation/inhibition of *Rac* by *Cdc*42 and *RhoA*, respectively, corresponding to Scheme C of fig.7.21.

Table 8.2: Model C: Non-dimensional RhoGTPase kinetic parameters

Model C	γ_0	ϕ	κ_0	η	δ
*Cdc*42	10	−0.5	1	0.5	10
Rac	10	−0.5	1	0.5	10
RhoA	10	−	1	−0.5	10

Model C is adopted because is the Crosstalk scheme that endows the cell with

the fastest gradient resolution, since *Cdc42* is inhibited at what will become the rear of the cell. Differences in polarization dynamics obtained with Model A and B will be discussed later. The value of intrinsic RhoGTPase hydrolysis rate is assumed $k_0 = 0.01\ s^{-1}$, according to values reported in[182]. Note that k_0 only sets the time-scale of RhoGTPase dynamics; as long as the speed of activation waves is of the order of the time-scales of FA maturation the mechanism of gradient sensing remains operative. Physical constants for receptor mechanical properties were given in table 8.1. The parameters required at Focal Adhesion scale are estimated from experimental measurements when available and from theoretical considerations otherwise:

Table 8.3: Focal Adhesion parameters

Parameter	Physical Meaning	Value
N_{FA}	Integrins available per FA	$5 \cdot 10^3$ [224]
w_0	Intrinsic bond rupture rate	$0.01 s^{-1}$ [215]
f_g	Ligand-Receptor characteristic force	5pN [216]
λ_1	Bond rupture scale	10^2
λ_2	Bond formation distance scale	0.5
λ_3	Activation energy scale	0.1
λ_4	Mechano-transduction energy scale	1
α	Bond formation/rupture rate ratio	2

The model's predictions will be compared with a recent Durotaxis essay [13] in which migration of *Vascular Smooth Muscle* cells along stiffness gradients was analyzed. The interest of the study by Joyce Wong's group is that a novel fabrication method of *PAAm* gels produced well defined gradients in a physiologically relevant range. Absolute rigidities spanned from $E_{S0} = 5-80$ kPa in Young's Modulus and superimposed gradients ranged from $\Delta E_S = 0.01 - 0.04 kPa \cdot \mu m^{-1}$, mimicking the properties of atherosclerotic tissues found *in vivo*. The main conclusion was that cell orientation and migration along the direction of increasing stiffness correlated with the magnitude of the gradient but not with the absolute rigidity of the substrates, which lead the authors to conclude that the mere existence of even a shallow gradient triggered polarization. The theoretical optimal range for stiffness gradient sensing is estimated as follows. The contractile power p_0 is by hypothesis independent of cell type, hence it is set to the value derived previously from the observations in [10] with *osteosarcoma* and *fibroblast* cells. The contraction time for *VSMCs* is set to $t_{cont}^{VSMC} = 2/3 \cdot t_{cont}^{fibro} \approx 6$ min., based on the assumption

that these cells are less contractile than *fibroblasts*. The characteristic rigidity in which the *VSMC* cells (defined of course by the parameter choices) can establish Focal adhesions is obtained from eq.8.18 as by $E_{ref}^{VSMc} \sim 10$kPa, which according to the theory matches their optimal range for gradient sensing. For the sake of clarity, the polarization mechanism is first shown on a large gradient of slope $\Delta E_S = 0.35\text{kPa}\cdot\mu\text{m}^{-1}$ on a substrate with $E_{S0} = 40$kPa, so that the asymmetries in force development and FA maturation can be better appreciated:

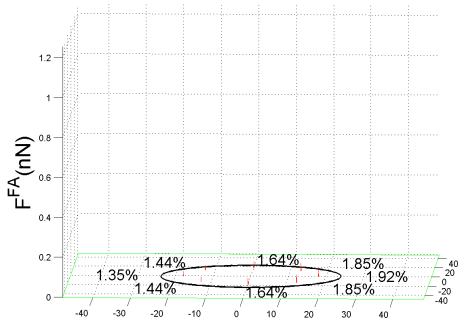

$t = 0.7$min

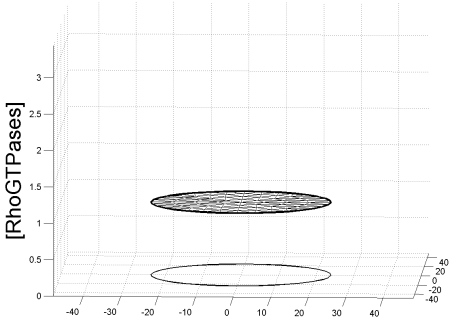

$t = 0.7$min

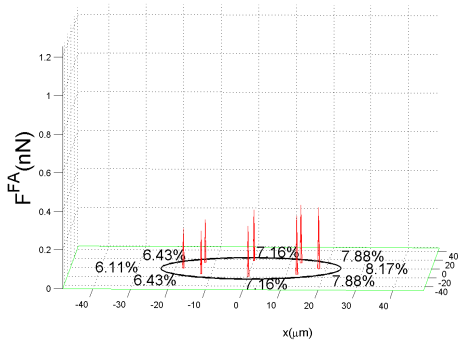

$t = 2.5$min

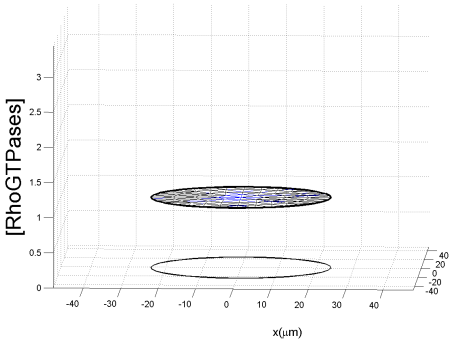

$t = 2.5$min

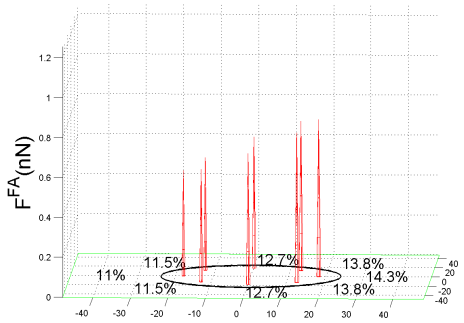

$t = 5$min

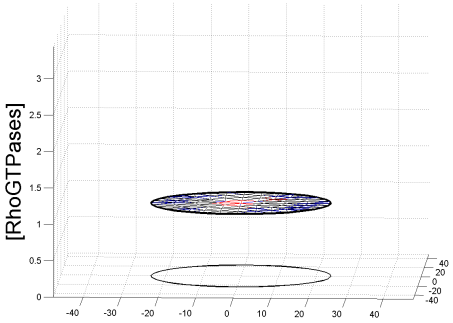

$t = 5$min

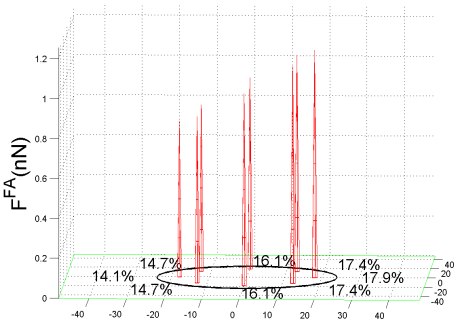

t = 10.5min

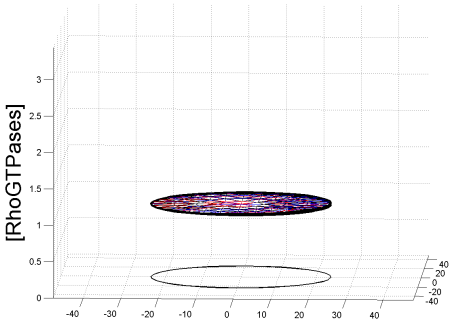

t = 10.5min

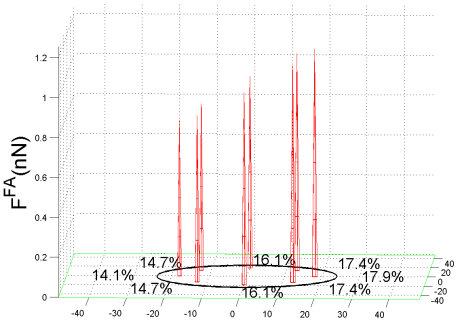

t = 17.5min

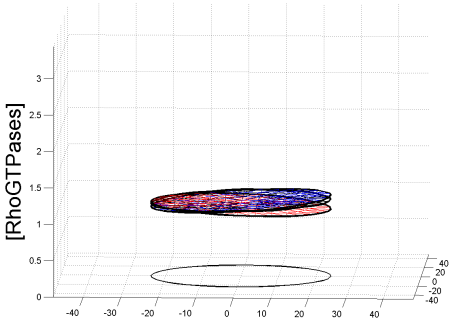

t = 17.5min

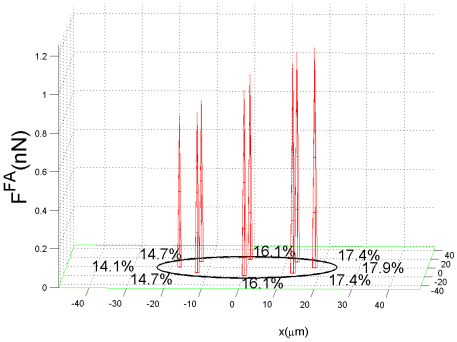

t = 20min

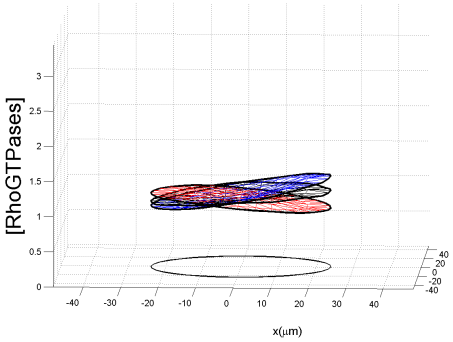

t = 20min

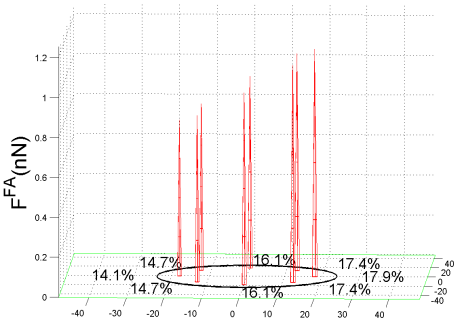

t = 21min

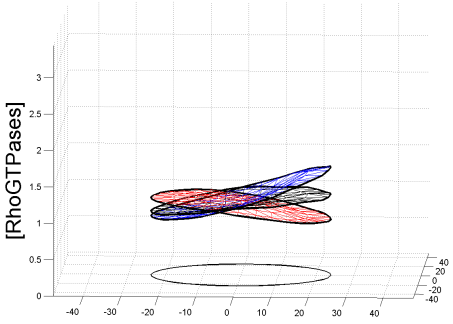

t = 21min

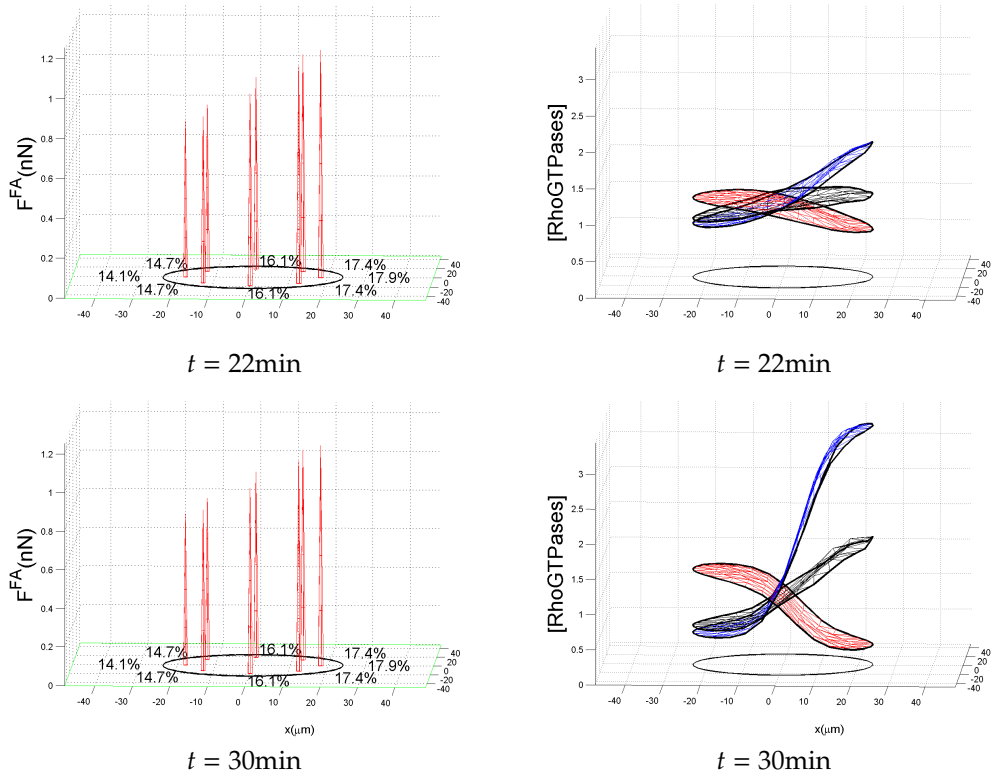

t = 22min t = 22min

t = 30min t = 30min

Figure 8.14: ⊗ Stiffness gradient sensing and polarization for E_{S0} = 40kPa+0.35 kPa·μm^{-1}. Number at the side of FAs indicates percentage of closed bonds.

The orders of magnitude of FA forces, size and polarization times are consistent with experimental observations. This computational result, using a larger gradient than in the experiment and those found in physiological conditions, is meant to illustrate the proposed mechanism of gradient sensing, whose theoretical foundations have been laid out previously. The rigthward-pointing gradient of stiffness induces a small delay in growth, smaller equilibrium size and less energy storage per receptor at the FAs anchored on the softer region of the substrate on left side of the cell. Note that forces developed at the adhesions on the softer end are also smaller and that FAs have matured after approximately 10 minutes. Thus, the small offset in the mechano-transduced signal transmitted to the RhoGTPase network results in the emergence of an activation wave propagating inwards from the edge of the cell on the stiffer side that establishes the polarized pattern after approximately 30 minutes. The evolution of the variables that determine the fate of Focal adhesion and the strength of the mecho-transduced signal reveals this principle; they are shown in the following figure together with their difference in

at FA_1 and FA_2, the contacts on the soft and stiff ends along the gradient:

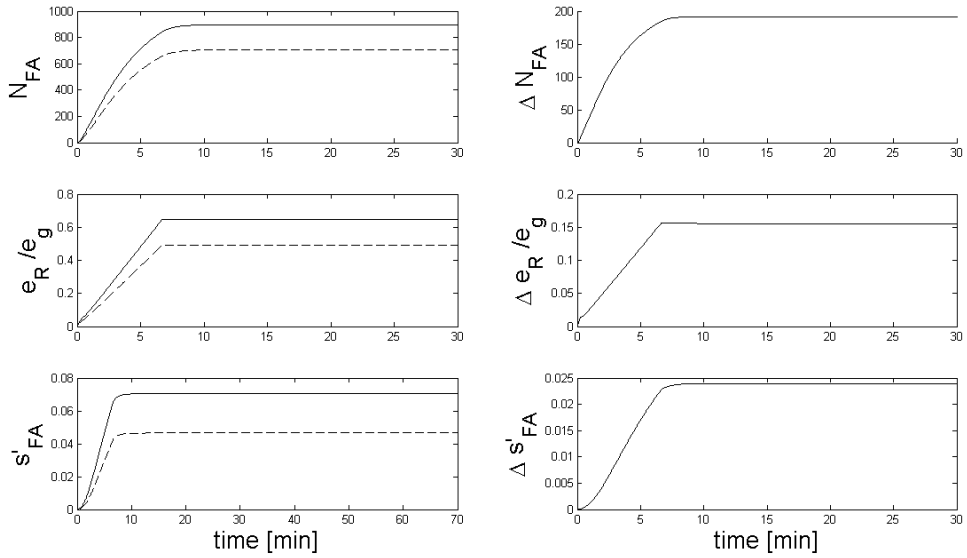

Figure 8.15: Left col: Evolution of number of bonds $N(t)$, displacement, and time-derivative of signal s_{FA} to RhoGTPases from FA_1 (solid line, stiff) and FA_2(dashed line,soft). Right col: evolution of the difference in the same variables. E_S = 40kPA+0.34kPA$\cdot\mu$m^{-1}.

It is now turn to compare the theory's predictions with actual experiments analyzing the relationship between mechanics, cell polarization, and movement.

8.3.2 Mechano-induced cell polarization: theory and experiments

The number of experimental observations for which the theory provides an interpretation for which there is currently none is quite substantial. Predicted forces of the order of $\sim 1-5$nN developed at Focal Adhesions are consistent with the values measured at individual contacts during the process of rigidity sampling reported in [14, 8]. The time of the order of $\sim$ 10 minutes required to establish mature contacts matches the values observed *in vivo* [49, 122, 8]. Polarization time is also consistent with experimental evidence, as it will be discussed later. Simulations varying the absolute Young's Modulus of the substrate from $E_{S0} \in (1, 90)$ kPa and the slope of the gradient from $\Delta E_s = 0.01 - 0.04$ kPa$\cdot\mu$m^{-1} show that the proposed mechanism of gradient sensing remains operative to for all the combinations of gradients and rigidities matching the properties of the *PAAm* in the Durotaxis essay discussed previously[13]. Thus, the theory proposed captures the remarkable sensitivity to shallow gradients that constitutes the main observation of the

experiment. Further, the simulations confirm the prediction of the theory that there is an upper and lower limit of substrate rigidities in which the cell can detect a gradient, which provides insight into observations in the experiment under discussion that can not be accounted for with the interpretation of the authors (i.e that polarization is determined *only* by the gradient slope). In the simulations, the lower bound for mechanically induced polarization is caused by the failure of FAs to mature in very compliant substrates. As shown previously, on very soft substrates the displacement of the contacts leads to a vanishing rate of bond formation, Focal adhesion shrinkage and disappearance. In this case, the signal transduced by the short-lived contacts does not trigger polarization, and RhoGTPase concentrations simply remain flat in the initial homogeneous concentration. This cell state will be labelled *apoptotic*.

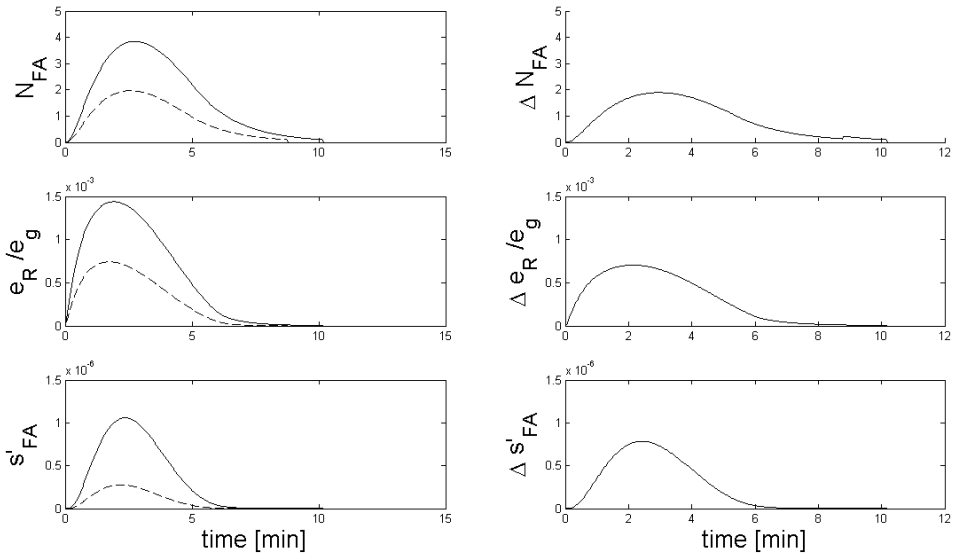

Figure 8.16: ⊗ FA maturation failure for E_S = 4kPA+0.04kPA·μm^{-1}.

For the parameter values adopted, Focal adhesions growth starts to weaken for stiffness bellow $E_{ref} \sim$ 10kPa and the rupture limit is found at substrates of $E^{FA}_{min} \sim$ 5 kPa. Interestingly, the recent study by Geiger's group analyzing the causal relationship between rigidity and cell polarization observed that *fibroblasts* plated on substrates bellow the range of 5kPA failed to polarize[210]. Intriguingly, the data reported in the Durotaxis essay by J.Wong's group also shows a qualitative change in the behavior of cells for rigidities on this range. Measures of the angle of cell orientation in populations of at least 30 individuals show a sudden decrease n the number of cells found and measured at 10kPa on both gradient *and* uniforms substrates (see figs 5B-C and 4E in [13]). The latter fact can not be accounted

for by the migration of cells towards in increasing stiffness but finds a simple explanation within the theory proposed.

Conversely, the upper limit for gradient sensing on rigid substrates found in the simulations is caused by the relative difference in stiffness $\Delta E_S \cdot L_{cell}/E_{S0}$ falling bellow the sensibility threshold, as predicted by the theory. In this case, the time-course of Focal adhesion maturation is nearly identical and the difference in mechano-transduced signal between the two FA's is small.

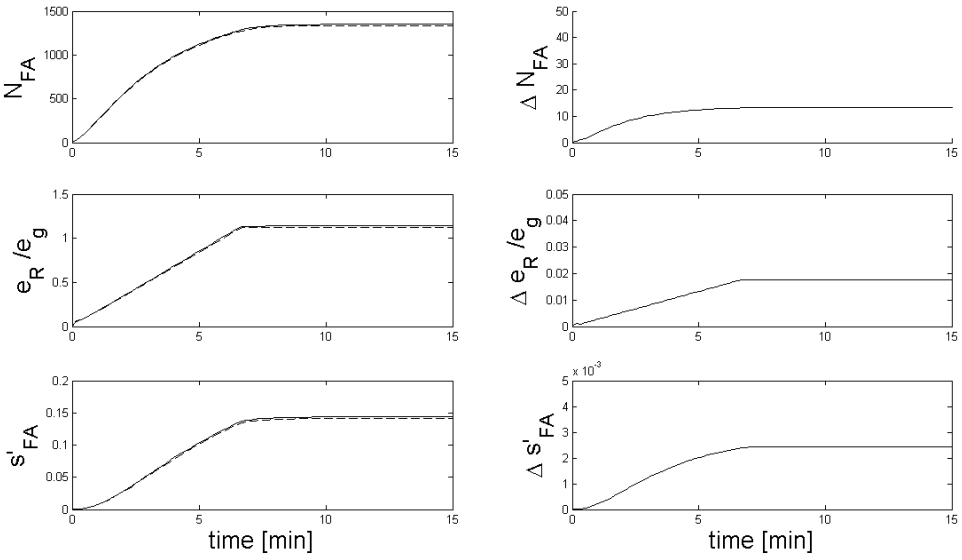

Figure 8.17: ⊗ Nearly identical FA maturation and mechano-transduced signal for E_S = 90kPA+0.04kPA·μm^{-1}.

Hence, the signal mechano-transduced to the RhoGTPase network can not be differentiated, so that RhoGTPases are activated almost simultaneously at both ends and the final distribution of protein activation is a bell-shaped pattern:

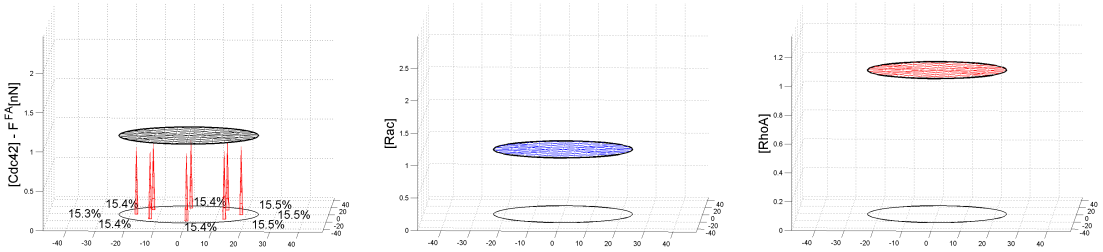

t=3 min.

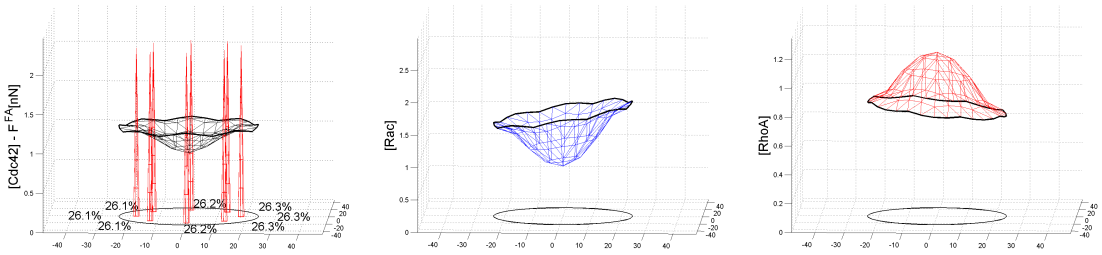

t= 20 min.

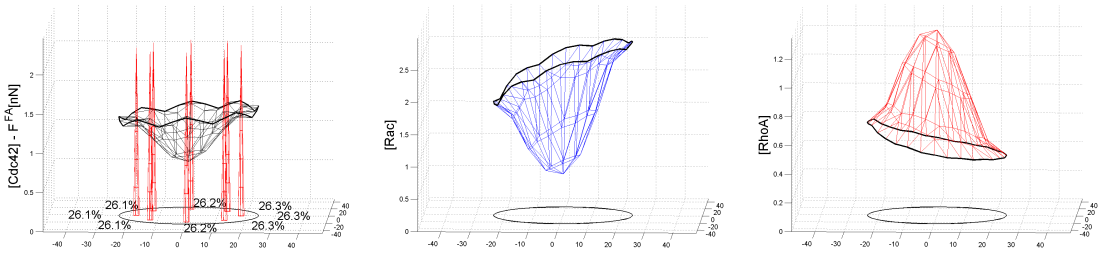

t=30 min.

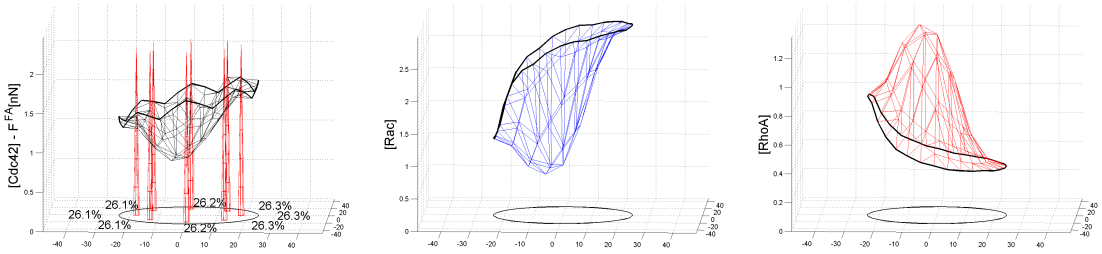

t= 40 min.

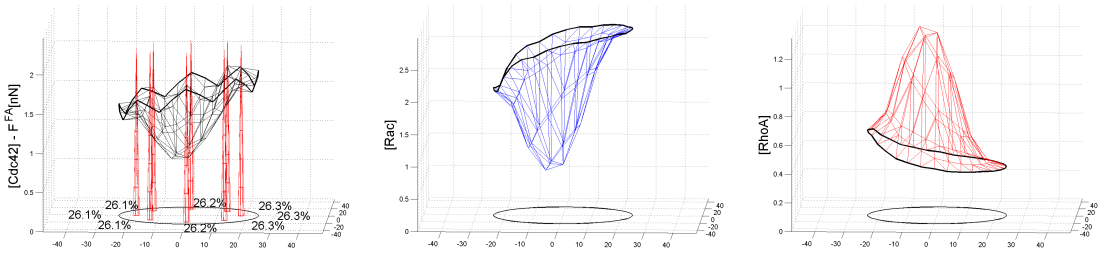

t= 48 min.

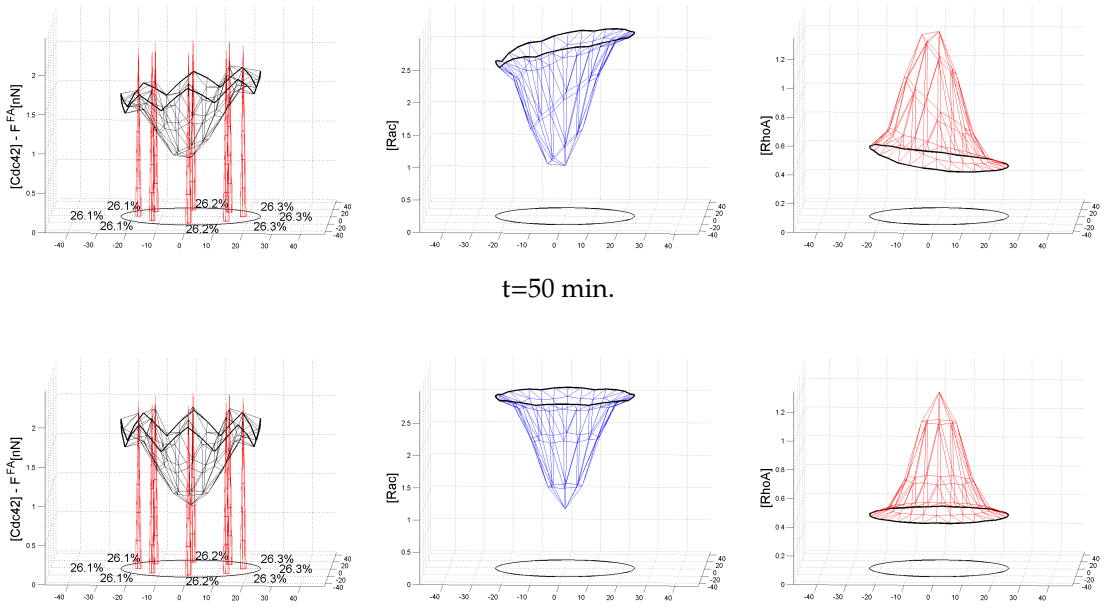

Figure 8.18: $^{\otimes}$ *Adherent* state for E_S = 90kPA+0.04kPA·μm^{-1} above upper bound for gradient sensing.

This state is qualitatively different from the *polarized* state and will be labeled *adherent*. The values obtained for the rigidity threshold above which a given gradient is not detected are could be likely an underestimation of range in which cells can detect mechanical anisotropies. First, the upper limit is set by the time-scale ratio of RhoGTPase polarization dynamics and the mechano-transduction process. Speeding the modulation of their kinetic constants by Crosstalk signals results in an increase in the velocity of the RhoGTPase activation waves[22]. Then, faster RhoGTPase dynamics and higher wave-speed allow the suppression of activation zones on the softer end of the substrate in the small time-window separating the emergence of activation at the two ends of the cell[23]. In addition,

[22]The speed of RhoGTPases activation-waves can be boosted in two ways. First, reducing the parameters s_0 (see eq. 7.12) that set the concentration scale for crosstalk modulation, given a shift from the equilibrium concentrations. Second, by reducing the speed of *Cdc*42 activation by FAs (i.e $\eta_{cdc} \downarrow$, see table 8.2), so that the time-scale of the mechano-transduction process is slower than the speed of activation-waves. Using the first method, a gradient $\Delta E_S = 0.04 kPA$ induced polarization for rigidities as large as $\sim$ 0.5MPa

[23]Similarly, increasing the strength of the inhibition of *Cdc*42 by *RhoA* and of *RhoA* by *Cdc*42 or *Rac* also facilitates the establishment polarity along the stiffness gradient. Stronger inhibition of *RhoA* at the stiff end leads to higher levels of *RhoA* at the other end, which in turn reinforces the

recent experimental evidence has shown that the *FAK*/*paxilin*/*vinculin* pathway is involved in broadening the range of sensitivity to stiffness variations[14], suggesting that the mechanism of gradient sensing proposed might be reinforced by biochemical feedback. Since these molecules are known targets/effectors of the RhoGTPases, a plausible mechanism to amplify gradient sensing could involve a channel of inside-out regulation from the RhoGTPases to adhesion sites[24]. For instance, there is substantial evidence that *Cdc*42 and *Rac* promote the formation and growth of nascent contacts in the early stages of FA formation [19, 48]; thus, introducing a positive effect of *Cdc*42/*Rac* activation on FA growth during the mechanosampling process would constitute a feedback loop (FAs→ *Cdc*42 → *Rac* →FAs) that could reinforce the sensitivity to mechanical anisotropies.

This discussion is meant to emphasize that the value of the upper limit of rigidity for gradient sensing is an estimation, the important point is the prediction that in principle it should exist and, according to the theory, depend on the relative magnitude of the gradient *and* and the value of absolute rigidity compared to the rigidities E_{ref}^{cell} of the tissues in which a particular cell type is found in physiological conditions. Also interesting is the observation that the developments of this section are based on the simplifying assumption that the model cell has a perfectly symmetrical distribution of Focal Adhesions, which is certainly not what is observed in real cells. A more realistic hypothesis would entail the introduction of an stochastic element in the number or nucleation process of Focal Adhesions. In this case, any initial asymmetry in the FAs undergoing maturation would be translated into an asymmetry in the mechano-tranducted signal, which in turn would lead to a random orientation of the polarization axis and randomly directed movement, even on uniform substrates. Indeed, *taxis* does not stand for directed linear movement, but for movement towards a source following a sequence of random moves and turns that is biased by the source or gradient. This applies to both chemotaxis and durotaxis. This hypothesis will prove to be fruitful in the next section, where actual movement induced by rigidity is discussed.
An important prediction that stems from the theory is that the time t^{pol} required by the cell to detect the stiffness gradient and polarize is a non-monotonic function

inhibition of *Cdc*42 and aids to resolve the gradient. This is the reason why the crosstalk scheme labelled as Model C has been selected as the interaction scheme for the RhoGTPases. Model A and B can also act as integrators of mechanical information, but since *Cdc*42 is not inhibited by any protein, transient peaks of activation of this protein emerge at the soft end. For intermediate rigidities, this secondary peak is eventually suppressed due to protein conservation, but it leads to slower resolution and a reduced rigidity-range for gradient detection. For larger rigidities, the RhoGTPases reach the bell-shaped distribution that corresponds to the *adherent state*.

[24]Plausible mechanisms to mediate inside-out regulation of FA affinity/avidity have been discussed previously and could be readily tested introducing a dependency on RhoGTPase concentrations in the λ parameters that control the dynamics of FAs

of the rigidity E_{S0} and the slope of gradient ΔE_S of the substrate. The relationship between these variables has been analyzed running simulations for $E_{S0} \in (1, 90)$ kPa and $\Delta E_s = 0.01 - 0.04$ kPa$\cdot\mu$m^{-1}, the ranges of substrate rigidities and gradient slopes of the Durotaxis essay in [13][25].

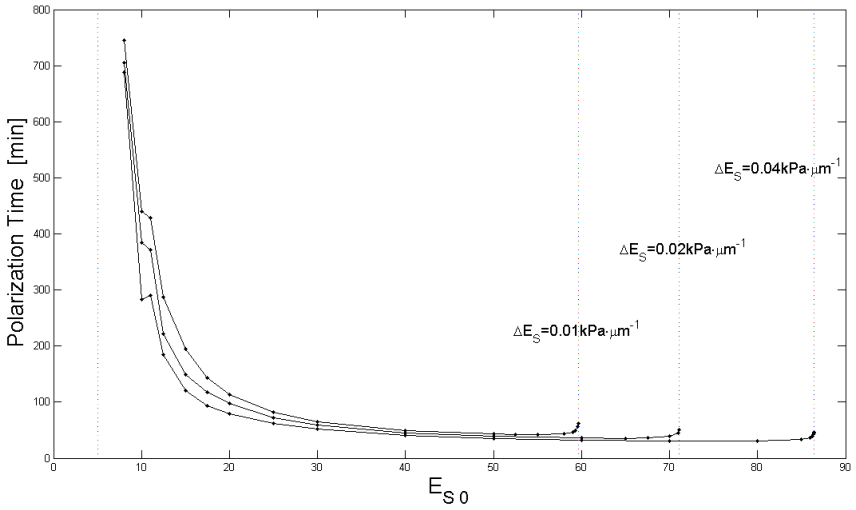

Figure 8.19: Predicted relationship between polarization time $t^{pol}(E_{S0}, \Delta E_S)$ and substrate rigidity for $\Delta E_s = [0.01, 0.02, 0.04]\cdot$KPa$\cdot\mu$m^{-1}

This result provides an interpretation for the experimental findings from two studies published in the past months [210, 232] and another recent Durotaxis essay[12]. In the study by Geiger's group, it was established that *fibroblast* polarization is preceded and requires focal adhesion mechanosensing[210]. Analysis of the time-course of rigidity-induced polarization showed that in compliant substrates is much slower than in rigid substrates, up to the point that bellow rigidities $E_{S_0} \sim$ 5kPa polarization does not occur at all, as discussed previously.

[25] In order to assess $t^{pol}(E_{S0})$ quantitatively from the simulations' results, the following measure of polarization has been defined: a cell point is considered activated when the active RhoGTPase concentration is above a certain threshold relative to the equilibrium levels. Analogously, a cell point is considered inactivated when the active RhoGTPase concentrations are bellow a certain threshold relative to the equilibrium levels. The polarization factor F_{Pol} can then be defined as the sum of active and inactive areas relative the total area of the cell, and a cell is considered *polarized* when the polarization factor is above a certain threshold. The polarization time t^{pol} is simply the time required to reach this value. Note that this measure of polarization allows to distinguish between the *apoptitic*, *adherent* and *polarized* states. Trivially, $F_{Pol}(apoptitic) = 0$, but also $F_{Pol}(adherent) < F_{Pol}(polarized)$, because the activated/inactivated area in the *adherent state* is smaller as a consequence of protein conservation.

For substrates above 30kPa, polarization was clearly observed in time-scales of the order of $2-4$ hours. The results depicted in figure 8.19 match this behavior. On low rigidities, the theory predicts that the sensitivity to stiffness anisotropies is maximized but, at the same time, adhesion maturation is slow and FA saturation size and mechanical energy stored by receptors are small. This results in a weak mechano-transduced signal and long times required to trigger RhoGTPase polarization. Particularly, rigidities between $10-5$kPA are close to the minimum threshold for FA maturation, so that $t^{pol}(E_{S0})$ increases up to $\sim$ 5kPa, where establishment of FAs fail and $t^{pol}(E_{S0}) \to \infty$. For larger rigidities, increasing speed of FA maturation and energy loading leads to strong mechano-tranduced signals and a reduction in the time required to polarize. By this simple mechanism, the observed decrease in polarization time with rigidity found in [210] and the absence of polarization in very compliant substrates observed in [210] and [13] finds a straightforward explanation[26]. The orders of magnitude obtained for $t^{pol} \sim 1$ hour are consistent but somewhat shorter than the values of $2-4$ hours reported in [210]. Note however that this study used cell aspect-ratio and stress fiber formation as a measure of polarity, which should take longer times than the polarization of RhoGTPases and other regulators of these remodeling process.

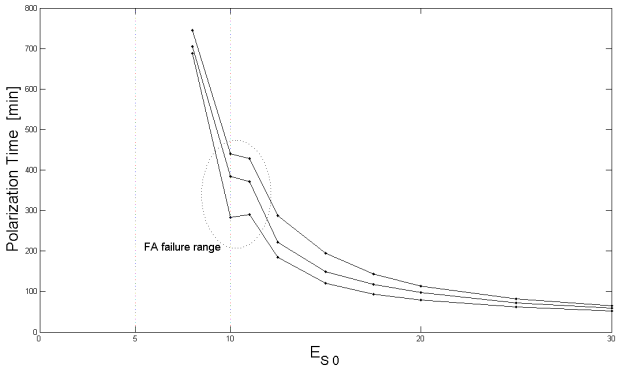

Figure 8.20: Focal adhesion failure affects polarization time

Close inspection of the relationship $t^{pol}(E_{S0}, \Delta E_S)$ reveals a small window close to 10KPa where polarization time decays. This value matches the range where FAs begin to fail. On a substrate with this value of midpoint rigidity and a stiffness

[26]This result can be also understood from the theoretical developments of the previous section: t^{pol} is limited by the time t^{wa}_{FA} required to trigger activation waves. From eq.8.23, it can be seen that for $E_{S0} < E_{ref} \sim$ 10kPA (i.e $a(\bar{k}) < 1$), t^{wa}_{FA} grows as $\sim exp(1/a(\bar{k}))$, whereas for $a(\bar{k}) \sim 1$, t^{wa}_{FA} decreases quadratically as $\sim 1/a(\bar{k})$ up to a minimum value for large rigidities that depends on the RhoGTPases wave-speed but is independent of E_{S_1}.

gradient, a cell would be adhering on the boundary that marks the threshold for FA maturation, i.e a fraction of its adhesions would form slightly above the minimum rigidity to mature and the rest bellow. The increase in the asymmetry of the signals emitted by the two sets of contacts explains the decay in t^{pol}[27]. This effect provides an explanation for the observations in early durotaxis essays, where the common procedure to create a gradient was to join two blocks with markedly different elastic moduli, creating a rigidity jump with a well defined boundary[28, 35]. These experimental set-ups showed that cells reaching the boundary from the stiff side were unable to cross the boundary, whereas cells reaching it from the soft side displayed a prominent bias to migrate away of the boundary towards the stiff side. In the theory's framework, the no crossing from stiff→soft is explained by the failure to establish FAs, and the increased bias to escape from soft→stiff is explained by the combination of a large gradient, large sensitivity at low rigidity and the additional asymmetry in FAs formation just described.

8.3.3 Durotaxis limits: theory and experiments

On the extreme of large rigidities, a different principle explains the sudden rise in $t^{pol}(E_{S0}, \Delta E_S)$ and eventual failure to polarize in response to a mechanical gradient. In this case the mechano-transduced signal by FAs is strong but its relative difference along the gradient is small, so that the distribution of RhoGTPases transiently adopts a bell-shaped distribution until crosstalk between the proteins eventually allows to resolve the gradient. This explains the sudden rise in the time required to polarize seen at the far right of the axis in fig.8.19 Above a certain threshold of rigidity, which increases with the magnitude of the gradient, the bell-shaped distribution is permanent and the cell adopts the *adherent* state. This explains the failure of gradients $\Delta E_S = [0.01, 0.02, 0.04]\text{kPa}\cdot\mu\text{m}^{-1}$ to induce polarization above a certain value of absolute rigidity seen in figure 8.19, and the shift of this threshold to larger rigidities as the magnitude of the gradient increases. The predicted biphasic relationship between t^{pol} and E_{S0} follows from these two simple principles. Be reminded that this prediction is not meant to imply that cells do not polarize above certain rigidity, since real cells are not symmetric; it concerns the limit in which mechanical anisotropies induce a bias in the direction of polarization. The threshold of rigidity above which a gradient of slope ΔE_S can not be detected is labeled as $E_D^{cell}(\Delta E_s)$, to denote that it marks the value where cells

[27] Note that the discontinuous jump in t^{pol} would become a smooth ondulation if more values for t^{pol} in $E_{S\,0} \in [10 \pm L_{cell} \cdot \Delta E_S]$ had been calculated.

should loose the ability to Durotax in response to it. [28]. A systematic assessment of the experimental limits of cellular sensitivity limits to mechanical anisotropies has not, to my knowledge, been made. In fact, this theoretical prediction seems to contradict the main conclusion of the authors of the Duroatxis essay under discussion, that the mere existence of a stiffness gradient induces biased migration. Further, they also observed that the bias of *VSMc* cells to move up the gradients of *PAAm* gels increased with the magnitude of the gradient but was not affected by the absolute rigidity (although the authors state that the number of cell datapoints measured is not large enough to have statistical significance), which lead them to conclude that the duro-tactic index depends on ΔE_S but not on E_{S0} (see experimental results in figs. 8 A,B,C in [13]). However, another recent Durotaxis essay by Kidoaki and coworkers[12] with 3*T*3 fibroblasts did indeed find a limit of cell sensitivity to mechanical anisotropies. The stiffness profiles and main observations of the different substrates used in these essays are depicted bellow:

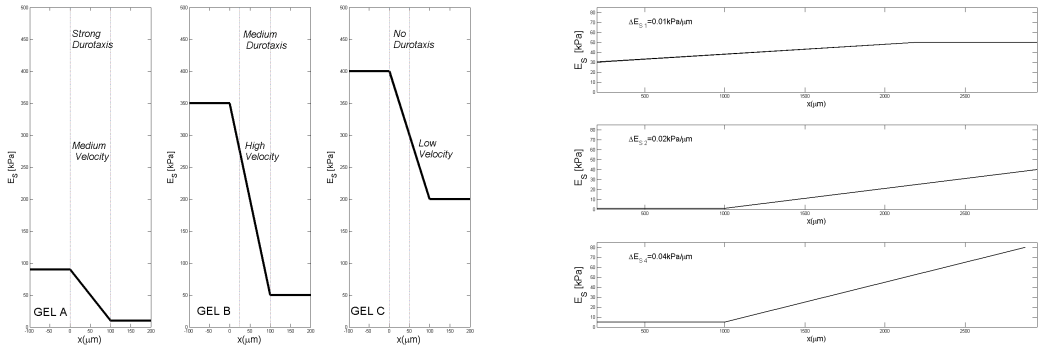

Figure 8.21: Stiffness profiles in Durotaxis essays by Kidoaki et. al [12] (left) and Isenberg et. al [13] (right). Gradient slopes in Gels A,B, C are 1-2 orders of magnitude larger than in *PAAm* gels. Vertical lines indicate the range where durotaxis was studied.

In Kidoaki's study, three gels labeled as A, B and C, with stiffness gradients as large as ΔE_S = [0.8, 3, 2]kPa·μm^{-1} were manufactured in order to asses quantitatively the bias induced by mechanical anisotropies in the direction of

[28]The fact that E_D^{cell} should depend on the cell type has already been discussed during the exposition of the theory. Briefly, it is explained by the fact that sensitivity to mechanical anisotropies depends on the range of stiffness on which the cell is plated compared to E_{ref}^{cell}, which in turn is determined by the contractility of the cell and the type of Focal adhesion receptors expressed.

migration of 3*T*3 fibroblasts. The results showed a clear bias to migrate up the gradient on Gels A and B; however trajectories on gel C where not influenced by the gradient. This result is quite surprising, considering that the gradient of Gel C was 300-fold larger than on the *PAAm* gel of $\Delta E_S = 0.01\text{kPa}\cdot\mu\text{m}^{-1}$ that was observed to induce biased migration of *VSM* cells in [13]. This proves that the mere existence of the gradient is not enough to induce durotaxis, and that another variable determines the process. The authors of [12] observe that the decrease in the *duro-tactic* index from Gel A to Gel B and the failure to induce *durotaxis* in Gel C could be accounted for considering the *jump* or ratio of rigidity at the high an low ends of the gradient, which for gels A, B, and C follows the relationship $9 < 7 < 2$. This hypothesis[29], however, can not explain that the shallowest gradient of the *PAAm* gels used in the study by J. Wong's group induced durotaxis, since the jump in stiffness in this gel as small as 1.66. The different outcomes of these experiments could be attributed to *fibroblasts* having a lower sensitivity to mechanical anisotropies than *VSMc* cells, although this interpretation goes against all the evidence of earlier mechanosensing essays, with *fibroblasts* being the main cell type studied and having showed a high sensitivity to mechanical cues[29, 30]. Next, it will be shown that the mechanosensing theory introduced previously provides a unifying explanation for this seemingly contradictory observations. According to the theory, a stiffness gradient can be resolved as long

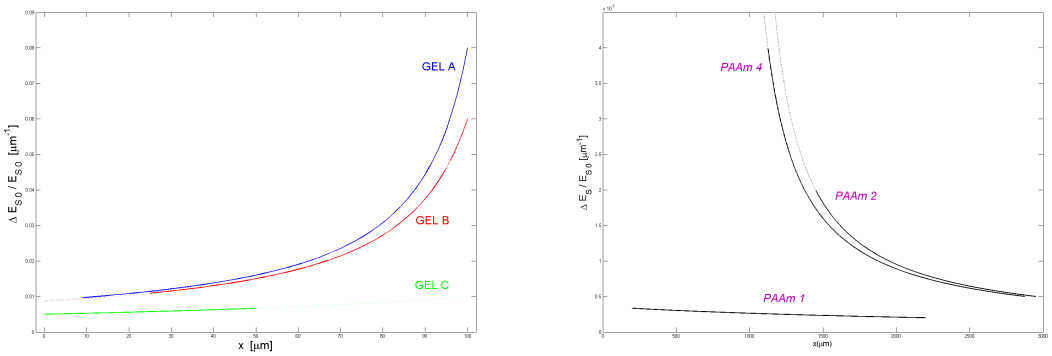

Figure 8.22: Stiffness gradient to rigidity ratio for Gels A, B, C in Durotaxis essay by Kidoaki et. al [12] and *PAAm* gels in Durotaxis essay by Isenberg et. al [13]

as the time-window separating the emergence of activation waves triggered by

[29]If the *jump* in stiffness $E_{S1} + \Delta E_S \cdot \Delta L_{substrate}$ was determining the migratory behavior observed in the experiment, it would imply that cells were perceiving the mechanical properties of points removed $100\mu m$ from them, which does not seem biologically reasonable

mechano-transduction signals is larger than the time required by the regulatory wave to travel a cell length and establish the polarized pattern. This condition, expressed mathematically in eq.8.25, leads to the intuitive prediction it is the relative difference in stiffness at the two extremes of the cell what determines if a gradient will induce durotaxis. For a given gradient of slope ΔE_S, the maximum rigidity E_D^{cell} above which it will not be perceived and will not bias cell migration is given by a relationship between $E_D^{cell} \propto \Delta E_S^{1/n}$, as given in eqs. 8.26. Further, the scaling of the relationship varies for different ranges of stiffness compared to E_{ref} (going as $E_D^{cell} \propto \Delta E_S^1$ for $E_S \sim E_{ref}$ and $E_D^{cell} \propto \Delta E_S^{1/2}$ for $E_S > E_{ref}$) and its independent of the cell size. An estimation of $E_D^{cell}(\Delta E_S)$ has been obtained performing repeated simulations with increasing values of absolute rigidity until the computational cell failed to polarize and instead adopted the *adherent* state. The

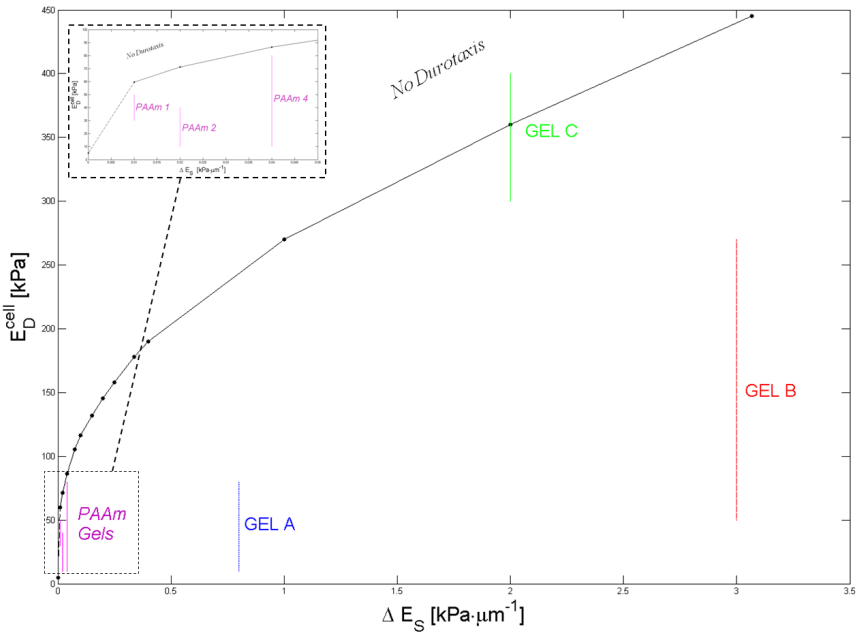

Figure 8.23: Theory and Simulation predict positive and false observations of Durotaxis in essays by Kidoaki et al. [12] and Isenberg et. al [13]

results of the simulation[30] show that the large gradient of Gel C in the Duroatxis

[30]The first data point $[E_D, \Delta E_S]$ = [5kPa, 0kPa·μm^{-1}] has been added because a cell plated at the limit where FAs fail finds half its body on a surface were FA can not form and half where they do, resulting in cell polarization even in the absence of a gradient. See discontinuous line in the inset figure.

essay by Kidoaki et al. is the only substrate falling in the No Durotaxis regime, whereas all the *PAAm* gels in Isenberg's study [13], despite the shallowness of their stiffness gradients, are bellow. Thus, this explains the observations that Gel C, despite having a gradient of stiffness of 2KPa$\cdot\mu m^{-1}$ did not induce Durotaxis, whereas even the shallowest gradient of 0.01KPa$\cdot\mu$m^{-1} of the *PAAm* gels did. This also shows why the conclusion of the authors of [13], that the mere existence of a gradient induces Durotaxis, is not accurate. They observed biased migration on all the *PAAm* gels because all their the their tests were performed at baseline levels of rigidity in which the gradients are predicted to induce Durotaxis; had they tested *PAAm1* above 60kPa or *PAAm4* above 80kPa and they would have observed a weakening and eventual vanishing of the duro-tactic index. In fact, the data reported seems to confirm this prediction: since the cell data points in the scatter plots of duro-tactic index vs rigidity for *PAAm1* and *PAAm4* indicate a weakening in the bias to migrate along the gradient as the rigidity approaches the predicted value of $E_D(\Delta_S)$, but this trend is not observed in *PAAm2* (see scatter plot figs 8A,B,C in [13] for the three gels), which is the gel that is further from the durotaxis limit (see inset plot in the previous figure). Note also that Gel C is only substrate at the limit of the Durotaxis limit but the simulations suggests that some weak bias to migrate towards the stiffer area of the cell should occur on the softest part of the gel, which was not observed. Of course this could be amended by fine-tuning the parameters given in table 8.3, which were assumed to illustrate the mechanism of gradient sensing without awareness of the experimental observations under discussion. But there is a more interesting observation that follows from this result: the scaling of E_D with ΔE depends on the assumption that the mechano-transduction process occurs on time-scales longer than the maturation of Focal adhesions. This assumption was based on the evidence that rigidity-induced polarization is preceded by FA mechano-sensing [210], which lead to derive the time-window between activation events approximating $N(t)$ as $N_{eq}(E_S)$. Assuming instead that the activation events occurs during the process of FA growths leads to a different scaling of E_D with ΔE. In this case, the theoretical prediction neatly predicts that Gel C falls entirely out of the durotaxis regime, whereas the other gels would remain inducing Durotaxis. In turn, the fact that the mechano-transduction event should occur simultaneously to FA maturation puts constraints on the actual bio-chemical mechanism of mechano-trasnduction, about which little is known.

8.3.4 Migration speed vs rigidity or adhesiveness : theory and observations

Another prediction of the theory is that migration velocity depends on the rigidity of the substrate and this, in turn, has interesting implications for the observed dependence of migration speed on the *adhesiveness* of the substrate, mainly determined by the density of ligands coating its surface. The theory proposed predicts that at low rigidities the time required to polarize is large because small contacts take long to trigger the activation of the regulatory apparatus of cell migration. Since cell polarization is necessary to attain directed migration, the time required to polarize must be a limiting factor of migration, and consequently $1/t^{pol}$ is a key factor determining cell speed. As shown in fig. 8.19, at the extreme of low rigidites t^{pol} is very large and as a consequence, cell migration should be slow. This mechanism explains the qualitative observation in the Durotaxis essay by Kidoaki and coworkers [12] that even though Gel A was more effective in biasing migration towards increasing rigidity, the speed of 3*T*3 fibroblasts was clearly larger on Gel B. Note that the rigidity of Gel A at the low end of the gradient was 10kPa, close to the predicted limit for FA formation, whereas the baseline rigidity for Gel B was 50kPA. The fact that the (non-biased) migration on the more rigid Gel C was also slower than in Gel B must be due to another mechanism, and the theory proposed also suggests an explanation: in this case, the velocity is limited by the fact that the size of Focal adhesion increases with stiffness, which results in longer times required to release the contacts at the cell trailing edge after contractile forces are applied by the cell. Therefore, the theory proposed predicts a biphasic relationship between cell migration speed and substrate rigidity resulting from two different processes: the long times required to trigger polarization on soft substrates and the increasing difficulty in tearing-off focal adhesions at large rigidities, with optimal velocities found at some intermediate level of rigidity. An illustration of the process of cell mechanosensing, polarization, force development, FA release and movement is given in the following simulation.

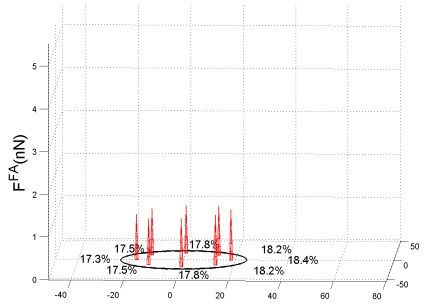

$t = 24min.$

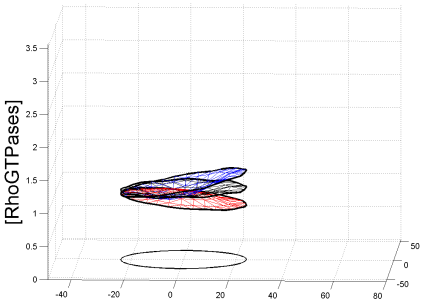

$v_{cell} = 0.0\mu\text{m}\cdot s^{-1}$

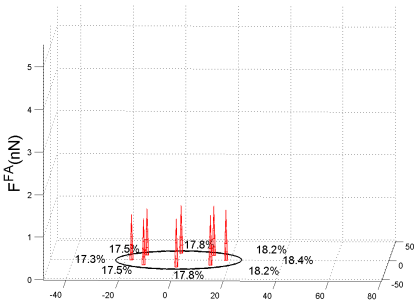

t=27 min.

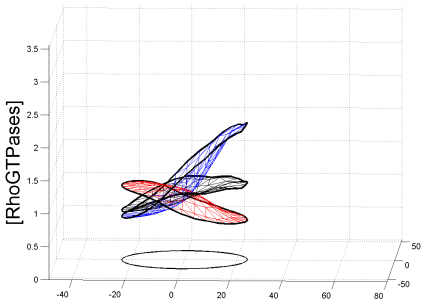

$v_{cell} = 0.0\mu\text{m}\cdot s^{-1}$

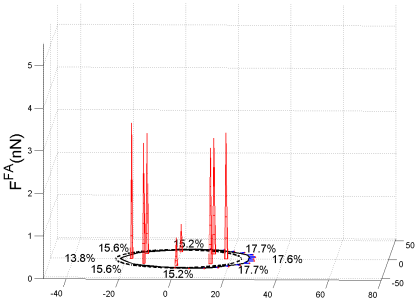

t=31 min.

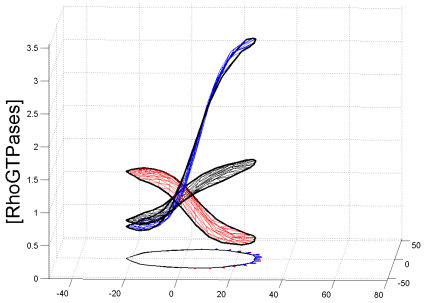

$v_{cell} = 0.1\mu\text{m}\cdot s^{-1}$

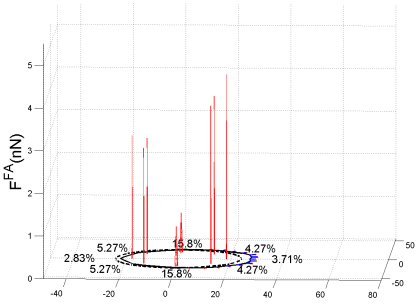

t=34 min.

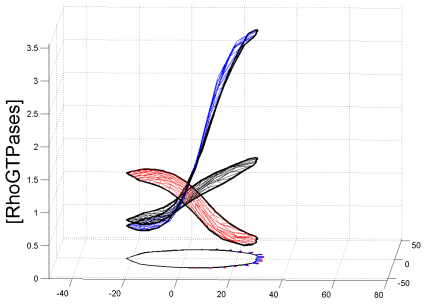

$v_{cell} = 0.11\mu\text{m}\cdot s^{-1}$

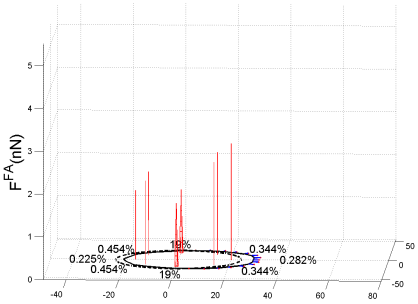

t=38 min.

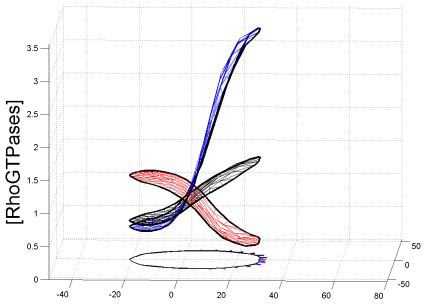

$v_{cell} = 0.12\mu\text{m}\cdot s^{-1}$

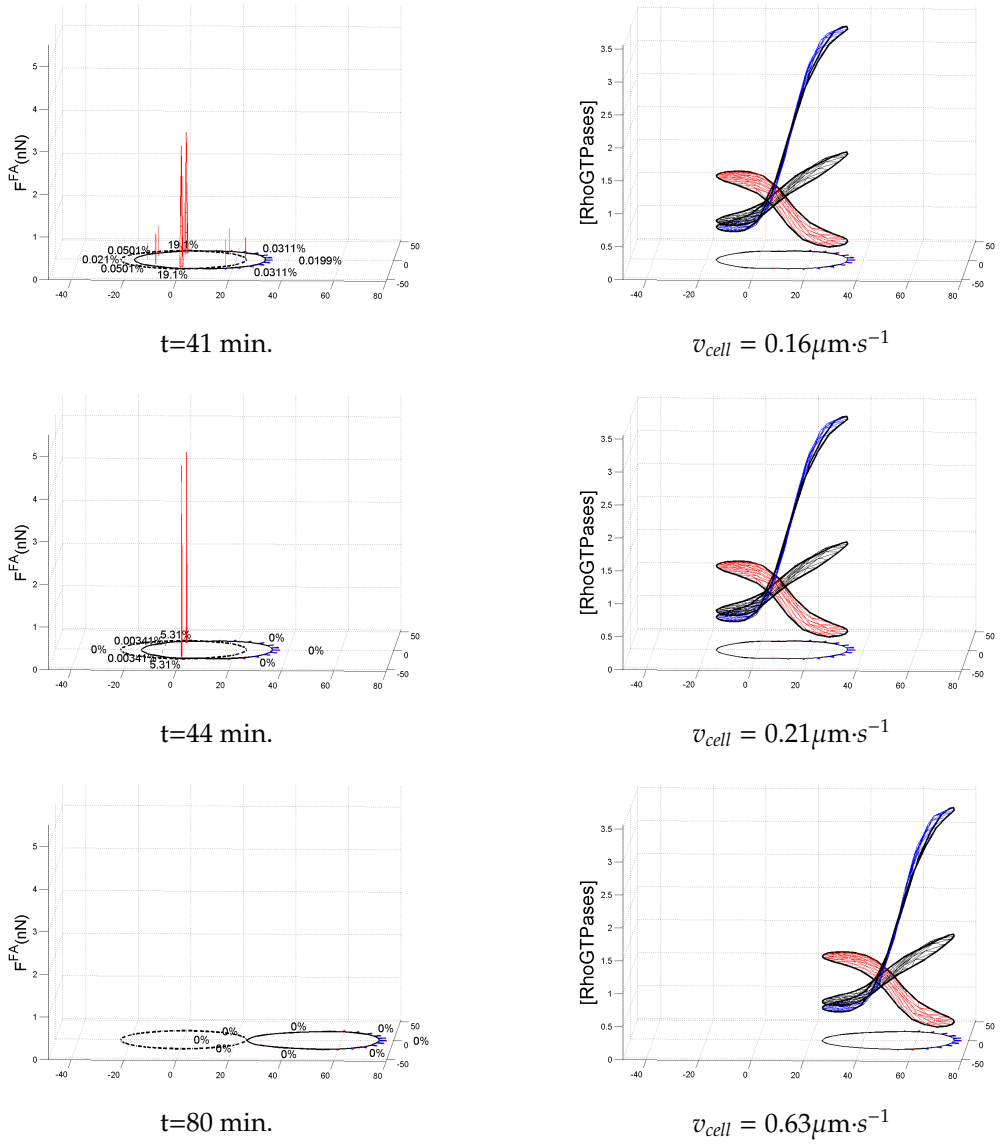

Figure 8.24: ⊗ Mechano-induced polarization, FA turnover-disassembly, and movement.

The magnitude of contraction and protrusion forces in the simulation of directed migration [31] are determined by the concentration of *Rho* and *Rac* through the

[31] A stiffness gradient of $0.1\text{kPA}\cdot\mu\text{m}^{-1}$ has been added to direct the motion. Note that small gradient has little effect on the speed of the mechano-transduction process and contact rupture, and thereby, on cell speed. This requirement can be removed introducing an stochastic element in the nucleation process of FAs

phenomenological laws introduced to study chemotactic movement and stated in eqs.7.18-7.19. Force and cell parameters were estimated from observations and given in table 7.2. In addition, a mechanism of inside-out regulation from RhoGTPases to Focal adhesions has been included: once the computational cell reaches the polarized state, *Rac* promotes FA disassembly at the cell front by reducing the rate of bond formation [32]. The previous simulation shows the basic steps of cell migration, initial formation of Focal adhesions, polarization of the regulatory apparatus induced in this case by mechanical cues, force development, eventual release of the contacts and forward movement. Values of forces and velocities match experimental observations: the velocity given in fig.8.24 corresponds to the mean velocity of the cell centroid, while the final instantaneous speed reaches a value of $v_{cell} \approx 1.24 \mu \text{m} \cdot s^{-1}$, close to the values reported in [232]. Note the change in the distribution of forces sustained by Focal Adhesions as protrusion and contraction forces are developed, with large forces at the cell front and back as observed experimentally [204, 122], and the sequential release of FAs depending on the position along the migration axis. Mean cell velocity is determined by t^{pol} and the time required to *disassemble* the contacts at the cell trailing edge and FA *turnover* at the front.

The relationship between rigidity, polarization time, Focal adhesion size and migration speed has been analyzed varying the rigidity of the substrate. This result, in turn, provides an explanation to the observations of a recent and fascinating study in which the relationship between descriptors of Focal adhesion (FA size, number, shape) and descriptors of cell migration (cell speed, persistence distance of migration, number of turns, distance traveled) was for the first time assessed quantitatively[232]. The central result of this experiment was quite surprising: the size of Focal adhesions, not their number, shape or molecular composition, was an accurate predictor of migration speed for both *mouse embryonic fibroblasts* (*MEFs*) and *human fibrosarcoma* cells (*HFs*). In order to compare the predictions with the experiment, repeated simulations of the migration process have been performed varying the substrate rigidity in $\Delta E_{S0} = [10, 80]$kPa: the relationship obtained between the (normalized) mean size of the Focal adhesions

[32]This is not a central property of the model: it has been added to account for the observed difference in the mechanisms of FA release at the rear and front of migrating cells, labeled as *disassembly* and *turnover*, respectively [48]. FA *disassembly* is a mechanical process primarily driven by contractile forces, as evidenced by the observation that migrating cells leave a trail of integrin receptors on the substrate that had been ripped-off from the contacts at the rear[233]. Conversely, FA *turnover* at the cell front is regulated by signaling involving the RhoGTPAses, evidenced by the sequential removal of different molecular components of adhesions[48]. The detailed mechanism of FA turnover aided by inside-out signaling influences quantitatively the speed of release of contacts at the front, but it does not change the qualitative prediction that highly developed FAs hinder cell movement.

developed by the computational cell $N(E_{S0})$ and (normalized) migration velocity is plotted in fig 8.25: This result provides a clarifying interpretation of the re-

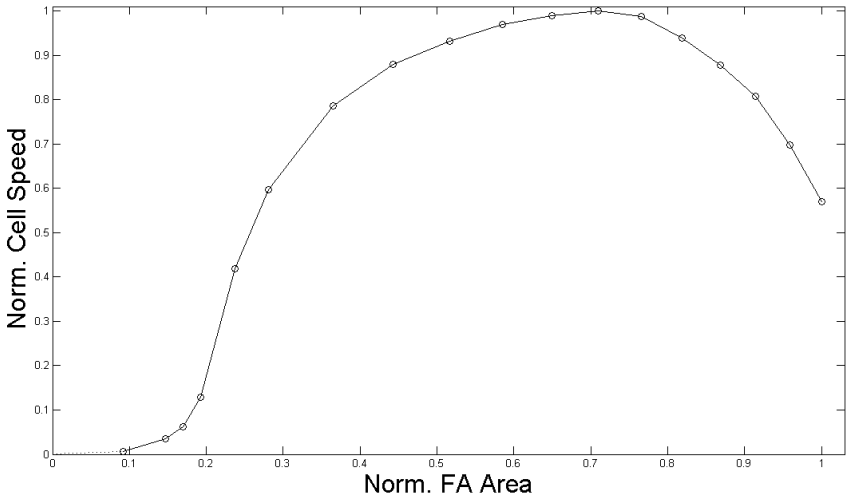

Figure 8.25: Cell speed and Focal Adhesion Biphasic relationship. Compare with observations given in fig. 2G-3G in migration study by Kim et al. [232]

markable experimental findings of the experiment under discussion [232]. For populations of $30 - 50$ individuals, the authors measured the *mean* area of Focal adhesions in every cell and their *mean* migration speed, finding a gaussian distribution in both the mean FA sizes (see fig. 1H in [232]) and speeds (see fig. 2C in [232]) for the cells in a population. Similar data was gathered for the rest of the descriptors of cell motility and FA morphology. Statistical analysis of the correlation between different variables showed, strikingly, that "the *mean* size focal adhesion area robustly and precisely predicted cell speed independently of focal adhesion surface density or molecular composition". Precisely, *mean* migration speed of a cell was found to be determined by the *mean* size of Focal adhesions, so that for small FA size, the observed cell speed was small, followed by a range of large migration speeds at intermediate FA sizes, and a decay for large size of adhesion sites (see fig. 2G in [232]). Strikingly, this result was robust against molecular knock-outs of several FA related proteins (see fig. 3G in [232]), suggesting that a simple basic principle underlies this correlation. Plausible principles that could explain this observation have already been presented: on compliant substrates, small contacts developed result in long times to switch the signaling cascade that leads to polarization and movement, conversely, on rigid substrates the cell develops large contacts, resulting in long times of FA disassembly at the cell and rear and front. The relationship obtained from the simulations fits the reported

quite well, the somewhat weaker decay obtained for large FAs is simply due to having assumed a too strong mechanism of inside-out regulation of FAs at the cell front. Thus, the theory provides plausible principles that explain the remarkable observation of a biphasic relationship between cell speed and FA adhesion size in[232].

This mechanism is qualitatively different from the mechanism proposed in the past to account for the observed dependence migration velocity and the density of ligands coating the substrate. As discussed in section 7.4 of Chapter 7, cell speed is also faster at intermediate levels of *adhesiveness* and decays for very large or very low adhesive strengths [194, 195]. Substrate *adhesiveness* is mainly determined by the density of ligands coating the substrate, which results in cells developing stronger Focal adhesions as the *adhesiveness* increased. The involvement of Focal adhesions in this behavior suggests that the biphasic dependence of migration speed on both adhesiveness and rigidity might have common underlying causes. The influence of adhesiveness in migration speed was predicted theoretically in the pioneering work by DiMilla and coworkers [94] and latter observed experimentally. The model accounted for this observation in terms of the physical trade-off between the need to establish sufficiently strong attachment points to exert traction in order to pull the cell body forward, and the increasing difficulty to release these contacts at high levels of cell-substrate adhesion strength. However, its becoming increasingly clear that the story is more complex: measurements of force at Focal adhesion level in migrating cells show that small contacts at the cell front can sustain large tractions[204, 122]. In addition, recent experiments have shown that the underlying mechanisms also involve decreased RhoGTPase activation and myosin-powered contraction at low adhesive strengths[196, 197]. These observations seem to support the idea that the biphasic relationship between velocity and rigidity or adhesiveness at the low range of this variables are caused by the interplay between weak FA formation and delayed mechanotransduction, and not by a simple mechanical principle. The theory proposed, in turn, suggests a common root to both type of observed motility behaviors.

8.3.5 Durotaxis: theory and observations

In the experimental study by Kim and coworkers [232] discussed previously, the observations of FA descriptors vs descriptors of Cell motility were repeated on three types of substrates: (very rigid) glass, rigid and soft gels. A change in the substrate only resulted in a shift in the observed distribution of FA sizes and cell speeds, but preserved its gaussian nature. Precisely, the *means* of the distribution of both FA sizes developed by individual cells and migration speeds increased with rigidity and, interestingly, the *variance* of the distributions also widened with

rigidity. These observations provide valuable information to extend the theory of cell migration and mechanosensing presented in this Thesis.

First, the fact that for a given rigidity the mean size of the contacts developed by individual cells follows a gaussian distribution, and that this distribution is conserved with an increase in rigidity puts constraints on the stochastic element in the initial process of Focal adhesion nucleation. The equation derived to describe focal adhesions is fully deterministic; for a given rigidity the predicted equilibrium size reached by a cell contact is completely determined by E_S and the energy $p_o \cdot t_{cont}$ invested testing the substrate. In this case, the number of closed ligand-receptor bonds will be proportional to the initial availability of integrin receptors N_T, as shown in eq.8.12. Hence, given a uniform substrate and a fixed value of available receptors, all the cell FAs reach the same equilibrium size $N_{eq}(E_S, t_{cont}) \propto N_T \cdot f(E_S, t_{cont})$. In this framework, there are three possible outcomes or states that the cell can reach after testing the substrate, as depicted schematically in fig.8.26. The *polarized* state, particularly, due to the simplifying assumption that all FAs are initiated simultaneously and symmetrically along the cell edge, is only reached in the presence of a mechanical anisotropies. Of course, as stressed previously, this is not what is observed in real cells, which are not perfectly symmetrical. In actuality, even in homogeneous substrates, cell polarize and migrate in a random direction; in my view, this is a consequence of the intrinsic cell asymmetries and the stochastic nature of the initial process of FA nucleation[33]. There are several parts of the initial process of Focal adhesion formation

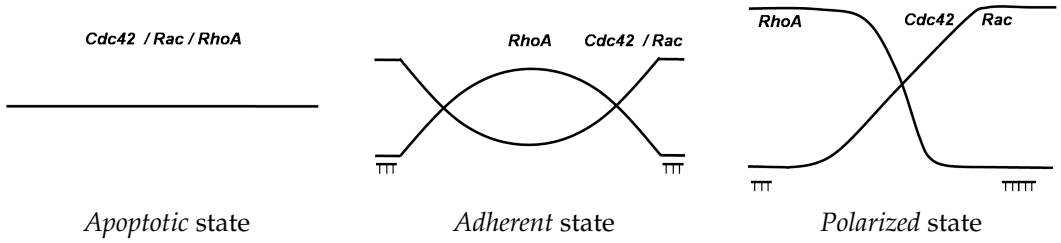

Figure 8.26: States adopted by an ideally symmetric cell with no-stochastic element in the nucleation process of Focal adhesions, depending on the rigidity of the substrate.

that could be stochastically driven: integrin availability in the initial contact, the position of nucleation, the number of contacts formed along the periphery, and so forth. However, the observations in [232] provide constraints on the process that

[33]Noise in the signalling pathways from FAs to the cell regulatory networks is likely to be involved too, but it will not be considered here

might underlie the nucleation of Focal adhesions. The simplest hypothesis that is consistent with the observations is that N_T, the number of available receptors per focal adhesion, is stochastically determined. This assumption reflects that the encounter and nucleation of the small clusters of receptors that constitute the seed of a Focal adhesion is driven by diffusion and thermal fluctuations. It follows that the number of receptors forming that initial cluster should be random, which will in turn determine N_T. Thus, the third hypothesis that completes the proposed theory of cell mechano-sensing is stated as follows: *Nucleation of cell adhesions is a diffusion-driven stochastic process that results in a random size of the initial clusters of receptors and can be described by a random distribution in an individual cell*.

The information provided in [232] does not allow to infer the actual distribution of Focal Adhesion sizes at cell level, since only the mean area of the FAs in every cell was reported (see figs. 1H,1N in [232])[34]. Hence, the simplest assumption that can explain the reported data is made: the number of available receptors $N_T(\sigma)$ per Focal adhesion within a cell is also given by a gaussian distribution, where the variance σ of the distribution is associated to the degree stochasticity in the nucleation process. With this assumption, different cell FAs will reach an equilibrium size dependent on E_S, the power p_o invested to test the substrate *and* the available number of receptors. Consequently, if $N_T(\sigma)$ is normally distributed, the equilibrium size of the contacts will also follow a gaussian distribution given by $N_{eq}(E_S, t_{cont}, \sigma) \propto N_T(\sigma) \cdot f(E_S, t_{cont})$. In this way, the mean size of cell contacts will be identical to the equilibrium size predicted in the deterministic framework. However, as a consequence of the new stochastic ingredient, the outcome of the mechanical test will not be deterministic, and the direction of polarization will be to some extent random, both on homogeneous and gradient substrates. This is so because the mechano-transduced signal is, by hypothesis, proportional to the number of receptors. The energy stored per receptors and the induced ligand-receptor distance will still favor FAs on stiffer anchorage points, and as a consequence, a stiffness gradient will bias the maturation and mechano-transduction process. This summarizes the core of the description of Durotaxis that stems from the theory proposed. In order prove that this description does indeed allow to match the observed behaviour of Durotactic cells, three simulations have been performed with the additional stochastic ingredient introduced. The baseline rigidity is kept at $E_{S0} = 40kPa$ and the stiffness gradients have magnitudes of the *PAAm* gels used in the study by J. Wong's group [13] and span the area in $-200\mu m < x < 200\mu m$.

[34]The fact that the mean area of the FAs in a cell follows a gaussian distribution in the population does not allow to infer much either: by the Central Limit Theorem, it is only possible to conclude that the areas of the FAs developed by an individual cell are independent of the other cells, and that the FA areas found in different cells should be similarly distributed

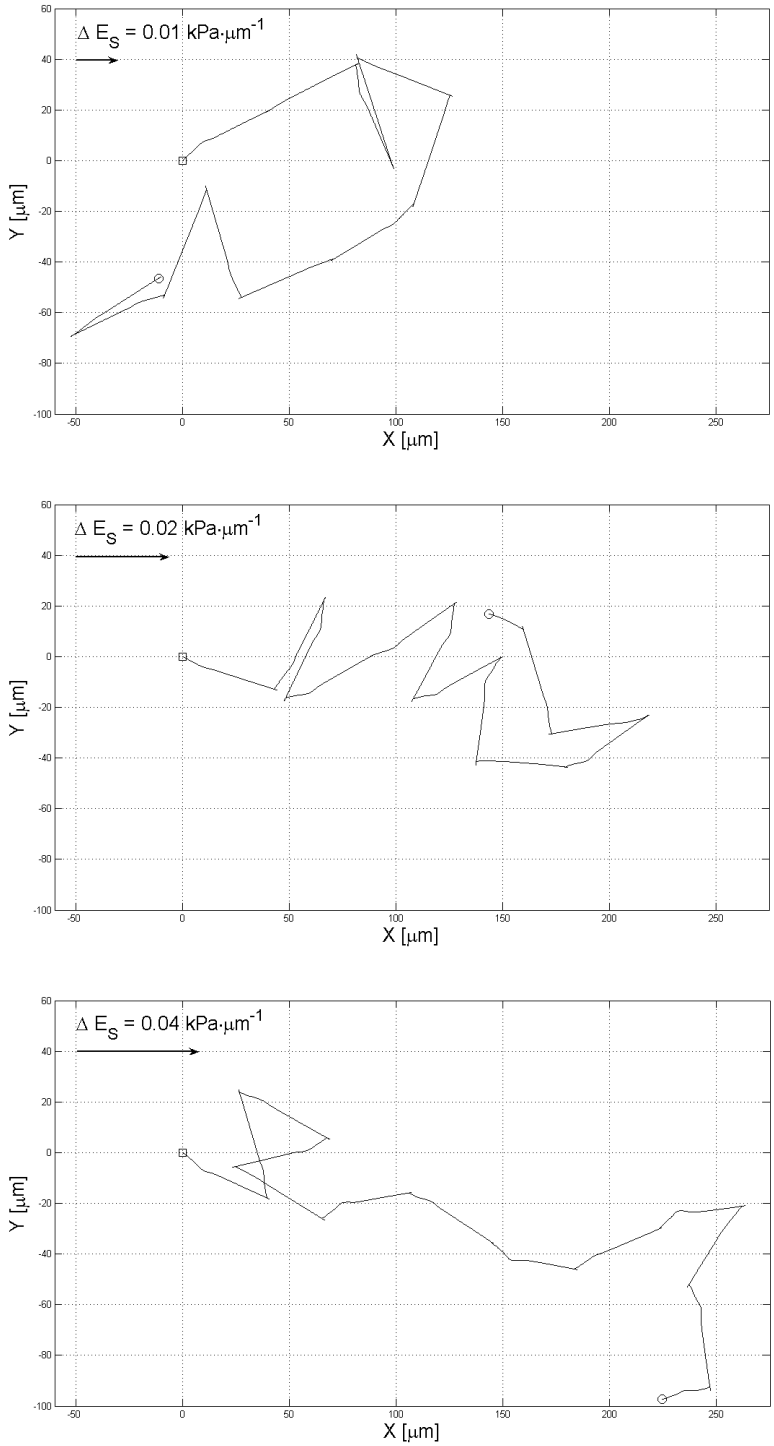

Figure 8.27: Simulation of Durotaxis. A square/circle mark the initial/final points of the cell trajectories. Simulated time 20h. Compare with Windrose plots reported in figs. 6b in Isenberg et. al [13] and figs. (4c-d-e) in Kidoaki et al. [12]

Persistent times of migration between mechanical samples of the order ~ 30min have been adopted from [232]. The simulated trajectories match all the qualitative features of *duro-tactic* migration. The *duro-tactic* index, defined (for long times) as the ratio of the displacement along the gradient direction to the total length of the cell path [234], increases with the magnitude of the gradient, explaining the decrease in the number of turns with an angle relative to the gradient as ΔE_S increases. The cell trajectories on the region $x > 200\mu m$ become essentially random because this is the area where the susbtrate has a uniform rigidity. Cell velocities, of the order of $1.24\mu m \cdot s^{-1}$ are similar in the three simulations, because they are mainly determined by the absolute rigidity of the substrate. Interestingly, setting a rigidity jump from stiff to a low value close to 10kPa allows to reproduce the no-crossing from stiff-to soft observed in early durotaxis essays, and conversely, a high rigidity close to $E^D(\Delta E_S)$ shows how the trajectories of the computational cells become essentially random once they trespass the sensitivity threshold.

A larger number of similar simulations should be performed to have statistical significance and be amenable to be compared with experimental data. However, the qualitative match between these preliminary results and observations shows that the theory proposed captures the main features of *duro-tactic* movement. This suggests that the main ingredients underlying Durotaxis may very well be explained by the mechanisms that naturally stem from the theoretical framework developed. Further, it suggests a new take on the relevance of Durotaxis essays: if the theory proposed is true, these type of essays could comprise an indirect way to gain information on the process of Focal adhesion nucleation, which has proved to be difficult to assess experimentally. To conclude, the observation in [232] that the variance of the FA descriptors (area, aspect ratio etc.) becomes wider as more rigids substrate are used, for which no interpretation is given, finds a simple explanation in the description proposed: during the nucleation phase the number of receptors in a Focal adhesion is very small, so that fluctuations in their number can be as large as the number of receptors itself, leading to the failure of the initial contact. However, as the rigidity of the substrate increases, according to the theory proposed, the growth of the FAs is faster and stronger, which would lead to an increase in the rate and initial minimal size required for contact *survival*, explaining the widening in the distribution of FAs featured by the cells cultured on glass vs soft gels(see figs. 1H-I-J-K-L in [232]).

8.3.6 Why Cells *Durotax?* Why neurons *anti-durotax*? What about mechanics and *Cancer*?

According to the theory developed, there is a rigidity E_{ref}^{cell} where a cell can develop the forces required to establish mature Focal adhesions. E_{ref}^{cell}, as defined in eq.8.18, is determined by the characteristic contractility t_{cont}^{cell} and molecular properties of the receptors expressed by a particular cell type. Further, this rigidity also sets the range of optimal detection of mechanical anisotropies (see eq.8.24 and follow-up discussion). In other words, given the small magnitude of the mechanical gradients usually found *in vivo*, E_{ref}^{cell} marks the upper bound above which a particular cell type gradually looses the capacity to *durotax* in response to mechanical anisotropies, and also matches the lower bound of rigidities to establish mature Focal adhesions. A rigorous derivation of the value of E_{ref}^{cell} would require a bifurcation analysis of the governing equation for FAs 8.6; but it can be estimated from the conditions $e_g(f_g) > e_0$ and $u_g(f_g) < u_0$, so that the energy stored per receptor is of the order required to activate them and the displacement induced between ligand-receptor pairs is small compared to those associated to the thermal fluctuations that drive the formation of bonds. From this inequalities, and introducing the expression for $u_0^2 \sim 2 \cdot K_B T/(k_p \sin^2\theta)$ developed in section 3.3, a rough estimate of the reference stiffness can be obtained:

$$E_{ref}^{cell} \gg \left(\frac{e_0}{p_0 \cdot t_{cont}^{cell}} \frac{e_0 \cdot \sin^2\theta}{K_B T}\right)^{1/3} \frac{k_p}{r_p} \tag{8.28}$$

This equation adds an interesting twist to the mechano-sensing theory proposed, related to *contact guidance* and the biological function of Durotaxis. Intuitively, the reference stiffness is determined, firsts, by the energy developed by the cell $p_o \cdot t_{cont}^{cell}$, which has to be of the larger than e_0 to activate the receptors. And secondly, by the angle θ formed by actin filaments with the substrate when pulling on adhesions (see fig.3.9), which has to be small so that the vertical displacement induced between receptors and ligands is also small and thermal fluctuations (of the order of the Boltzmann factor $K_B T$) can "jolt" the receptors close to ligands, allowing the formation of bonds. The vertical displacement $u_o \cdot \sin\theta$ has to be of the order of nano-meters, the characteristic distance at molecular scale; introducing characteristic values for receptor springs constant $\sim 1pN/nm$, $K_B T = 4.1$pN·nm and FA displacements of the order of $u_0 \sim 0.5 - 1\mu$m leads to predict that the angle formed by actin filaments when pulling has to be of the order of $\theta < 0.1 - 0.01$ degrees (almost parallel), which is indeed what is observed experimentally.

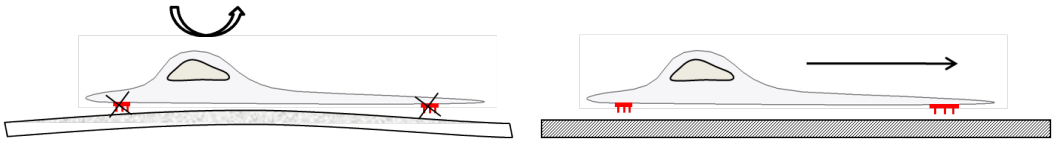

Figure 8.28: Contact guidance and Durotaxis could be explained by common principles concerning the formation of cell adhesions with the substrate

Contact guidance, in turn, is an effect of the topography of the substrate on cell orientation, which tend to align themselves so that the curvature underneath them is minimized[235]. This means that the two guidance principles could be explained by common principles, since the curvature of the substrate results in an increase in θ and consequently hinders or even blocks adhesion formation.
The second discussion concerns a possible biological function of *Durotaxis*. Provided that a constant power p_0 independent of cell type is invested during mechanical samples of the ECM, the characteristic contraction time t_{cont}^{cell} should reflect the energy $p_0 \cdot t_{cont}$ spent or available to test the substrate, that is, the contractility of this particular cell type. Further, the more contractile a cell type is, the smaller the E_{ref}^{cell} in which it can establish adhesions (depending also on the receptors expressed). It follows that highly contractile cells, such as *fibroblasts*, can thrive and adhere on compliant substrates but should loose their ability to detect mechanical anisotropies at low rigidities. Conversely, a less contractile cell type, such as *osteosarcomas*, requires more rigid substrates to adhere but on the other hand maintains the ability to detect stiffness gradients up to high rigidities. This view suggests that *durotaxis* provides *osteosarcomas* and *fibroblasts* with a mechanism to find their way to rigid and soft tissues such as bone and connective tissue, respectively. And it also follows that these tissues match the rigidities where they can establish mature contacts and adhere. Fittingly, there is where they are found in physiological conditions, which suggests why evolution has implemented the ability to *durotax* in biological cells. This interpretation of Durotaxis is not dependent on the hypothesis that some cell type are more contractile than others (for which I have no evidence); the type of receptors expresses by a cell can play the role of t_{cont}, determining the adequate range of rigidities to develop adhesions *and* the range of sensitivity to mechanical anisotropies.
Another experimental observation finds an explanation and comprises an unexpected source of support for the mechano-sensing theory proposed. *Neurons*, the only cell type that is known to *anti-durotax*[35]. I am not aware of any experimental assessment on how contractile *neurons* are. But if the theory is correct, since

[35]The rate of neurite branching and neurite extension is higher on *softer* substrates. Neurite extension is analogous to migration in other cell types. See [29] and references therein

these cells are found in the brain (and nerves), the softest tissues in animals, they should be *very* contractile. Alternatively, *neurons* could be not so contractile compared to other cells, but use a type of receptors (i.e not integrins) for which the characteristic forces of bond-rupture f_0 were small. In both scenarios, most likely the second of them, the principle that explains that establishment of adhesions is favored on stiff substrates does not apply (see eq.8.3 and follow-up discussion). In the first scenario, highly contractile neurons on soft tissue would induce large receptor-ligand displacements resulting in a vanishing rate of bond formation. In the second, even small forces would lead to an exponential growth of the rate of bond-rupture. It follows that *neuron* adhesions/extensions on soft substrates, where smaller forces are developed, should be more stable, and by the same principle, why these cells *anti-durotax*.

Then there is *cancer*. A characteristic property of tumors is that they become more rigid than healthy tissue during the progression of cancer. In addition, experimental evidence shows that, amongst many other abnormalities, the receptors expressed by malignant cells have their type and structural/mechanical properties altered[32, 43, 44, 45]. In the framework of the theory proposed, this could partially explain why cancer cells show abnormally high proliferation rates during the first stages of cancer and high motility rates in the later stage of metastasis. The ability of a cell to infer the mechanical properties of the ECM depends on a basic requirement: the molecular "spring constant" of its receptors has to be well above that of the point on the substrate where ligands are anchored. This is can be understood considering the simple system of two springs in series: its rigidity is determined by the weakest link. For a ligand-receptor pair in the cell membrane, these are the two extreme possibilities:

$$\bar{k}_{P-S} = \frac{k_P \cdot k_S(E_S, r_P)}{k_P + k_S(E_S, r_P)} \approx \begin{cases} k_S(E_S, r_P) & k_P >> k_S(E_S, r_P) \\ k_P & k_P << k_S(E_S, r_P) \end{cases} \tag{8.29}$$

where k_P is the compound molecular spring constant of a ligand receptor pair and $k_S(E_S, r_P)$ is the effective stiffness of the anchorage point, determined by the Young's modulus of the substrate and the contact area. In turn, $\bar{k}_{P-S}$ is the compound stiffness of the ligand-receptor pair and the anchorage point on the substrate, which determines the dynamics of the molecular bond. As discussed earlier, typical physiological values for tissues Young's modulus and the molecular radius of ligand or receptor molecules (see eq.3.35 and footnote[2] in this chapter for experimental values) leads to the first case, $k_P >> k_S(E_S)$. Hence, in normal conditions, the stiffness of the substrate determines the stability of

adhesions on the extracellular matrix. Conversely, if the progressive rigidization of a tumor environment resulted in $k_P << k_S(E_S)$, the properties of the environment would cease to influence the cell fate, as the cell would "sense" a uniform and *high* stiffness k_P of its own receptors as that of the environment, explaining the abnormally high proliferation rates exhibited by cells in tumors. Further, if in a later stage an alteration in the structural properties of the cell receptors (somehow becoming "loose springs" or if the cell expressed an altered receptor type) resulted in $k_P << k_S(E_S)$, the properties of the extracellular environment would again cease to affect the fate of the cell. In this case, however, the malignant cell would "sense" the *low* stiffness of its own receptors independently of the external conditions. According to the views presented, cells on a soft environment show high sensitivity to external anisotropies, which triggers a phase of search for a more rigid tissue. In the case of a malignant cells, it would not to be found, on account of them having lost their mechanical compass. This could explain the high motility rates exhibited by cancer cells during metastasis.

Indeed, the two mechanisms could occur simultaneously and reinforce each other: if cell receptors were to become gradually loose, it is plausible that cells would increase their level of contractility in order to restore the perceived integrity of the tissue, leading to a progressive rigidization of the tissue. The progression of these abnormal trends would then constitute a feedback loop, leading to further rigidization and cells eventually perceiving the environment as soft, explaining the explosion of proliferation and motility observed in tumors. Certainly, these speculations, if true, must be only part of the story of the much more complex process that is cancer, but is also true that they are plausible mechanisms that could be involved in a fatal disease, and that it would be interesting to explore them experimentally.

Well, you know, that's just like... your opinion, man.

Jeffrey Lebowski

Goodbye, blue Monday!

Kurt Vonnegut, writter

Chapter 9

Conclusions

9.1 Conclusions

I tried to keep the quotes from accounts of ancient travelers and old mountaineering expeditions, of which I am very fond, as low as possible. Drawing parallels between research and exploration is as tempting as prone to end on the campy side. However, the one by Edward Whymper[1] at the beginning of chapter 8, where the theory of mechano-sensing and Durotaxis is developed, is fitting. The problem of how cells sense the mechanical properties of the environment was the first topic that attracted my attention when I started this Thesis. However, many times I hit dead ends and I was ready to give up this aspect of cell migration. How could it be that cells seem to advance in the direction of increasing stiffness when Focal adhesions are more developed and therefore should be more difficult to release on rigid substrates? Finally, a simple (an almost desperate) hypothesis, that a constant power defined by the kinetics of actin-myosin filaments and integrin receptors is invested testing the substrate, provided a plausible answer. The predictions that follow from this hypothesis provide an interpretation to a

[1]Edward Whymper (1840-1911) was en English engraver that started climbing after being commissioned by the London Alpine Club to make a series of engravings of the Alps. The account of his wanderings with the hunchback Luc Meynet in at those times god-forsaken valleys, his fabulous etchings, the fine irony with which his birthland seems to have blessed most of its dwellers, a gripping description of an avalanche and the curious observation that wine seems to evaporate faster at high altitude in the company of mountain guides can all be found in his book *Scrambles amongst the alps in the years 1860-69*[236]. Whymper tried repeatedly an unsuccessfully to climb the Mattherhorn by the Lyon ridge on the Italian side until, in part by chance and by his realization that the Hornly ridge was only deceptively unclimbable, decided to attack the mountain from Zermatt in Switzerland. This lead, one 14th of July of 1865, to a thrilling race against a rope lead by an Italian Duke on the other ridge, his conquest of the mountain, and tragedy.

substantial amount of recent observations on Focal adhesion growth, force development in real time and their dependence of stiffness, and constitute perhaps the most satisfying result of this Thesis. The good match with these observations, stemming from studies with different cell types and experimental set-ups, shows that this hypothesis has the attractive capacity to unify phenomena for which there was no conclusive explanation. Once this hypothesis is made, the mechanisms that could explain how cells integrate mechanical gradients follow virtually on its own, and also the interpretation of various observations regarding the relationships between cell polarization times, migration speed, Durotaxis, mechano-sensing limits, and rigidity. Further, it suggests a biological function to cell Duroatxis, which to my knowledge has not been proposed before.

A similarly radical hypothesis was made to formulate the description of the RhoGTPases. Essentially, the Graph/Matrix structure of their Crosstalk was imposed to block the emergence of Turing patterns during the polarization process. They are not observed and would hinder the dynamical spatio-temporal distribution of the proteins regulating cell migration. This, in turn, forced me to assume that some form of auto-catalyisis is at play in the process of RhoGTPase activation, so that the system describing them was Turing-stable but had wave-like solutions to support polarization. Indeed, experimental evidence seems to suggests the existence of various biochemical processes that could lead to this type of Hill-like kinetics in the RhoGTpase cycle of activation. On the other hand, this theoretical assumption naturally leads, first, to suggest plausible biochemical mechanisms of RhoGTPase crosstalk, which are not well understood. They are based on competition to bind limited amounts of GEFs and GDIs, for which there is incipient evidence. And secondly, to properties that are desirable for a regulatory network whose function is to integrate external cues: amplification of external signals, sensitivity to ensuing stimuli, and cell-length independence.

This leads to another notion that is pervasive in this Thesis, and that is the idea of finding unifying principles for observations made in different contexts or cell types. For cell migration (although I believe that the same idea should be useful in other biological problems) particularly, a motivation for this rationale is the observed *plasticity* of cell migration, which suggests that different arrangements of a common machinery can explain the different migration phenotypes observed *in vitro*. A nice result that stems from this approach is that different cell morphologies characteristic of keratocytes and neutrophiles can be recapitulated with a simple shift in the parameters that control cell force, cytoskeleton anisotropy and, more interestingly, RhoGTPases crosstalk. The connection drawn between contact guidance and durotaxis also falls in this category.

More broadly, it must be emphasized that the mechanisms proposed to explain the detection of chemical and stiffness gradients have also a common root. They

are based on these stimuli triggering the emergence of waves of the regulatory proteins. A (linear) gradient Δs of the stimulus, regardless of its nature, leads to a difference $\Delta s \cdot L_{cell}$ experienced at the different ends of the cell. These difference results in a delay in the time in which activation waves are triggered by the receptor machinery, an this offset allows the wave on the high side of the gradient to reach the opposite cell edge; then crosstalk does the rest and the polarized pattern is established. Further, the time delay is essentially determined by the signal difference, so that $\Delta t^{act} \propto \Delta s \cdot L_{cell}$. However, since a traveling wave also requires a time given by L_{cell}/v_{wave}, the mechanism of gradient sensing is independent of the cell length and remains functional against biological variability. Hence, in the same way that Turing-type mechanisms have proved to be a general patterning-forming mechanism in the context of morphogenesis, regulatory waves could comprise a plausible and general mechanism to organize the spatio-temporal distribution of regulatory proteins in more dynamical contexts such as cell migration.

On the computational level, the value of this work lays in the development of a numerical framework specifically tailored to address the numerous challenges associated to cell migration modeling. This method provides a general platform in which different hypothesis and competing models can be readily implemented to compare their predictions with reasonably short computational times, which is an essential requirement for modeling purposes.

Regarding future work, cell migration is ripe with promising lines of inquiry. The progress of microscopy provides access to data in real time that was not accessible barely five years ago. This means that soon it will be possible to have detailed information on the spatio-temporal aspects the regulatory processes (including RhoGTPase distribution) and Focal adhesion dynamics, which should allow to formulate more refined models. The same goes with the cytoskeleton, that has been largely neglected in this thesis. Finally, an exciting topic that has only been tangentially touched is the stochastic nature of cell migration, which must be included since is a fundamental part of the process. Exciting as it is, I will leave it here.

List of Figures

1.1 Ultra-thin PDMS membrane designed by A.Thangawng *et al.*to perform Durotaxis essays[33] 20
1.2 Accumulation zones of HEK cells on the PDMS membrane observed by A.Thangawng *et al.*[33] are framed in blue. Yellow and blue circles indicate dead cells and those whose velocity was tracked. Green vertical lines correspond to the areas where the membrane has a constant thickness of 1μm. 21
1.3 Effective Stiffness profile of the PDMS membrane calculated numerically with 1D beam Finite Elements of varying cross section (blue line) and Ansys (red line). 22
1.4 Fundamental modules involved in cell migration triggered by external signals. Bidirectional coupling between the sensing machinery and the regulatory system are mediated by the so called mechanisms of outside-in and inside-out signaling. Forces are coupled to these pathways by their influence in the dynamics of focal adhesions 23

2.1 Representation of the spatial segregation of RhoGTPases and their function in a migrating cell 27
2.2 Accepted biological model of the RhoGTPase and corresponding reaction equations. 28
2.3 Giniger scheme mediated only by active RhoGTPases. Arrows and bars at the end of a line represent up-regulation and down-regulation. 31
2.4 Reaction, diffusion and volumetric changes drive the change in concentration 33

3.1 Cell modeled as a continuum material. Different structures, such as focal adhesions (red dots) and the nucleus, can be included in this description 46
3.2 Balance of forces acting on an arbitrary cell volume 48
3.3 Basic molecular processes behind force generation in cell migration 52

3.4 A Kelvin-model is formed by a spring and a dashpot in parallel. It is the most simple model that predicts viscous creep 53
3.5 Hookean spring analogy of the actin-myosin contraction 57
3.6 Cell migration results from the coupled dynamics of FA's, rhoGTPase signalling and Cytoskleton generated forces 60
3.7 Kinetic FA model as a cluster of parallel springs binding and unbinding substrate ligands 62
3.8 Energy Landscape of the ligand-receptor system along reaction coordinate χ. The energy barrier ΔE is tilted by the application of a mechanical load 64
3.9 Distance dependence of bond formation rate 66
3.10 Integrin-ligand tangential load on the substrate 69

4.1 Initial and current configuration of a 2D migrating cell. 74
4.2 2D cell meshed with 6-node triangular elements. Red nodes match the position of adhesions sites. 78
4.3 Quadratic shape function for the 6-node triangle element 79
4.4 Initial, current and parent coordinates of a triangular element and mapping between them. 80
4.5 Staggered advance of the nodal variables in a weakly coupled problem. 88
4.6 4th-order Runge-Kutta integration scheme. 90
4.7 Geometry of CFL condition for triangular element. 94
4.8 Shape functions for the 3- node 1d element. 96

5.1 Different distributions of external signals considered 108
5.2 Initial distribution of the RhoGTPases in the cell 108
5.3 Linear gradient of external stimulus 109
5.4 ⊗ Gradient stimulus and active concentration 110
5.5 ⊗ No polarization switch after stimulus is reversed 112
5.6 ⊗ Polarization switch after exposure to large secondary stimulus . . 113
5.7 Dispersion of diffusible migration promoting agent 114
5.8 ⊗ Bipolar pattern after exposure to localized Stimulus 116
5.9 ⊗ Multipolar pattern after exposure to gaussian Stimulus 117
5.10 ⊗ Final RhoGTPases distribution in circular cells of increasing radius 118
5.11 ⊗ Final RhoGTPases distribution in star-shaped cell and nucleus cell 118
5.12 Phase Plane trajectories during exposure to 1st linear gradient . . . 121
5.13 Phase Plane trajectories during exposure to 2nd linear gradient . . 122
5.14 Phase Plane trajectories during exposure to Large 2nd linear gradient 123
5.15 ⊗ Emergence of Bipolar pattern in a 1d cell of L=10μm. 129
5.16 ⊗ Multipolar patterns in cells of increasing length. 130

5.17 Up: $P_{q/\Phi}(0) = \det[-\mathbf{F}^{RD}(q/\phi)]$ for Φ(L = 10μm). Down: Maximum eigenvalue $\lambda_M(q/\pi)$. 131
5.18 Dispersion relation for Jilkine's model. Eigenmodes $q = 1\pi,\ 2\ \pi,\ 3\pi$ have positive eigenvalues. 132
5.19 Interactions Cycles in Jiniker Crosstalk scheme. 138

6.1 Interaction Graph associated to matrix **A**. 153
6.2 Cycles of length $m > 1$ in $G_R[\mathbf{A}]$ 154
6.3 I-subgraph induced by $\mathbf{A}(\gamma_3)$. 155
6.4 Linear spanning subgraphs of $G_R[\mathbf{A}]$ 156
6.5 Exclusion wedge for the eigenvalues of a P_0-matrix **A** and $\mathbf{A} - q \cdot \mathbf{D}$. For $N = 6$, $\theta = 30°$ 164
6.6 General I-subgraph of order 2 167
6.7 I-subgraph of order 3 168

7.1 Phase plane with cubic Reaction term. High an low activation states correspond to stable zeroes of $F_1(c_a, c_i)$. 176
7.2 Right: Wave-pinning of an Activation wave. Left: Heteroclinic trajectory on the Phase Plane of Activated points 177
7.3 Right: Wave-pinning of an Inactivation wave. Left: Heteroclinic trajectory on the Phase Plane for inactivated points 178
7.4 Inactive concentration bounds for multistationarity 182
7.5 Variation of the Activation rate due to Crosstalk 183
7.6 Reaction Graph of the minimal Reaction scheme that supports polarization 187
7.7 $^{\otimes}$ Polarization switch after exposure to reversal of stimulus 189
7.8 $^{\otimes}$ Robust Polarization in cells of increasing size 191
7.9 $^{\otimes}$ Polarization reponse in a Fribroblast-like cell geometry 192
7.10 Alternative Reaction Graph 193
7.11 $^{\otimes}$ Transient Polarization switch 194
7.12 $^{\otimes}$ Persistent amoeboid motion 201
7.13 $^{\otimes}$ Transient amoeboid motion 203
7.14 Migration speed approximated as the velocity of the cell centroid. Black: Persistent migration. Red: Transient migration 204
7.15 $^{\otimes}$Persistent migration following chemoattractant releases at t_1 = 1.7min. , t_2 = 33.3min. and t_3 = 66.6min. from different point-sources. 206
7.16 $^{\otimes}$ Realignment of polarization axis after new stimulus S_3 207
7.17 $^{\otimes}$Persistent migration following chemoattractant releases at t_1 = 2min. , t_2 = 72min. and t_3 = 140min. from different point-sources. . 209
7.18 $^{\otimes}$ Realignment of polarization axis after release of stimulus S_2 . . . 211

7.19 ⊗Migration triggered by large chemoattractant discharges at t_1 = 2min. , t_2 = 52min. and t_3 = 100min. 213
7.20 ⊗ Sequence of polarization, saturation and repolarization after release of stimulus S_2 214
7.21 Alternative Reaction Schemes for the RhoGTPases with additional inhibitory interactions from RhoA 216
7.22 ⊗ Y-shaped extension and subsequent dominance of pseudopod closer to larger stimulus 218
7.23 ⊗ Cell Trajectory after discharging simultaneously two stimulus with only a 10% difference in chemoattratant amount 219
7.24 ⊗ Spontaneous polarization induced by noise 222
7.25 Cell morphologies recapitulated varying force parameters (first row), cytoskeleton anisotropy (second row), and Cdc42-Rho mutual inhibition strength (third row) 224
7.26 Crosstalk strength determines RhoGTPase distribution and cell morphology. Shapes characteristic of *neutrophiles* (upper row) and *keratoctyes* (lower row) are obtained for strong and weak crosstalk between proteins. 225

8.1 Detection of a stiffness gradient requires integrating the mechanical information gathered locally at FAs 230
8.2 Schematic description of FA mechanics 231
8.3 Focal adhesion nucleation is favored at the stiffer edge of the cell . 232
8.4 Predicted Initial regime of stiffness-dependent Focal adhesion Area growth. Compare to fig. 2B in [11] 239
8.5 Predicted Focal adhesion growth and saturation for $t \in [0, t_{cont}]$. Compare to fig. 2B in [11] and figures 3a(top) and 4b(top) in [10] . . 240
8.6 Theoretical prediction of the saturation area of Focal adhesion as a function of the stiffness 241
8.7 Force developed per Focal adhesion during mechosensing test . Compare to fig. 2A in [11] and figure 2 in [9] 244
8.8 Theoretical relationship between stiffness and saturation Force developed by Focal adhesions. Compare to fig. 2C in [11] and note the decay of the experimental data of $F_{sat}^{FA}(\bar{k})$ bellow the linear regime for large rigidities 245
8.9 Predicted dependency of F_{sat}^{FA} with $\bar{k}$ in terms of receptor kinetic and molecular parameters. Weakening in the dependency of $F_{sat}^{FA}(\bar{k})$ with $\bar{k}$ for large rigidities is conserved 246
8.10 Predicted time-course of normalized stress at FAs. Compare to fig. 3b(bottom) and 4b(bottom) in [10] 249

8.11 Stress time-course for two cell types in [10]. Compare fibroblasts prediction to fig. 3b(bottom) and osteosarcoma's with 4b(bottom) in[10] 253
8.12 Stress dependence with stiffness for large times at FAs. Compare data in fig. 3B of in[11]. Compare prediction of $\sigma^{FA} = 4.2\text{nN}\cdot\mu\text{m}^{-2}$ for $E_S = 12\text{kPa}$ (highlighted with a circle) with fig.5e in [8]. 253
8.13 Cell geometry and symmetric Focal Adhesion distribution adopted to illustrate gradient sensing and durotaxis 258
8.14 ⊗ Stiffness gradient sensing and polarization for $E_{S0} = 40\text{kPa}+0.35\ \text{kPa}\cdot\mu\text{m}^{-1}$. Number at the side of FAs indicates percentage of closed bonds. 266
8.15 Left col: Evolution of number of bonds $N(t)$, displacement, and time-derivative of signal s_{FA} to RhoGTPases from FA_1 (solid line, stiff) and FA_2(dashed line,soft). Right col: evolution of the difference in the same variables. $E_S = 40\text{kPA}+0.34\text{kPA}\cdot\mu\text{m}^{-1}$. 267
8.16 ⊗ FA maturation failure for $E_S = 4\text{kPA}+0.04\text{kPA}\cdot\mu\text{m}^{-1}$. 268
8.17 ⊗ Nearly identical FA maturation and mechano-transduced signal for $E_S = 90\text{kPA}+0.04\text{kPA}\cdot\mu\text{m}^{-1}$. 269
8.18 ⊗ *Adherent* state for $E_S = 90\text{kPA}+0.04\text{kPA}\cdot\mu\text{m}^{-1}$ above upper bound for gradient sensing. 271
8.19 Predicted relationship between polarization time $t^{pol}(E_{S0}, \Delta E_S)$ and substrate rigidity for $\Delta E_s = [0.01, 0.02, 0.04]\cdot\text{KPa}\cdot\mu\text{m}^{-1}$ 273
8.20 Focal adhesion failure affects polarization time 274
8.21 Stiffness profiles in Durotaxis essays by Kidoaki et. al [12] (left) and Isenberg et. al [13] (right). Gradient slopes in Gels A,B, C are 1-2 orders of magnitude larger than in *PAAm* gels. Vertical lines indicate the range where durotaxis was studied. 276
8.22 Stiffness gradient to rigidity ratio for Gels A, B, C in Durotaxis essay by Kidoaki et. al [12] and *PAAm* gels in Durotaxis essay by Isenberg et. al [13] 277
8.23 Theory and Simulation predict positive and false observations of Durotaxis in essays by Kidoaki et al. [12] and Isenberg et. al [13] . . 278
8.24 ⊗ Mechano-induced polarization, FA turnover-disassembly, and movement. 282
8.25 Cell speed and Focal Adhesion Biphasic relationship. Compare with observations given in fig. 2G-3G in migration study by Kim et al. [232] 284
8.26 States adopted by an ideally symmetric cell with no-stochastic element in the nucleation process of Focal adhesions, depending on the rigidity of the substrate. 286

8.27 Simulation of Durotaxis. A square/circle mark the initial/final points of the cell trajectories. Simulated time 20h. Compare with Windrose plots reported in figs. 6b in Isenberg et. al [13] and figs. (4c-d-e) in Kidoaki et al. [12] 288
8.28 Contact guidance and Durotaxis could be explained by common principles concerning the formation of cell adhesions with the substrate 291

Bibliography

[1] Alexandra Jilkine and Leah Edelstein-Keshet. A comparison of mathematical models for polarization of single eukaryotic cells in response to guided cues. *PLoS Comput Biol*, 7(4):e1001121, 04 2011.

[2] N. Andrew and R.H. Insall. Chemotaxis in shallow gradients is mediated independently of ptdins 3-kinase by biased choices between random protrusions. *Nature cell biology*, 9(2):193–200, 2007.

[3] J. Dalous, E. Burghardt, A. Mller-Taubenberger, F. Bruckert, G. Gerisch, and T. Bretschneider. Reversal of cell polarity and actin-myosin cytoskeleton reorganization under mechanical and chemical stimulation. *Biophysical Journal*, 94(3):1063 – 1074, 2008.

[4] A.S. Howell, N.S. Savage, S.A. Johnson, I. Bose, A.W. Wagner, T.R. Zyla, H.F. Nijhout, M.C. Reed, A.B. Goryachev, and D.J. Lew. Singularity in polarization: rewiring yeast cells to make two buds. *Cell*, 139(4):731–743, 2009.

[5] C. Janetopoulos, L. Ma, P.N. Devreotes, and P.A. Iglesias. Chemoattractant-induced phosphatidylinositol 3, 4, 5-trisphosphate accumulation is spatially amplified and adapts, independent of the actin cytoskeleton. *Proceedings of the National Academy of Sciences of the United States of America*, 101(24):8951–8956, 2004.

[6] Christophe Guilluy, Rafael Garcia-Mata, and Keith Burridge. Rho protein crosstalk: another social network? *Trends in Cell Biology*, 21(12):718–726, December 2011.

[7] A. Mogilner and K. Keren. The shape of motile cells. *Current Biology*, 19(17):R762–R771, 2009.

[8] N.Q. Balaban, U.S. Schwarz, D. Riveline, P. Goichberg, G. Tzur, I. Sabanay, D. Mahalu, S. Safran, A. Bershadsky, and L. Addadi. Force and focal adhesion assembly: a close relationship studied using elastic micropatterned substrates. *Nature cell biology*, 3(5):466–472, 2001.

[9] Myriam Allioux-Guerin, Delphine Icard-Arcizet, Christiane Durieux, Sylvie Henon, Franois Gallet, Jean-Claude Mevel, Marie-Jo Masse, Marc Tramier, and Maite Coppey-Moisan. Spatiotemporal analysis of cell response to a rigidity gradient: a quantitative study using multiple optical tweezers. *Biophysical journal*, 96(1):238–247, 2009.

[10] Jonathan Stricker, Yvonne Aratyn-Schaus, PatrickW. Oakes, and MargaretL. Gardel. Spatiotemporal constraints on the force-dependent growth of focal adhesions. *Biophysical Journal*, 100(12):2883–2893, June 2011.

[11] Lea Trichet, Jimmy Le Digabel, Rhoda J Hawkins, Sri Ram Krishna Vedula, Mukund Gupta, Claire Ribrault, Pascal Hersen, Raphael Voituriez, and Benoit Ladoux. Evidence of a large-scale mechanosensing mechanism for cellular adaptation to substrate stiffness. *Proceedings of the National Academy of Sciences*, 109(18):6933–6938, 2012.

[12] Satoru Kidoaki and Takehisa Matsuda. Microelastic gradient gelatinous gels to induce cellular mechanotaxis. *Journal of biotechnology*, 133(2):225–230, 2008.

[13] B.C. Isenberg, P.A. DiMilla, M. Walker, S. Kim, and J.Y. Wong. Vascular smooth muscle cell durotaxis depends on substrate stiffness gradient strength. *Biophysical journal*, 97(5):1313–1322, 2009.

[14] Sergey V Plotnikov, Ana M Pasapera, Benedikt Sabass, and Clare M Waterman. Force fluctuations within focal adhesions mediate ecm-rigidity sensing to guide directed cell migration. *Cell*, 151(7):1513–1527, 2012.

[15] M. Abercrombie. The croonian lecture, 1978: The crawling movement of metazoan cells. *Proceedings of the Royal Society of London. Series B. Biological Sciences*, 207(1167):129–147, 1980.

[16] A.K. Harris, P. Wild, and D. Stopak. Silicone rubber substrata: a new wrinkle in the study of cell locomotion. *Science*, 208(4440):177–179, 1980.

[17] Albert K. Harris, David Stopak, and Patricia Wild. Fibroblast traction as a mechanism for collagen morphogenesis. *Nature*, 290(5803):249–251, March 1981.

[18] M. Chicurel. Cell migration research is on the move. *Science*, 295(5555):606–609, 2002.

[19] C.D. Nobes and A. Hall. Rho, rac, and cdc42 gtpases regulate the assembly of multimolecular focal complexes associated with actin stress fibers, lamellipodia, and filopodia. *Cell*, 81(1):53–, 1995.

[20] E. Sahai and C. J. Marshall. Rho-gtpases and cancer. *Nat Rev Cancer*, 2(2):133–142, February 2002.

[21] U. Laufs and J. K. Liao. Targeting rho in cardiovascular disease. *Circ Res*, 87(7):526–528, 2000.

[22] Rebecca Siegel, Deepa Naishadham, and Ahmedin Jemal. Cancer statistics, 2012. *CA: A Cancer Journal for Clinicians*, 62(1):10–29, 2012.

[23] Gaorav P. Gupta and Joan Massague. Cancer metastasis: Building a framework. *Cell*, 127(4):679–695, November 2006.

[24] A. Mogilner. Mathematics of cell motility: have we got its number? *Journal of mathematical biology*, 58(1):105–134, 2009.

[25] G. Maheshwari and D.A. Lauffenburger. Deconstructing (and reconstructing) cell migration. *Microscopy research and technique*, 43(5):358–368, 1998.

[26] Y. Lazebnik. Can a biologist fix a radio?–or, what i learned while studying apoptosis. *Cancer cell*, 2(3):179–, 2002.

[27] R.J. Pelham and Y. Wang. Cell locomotion and focal adhesions are regulated by substrate flexibility. *Proceedings of the National Academy of Sciences*, 94(25):13661–13665, 1997.

[28] C. M. Lo, H. B. Wang, M. Dembo, and Y. L. Wang. Cell movement is guided by the rigidity of the substrate. *Biophysical journal*, 79(1):144–152, July 2000.

[29] Joyce Y Wong, Jennie B Leach, and Xin Q Brown. Balance of chemistry, topography, and mechanics at the cellbiomaterial interface: issues and challenges for assessing the role of substrate mechanics on cell response. *Surface Science*, 570(1):119–133, 2004.

[30] Stephanie Nemir and Jennifer L West. Synthetic materials in the study of cell response to substrate rigidity. *Annals of biomedical engineering*, 38(1):2–20, 2010.

[31] Paul A Janmey and Christopher A McCulloch. Cell mechanics: integrating cell responses to mechanical stimuli. *Annu. Rev. Biomed. Eng.*, 9:1–34, 2007.

[32] Matthew J PaszeK, Nastaran Zahir, Kandice R Johnson, Johnathon N Lakins, Gabriela I Rozenberg, Amit Gefen, Cynthia A Reinhart-King, Susan S Margulies, Micah Dembo, and David Boettiger. Tensional homeostasis and the malignant phenotype. *Cancer cell*, 8(3):241–254, 2005.

[33] Abel L Thangawng, Rodney S Ruoff, Melody A Swartz, and Matthew R Glucksberg. An ultra-thin pdms membrane as a bio/micronano interface: fabrication and characterization. *Biomedical Microdevices*, 9(4):587–595, 2007.

[34] J.Y. Wong, A. Velasco, P. Rajagopalan, and Q. Pham. Directed movement of vascular smooth muscle cells on gradient-compliant hydrogels. *Langmuir*, 19(5):1908–1913, 2003.

[35] D.S. Gray, J. Tien, and C.S. Chen. Repositioning of cells by mechanotaxis on surfaces with micropatterned young's modulus. *Journal of Biomedical Materials Research Part A*, 66(3):605–614, 2003.

[36] X.Q. Brown, E. Bartolak?Suki, C. Williams, M.L. Walker, V.M. Weaver, and J.Y. Wong. Effect of substrate stiffness and pdgf on the behavior of vascular smooth muscle cells: implications for atherosclerosis. *Journal of cellular physiology*, 225(1):115–122, 2010.

[37] R Tse Justin and Adam J Engler. Stiffness gradients mimicking in vivo tissue variation regulate mesenchymal stem cell fate. *PLoS One*, 6(1):e15978–, 2011.

[38] Matthew Raab, Joe Swift, P.C. Dave P. Dingal, Palak Shah, Jae-Won Shin, and Dennis E. Discher. Crawling from soft to stiff matrix polarizes the cytoskeleton and phosphoregulates myosin-ii heavy chain. *The Journal of Cell Biology*, 199(4):669–683, 2012.

[39] Ludovic G. Vincent, Yu Suk Choi, Baldomero Alonso-Latorre, Juan C. del Alamo, and Adam J. Engler. Mesenchymal stem cell durotaxis depends on substrate stiffness gradient strength. *Biotechnology Journal*, pages n/a–n/a, 2013.

[40] S.F. Gilbert. *Developmental Biology*. Sinauer Associates, 2010.

[41] Hong-Bei Wang, Micah Dembo, and Yu-Li Wang. Substrate flexibility regulates growth and apoptosis of normal but not transformed cells. *American Journal of Physiology - Cell Physiology*, 279(5):C1345–C1350, November 2000.

[42] Tzvetelina Tzvetkova-Chevolleau, Anglique Stphanou, David Fuard, Jacques Ohayon, Patrick Schiavone, and Philippe Tracqui. The motility

of normal and cancer cells in response to the combined influence of the substrate rigidity and anisotropic microstructure. *Biomaterials*, 29(10):1541–1551, 2008.

[43] Sanjay Kumar and Valerie M Weaver. Mechanics, malignancy, and metastasis: the force journey of a tumor cell. *Cancer and Metastasis Reviews*, 28(1):113–127, 2009.

[44] Hongmei Yu, Janna Kay Mouw, and Valerie M Weaver. Forcing form and function: biomechanical regulation of tumor evolution. *Trends in cell biology*, 21(1):47–56, 2011.

[45] Denis Wirtz, Konstantinos Konstantopoulos, and Peter C. Searson. The physics of cancer: the role of physical interactions and mechanical forces in metastasis. *Nat Rev Cancer*, 11(7):512–522, July 2011.

[46] Douglas A Lauffenburger and Alan F Horwitz. Cell migration: A physically integrated molecular process. *Cell*, 84(3):359–369, February 1996.

[47] Thomas D Pollard and Gary G Borisy. Cellular motility driven by assembly and disassembly of actin filaments. *Cell*, 112(4):453–465, February 2003.

[48] Donna J Webb, J Thomas Parsons, and Alan F Horwitz. Adhesion assembly, disassembly and turnover in migrating cells over and over and over again. *Nature cell biology*, 4(4):E97–E100, 2002.

[49] D. Riveline, E. Zamir, N.Q. Balaban, U.S. Schwarz, T. Ishizaki, S. Narumiya, Z. Kam, B. Geiger, and A.D. Bershadsky. Focal contacts as mechanosensors: externally applied local mechanical force induces growth of focal contacts by an mdia1-dependent and rock-independent mechanism. *Science Signalling*, 153(6):1175–, 2001.

[50] Benjamin Geiger, Joachim P. Spatz, and Alexander D. Bershadsky. Environmental sensing through focal adhesions. *Nat Rev Mol Cell Biol*, 10(1):21–33, January 2009.

[51] Keith Burridge and Magdalena Chrzanowska-Wodnicka. Focal adhesions, contractility, and signaling. *Annual review of cell and developmental biology*, 12(1):463–519, 1996.

[52] Alan Hall. Rho gtpases and the actin cytoskeleton. *Science*, 279(5350):509–514, 1998.

[53] Catherine D. Nobes and Alan Hall. Rho gtpases control polarity, protrusion, and adhesion during cell movement. *The Journal of Cell Biology*, 144(6):1235–1244, 1999.

[54] A.J. Ridley. Rho gtpases and cell migration. *Journal of Cell Science*, 114(15):2713–2722, 2001.

[55] Anne J. Ridley, Martin A. Schwartz, Keith Burridge, Richard A. Firtel, Mark H. Ginsberg, Gary Borisy, J. Thomas Parsons, and Alan Rick Horwitz. Cell migration: Integrating signals from front to back. *Science*, 302(5651):1704–1709, 2003.

[56] J. Thomas Parsons, Alan Rick Horwitz, and Martin A. Schwartz. Cell adhesion: integrating cytoskeletal dynamics and cellular tension. *Nat Rev Mol Cell Biol*, 11(9):633–643, September 2010.

[57] Margaret L. Gardel, Ian C. Schneider, Yvonne Aratyn-Schaus, and Clare M. Waterman. Mechanical integration of actin and adhesion dynamics in cell migration. *Annual Review of Cell and Developmental Biology*, 26(1):315–333, 2010.

[58] Peter Friedl and Katarina Wolf. Plasticity of cell migration: a multiscale tuning model. *The Journal of Cell Biology*, 188(1):11–19, 2010.

[59] M.P. Sheetz, D.P. Felsenfeld, and C.G. Galbraith. Cell migration: regulation of force on extracellular matrix-integrin complexes. *Trends Cell Biol.*, 8:5154, 1998.

[60] Ronen Zaidel-Bar, Shalev Itzkovitz, Avi Ma'ayan, Ravi Iyengar, and Benjamin Geiger. Functional atlas of the integrin adhesome. *Nat Cell Biol*, 9(8):858–867, August 2007.

[61] Song Li, Jun-Lin Guan, and Shu Chien. Biochemistry and biomechanics of cell motility. *Annual Review of Biomedical Engineering*, 7(1):105–150, 2005.

[62] Boris N. Kholodenko, John F. Hancock, and Walter Kolch. Signalling ballet in space and time. *Nat Rev Mol Cell Biol*, 11(6):414–426, June 2010.

[63] Erik S. Welf and Jason M. Haugh. Signaling pathways that control cell migration: models and analysis. *Wiley Interdisciplinary Reviews: Systems Biology and Medicine*, 3(2):231–240, 2011.

[64] S. Etienne-Manneville and A. Hall. Rho gtpases in cell biology. *Nature*, 420(6916):629–635, December 2002.

[65] S. J. Heasman and A.J. Ridley. Mammalian rho gtpases: new insights into their functions from in vivo studies. *Nat Rev Mol Cell Biol*, 9(9):690–701, September 2008.

[66] M. Parri and P. Chiarugi. Rac and rho gtpases in cancer cell motility control. *Cell Communication and Signaling*, 8:1–14, 2010.

[67] A. Ridley, M. Peckham, and P. Clark, editors. *Cell Motility: From Molecules to Organisms*. John Wiley & Sons, 2004.

[68] C. DerMardirossian and G. M. Bokoch. Gdis: central regulatory molecules in rho gtpase activation. *Trends in Cell Biology*, 15(7):356 – 363, 2005.

[69] W.M. Bement, A.L. Miller, and G. von Dassow. Rho gtpase activity zones and transient contractile arrays. *BioEssays*, 28(10):983–993, 2006.

[70] M. Symons and Settleman J. Rho family gtpases: more than simple switches. *Trends in Cell Biology*, 10(10):415 – 419, 2000.

[71] E. Giniger. How do rho family gtpases direct axon growth and guidance? a proposal relating signaling pathways to growth cone mechanics. *Differentiation*, 70(8):385 – 396, 2002.

[72] A. Jilkine, A. Marée, and L. Edelstein-Keshet. Mathematical model for spatial segregation of the rho-family gtpases based on inhibitory crosstalk. *Bulletin of Mathematical Biology*, 69:1943–1978, 2007.

[73] G.T. Mase and G.E. Mase. *Continuum mechanics for engineers*. Computational Mechanics and Applied Analysis Series. CRC Press, 1999.

[74] Mikiya Otsuji, Shuji Ishihara, Carl Co, Kozo Kaibuchi, Atsushi Mochizuki, and Shinya Kuroda. A mass conserved reaction-diffusion system captures properties of cell polarity. *PLoS Comput Biol*, 3(6):e108, 06 2007.

[75] R. Thomas and M. Kaufman. Multistationarity, the basis of cell differentiation and memory. i. structural conditions of multistationarity and other nontrivial behavior. *Chaos: An Interdisciplinary Journal of Nonlinear Science*, 11(1):170–179, 2001.

[76] A. M. Turing. The Chemical Basis of Morphogenesis. *Philosophical Transactions of the Royal Society of London. Series B, Biological Sciences*, 237(641):37–72, August 1952.

[77] Rushikesh Sheth, Luciano Marcon, M Flix Bastida, Marisa Junco, Laura Quintana, Randall Dahn, Marie Kmita, James Sharpe, and Maria A Ros. Hox genes regulate digit patterning by controlling the wavelength of a turing-type mechanism. *Science*, 338(6113):1476–1480, 2012.

[78] E. Boulter, R. Garcia-Mata, C. Guilluy, A. Dubash, G. Rossi, P. J. Brennwald, and K. Burridge. Regulation of rho gtpase crosstalk, degradation and activity by rhogdi1. *Nat Cell Biol*, 12(5):477–483, May 2010.

[79] E. Boulter, S. Estrach, R. Garcia-Mata, and C.C. Feral. Off the beaten paths: alternative and crosstalk regulation of rho gtpases. *The FASEB Journal*, 26(2):469–479, 2012.

[80] S. Timoshenko and J.N. Goodier. *Theory of elasticity*. McGraw-Hill classic textbook reissue series. McGraw-Hill, 1969.

[81] T. Belytschko, W.K. Liu, and B. Moran. *Nonlinear Finite Elements for Continua and Structures*. Wiley & Sons, 2005.

[82] George I. Bell. Models for the Specific Adhesion of Cells to Cells. *Science*, 200(4342):618–627, 1978.

[83] Daniel A. Fletcher and R. Dyche Mullins. Cell mechanics and the cytoskeleton. *Nature*, 463(7280):485–492, January 2010.

[84] D. Boal. *Mechanics of the Cell*. Cambridge University Press, 2001.

[85] T. D. Pollard, L. Blanchoin, and R. D. Mullins. Molecular mechanisms controlling actin filament dynamics in nonmuscle cells. *Annual review of biophysics and biomolecular structure*, 29:545–576, 2000.

[86] Alex Mogilner. On the edge: modeling protrusion. *Current Opinion in Cell Biology*, 18(1):32–39, February 2006.

[87] Marie-France Carlier, editor. *Actin-based Motility*. Springer Netherlands, Dordrecht, 2010.

[88] C.T. Lim, E.H. Zhou, and S.T. Quek. Mechanical models for living cells-a review. *Journal of Biomechanics*, 39(2):195–216, 2006.

[89] B. Flaherty, JP McGarry, and PE McHugh. Mathematical models of cell motility. *Cell biochemistry and biophysics*, 49(1):14–28, 2007.

[90] P.G. De Gennes. *Scaling Concepts in Polymer Physics*. Cornell University Press, 1979.

[91] L.E. Malvern. *Introduction to the mechanics of a continuous medium*. Prentice-Hall series in engineering of the physical sciences. Prentice-Hall, 1969.

[92] F. Julicher, K. Kruse, J. Prost, and J.-F. Joanny. Active behavior of the cytoskeleton. *Physics Reports*, 449(13):3–28, September 2007.

[93] Karen E Kasza, Amy C Rowat, Jiayu Liu, Thomas E Angelini, Clifford P Brangwynne, Gijsje H Koenderink, and David A Weitz. The cell as a material. *Current Opinion in Cell Biology*, 19(1):101–107, February 2007.

[94] P.A. DiMilla, K. Barbee, and D.A. Lauffenburger. Mathematical model for the effects of adhesion and mechanics on cell migration speed. *Biophysical Journal*, 60(1):15–37, July 1991.

[95] ME Gracheva and HG Othmer. A continuum model of motility in ameboid cells. *Bull Math Biol*, 66(1):167–193–, January 2004.

[96] Kamila Larripa and Alex Mogilner. Transport of a 1d viscoelastic actin-myosin strip of gel as a model of a crawling cell. *Physica A: Statistical Mechanics and its Applications*, 372(1):113–123, December 2006.

[97] Xavier Martinez, Sergio Oller, Fernando Rastellini, and Alex H. Barbat. A numerical procedure simulating rc structures reinforced with frp using the serial/parallel mixing theory. *Computers and Structures*, 86(1516):1604–1618, August 2008.

[98] E. Oñate Ibañez de Navarra. *Cálculo de Estructuras Por el Método de Elementos Finitos: Análisis Estático Lineal*. Centro Internacional de Métodos Numéricos en Ingeniería, 1995.

[99] J. Bonet and D. Wood. *Nonlinear continuum mechanics for finite element analysis*. Cambridge University Press, 2005.

[100] John G. Lock, Bernhard Wehrle-Haller, and Staffan Strmblad. Cell-matrix adhesion complexes: Master control machinery of cell migration. *Seminars in Cancer Biology*, 18(1):65–76, February 2008.

[101] Filippo G. Giancotti and Erkki Ruoslahti. Integrin signaling. *Science*, 285(5430):1028–1033, 1999.

[102] R.O. Hynes. Integrins: bidirectional, allosteric signaling machines. *Cell*, 110(6):673–687, 2002.

[103] J.D. Hood and D.A. Cheresh. Role of integrins in cell invasion and migration. *Nature Reviews Cancer*, 2(2):91–100, 2002.

[104] A.D. Bershadsky, N.Q. Balaban, and B. Geiger. Adhesion-dependent cell mechanosensitivity. *Annual review of cell and developmental biology*, 19(1):677–695, 2003.

[105] Viola Vogel and Michael Sheetz. Local force and geometry sensing regulate cell functions. *Nat Rev Mol Cell Biol*, 7(4):265–275, April 2006.

[106] E. Puklin-Faucher and M.P. Sheetz. The mechanical integrin cycle. *Journal of cell science*, 122(2):179–186, 2009.

[107] U.S. Schwarz and M.L. Gardel. United we stand: integrating the actin cytoskeleton and cell-matrix adhesions in cellular mechanotransduction. *Journal of Cell Science*, 125(13):3051–3060, 2012.

[108] R. Bruinsma. Theory of force regulation by nascent adhesion sites. *Biophysical journal*, 89(1):87–94, 2005.

[109] A. Besser and S.A. Safran. Force-induced adsorption and anisotropic growth of focal adhesions. *Biophysical journal*, 90(10):3469–, 2006.

[110] T. Shemesh, B. Geiger, A.D. Bershadsky, and M.M. Kozlov. Focal adhesions as mechanosensors: a physical mechanism. *Proceedings of the National Academy of Sciences of the United States of America*, 102(35):12383–12388, 2005.

[111] A. Nicolas, A. Besser, and S.A. Safran. Dynamics of cellular focal adhesions on deformable substrates: consequences for cell force microscopy. *Biophysical journal*, 95(2):527–, 2008.

[112] U. Seifert. Rupture of multiple parallel molecular bonds under dynamic loading. *Physical Review Letters*, 84(12):2750–2753, 2000.

[113] T. Erdmann and US Schwarz. Stability of adhesion clusters under constant force. *Physical review letters*, 92(10):108102–, 2004.

[114] P. Hanggi, P. Talkner, and M. Borkovec. Reaction-rate theory: fifty years after Kramers. *Reviews of Modern Physics*, 62(2):251–341, April 1990.

[115] S.N. Zhurkov. Kinetic concept of the strength of solids. *Int J Fracture Mech*, 1(4):311–323, 1965.

[116] T. Erdmann and U.S. Schwarz. Bistability of cell-matrix adhesions resulting from nonlinear receptor-ligand dynamics. *Biophysical journal*, 91(6):L60–L62, 2006.

[117] N.G. Van Kampen. *Stochastic processes in physics and chemistry*, volume 1. North holland, 1992.

[118] H.A. Kramers. Brownian motion in a field of force and the diffusion model of chemical reactions. *Physica*, 7(4):284 – 304, 1940.

[119] E. Evans. Probing the relation between force-lifetime-and chemistry in single molecular bonds. *Annual review of biophysics and biomolecular structure*, 30(1):105–128, 2001.

[120] E. Evans and K. Ritchie. Dynamic strength of molecular adhesion bonds. *Biophysical journal*, 72(4):1541–1555, 1997.

[121] C.V. Carman and T.A. Springer. Integrin avidity regulation: are changes in affinity and conformation underemphasized? *Current opinion in cell biology*, 15(5):547–556, 2003.

[122] C.G. Galbraith, K.M. Yamada, and M.P. Sheetz. The relationship between force and focal complex development. *The Journal of cell biology*, 159(4):695–705, 2002.

[123] D. Choquet, D.P. Felsenfeld, and M.P. Sheetz. Extracellular matrix rigidity causes strengthening of integrin-cytoskeleton linkages. *Cell*, 88(1):39–48, 1997.

[124] K.L. Johnson. *Contact Mechanics*. Cambridge University Press, 1987.

[125] O. C. Zienkiewicz and R. L. Taylor. *Finite Element Method: Volume 1, Fifth Edition (Finite Element Method Ser)*. Butterworth-Heinemann, 5 edition, September 2000.

[126] C.A. Felippa, K.P. Park, and C. Farhat. Partitioned analysis of coupled mechanical systems. *Computer Methods in Applied Mechanics and Engineering*, 190(24-25):3247 – 3270, 2001. Advances in Computational Methods for Fluid-Structure Interaction.

[127] George B. Arfken and Hans-Jurgen Weber. *Mathematical Methods for Physicists*. Academic Press, Fourth (International) edition, 1995.

[128] F. Armero and J. C. Simo. A new unconditionally stable fractional step method for non-linear coupled thermomechanical problems. *International Journal for Numerical Methods in Engineering*, 35(4):737–766, 1992.

[129] Steven J. Ruuth. Implicit-explicit methods for reaction-diffusion problems in pattern formation. *Journal of Mathematical Biology*, 34:148–176, 1995. 10.1007/BF00178771.

[130] Raymond J. Spiteri and Steven J. Ruuth. A new class of optimal high-order strong-stability-preserving time discretization methods. *SIAM Journal on Numerical Analysis*, 40(2):469–491, January 2003.

[131] Sigal Gottlieb, Chi-Wang Shu, and Eitan Tadmor. Strong stability-preserving high-order time discretization methods. *SIAM Review*, 43(1):pp. 89–112, 2001.

[132] R. Ribo. *Gid, the Personal Pre and Postprocessor: . User manual [2]. Reference manual*. Gid, the Personal Pre and Postprocessor: The Universal, Adaptive and User Friendly Pre and Post Processing System for Computer Analysis in Science and Engineering : Version 7. International Center for Numerical Methods in Engineering, 2002.

[133] M. Abramowitz and I.A. Stegun. *Handbook of mathematical functions with formulas, graphs, and mathematical tables*. Number v. 55,n.º 1972 in Applied mathematics series. U.S. Govt. Print. Off., 1964.

[134] Y. Mori, A. Jilkine, and L. Edelstein-Keshet. Wave-pinning and cell polarity from a bistable reaction-diffusion system. *Biophysical Journal*, 94(9):3684 – 3697, 2008.

[135] Myrto Raftopoulou and Alan Hall. Cell migration: Rho gtpases lead the way. *Developmental Biology*, 265(1):23–32, January 2004.

[136] Peter Grindrod. *Patterns and Waves: Theory and Applications of Reaction-diffusion Equations*. Clarendon Press, Oxford, second edition, September 1991.

[137] Y. Mori, A. Jilkine, and L. Edelstein-Keshet. Asymptotic and bifurcation analysis of wave-pinning in a reaction-diffusion model for cell polarization. *SIAM Journal on Applied Mathematics*, 71(4):1401–1427, 2011.

[138] B. Cushman-Roisin and J.M. Beckers. *Introduction to Geophysical Fluid Dynamics: Physical and Numerical Aspects*. International Geophysics. Elsevier Science, 2011.

[139] S. H. Strogatz. *Nonlinear dynamics and chaos*. Addison-Wesley Reading, MA, 1994.

[140] J. D. Murray. *Mathematical Biology II*. Springer, 3rd edition, January 2003.

[141] M. C. Cross and P. C. Hohenberg. Pattern formation outside of equilibrium. *Rev. Mod. Phys.*, 65(3):851–, July 1993.

[142] Hidde de Jong. Modeling and simulation of genetic regulatory systems: A literature review. *Journal of Computational Biology*, 9(1):67–103, 2002.

[143] J. Guckenheimer and P. Holmes. *Nonlinear oscillations, dynamical systems, and bifurcations of vector fields*. Springer, 1983.

[144] C. Soulé. Graphic requirements for multistationarity. *Complexus*, 1(3):123–133, 2003.

[145] F.R. Gantmacher. *Applications Of The Theory Of Matrices*. Interscience Publishers, 1959.

[146] R. G. Casten and C. J. Holland. Stability properties of solutions to systems of reaction-diffusion equations. *SIAM Journal on Applied Mathematics*, 33(2):353–364, September 1977.

[147] F. R. Gantmacher. *The theory of matrices. Vol. 1. Transl. from the Russian by K. A. Hirsch. Reprint of the 1959 translation.* Providence, RI: AMS Chelsea Publishing. , 1998.

[148] R.A. Horn and C. R. Johnson. *Matrix Analysis*. Cambridge University Press, February 1990.

[149] R.S. Varga. *Geršgorin and His Circles*. Springer Series in Computational Mathematics. Springer, 2011.

[150] R.A. Brualdi and D. Cvetkovic. *A Combinatorial Approach to Matrix Theory and Its Applications*. Chapman and Hall/CRC, 2008.

[151] W.K. Chen. *Graph-Theory and its engineering applications*. World Scientific, 1997.

[152] B.L. Clarke. Graph theoretic approach to the stability analysis of steady state chemical reaction networks. *J. Chem. Phys.*, 60:1481–1492, 1974.

[153] G. W. Cross. Three types of matrix stability. *Linear Algebra and its Applications*, 20(3):253 – 263, 1978.

[154] D. Hershkowitz. Recent directions in matrix stability. *Linear Algebra and its Applications*, 171:161 – 186, 1992.

[155] L. Wang and M. Y. Li. Diffusion-driven instability in reaction-diffusion systems. *Journal of Mathematical Analysis and Applications*, 254(1):138 – 153, 2001.

[156] R. B. Kellogg. On complex eigenvalues of m and p matrices. *Numerische Mathematik*, 19:170–175, 1972. 10.1007/BF01402527.

[157] B.L. Clarke and W. Jiang. Method for deriving hopf and saddle-node bifurcation hypersurfaces and application to a model of the belousovzhabotinskii system. *J. Chem. Phys*, 99(6):4464–4478, 1993.

[158] M. Kaufman, C. Soule, and R. Thomas. A new necessary condition on interaction graphs for multistationarity. *Journal of Theoretical Biology*, 248(4):675–685, October 2007.

[159] James Cotterell and James Sharpe. An atlas of gene regulatory networks reveals multiple three-gene mechanisms for interpreting morphogen gradients. *Molecular systems biology*, 6(1):–, 2010.

[160] A. Gierer and H. Meinhardt. A theory of biological pattern formation. *Biological Cybernetics*, 12(1):30–39, 1972.

[161] David Gale and Hukukane Nikaido. The jacobian matrix and global univalence of mappings. *Mathematische Annalen*, 159:81–93, 1965. 10.1007/BF01360282.

[162] R. Thomas. On the relation between the logical structure of systems and their ability to generate multiple steady states or sustained oscillations. *Springer series in Synergetics*, 9:180–193, 1981.

[163] J.P. Keener and J. Sneyd. *Mathematical Physiology: With 360 Illustrations*. Interdisciplinary applied mathematics: Mathematical biology. Springer Verlag, 1998.

[164] J.D. Murray. *Mathematical Biology: I. An Introduction*. Springer, 2002.

[165] D.L. Nelson and M.M. Cox. *Lehninger Principles of Biochemistry*. W. H. Freeman, 2010.

[166] J.E. Ferrell. Tripping the switch fantastic: how a protein kinase cascade can convert graded inputs into switch-like outputs. *Trends in biochemical sciences*, 21(12):460–466, 1996.

[167] Hong Qian. Cooperativity in cellular biochemical processes: Noise-enhanced sensitivity, fluctuating enzyme, bistability with nonlinear feedback, and other mechanisms for sigmoidal responses. *Annual Review of Biophysics*, 41:179–204, 2012.

[168] RWD Nickalls. A new approach to solving the cubic: Cardan's solution revealed. *The Mathematical Gazette*, pages 354–359, 1993.

[169] R.A. Harvey, R.A. Harvey, and P.D. Denise R. Ferrier. *Biochemistry: Lippincott's Illustrated Reviews, North American Edition*. Health, 2011.

[170] G. Di Paolo and P. De Camilli. Phosphoinositides in cell regulation and membrane dynamics. *Nature*, 443(7112):651–657, 2006.

[171] C. Janetopoulos and R.A. Firtel. Directional sensing during chemotaxis. *FEBS letters*, 582(14):2075–2085, 2008.

[172] K.L. Rossman, C.J. Der, and J. Sondek. Gef means go: turning on rho gtpases with guanine nucleotide-exchange factors. *Nature reviews Molecular cell biology*, 6(2):167–180, 2005.

[173] R.J. Cain and A.J. Ridley. Phosphoinositide 3-kinases in cell migration. *Biology of the Cell*, 101(1):13–29, 2009.

[174] S.J. Harris, R.V. Parry, J. Westwick, and S.G. Ward. Phosphoinositide lipid phosphatases: natural regulators of phosphoinositide 3-kinase signaling in t lymphocytes. *Journal of Biological Chemistry*, 283(5):2465–2469, 2008.

[175] B. Lin, W.R. Holmes, C.C. Wang, T. Ueno, A. Harwell, L. Edelstein-Keshet, T. Inoue, and A. Levchenko. Synthetic spatially graded rac activation drives directed cell polarization and locomotion. *arXiv preprint arXiv:1204.5517*, pages –, 2012.

[176] A.T. Dawes and L. Edelstein-Keshet. Phosphoinositides and rho proteins spatially regulate actin polymerization to initiate and maintain directed movement in a one-dimensional model of a motile cell. *Biophysical journal*, 92(3):744–768, 2007.

[177] A.F.M. Maree, V.A. Grieneisen, and L. Edelstein-Keshet. How cells integrate complex stimuli: The effect of feedback from phosphoinositides and cell shape on cell polarization and motility. *PLoS Computational Biology*, 8(3):e1002402–, 2012.

[178] S. Lu, T. Kim, C.E. Chen, M. Ouyang, J. Seong, X. Liao, and Y. Wang. Computational analysis of the spatiotemporal coordination of polarized pi3k and rac1 activities in micro-patterned live cells. *PloS one*, 6(6):e21293–, 2011.

[179] W.R. Holmes, B. Lin, A. Levchenko, and L. Edelstein-Keshet. Modelling cell polarization driven by synthetic spatially graded rac activation. *PLoS Computational Biology*, 8(6):e1002366–, 2012.

[180] R. Li, B. Zhang, and Y. Zheng. Structural determinants required for the interaction between rho gtpase and the gtpase-activating domain of p190. *Journal of Biological Chemistry*, 272(52):32830–32835, 1997.

[181] K. Zhu, B. Debreceni, R. Li, and Y. Zheng. Identification of rho gtpase-dependent sites in the dbl homology domain of oncogenic dbl that are required for transformation. *Journal of Biological Chemistry*, 275(34):25993–26001, 2000.

[182] Baolin Zhang, Yaqin Zhang, Zhi-xin Wang, and Yi Zheng. The role of mg2+ cofactor in the guanine nucleotide exchange and gtp hydrolysis reactions of rho family gtp-binding proteins. *Journal of Biological Chemistry*, 275(33):25299–25307, 2000.

[183] L. Hemsath and M.R. Ahmadian. Fluorescence approaches for monitoring interactions of rho gtpases with nucleotides, regulators, and effectors. *Methods*, 37(2):173–182, 2005.

[184] A.P. Minton. How can biochemical reactions within cells differ from those in test tubes? *Journal of cell science*, 119(14):2863–2869, 2006.

[185] H.X. Zhou, G. Rivas, and A.P. Minton. Macromolecular crowding and confinement: biochemical, biophysical, and potential physiological consequences. *Annual review of biophysics*, 37:375–, 2008.

[186] Olivier Pertz. Spatio-temporal rho gtpase signaling are where are we now? *Journal of Cell Science*, 123(11):1841–1850, 2010.

[187] Peter Friedl and Katarina Wolf. Tumour-cell invasion and migration: diversity and escape mechanisms. *Nat Rev Cancer*, 3(5):362–374, May 2003.

[188] A.J. Ridley and A. Hall. The small gtp-binding protein rho regulates the assembly of focal adhesions and actin stress fibers in response to growth factors. *Cell*, 70(3):389 – 399, 1992.

[189] A.J. Schmidt and A. Hall. Guanine nucleotide exchange factors for rho gtpases: turning on the switch. *Genes & development*, 16(13):1587–1609, 2002.

[190] E. Boulter and R. Garcia-Mata. Rhogdi: A rheostat for the rho switch. *Small Gtpases*, 1(2154-1248):65–68, July 2010.

[191] A. Bernards and J. Settleman. Gap control: regulating the regulators of small gtpases. *Trends in Cell Biology*, 14(7):377 – 385, 2004.

[192] Estelle Dransart, Birgitta Olofsson, and Jacqueline Cherfils. Rho-gdis revisited: Novel roles in rho regulation. *Traffic*, 6(11):957–966, 2005.

[193] R. Ananthakrishnan and A. Ehrlicher. The forces behind cell movement. *International journal of biological sciences*, 3(5):303–, 2007.

[194] P.A. DiMilla, J.A. Stone, J.A. Quinn, S.M. Albelda, and D.A. Lauffenburger. Maximal migration of human smooth muscle cells on fibronectin and type iv collagen occurs at an intermediate attachment strength. *The Journal of cell biology*, 122(3):729–737, 1993.

[195] S.P. Palecek, J.C. Loftus, M.H. Ginsberg, D.A. Lauffenburger, and A.F. Horwitz. Integrin-ligand binding properties govern cell migration speed through cell-substratum adhesiveness. *Nature*, 385(6616):537–540, 1997.

[196] S.L. Gupton and C.M. Waterman-Storer. Spatiotemporal feedback between actomyosin and focal-adhesion systems optimizes rapid cell migration. *Cell*, 125(7):1361–1374, 2006.

[197] M.A. Schwartz and A.R. Horwitz. Integrating adhesion, protrusion, and contraction during cell migration. *Cell*, 125(7):1223–1225, 2006.

[198] Carole A Parent and Peter N Devreotes. A cell's sense of direction. *Science*, 284(5415):765–770, 1999.

[199] Leonard Bosgraaf and Peter JM Van Haastert. The ordered extension of pseudopodia by amoeboid cells in the absence of external cues. *PloS one*, 4(4):e5253–, 2009.

[200] Julian Weichsel, Edit Urban, J Victor Small, and Ulrich S Schwarz. Reconstructing the orientation distribution of actin filaments in the lamellipodium of migrating keratocytes from electron microscopy tomography data. *Cytometry Part A*, pages –, 2012.

[201] Julian Weichsel and Ulrich S Schwarz. Two competing orientation patterns explain experimentally observed anomalies in growing actin networks. *Proceedings of the National Academy of Sciences*, 107(14):6304–6309, 2010.

[202] Wouter-Jan Rappel and William F Loomis. Eukaryotic chemotaxis. *Wiley Interdisciplinary Reviews: Systems Biology and Medicine*, 1(1):141–149, 2009.

[203] Ben Vanderlei, James J Feng, and Leah Edelstein-Keshet. A computational model of cell polarization and motility coupling mechanics and biochemistry. *Multiscale Modeling & Simulation*, 9(4):1420–1443, 2011.

[204] Karen A Beningo, Micah Dembo, Irina Kaverina, J Victor Small, and Yu-li Wang. Nascent focal adhesions are responsible for the generation of strong propulsive forces in migrating fibroblasts. *The Journal of cell biology*, 153(4):881–888, 2001.

[205] Marino Arroyo, Luca Heltai, Daniel Milln, and Antonio DeSimone. Reverse engineering the euglenoid movement. *Proceedings of the National Academy of Sciences*, 109(44):17874–17879, 2012.

[206] Jerome Solon, Aynur Kaya-Copur, Julien Colombelli, and Damian Brunner. Pulsed forces timed by a ratchet-like mechanism drive directed tissue movement during dorsal closure. *Cell*, 137(7):1331–1342, 2009.

[207] Adam J Engler, Shamik Sen, H Lee Sweeney, and Dennis E Discher. Matrix elasticity directs stem cell lineage specification. *Cell*, 126(4):677–689, 2006.

[208] Thomas Lecuit and Pierre-Francois Lenne. Cell surface mechanics and the control of cell shape, tissue patterns and morphogenesis. *Nat Rev Mol Cell Biol*, 8(8):633–644, August 2007.

[209] Jeroen Eyckmans, Thomas Boudou, Xiang Yu, and Christopher S Chen. A hitchhiker's guide to mechanobiology. *Developmental cell*, 21(1):35–47, 2011.

[210] Masha Prager-Khoutorsky, Alexandra Lichtenstein, Ramaswamy Krishnan, Kavitha Rajendran, Avi Mayo, Zvi Kam, Benjamin Geiger, and Alexander D Bershadsky. Fibroblast polarization is a matrix-rigidity-dependent process controlled by focal adhesion mechanosensing. *Nature Cell Biology*, 13(12):1457–1465, 2011.

[211] Benjamin Geiger and Alexander Bershadsky. Exploring the neighborhood: adhesion-coupled cell mechanosensors. *Cell*, 110(2):139–142, 2002.

[212] Christopher S Chen, John Tan, and Joe Tien. Mechanotransduction at cell-matrix and cell-cell contacts. *Annu. Rev. Biomed. Eng.*, 6:275–302, 2004.

[213] Demosthene Mitrossilis, Jonathan Fouchard, David Pereira, Franois Postic, Alain Richert, Michel Saint-Jean, and Atef Asnacios. Real-time single-cell response to stiffness. *Proceedings of the National Academy of Sciences*, 107(38):16518–16523, 2010.

[214] Jian-Ping Xiong, Thilo Stehle, Beate Diefenbach, Rongguang Zhang, Reinhardt Dunker, David L Scott, Andrzej Joachimiak, Simon L Goodman, and M Amin Arnaout. Crystal structure of the extracellular segment of integrin v3. *Science*, 294(5541):339–345, 2001.

[215] Junichi Takagi, Benjamin M Petre, Thomas Walz, and Timothy A Springer. Global conformational rearrangements in integrin extracellular domains in outside-in and inside-out signaling. *Cell*, 110(5):599–611, 2002.

[216] Bryan T Marshall, Krishna K Sarangapani, Jianhua Wu, Michael B Lawrence, Rodger P McEver, and Cheng Zhu. Measuring molecular elasticity by atomic force microscope cantilever fluctuations. *Biophysical journal*, 90(2):681–692, 2006.

[217] Adam J Engler, Maureen A Griffin, Shamik Sen, Carsten G Bnnemann, H Lee Sweeney, and Dennis E Discher. Myotubes differentiate optimally on substrates with tissue-like stiffness pathological implications for soft or stiff microenvironments. *The Journal of cell biology*, 166(6):877–887, 2004.

[218] Dennis E. Discher, Paul Janmey, and Yu-li Wang. Tissue cells feel and respond to the stiffness of their substrate. *Science*, 310(5751):1139–1143, November 2005.

[219] Tony Yeung, Penelope C. Georges, Lisa A. Flanagan, Beatrice Marg, Miguelina Ortiz, Makoto Funaki, Nastaran Zahir, Wenyu Ming, Valerie Weaver, and Paul A. Janmey. Effects of substrate stiffness on cell morphology, cytoskeletal structure, and adhesion. *Cell Motility and the Cytoskeleton*, 60(1):24–34, 2005.

[220] Wei-hui Guo, Margo T Frey, Nancy A Burnham, and Yu-Li Wang. Substrate rigidity regulates the formation and maintenance of tissues. *Biophysical journal*, 90(6):2213–2220, 2006.

[221] Alexandre Saez, Axel Buguin, Pascal Silberzan, and Benot Ladoux. Is the mechanical activity of epithelial cells controlled by deformations or forces? *Biophysical journal*, 89(6):L52–L54, 2005.

[222] Ai Kia Yip, Katsuhiko Iwasaki, Chaitanya Ursekar, Hiroaki Machiyama, Mayur Saxena, Huiling Chen, Ichiro Harada, Keng-Hwee Chiam, and Yasuhiro Sawada. Cellular response to substrate rigidity is governed by either stress or strain. *Biophysical journal*, 104(1):19–29, 2013.

[223] John L Tan, Joe Tien, Dana M Pirone, Darren S Gray, Kiran Bhadriraju, and Christopher S Chen. Cells lying on a bed of microneedles: an approach to isolate mechanical force. *Proceedings of the National Academy of Sciences*, 100(4):1484–1489, 2003.

[224] Paul W Wiseman, Claire M Brown, Donna J Webb, Benedict Hebert, Natalie L Johnson, Jeff A Squier, Mark H Ellisman, and AF Horwitz. Spatial mapping of integrin interactions and dynamics during cell migration by image correlation microscopy. *Journal of cell science*, 117(23):5521–5534, 2004.

[225] Tanmay P Lele, Charles K Thodeti, and Donald E Ingber. Force meets chemistry: analysis of mechanochemical conversion in focal adhesions using fluorescence recovery after photobleaching. *Journal of cellular biochemistry*, 97(6):1175–1183, 2006.

[226] T Erdmann and US Schwarz. Stochastic dynamics of adhesion clusters under shared constant force and with rebinding. *J Chem Phys*, 121(18):8997–9017–, November 2004.

[227] Marion Ghibaudo, Alexandre Saez, La Trichet, Alain Xayaphoummine, Julien Browaeys, Pascal Silberzan, Axel Buguin, and Benot Ladoux. Traction forces and rigidity sensing regulate cell functions. *Soft Matter*, 4(9):1836–1843, 2008.

[228] Dale C Bickham, Timothy G West, Martin R Webb, Roger C Woledge, Nancy A Curtin, and Michael A Ferenczi. Millisecond-scale biochemical response to change in strain. *Biophysical Journal*, 101(10):2445–2454, 2011.

[229] J.M. Berg, J.L. Tymoczko, and L. Stryer. *Biochemistry, Fifth Edition*. W.H. Freeman, 2002.

[230] M Dembo, DC Torney, K Saxman, and D Hammer. The reaction-limited kinetics of membrane-to-surface adhesion and detachment. *Proceedings of the Royal Society of London. Series B. Biological Sciences*, 234(1274):55–83, 1988.

[231] C.S. Houston, C.C. Houston, and American Alpine Club. *K2, the Savage Mountain: By Charles S. Houston and Robert H. Bates*. McGraw-Hill Book Company, 1954.

[232] Dong-Hwee Kim and Denis Wirtz. Focal adhesion size uniquely predicts cell migration. *The FASEB Journal*, pages –, 2012.

[233] Sean P Palecek, Christine E Schmidt, Douglas A Lauffenburger, and Alan F Horwitz. Integrin dynamics on the tail region of migrating fibroblasts. *Journal of cell science*, 109(5):941–952, 1996.

[234] Hans G Othmer, Steven R Dunbar, and Wolfgang Alt. Models of dispersal in biological systems. *Journal of mathematical biology*, 26(3):263–298, 1988.

[235] Adam Curtis and Chris Wilkinson. Topographical control of cells. *Biomaterials*, 18(24):1573–1583, 1997.

[236] E. Whymper. *Scrambles Amongst the Alps: In the Years 1860-69*. Dover Publications, Incorporated, 1996.